UNIVERSITÉ D'ORLÉANS

École Doctorale Énergie, Matériaux, Sciences de la Terre et de l'Univers

Laboratoire GREMI (UMR 7344, CNRS)
Groupe de Recherches sur l'Energétique des Milieux Ionisés

THÈSE présentée par :

Jack NOS

soutenue le : **6 novembre 2025**

pour obtenir le grade de : **Docteur de l'Université d'Orléans**

Discipline/ Spécialité : Physique

Study of cryoetching plasma processes using fluorocarbon gases

THÈSE dirigée par :

M. DUSSART Rémi	Professeur des universités, Université d'Orléans
M. TILLOCHER Thomas	Maître de conférences HDR, Université d'Orléans

RAPPORTEURS :

M. BOOTH Jean-Paul	Chargé de recherche, CNRS
M. EON David	Maître de conférences, Université Grenoble Alpes

---

JURY :

M. CARDINAUD Christophe	Directeur de recherche, Université de Nantes, Président du jury
Mme. DESPIAU-PUJO Émilie	Maîtresse de conférences, Université Grenoble Alpes
M. DE MARNEFFE Jean-François	Principal Member of Technical Staff, IMEC
Mme. GIRARD Aurélie	Maîtresse de conférences, Université de Nantes

Jack NOS

Etude de procédés de cryogravure à base de gaz fluorocarbonés

Résumé :

Cette thèse a été réalisée au GREMI dans le cadre du projet ANR PSICRYO, en collaboration avec le laboratoire des technologies de la microélectronique (LTM) et l'institut des matériaux de Nantes Jean Rouxel (IMN). Le but de ce projet de recherche était d'étudier les interactions plasma-surface dans les procédés de cryogravure avancés. Les procédés de cryogravure par plasma se caractérisent par une thermalisation du substrat en dessous de -40°C ce qui permet de renforcer certains mécanismes de passivation. Ces procédés sont à l'étude dans le secteur de la microélectronique car ils permettent des gravures d'une grande précision avec une altération moindre des couches minces de surface. Ce manuscrit résume les résultats de cryogravure obtenus sur des matériaux à base de silicium (principalement Si et SiO_2) en utilisant des procédés cycliques de type Bosch avec la répétition de plasmas fluorocarbonés (c-C_4F_8 et CF_4) suivi de plasma SF_6. Ce travail a été réalisé avec un réacteur ICP qui dispose d'un porte-substrat cryogénique utilisant de l'azote liquide pouvant atteindre -150°C. L'étude s'est principalement portée sur la relation entre les propriétés de gravure obtenues et les paramètres du plasma qui ont pu être caractérisés en fonction de la température du porte-substrat entre 20°C et -150°C. La caractérisation des profils, vitesses et sélectivités de gravure a été réalisée par microscopie électronique par balayage (MEB) et ellipsométrie in-situ. La caractérisation des propriétés des plasmas étudiés a été réalisée par spectrométrie de masse, spectroscopie d'absorption UV ainsi que par sonde capacitive. L'étude s'est principalement portée sur les procédés de type Bosch où il a été démontré que la diminution de la température permettait de renforcer les mécanismes de passivation apportés par plasmas c-C_4F_8. Par la suite, un procédé cyclique utilisant du CF_4 comme gaz de passivation a pu être développé permettant d'obtenir des profils de gravure anisotropiques à -100°C.

Mots clés : Gravure plasma, Cryogravure, Procédé Bosch, Interactions plasma-surface

Study of cryoetching plasma processes using fluorocarbon gases

Summary :

This PhD thesis was carried out at the GREMI laboratory as part of the ANR PSICRYO project in collaboration with the Laboratoire des Technologies de la Microélectronique (LTM) and the Institut des Matériaux de Nantes Jean Rouxel (IMN). The aim of this research project was to study plasma-surface interactions in advanced cryo-etching processes. Plasma cryoetching processes are characterized by a substrate thermalization below -40°C, which enhances certain passivation mechanisms. These processes are currently studied in the microelectronics industry, as they enable high-precision etching with reduced surface damage. This manuscript summarizes cryo-etching test results obtained on silicon-based materials (mainly Si and SiO_2) using cyclical Bosch type processes consisting in the repetition of fluorocarbon plasmas (c-C_4F_8, CF_4) followed by SF_6 plasma steps. This work was carried out using an ICP reactor equipped with a cryogenic substrate holder using liquid nitrogen which can reach -150°C. The study focused on the relationship between the etching properties obtained and the plasma parameters which were characterized in relation to the substrate temperature between 20°C and -150°C. Characterization of etching profiles, etch rates and selectivities were carried out using scanning electron microscopy (SEM) and in-situ ellipsometry. Plasma characteristics were analyzed by mass spectrometry, UV absorption spectroscopy and capacitive probe measurements. The study focused mainly on Bosch-type processes, where it was demonstrated that the decrease of substrate temperature enhanced fluorocarbon passivation mechanisms provided by c-C_4F_8 plasma. Subsequently, a similar cyclical process using CF_4 plasma for sidewall passivation was developed which allowed to obtain anisotropic etch profiles at -100°C.

Keywords : Plasma etching, Cryoetching, Bosch process, Plasma-surface interactions

Groupe de Recherches sur l'Energétique des Milieux Ionisés (GREMI)
14 rue d'Issoudun BP 6744 45067 Orléans Cedex 2

Acknowledgments

The results presented in this PhD manuscript concern a French research project entitled PSICRYO which regroups the LTM (Laboratoire des Technologies de la Microélectronique), GREMI (Groupe de Recherches sur l'Energétique des Milieux Ionisés) and IMN (Institut des Matériaux de Nantes Jean Rouxel) laboratories. This PhD research project covered the experimental aspect of the program which aimed for a better understanding of plasma-surface interactions in cryogenic etching for advanced patterning applications. It was carried out at the GREMI laboratory which is a joint research laboratory unit led by the CNRS and the University of Orléans. This research project was funded by the ANR (French National Research Agency) as well as the ERDF (European Regional Development Fund). I would like to thank the CERTeM (Centre d'Etudes et de Recherches Technologiques en Microélectronique) for providing most of the equipment which was necessary for the experimental part of this project. The realization of this thesis would not have been possible without the help and support of many people, whom I would like to thank sincerely.

Firstly, I would like to thank my PhD directors, Rémi Dussart (GREMI), Thomas Tillocher (GREMI) and Aurélie Girard (LTM). I learned a great deal from their scientific expertise and their guidance. I am grateful to Rémi and Thomas for accompanying me in the analysis and synthesis of my experimental results, as well as their help with the preparation of talks for the various conferences I was privileged to attend. I would also like to thank Emilie Despiau-Pujo (LTM) for instigating and leading the PSICRYO research project.

I would like to express my gratitude to Philippe Lefaucheux who was present every day to resolve technical issues on the diverse plasma reactors and characterization tools that we use at GREMI. His guidance and encouragement were a tremendous help throughout my thesis. I learnt a lot from his technical expertise and I appreciated working with him concerning the installation, preliminary testing and maintenance of the etching reactor I used for the experiments.

During the first months of my PhD, I went several times to the IMN laboratory in Nantes to work on the implementation of reference processes that were necessary for the PSICRYO project. I thank Christophe Cardinaud and Aurélie Girard for always welcoming me and for their help with the experiments I carried out on the OPTIMIST platform. I enjoyed attending the XPS workshop they co-organized in September 2022. Unfortunately, this aspect of the PhD program could not be further explored due to technical difficulties. Sincere thanks to Felipe Cemin, post-doc student who also worked on the OPTIMIST platform for this research project.

This research project was also done in collaboration with the LTM laboratory which focused on the task of developing molecular dynamics simulations based on the cryogenic process tests that were studied at GREMI and the IMN. Several exchanges were organized to share experimental results obtained as well as general knowledge on the subject of cryoetching processes. I thank again Emilie Despiau-Pujo for the organization of these meetings. Sincere thanks to Jonathan Cedillo, PhD student at the LTM

laboratory who is also part of the PSICRYO project. I wish him the very best towards his research on simulation models applied to cryo-etching processes.

I would like to commend and thank Sylvain Iséni (GREMI), Gilles Cunge and Martin Kogelschatz (LTM) for their expertise in absorption spectrometry. Their help in the preparation and organization of the absorption spectroscopy experiments was crucial. I would like to thank them for the time they gave to carrying out these experiments and for their help concerning data treatment and analysis.

I was also lucky to carry out several process experiments in the company and help of Lawrence (Larry) Overzet (University of Texas at Dallas). His knowledge, curiosity and humor were enlightening to me.

I would also like to thank my fellow PhD students and post-doc colleagues in the etching and micro-discharge team at GREMI: Gaëlle, Rim, Lamiae, Elane, Angela, Fériel, Ayoub, Madjid and Baptiste. It was fantastic to work in your company and to learn from you all !

Many thanks to Sylvie Jauffrion and Corinne Delhaye for their help in all the administrative tasks during my PhD as well as for the organization of scientific conferences we held in Orléans.

My warmest thanks to my fellow PhD students and post-docs at GREMI involved in other research groups, in instance Andrea, Rubenson, Soumya, Dimitri, Amaury, Alex, Charaf, Augusto, Vinni, Eloïse, Robin, Glenn, Sibel, Tian, Taleb, Sara and Stéphanie.

I would also like to thank my previous apprenticeship tutor, Mohamed Boufnichel, as well as all my former colleagues at ST Microelectronics from the Research & Development Process Etch Team including Julien Ladroue, Vincent Caro, Morgane Dutour and Philippe Martinez. Their help as well as the experience I gained working with them during my 3 years as an apprentice engineer were a tremendous help as I started my PhD.

Last but not least, I would like thank my family, my partner and my close friends. Completing my PhD without their support would have been very difficult.

Table of contents

List of abbreviations and acronyms

ALD	Atomic Layer Deposition
ALE	Atomic Layer Etching
ANR	Agence Nationale de la Recherche (French National Research Agency)
APC	Automatic Pressure Control
AR	Aspect Ratio
ARDE	Aspect Ratio Dependent Etching
AOI	Angle Of Incidence
a- Si	Amorphous Silicon
BEOL	Back-End Of Line
b- Si	Black Silicon
CCD	Charge-Coupled Device
CCP	Capacitively Coupled Plasma
CERTeM	Centre d'Études et de Recherches Technologiques en Microélectronique
CNRS	Centre National de la Recherche Scientifique (French National Centre for Scientific Research)
Cobra	Oxford Instruments Plasma Pro 100 Cobra Reactor
c-Si	Crystalline Silicon
c- C_4F_8	Octafluorocyclobutane
CVD	Chemical Vapor Deposition
DRAM	Dynamic Random Access Memory
EEPF	Electron Energy Probability Function
ERDF	European Regional Development Fund
FC	Fluorocarbon
FEOL	Front-End Of Line
FET	Field Effect Transistor
GREMI	Groupe de Recherche sur l'Energétique des Milieux Ionisés
GWP	Global Warming Potential
HF	High Frequency
HJY	Horiba Jobin Yvon
ICP	Inductively Coupled Plasma
IEDF	Ion Energy Distribution Function
kTe	Electronic potential
LF	Low Frequency
LPCVD	Low Pressure Chemical Vapor Deposition
LTM	Laboratoire des Technologies de la Microélectronique
MEMS	Micro-Electrical-Mechanical Systems
MFC	Mass Flow Controller
MID	Multiple Ion Detection
Mono	Monochromator
MOSFET	Metal Oxide Semiconductor Field Effect Transistor
MWL	Multiwavelength
Ne	Electron density
Ni	Ion density
NIR	Near Infrared
OES	Optical Emission Spectroscopy
OPTIMIST	Opening of a Technical Platform for the Investigation of the Mechanisms of Interaction between plasma and Surface on a large Temperature range
PhD	Doctor of Philosophy
p-Si	Polycrystalline Silicon

PECVD	Plasma Enhanced Chemical Vapor Deposition
PID	Proportional Integral Derivative
PR	Photoresist
PSICRYO	Understanding Plasma-Surface Interactions in Cryogenic etching for advanced patterning applications (ANR Project)
RGA	Residual Gas Analysis
RF	Radio Frequency
RFEA	Retarding Field Energy Analyzer
RIE	Reactive Ion Energy
DRIE	Deep Reactive Ion Energy
sccm	Standard cubic centimeters per minute (unit)
SE	Spectroscopic Ellipsometry
SEM	Scanning Electron Microscopy
SiO_2	Silicon Dioxide
Si_3N_4	Silicon Nitride
STiGer	Deep etching cryoetching process developed and patented by ST Microelectronics and GREMI
TEL	Tokyo Electron Limited
TSV	Through-Silicon-Via
TVT	Trench Via Trench sample
QMS	Quadrupole Mass Spectrometry
Vp	Plasma Potential
Vf	Floating Potential
XPS	X-ray Photoelectron Spectroscopy
Ws	Source Power in watts (unit)
Wb	BIAS Power in watts (unit)

Chapter I: Introduction to plasma etching and interest of cryogenic processes

1.1 General Introduction

The semiconductor industry and microelectronics technology is one of the sectors that has undergone the most thriving advances in the last century. From the very first point-contact transistor device introduced in 1947 by W. Shockley, J. Bardeen and W. Brattain at Bell Laboratories [1–3] to the most up to date microprocessors which feature more than 208 billion transistors [4,5], tremendous technological advancements have been realized in order to miniaturize and mass produce electronic devices which have shaped the contemporary digital landscape.

The inventions of the planar field effect transistor (FET) by W. Shockley in 1952 [6] followed by the metal-oxide-semiconductor FET (MOSFET) developed by D. Kahng and M. Atalla in 1960 also at Bell Laboratories [1,7–9] gave way to a series of innovations concerning the structure and design of transistors which have become increasingly complex and performant [10–13]. All of these technologies contributed to the decrease of transistor critical sizes including the gate length and width, channel length as well as the pitch size. Nowadays, companies such as TSMC, Samsung and Intel have managed to reduce the critical dimensions of these MOSFETs which have reached the node scale of 3 nm which are also referred to as 3nm process technology nodes [14–16]. Transistor nodes inferior to 2 nm are currently being developed and should reach the production stage no later than in 2025 [15–19]. **Figure I.1** shows the structure of the IBM 2nm three-stack gate-all-around / nanosheet field effect transistors (GAAFET).

Alongside other electrical components such as diodes, resistors and capacitors which have also passed through the miniaturization stage, transistors are fabricated on a variety of integrated circuits. A first example was invented by J. Kilby at Texas Instruments in 1959 using discrete wire interconnections to connect components on a silicon piece [20] which were then replaced by thin-film metal interconnections deposited directly on the substrate as proposed by R. Noyce from Fairchild Semiconductor Corporation [21].

Since its prediction in 1965 [22], Moore's law, which stated that the number of transistors on a given microchip area should double every 2 years, has been globally respected until the early 2000s notably due to Dennard scaling [10,13]. This scaling law proposed to shrink the feature size of by 0.7 for every new generation of transistors which enables to double their density while conserving its surface power consumption. Since this point of disruption, Dennard geometrical scaling for planar FETs was no longer a viable option to reduce the size of transistors due to inherent high leakage currents that occurred near the 90nm node scale. As a result, the innovation pace imposed by Moore's law has slightly slowed down despite the appearance of new FET architectures and the use of other materials enabled to further decrease their size while limiting power consumption as is shown in **figure I.2**. Technological solutions were also found to improve computing performance such as the appearance of multicore processors. Since this period, manufacturing costs have surged for every new transistor generation.

Figure I.1: SEM image of the IBM 2nm three-stack Gate-All-Around / nanosheet Field Effect Transistors (GAAFET) (taken adapted from [18,19])

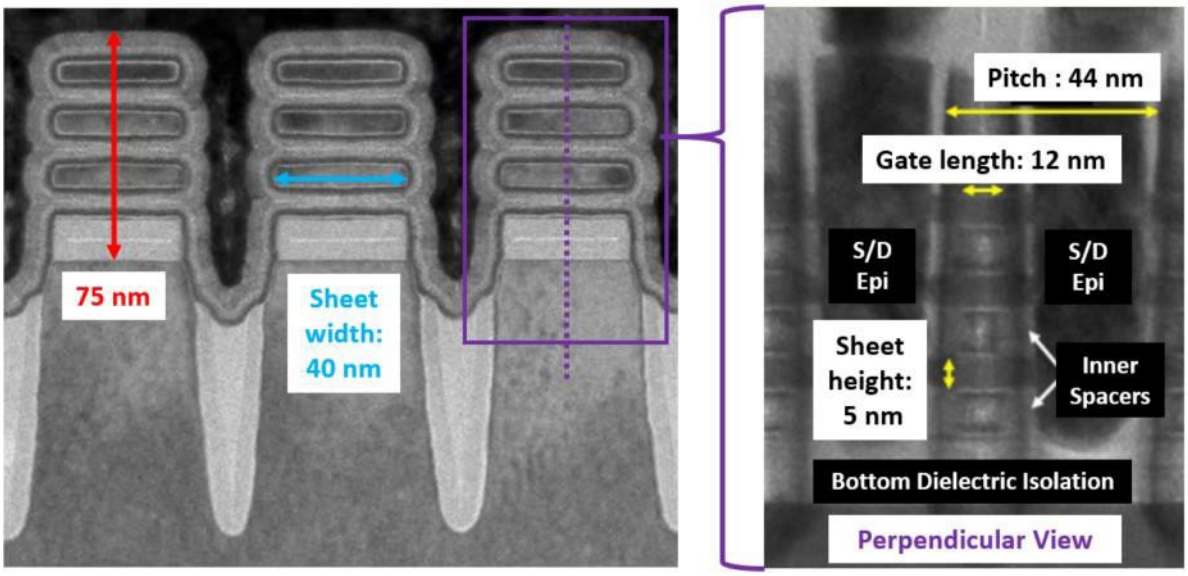

It is believed that transistor nodes should attain the scale of 1 nm by 2031 [10] where they could go down to the size of a single monoatomic layer which typically ranges from 1 to 7 Å depending on the elements and estimation method for the determination of a monolayer [23–25]. At this point, the maximal physicochemical limits will be reached. The development of these future FETs requires the implementation of new designs and structures which are less inclined to short channel effects at the 10nm channel length limit such as self-heating, interface issues and large process variability. To that matter, the emergence of two-dimensional semiconductor materials and carbon nanotubes amongst other solutions are being studied for their higher performances and their atomic scale processing uniformity [10,26].

As a result, semiconductor manufacturing processes have become increasingly demanding and require ever more precise and expensive equipment. Numerous challenges await the semiconductor industry in the upcoming years. The cyclical demands for an increasing variety of chips creates tensions in the supply flow. For the most complex chips, several hundreds of fabrication steps are needed which can amount up to several months of processing between the beginning of production to the final product [27,28]. The supply chain and production volume for certain fabrication plants is now so large that they are now often referred to as chip gigafactories. These are usually dedicated to the manufacturing of certain components by regrouping the necessary compatible equipment and become increasingly expensive as the technology of these chips advances. As an example, TSMC invested roughly $14 billion to build its Fab 18 finished in 2020 for the production of 5 nm chips in Taiwan [29]. Between 2020 and 2023, it was seen that the concentration of chip production of key components around a handful of these gigafactories coupled to the high flow of orders, temporary closings or shortages due to Covid-19 and environmental hazards caused important supply delays. It affected numerous sectors of the global economy as was seen for the automotive industry or the production of graphic cards or household appliances [30–32].

Figure I.2: Evolution of MOSFET structures and scaling stages from 2003 (taken from [10])

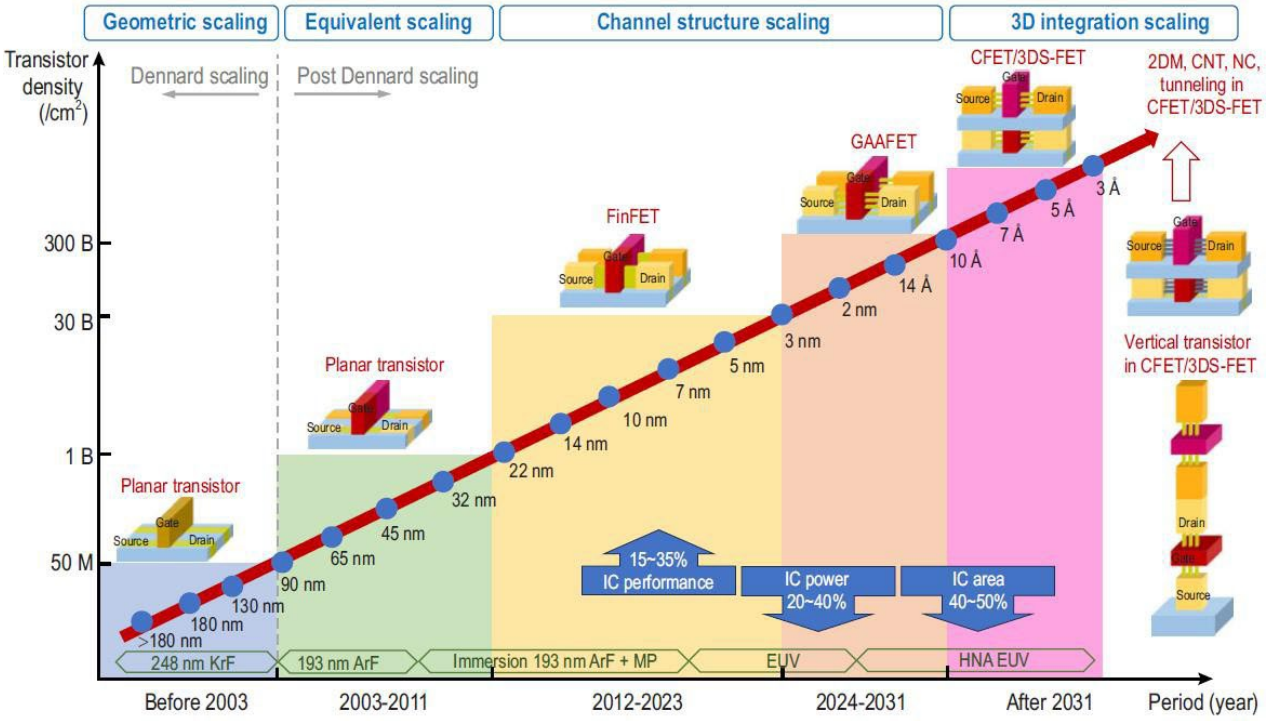

Since then, the semiconductor sector is the focus of massive public and private investments from all major industrial powers which include the USA, Taiwan, China, Japan, South Korea and to a lesser extent the European Union (EU) which wants to maintain or increase their share in this growing market [27,33–37]. From 2012 to 2022, the global sales of semiconductor chips doubled to reach a value of over $602 billion [27]. The technological leadership in this sector is a source of geopolitical and commercial tensions between major economic powers. Nevertheless, there is a general desire to relocate and spread-out chip production to ensure a more sustainable supply for other industries with the construction of new chip gigafactories across the world. However, the increasing demand in chips is set to continue especially with the rise of artificial intelligence (AI) which will generate strong additional demand in terms of orders and innovation towards the enhancement of computational performances [38,39].

The semiconductor industry is also under growing criticism for its environmental impact [40–43]. Indeed, chip production takes up an increasing amount of resources including fresh water, energy and rare metals. In 2021, the total energy and water consumptions of 27 of the biggest semiconductor manufacturers around the world amounted to 1.49×10^{11} kWh and 7.89×10^{8} m^3 respectively [42]. This represents approximately 19.2% of the French annual water consumption and 35.1% of the French annual energy consumption in the same year [44,45]. Microfabrication also requires the use of toxic substances which are not environmentally friendly such as acids and gases. Important efforts are consented towards the reduction of its environmental footprint including water and gas recycling treatments as well as process optimization [42,43,46]. Concerning the last aspect, continuous research and development is carried out concerning plasma processes which are necessary to microfabrication for deposition and etching applications. In this field, process engineers and researchers develop

processes which are increasingly demanding in terms of accuracy and productivity but also have to consider the reduction of their environmental impact.

Most process gases, which include per- and polyfluoroalkyls substances (PFASs), per-and polyfluorinated compounds (PFCs) and hydrofluorocarbons (HFCs) are subject to international regulations due to their high environmental impact [41,47]. These gases have a significant impact on global warming due to their global warming potential (GWP) and long lifetime in the atmosphere. The global warming potential index of a greenhouse gas (GHG) is defined as the heat it can trap through infrared thermal radiation absorption in the atmosphere over a specific time. It is expressed in carbon dioxide equivalent unit (CO_2-eq) which corresponds to the mass of CO_2 which would capture as much heat as the mass of the specific gas over the period of 100 years [41,43,48]. However, most of these substances have a longer lifetime in the atmosphere than CO_2 which remains in the atmosphere between 5 and 200 years. This is due to their high chemical stability with the presence of strong CF bonds and their low reactivity with chemicals present in the atmosphere which could lead to their degradation.

Moreover, the global estimation of the ecological impact of these chemicals is more complicated to grasp than just considering their GWP index when they are emitted. All direct and indirect ecological impacts of these substances are accounted for in the greenhouse gas protocol [41,49]. This calculation method also encompasses the effectiveness of abatement systems for these specific gases. Indeed, scrubbers are now used in the semiconductor industry to treat greenhouse gases at the exhaust of processing reactors. They can take many forms including heating, burning, plasma and wet treatment technologies which can be combined to crack PFC and HFC chemicals. This sector is the subject of active research at the moment [50]. Generally, the efficiency of abatement systems depends on the substance and its proper chemical properties such as bind energies. They are defined by their destruction and removal efficiency (DRE) as well as the potential by-products they may generate [41,50]. In many cases, the cracking of C_xF_y molecules leads to the generation of CF_4 by-product which is difficult to crack and amounts to 32% of the fluorinated gas emissions produced by front-end semiconductor manufacturing in 2020 whereas it only represents 11% of the fluorinated gas consumption by this industry in the same period [41]. To that matter, **table I.1** presents the GWP index and lifetime in the atmosphere of key fluorinated gases used in the semiconductor industry in 2020 as well as the share they represented in consumption and emissions. In 2020, the semiconductor industry emitted 4.7 $MMtCO_2$-eq (million metric ton of carbon dioxide equivalent) of PFC gases which is roughly ten times more important than the French emissions of PFCs during the same year [41,51].

In Europe, all these substances are subject to emission allowances traded on the EU emissions trading system (ETS). It follows a cap-and-trade principle which gradually increases production costs [52]. To comply with environmental objectives, semiconductor manufacturers explore new pathways to modify and change their processes. These include different solutions such as gas dilution, gas consumption reduction, the use of new gases of interest, power consumption reduction, gas abatement technology improvement and the reduction of process steps [41,50,53]. As an example, most industrial processes which included SF_6 as an etching gas have been modified to include NF_3 gas which has a lower GWP

potential and lifetime in the atmosphere while having a similar etching potential [41]. However, the full implementation of non-PFAS alternatives in the industry is expected to take at least 15 years.

Another solution which has not yet been deeply explored is the reduction of substrate temperature and cryogenic processing. Introduced in 1987 by *Tachi et al* [54], cryo-etching processes have long been sidelined by manufacturers in favor of room-temperature processes, which are deemed more robust and do not require the installation of cryogenic infrastructures. Today, however, these processes are attracting renewed interest in R&D, particularly for applications involving precise etch control with important chemical selectivities between different materials [46,55–57]. Cryogenic processes are currently being studied for the etching of conventional semiconductor materials such as Si or Ge but also for emerging semiconductors including GaN, 2D materials (MoS_2, graphene) as well as porous and low-K materials [46,56].

Table I.1: GWP and atmospheric lifetime of main fluorinated gases with their consumption and emissions percentage in the semiconductor manufacturing industry in 2020 (taken and adapted from [41])

Gas	GWP (index)	Lifetime (years)
CO_2	1	5-200
CHF_3	14,600	228
CF_4	7,380	50,000
C_2F_6	12,400	10,000
C_3F_8	9,290	2,600
C_4F_8	9,540	3,200
NF_3	17,400	569
SF_6	25,200	3,200

Gas	Consumption (%)	Emissions (%)
TOTAL	23.2 x 10^6 kg	4.7 $MMtCO_2$-eq
CHF_3	3 %	8 %
CF_4	11 %	32 %
C_2F_6	3 %	17 %
C_3F_8	1 %	2 %
C_4F_8	5 %	7 %
NF_3	70 %	22 %
SF_6	3 %	8 %
Other	4 %	4 %

They rely on the thermalization of the substrate holder at very low temperatures which allows to enhance gas condensation on the substrates which are etched. It represents a promising approach of optimizing gas flows required for device manufacturing, in order to reduce the gas consumption and environmental impact of these processes. Moreover, cryogenic processes can contribute to reducing surface roughness, especially on the trench sidewalls which can be applied to the obtention of high aspect ratio features. It also allows to limit the eventual damaging effects of ion bombardment on the underlying thin layers of material. The standard cryoetching process and cryogenic STiGer process are also polymer-free which can be useful for certain applications to reduce carbon contaminants [58].

However, many of the mechanisms involved in gas condensation and plasma-surface interactions at cryogenic temperatures are not yet clearly established. The simulation of plasma processes is becoming increasingly important to account for chemical and physical etching mechanisms as well as plasma-surface interactions in general. Different types of simulation techniques have progressively emerged. They enable a better understanding of plasma processes and can contribute to their optimization while anticipating certain undesirable phenomena [59,60]. To that matter, the

development of artificial intelligence (AI) programs is currently being investigated with the objective of reducing process testing costs [61]. In this context, molecular dynamics (MD) simulations can provide helpful information regarding etching reactions occurring at the atomic scale [62–64]. This simulation method has been successfully applied to model numerous ambient temperature etching processes. These types of simulations rely on the implementation of a potential function which defines how specific chemicals will interact. The first many-body potential for silicon etching including Si-F interactions was introduced by *Stillinger et al* in 1989 [65]. Many other potentials have since been developed to model plasma-surface interactions using specific conditions and to simulate different types of plasma etching chemistries. Molecular dynamics simulations are now facing growing interest concerning their application to cryogenic processes which represents a new challenge.

For their implementation and enhanced accuracy, many of these simulations and their interatomic potentials are based on experimental data [63,64,66]. These include quantitative parameters such as sticking probabilities, thermal desorption rates, surface diffusion rates as well as sputtering yields of reactive species involved during these processes, which all vary in relation to substrate temperature. Moreover, this technique aims to correlate plasma properties with etching characteristics as is shown in **figure I.3.** Therefore, this work requires a substantial input of experimental data, both in terms of characterizing plasma properties in relation to the process inputs but also their etching result on a given substrate.

Figure I.3: Schematic diagram representing the properties and diagnostics methods of a plasma etching process (taken and adapted from [62])

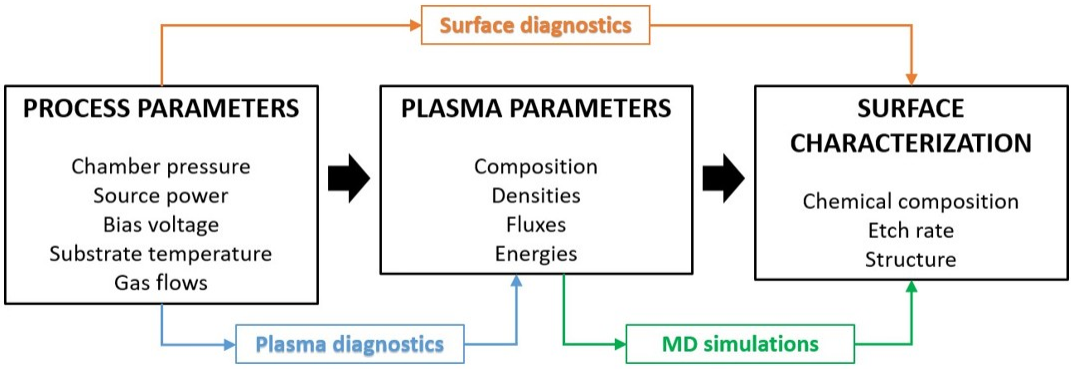

The investigation and experimental measurement of these quantitative parameters during cryogenic processes can also be quite challenging. Indeed, elementary reactions which take place at the plasma-substrate interface cannot be easily and directly characterized experimentally during a plasma process. Moreover, the characterization of cryogenic reactions implies necessarily in-situ diagnostics such as ellipsometry, mass spectrometry or XPS in order to quantify species that will inevitably desorb and be absent during ex-situ analysis [67].

It is in this context that this research project takes place. The PSICRYO project aims at investigating the fundamental mechanisms of plasma-surface interactions (PSI) at cryogenic temperature (CRYO) and

to develop cryo-ALE processes of various materials for advanced patterning applications. It is a joint collaboration which regroups three French research laboratories : LTM (Laboratoire des Technologies de la Microélectronique), GREMI (Groupe de Recherche sur l'Energétique des Milieux Ionisés) and IMN (Institut des Matériaux de Nantes Jean Rouxel).

The main objective of this research project was to characterize etch results and plasma properties during the performance of various cryogenic etching processes of interest. The accumulation and analysis of experimental data is intended to contribute to the development of MD simulations at the LTM laboratory which aim to model plasma-surface interactions involved during these cryogenic etching processes. This work was first done for conventional cryogenic etching processes including standard cryoetching and STiGer processes. Subsequently, it was decided to focus on the study of fluorocarbon plasma processes in relation to the substrate temperature, both for deep and thin etching applications. The experimental results obtained within this particular framework will be discussed in the following manuscript.

For this research study, the impact of Bosch processing at cryogenic temperatures was first evaluated for deep-silicon etching. To that matter, c-C_4F_8 and CF_4 plasma deposition properties were examined in relation to process parameters. Furthermore, c-C_4F_8 condensation and desorption properties were studied on SiO_2 substrates at cryogenic temperatures.

In order to summarize the main experimental results obtained during this research project, this manuscript is organized in the following way:

The first chapter will cover the general aspects of semiconductor microfabrication and introduce the main characteristics which are associated with plasma etching processes. The principal plasma etching techniques of interest will be presented and commented within the scope of this research study.

The second chapter presents the experimental set-up and characterization methods that were used for this research project. The ICP reactor characteristics will be presented as well as the various samples that were used. The characterization techniques that were used will be described as well as the main acquisition parameters and analysis methods.

The third chapter will focus first on the results obtained concerning the performance of standard Bosch processing using c-C_4F_8 at a substrate temperature of -100°C with different process configurations. Etch profiles obtained at ambient temperature and at -100°C using the same process conditions will be compared to evaluate at which extent fluorocarbon passivation is more efficient at cryogenic temperatures.

The fourth chapter will present the results of an exhaustive parametric study which was carried out on the c-C_4F_8 plasma deposition step where the substrate temperature was varied from 20°C to -150°C. The chapter will also focus on the study of c-C_4F_8 adsorption at cryogenic temperatures. A brief introduction to adsorption mechanisms will first be given before presenting the experimental results of c-C_4F_8 adsorption and subsequent desorption tests which were realized on silicon surfaces in relation to substrate temperature.

Subsequently, optical emission spectroscopy (OES) acquisitions using CF_4 plasma in relation to substrate temperature will be presented in the fifth chapter. These OES acquisitions enabled to estimate and compare the density of CF and CF_2 radicals just above the substrate surface during CF_4 plasma exposition where the substrate was either thermalized at -130°C or at ambient temperature. The results obtained through these acquisitions enabled to implement a Bosch-type process using CF_4 as a passivation gas which will also be discussed.

1.2 Presentation of the main semiconductor actors, products and microfabrication processes

1.2.1 Semiconductor actors

The semiconductor industry involves numerous companies which are part of an extensive worldwide supply chain. It regroups chip design, fabrication as well as chip assembly, testing and packaging [27]. Front-end manufacturing includes all the processes which are necessary to fabricate integrated circuits on silicon wafers. Back-end manufacturing refers to all the processes which are necessary to individually separate the integrated circuits from the silicon wafer and assemble the final electronic products. It includes dicing, molding, packaging as well as individual testing. Although these activities are often separated in different locations, they are highly interconnected and require constant collaboration to ensure product quality and overall productivity. Moreover, manufacturers depend on equipment, materials, chemicals and gas suppliers.

Semiconductor manufacturers are classified according to the activities they operate in the supply chain [27]. Integrated device manufacturers (IDMs) take care of nearly all the operations needed to fabricate their products from the design to the packaging of the chips. Examples of contemporary IDMs include Samsung, Intel, STMicroelectronics and Texas Instruments. Until the 1960s, most companies operated according to this model. Since then, other companies which specialize in certain activities of the supply chain have emerged. This allowed several IDMs to progressively delegate back-end activities which are generally less lucrative and offer lower added value to other actors referred to as OSATs (Outsourced Semiconductor Assembly and Testing companies). This enabled chip designers to reduce costs and focus on front-end manufacturing activities. With the increasing complexity and cost of semiconductor manufacturing, chip designers also progressively delegated front-end manufacturing activities to other companies which greatly reduced the number of IDMs. Today, a fabless company refers to an entity which designs electronic products without manufacturing them. To do so, they contract foundries, which are companies that concentrate manufacturing activities in a fabless/foundry business model. Examples of contemporary fabless companies include Apple, Broadcom and Nvidia whereas examples of contemporary foundries include TSMC, Global Foundries, SMIC and UMC. Major OSAT companies include ASE, Amkor and JCET.

The design of new products and complex electronic circuits is usually done via Electric Design Automation (EDA) software [27]. This software includes intellectual property (IP) blocks which can be used for various functions. These licensed products allow to refine and adapt chip designs to fit customer requirements without having to redevelop a completely new design every time. In order to implement a fabrication process from a design realized through EDA software, foundries develop Process Design Kits (PDKs) which allows designers to verify their design according to the processing capabilities of the foundry in question. To date, major EDA software providers include Synopsys, Cadence Design Systems and Siemens EDA whereas Arm Holdings plc is one of the leading providers of IP blocks in various chip technologies.

Equipment suppliers provide the necessary tools to ensure front-end and back-end manufacturing. Major photolithography manufacturers include ASML, Canon and Nikon which provide advanced photolithography tools equipped with extreme or deep ultraviolet (EUV or DUV) light source technology to pattern the most advanced chips. Other complex front-end manufacturing tools include deposition, cleaning, etching, implantation and diffusion equipment. Major companies that provide this type of equipment for semiconductor manufacturers include Applied Materials, LAM Research, TEL and KLA Corporation. Wafer characterization, handling and planarization tools are also required for microfabrication and verify the accuracy of every process step.

All the necessary equipment for front-end manufacturing is regrouped in facilities called fabs or foundries where the processes are optimized to produce the highest yield of functioning chips where several hundreds of process steps are required for the most complex chips [27,28]. Fabs are often classified according to their wafer size (usually 150, 200 and 300 mm), their process technology node and production capacity. Raw silicon wafers are produced through single crystal silicon ingots which are sliced, ground and polished according to the manufacturer's needs. Silicon wafer suppliers include SUMCO, Shin-Etsu, GlobalWafers, Siltronic and SK Siltron. While silicon is still the main substrate used, other types of semiconductor substrate material, such as germanium (Ge), silicon carbide (SiC), indium phosphide (InP) or gallium arsenide (GaAs) have appeared in the industry thanks to their proper enhanced semiconducting performances.

1.2.2 Main electronic products

Semiconductor fabrication regroups a wide variety of chips which have different functions. They are produced in separate facilities usually by different manufacturers which specialize in their specific processing. Once they are each assembled, they are integrated together on circuit boards of proper electronic products such as computers, smartphones etc. The main type of semiconductor chips regroup logic, memory, analog and OSD (Optoelectronic, sensors and discrete) products.

Logic chips are used to process information. They include microprocessors as well as microcontrollers which are used notably in smartphones, computers and other smart devices. They represent the largest share in semiconductor market sales (approximately 42% in 2021) [27]. They are complex chips which concentrate the latest FET structure and processing innovations to maximize computing efficiency and usually focus the most attention.

Memory chips are used to store information. They include products such as NAND flash and DRAM (Dynamic Random Access Memory). They present the second largest share in semiconductor market sales (roughly 28% in 2021) [27]. NAND products have considerably evolved over the past years with the development of increasingly complex structures (3D NANDs and 4D NANDs) that can accumulate now up to more than two hundred layers [68]. This has allowed a sharp increase in the memory capacity of USB sticks which could store a few gigabytes in 2008 and can now reach up to 1 Tb in

2024 [69]. Consequently, the processing flow of these structures has become increasingly complex yet they do not use the most up to date process node technologies.

Analog chips regroup a great variety of functions which include signal conversion and power management with products such as amplifiers or RF filters. They represented 13% of semiconductor sales in 2021 [27]. Concerning OSD chips, optoelectronic products are used for light applications (LEDs, photodiodes, laser diodes). Sensor products are used to measure physical properties such as temperature (thermocouples, thermistors) and pressure (diffused silicon pressure sensor, MEMS pressure sensors). Discrete products are single devices which regroup a single function concerning data treatment (diodes, capacitors, transistors, thyristors). In total, OSD products regrouped roughly 17 % of semiconductor sales in 2021 [27].

1.2.3 Microfabrication steps

The first basic steps for semiconductor microfabrication starting from a bare silicon wafer are resumed simplistically in **figure I.4**. It is in reality a complex process which requires an increasing number of patterning steps followed by material modification steps depending on the chip technology [27,28,70,71]. The main process steps of the process flow are summarized below.

Silicon wafer production: Silicon wafers are produced through single crystal silicon ingots which are grown using molten polycrystalline silicon heated at high temperature and conditioned by argon gas using the Czochralski method or the float-zone method [70]. Chemicals such as phosphorus, boron or arsenic can be added to dope the silicon ingot (N-type or P-type). A single crystal silicon seed is then introduced in the furnace and pulled out delicately to form the silicon ingot with a single crystalline orientation (<100>, <110>, <111>…) with a high purity and a given diameter. The ingots are grown to the adequate diameter and cut into wafers at a given thickness using an annular or wire saw. Wafers are then lapped and etched to remove damaged surfaces before being polished to smoothen the surface. They are then cleaned to remove any contaminants and are then ready to be processed.

Deposition: From a blank silicon wafer or after a photolithography process, multiple deposition processes exist in order to add a new material with a given thickness on the exposed surface area. This step can be done for two opposite reasons. Either to add a conductive layer (usually metallic layers) to electrically interconnect different areas of the wafer or to add a dielectric layer (SiO_2, Si_3N_4, TiO_2, Al_2O_3, …) to electrically insulate them. Different techniques exist according to the material, thickness and structure that is desired [70,71].

Chemical vapor deposition (CVD) techniques enable the deposition a thin layer of material using gaseous chemical precursors that decompose in a reactor chamber and react on the surface to produce the desired material. These techniques are classified depending on the activation energy and precursors

which are used to trigger the deposition reaction which include thermal CVD (TCVD), plasma-enhanced CVD (PECVD) and Metal-Organic CVD (MOCVD).

Physical vapor deposition (PVD) techniques enable the deposition of thin layers of material using a solid or liquid chemical source which will transition to a vapor phase in order to be transported to the surface layer in order to deposit in a condensed phase. The deposited material is physically transferred from a source to the wafer surface. These techniques include sputtering, evaporation and molecular beam epitaxy (MBE).

Thermal oxidation is a technique that allows the modification of the surface layer of the silicon substrate and generate a SiO_2 layer. The process is performed at high temperature (800°C to 1200°C) and uses an oxidizing agent (O_2 or water vapor) that diffuses inside the silicon material.

Atomic layer deposition (ALD) techniques enable the deposition of thin layers of materials (pure metals, metal oxides, metal nitrides, …) with atomic scale precision [72]. Just like CVD processes, they imply chemical precursors that are introduced sequentially to deposit monoatomic layers of material.

Lithography: During a photolithography step, the wafer is coated with a photoresist which is a light-sensitive material. When exposed to a UV light treatment, which is conveyed to the silicon wafer through a patterned mask, the chemical properties of the photoresist change in the exposed areas [28,70]. After a chemical treatment called development phase, the mask pattern image (positive or negative) is printed on the silicon wafer depending on the photoresist type with a specific thickness. This patterned photoresist layer is meant to protect the underlying layer from being altered during the next material modification stages. Therefore, only the exposed areas will be processed until the photoresist layer is removed through a chemical stripping process.

Etching: Following a photolithography process, the pattern printed on the silicon wafer is etched in the exposed areas. The etching process step has to be controlled in order to reach a certain etch depth and must not etch completely the photoresist material to not affect the protected areas. To do so, two etching techniques exist, wet etching which uses chemical solutions such as acids and dry etching which uses plasmas. In general, dry etching techniques are preferred because they enable etching the exposed areas anisotropically which allows to maximize the wafer area. On the contrary, wet etching techniques are usually isotropic. It means the exposed material will be etched in a uniform manner and will remove material situated under the area which is protected by the photoresist mask.

Doping: Ion implantation enables to locally dope the substrate by adding impurities to the exposed material which will ultimately deliver its semiconducting properties. Common ions used for silicon doping include phosphorus, boron and arsenic. After ion bombardment exposition, the wafer undergoes an annealing thermal treatment to activate dopants and repair the damage caused by ion implants.

Chemical mechanical polishing/planarization (CMP) and cleaning processes: CMP techniques are used for surface planarization of the silicon wafer substrate. They can be used after or before material modification steps during the microfabrication process in order to remove different types of contaminants (metal or oxide particles) and smooth uneven surfaces. During the process, the wafer is

positioned on a rotating polishing pad which is fed by a chemical slurry containing water, abrasives and chemicals. A conditioning disk and a chemical head maintain a homogeneous force to distribute the slurry homogeneously. Following this process, the wafer is rinsed, brushed and dried to remove remaining contaminants. Other cleaning processes such as acid and rinsing baths or O_2 plasma treatments can be used to remove contaminants or to descum photoresist which may have partially developed in unwanted areas. All these planarization and cleaning processes are crucial to maintain a clinical result after each step throughout the whole microfabrication process.

Assembly & Packaging: Once the silicon wafer has undergone all the necessary microfabrication steps, it is then transferred for back-end manufacturing. It is first diced in order to cut and separate the chips it contains. It can be done using various techniques such as diamond blades or laser beams. The final electronic component is then assembled by fixing the single chip on a lead frame terminal (die bonding) and adding wire interconnections adequately (wire bonding). The chip is then placed in a case with molded epoxy resin to protect it from damage (molding or packaging) to obtain the final electronic product.

Figure I.4: Schematic diagram of semiconductors microfabrication steps

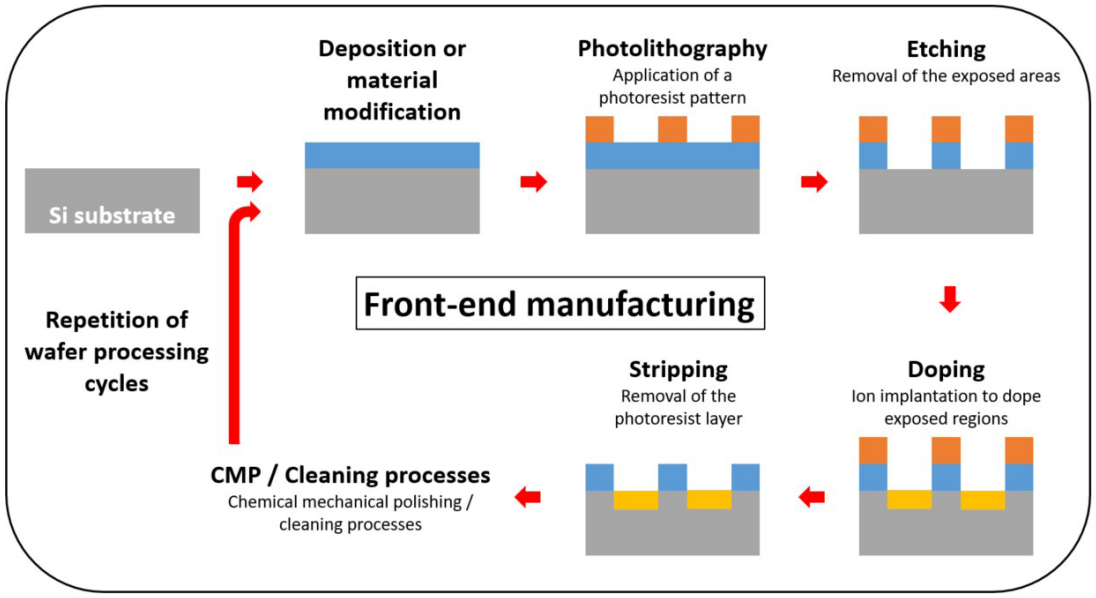

1.3 Introduction to plasma etching processing

1.3.1 Short introduction on low-temperature plasmas

Often referred to as the fourth state of matter, plasmas compose more than 99% of the baryonic matter of the Universe through various forms (stars, comet tails, supernovae, nebulae, …). On Earth, natural forms of plasmas are quite rare although they include lightning and polar auroras [73]. A plasma is defined as a state where a sufficient portion of particles are ionized and follow a collective behavior. It is composed in instance of neutral species, radicals, ions and electrons moving in random directions which respect a quasineutral distribution on the macroscopic scale [74–76]. Plasmas are electrically conductive, highly reactive and sensitive to their surrounding electromagnetic fields.

Human knowledge and use of plasma applications only began in the 19th century with the observation of arc discharges by Sir Humphry Davy as well as Vasily Petrov who initiated the development of electric arc lighting and fluorescent lamps [77]. Later, the observation of cathode rays was made in instance by Julius Plücker, Johann Wilhelm Hittorf as well as Sir William Crookes during the study of electric discharges in low pressure gases using Geissler or Crookes-Hittorf tubes [78–80]. Irving Langmuir was the first scientist to describe and study plasma in the 1920s and gave it its name due to its operating similarity with blood plasma [81,82]. He introduced the concept of electron temperature and developed the Langmuir probe to characterize diverse plasma properties. Subsequently, diverse plasma applications were developed in the late 20^{th} century such as plasma arc welding, plasma display screens as well diverse material plasma treatments including plasma etching. Future potential plasma applications include the treatment of cancer diseases and nuclear fusion plasma as an energy source.

Due to their nature, plasmas can be subclassified into diverse categories. One of the most important distinctions is the notion of low-temperature and high-temperature plasmas. In the semiconductor industry, low-temperature (or non-thermal) plasmas are used for etching applications. They are characterized by a low ion temperature (T_i) that is usually equivalent to the gas temperature (T_g) and both of them being greatly inferior to the electron temperature (T_e) that can reach up to 10^5 K (≈ 10 eV) [76]. These types of plasma are usually performed at low pressure (< 13 Pa) where they are easier to strike and maintain by pumping the reactor with sophisticated vacuum pumps. A picture of a low temperature plasma performed on a clamped silicon wafer in an ICP (inductively coupled plasma) reactor is shown in **figure I.5**.

Figure I.5: Image of a low temperature C_4F_8 plasma in an ICP reactor applied on a clamped wafer with a glued sample

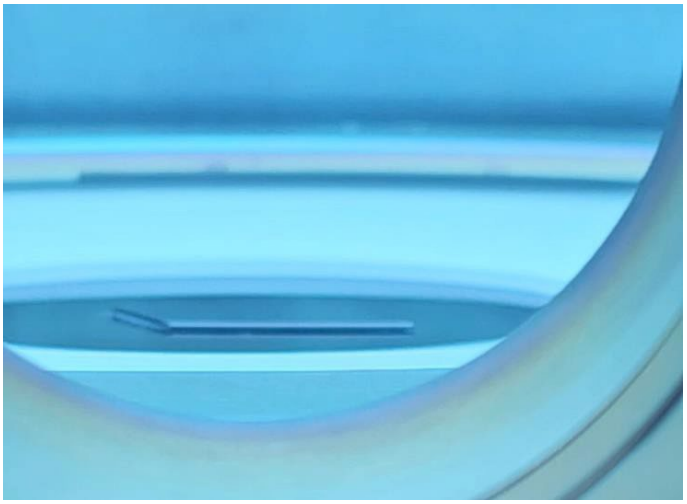

1.3.2 Main plasma etching parameters

In the semiconductor manufacturing industry, the objective of a plasma etching process is to etch the areas of a wafer which are not protected by the mask pattern with a high precision [70,83]. The goal is to find a plasma process which will remove the exposed surface material while conserving the pattern of the mask area which must resist during the whole process duration. Ideally the aim is to reach a precise etch depth for the cavities being created within the surface layer or to etch the whole surface layer completely while preserving the underlying thin layers of material. An example of a pristine silicon wafer which is then covered with a protective resin or hardmask pattern realized through lithography is shown in **figure I.6**. A plasma etching process is defined by many parameters which all have an influence on the final etching result.

Figure I.6: Application of a photoresist pattern before etching process

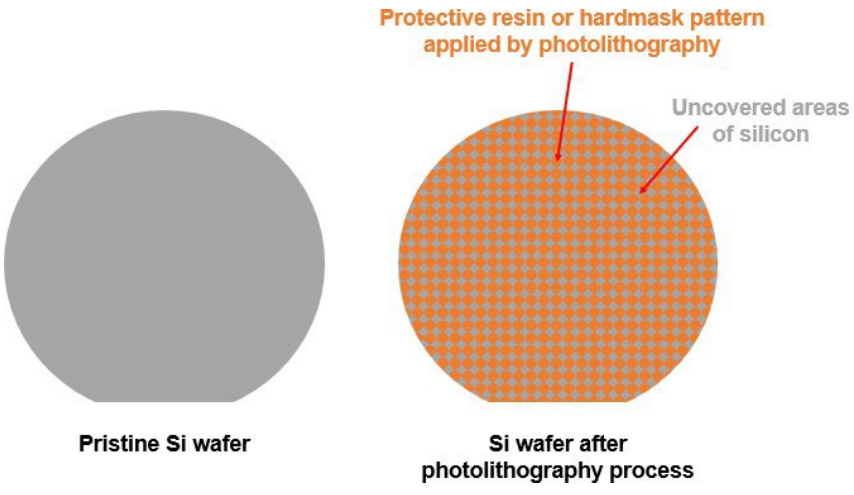

1.3.2.1 Reactor types

Different plasma reactor types or sources can be used for etching applications. Generally, radiofrequency (RF) plasma sources are used over DC (Direct Current) or microwave plasma sources. Radiofrequency plasma sources differ according to the technique that is used to strike the plasma. Nowadays, the most common RF plasma sources used for plasma etching include inductively coupled plasma (ICP) reactors and capacitively coupled plasma (CCP) reactors [76,84].

CCP reactors consist of two planar electrodes facing each other and separated by a certain distance. An RF voltage is applied between them to generate an electric field which will accelerate electrons and cause an ionization avalanche to strike the plasma. For ICP reactors, an external antenna (or coil) is placed above or around the chamber. The plasma is first initiated through capacitive coupling in the same manner as a CCP reactor. However, by applying an RF current to this antenna, an oscillating electromagnetic field is generated in the chamber through induction. The resulting azimuthal RF electric field will accelerate electrons and enhance ionization and dissociation reactions (inductive coupling). ICP reactors are categorized according to the inductance geometry or nature (planar type, cylindrical type or immersed in ferrite cores) [85]. Since their invention, these two types of reactors have undergone several technical improvements. However, ICP sources are usually preferred for etching applications due to the relatively higher plasma densities they can achieve compared to CCP sources which leads to higher etch rates. Inductively coupled plasmas tend to be more uniform and allow controlling the ion energy as well as the ion flux independently [84].

The nature of a plasma reactor will have a key influence over the range of plasma properties it can possibly generate. The chamber geometry as well as the disposition of the electrodes and antenna have a significant influence on the density and distribution of reactive species generated in the plasma source. As a result, the distance between the substrate and the plasma source will also affect the density of reactive species at the wafer surface. In addition, the total volume of the reactor is also a key parameter which will affect the residence time of reactive species in the chamber and their density. All these chamber parameters are also important for plasma modeling applications which aim to predict etching results (process outputs) on a substrate in relation to the process parameters (process inputs) applied on a given reactor (**see figure I.3**).

1.3.2.2 Input process parameters

Plasma etching processes depend on several input parameters [83,86]. The main input parameters for an etching process realized with an ICP reactor and their main effects are briefly detailed below.

Gas chemistry and gas flow rates: The reactive gases which are used to generate the plasma medium have to be carefully chosen according to their chemical affinity with the material that has to be etched. They usually include halogen-based gases (Fluorine, Chlorine, Bromine) and noble gases (mostly Argon). Other gases such as oxygen, hydrogen, nitrogen or helium can also be included in the gas mix

to enhance the etch rate or selectivity. It is important to note that these gas molecules will be fragmented in the plasma medium and will generate a very reactive environment composed of ions, neutrals and radical species. The flow rate and chemical mixture of the gases used for the process will have a direct influence on the concentration and composition of these reactive species in the plasma. An accurate dosing is key to ensure that the balance of reactive species allows etching the material through chemical and physical reactions while protecting the sidewalls through passivation reactions to achieve anisotropic etching.

Chamber pressure: The adjustment of chamber pressure will have a direct impact on the main free path of reactive species in the plasma and their residence time. Indeed, a higher pressure implies an increased probability of reactive species to collide with each other and lose their energy. However, increased collisions can also trigger chemical reactions and generate additional reactive products.

Source Power: The adjustment of the source power will have a direct influence on the density of reactive species present in the plasma. The increase of RF power on the antenna will increase the electromagnetic field in the chamber and enhance ionization reactions.

Bias power: The application of a bias power to ensure a stabilized negative voltage on the lower electrode allows to attract and accelerate positive ions (cations) from the plasma medium towards the substrate. These charged particles will bombard the surface following the electric field in a very directional manner and with an important energy which will contribute to remove the material. This particular physical aspect of plasma etching is referred to as ion bombardment or physical etching. It has a significant influence on the global etching process alongside chemical etching reactions.

Substrate temperature: Chemical reaction rate coefficients (k) are all influenced by temperature according to the Arrhenius equation. By applying a fixed substrate temperature, several chemical reactions between the reactive species of the plasma and the substrate material may be privileged while preventing the occurrence of other types of reactions. For instance, the decrease of substrate temperature allows enhancing condensation and passivation mechanisms on the cooled substrate depending on the gaseous species which are used. On the contrary, the increase of substrate temperature can increase the reaction rate of chemical etching reactions. It is important to note that a low substrate temperature may prevent the removal of chemical byproducts. Indeed, if their boiling point temperature is above that value, they will remain on the substrate in liquid or solid phase and not be pumped away by the reactor.

Other parameters: Plasma etching processes can also be influenced by other parameters which include the chamber wall temperature, the reactor conditioning as well as the wafer clamping parameters.

The chamber wall temperature has a significant influence on the eventual deposition of contaminants on the chamber walls during plasma processing. Over time, the accumulation and increasing amount of contaminants can considerably affect the stability of etching processes. Indeed, these species can react again and affect the plasma which will continuously drift and lose its original etching capacity due to an increasing feed of external chemicals.

Chamber conditioning has an important role in plasma processing. The regular performance of plasma cleaning processes using oxygen or argon allows to remove fluorocarbon and other type of contaminants from the chamber walls. However, these cleaning processes are time-costly and therefore have to be performed at adequate moments. Moreover, the presence or absence of contaminants on the chamber walls can significantly influence the occurrence of plasma striking during cyclical etching processes where a succession of plasma and non-plasma steps are performed. As a result, it is sometimes preferable to perform a plasma conditioning treatment after a cleaning process using the same gas chemistry as the following etching processes of interest.

During wafer processing, the wafer is held in position on the substrate holder using a clamping system. Various technologies exist including mechanical, electrostatic, vacuum and magnetic clamping. The system should provide a uniform clamping without distorting or damaging the wafer. Moreover, if the substrate holder is thermalized, the clamping system needs to ensure an efficient thermal transfer between the chuck and the wafer. For mechanical clamping systems, a helium backing flow is introduced to maintain the wafer against a clamping ring with a certain pressure while thermalizing it due to its high thermal conductivity.

1.3.3 Main plasma properties for etching applications

During the performance of dry etching process, plasma properties are directly influenced by the input parameters [62,83,84,86]. The main plasma characteristics of interest will be detailed below. Various methods exist to characterize them and will be detailed in experimental equipment and characterization tools section (**see chapter II**). Determining these parameters provides a better understanding of the potential chemical mechanisms that can occur in the bulk plasma as well as the etching mechanisms that can occur during a plasma process as is shown in **figure I.7**. These parameters are related to the mechanisms which take place in the plasma source and the formation of reactive species.

Plasma potential: The plasma potential corresponds to the potential of the space that occupies the bulk plasma in the reactor chamber.

Floating potential: This is the potential at which an electrically isolated material will float when placed in the bulk plasma due to the equilibrium between the ion current and ion retarding current in the plasma sheath region.

Nature of plasma ions: The determination of the exact nature of plasma ions and their quantification is useful to evaluate the eventual reactions that might occur with the substrate material.

Ion density: Ion density corresponds to the total concentration of ions in a given volume inside the bulk plasma. It is useful to determine the impact of physical etching reactions occurring during a plasma process.

Ion flux: Ion flux corresponds to the total flux of incoming ions on a given surface during a plasma process. It can be useful to approximate the ion sputter etch rate.

Ion energy distribution: The ion energy distribution corresponds to the range and distribution of energies which ions possess when they hit the substrate material. The average ion energy value and the broadness of the distribution can be helpful to determine the impact of physical etching due to ion bombardment during a process. Indeed, sputtering occurs if incoming ions have an energy above the threshold energy for sputtering of the substrate material.

.

Figure I.7: Schematic diagram representing the main reactions involved in a plasma etching process

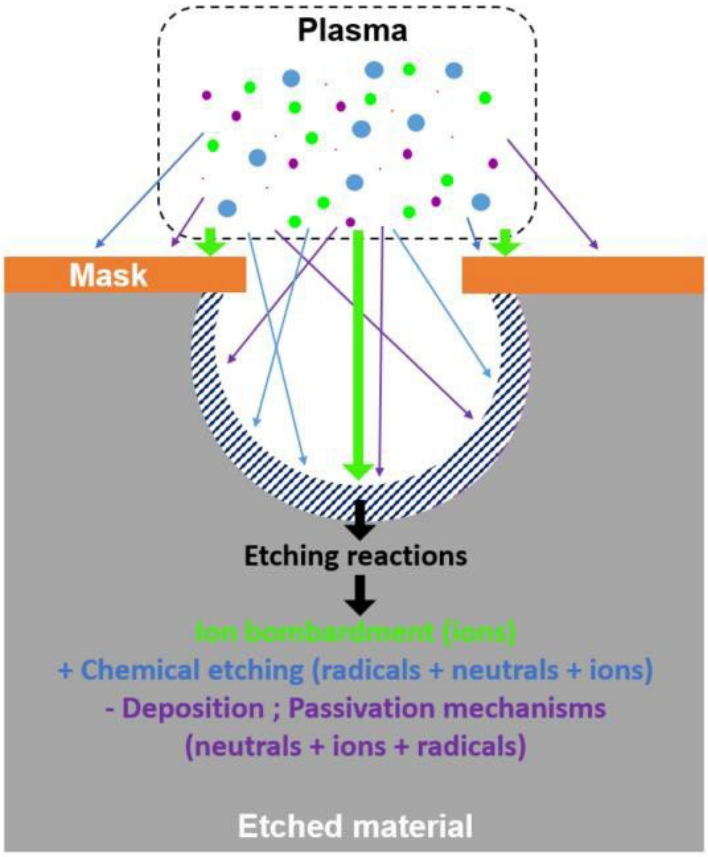

Electron density: The electron density corresponds to the concentration of electrons in a given volume inside the bulk plasma. It is a valuable parameter to evaluate reaction rates occurring in the plasma medium.

Electron temperature: The electron temperature describes the average kinetic energy that possess electrons in the plasma medium. It is a useful parameter to evaluate the eventual chemical reactions that can occur in the plasma medium and their rate coefficients. The electron energy distribution and electron flux can also be useful to assess the chemical reactions which can occur in the plasma and on the substrate material.

Nature of plasma radicals: Radicals have an important role in the chemical etching which occurs during a plasma process. The identification of these species can help in the understanding of the chemical reactions which occur in the plasma medium.

Radical density: Radical density corresponds to the concentration of a given radical in a given volume in the bulk plasma. This value is useful to determine certain reaction rate coefficients and to describe chemical etching reactions taking place

1.4 Principal etch trench characteristics

The key aspects which characterize a satisfactory plasma etching process include the achievement of an anisotropic etch profile presenting no particular defects with a high selectivity and uniformity [83]. Ideally the etch rate should be the highest possible to increase productivity. The detail of these etching aspects and eventual defects that can occur will be presented hereafter.

1.4.1 Anisotropy and principal etching dimensions

One of the first aspects that describes an etching pattern is its directionality. Indeed, as mentioned in the previous section, dry etching processes were mainly developed to achieve anisotropic etchings. The goal is to etch the substrate material or deposited material layers at a certain uniform depth by respecting the 2D pattern delimited by lithography beforehand without exceeding the mask borders. As a result, an anisotropic etching process describes its capacity to remove material only in one direction. In this case, the etched material is removed vertically (vertical etching, E_v) following the mask delimitations. In contrast, an isotropic etching process removes material in all directions. Therefore, material will be removed under the mask area (lateral etching, E_L). **Figure I.8** schematizes anisotropic and isotropic etching examples obtained from a pristine sample with a mask pattern.

Following the determination of this first characteristic, the etch depth (d_{etch}) can then be measured as well as the etch angle in the case of an anisotropic etch pattern. The etch depth corresponds to the maximal etch depth that can be measured at the bottom of the trench from the sample surface. The etch angle corresponds to the angle than can be measured between the normal surface plane and the trench sidewalls as shown in **figure I.9**. The etch width (w_{etch}) of the trench can also be measured in the case of isotropic trenches or when several defects can be observed in an anisotropic trench. Usually, the maximal width of the etch trench under the mask layer is considered for w_{etch}. In some cases, the remaining mask thickness (t_{mask}) can also be measured and compared to the initial mask thickness $(t_{0\,mask})$ to assess the etching selectivity of the etched material compared to the mask material which will be further described. The initial opening width (w_0) and opening width subsequent to the etching process (w) as well as the geometry of the pattern must also be considered when analyzing the etching

result. Indeed, the etching result will not necessarily be the same depending on the opening width. Moreover, different etching profiles can be obtained for a same opening width if ever the mask opening surface pattern is different. In instance, a hole pattern with a given diameter will not have necessarily the same etching result compared to a trench pattern with the same width. From these measurements, it is possible to calculate the etching anisotropy (A) of a defined etch trench. Although several equations can be used, the most common is described in **equation I.1.** By applying this formula, a perfectly isotropic trench will have an etching anisotropy equal to 1 $(A = 1)$ whereas a perfectly anisotropic trench will have an infinite etching anisotropy $(A \rightarrow +\infty)$ [83].

Figure I.8: Isotropic and anisotropic etch profiles

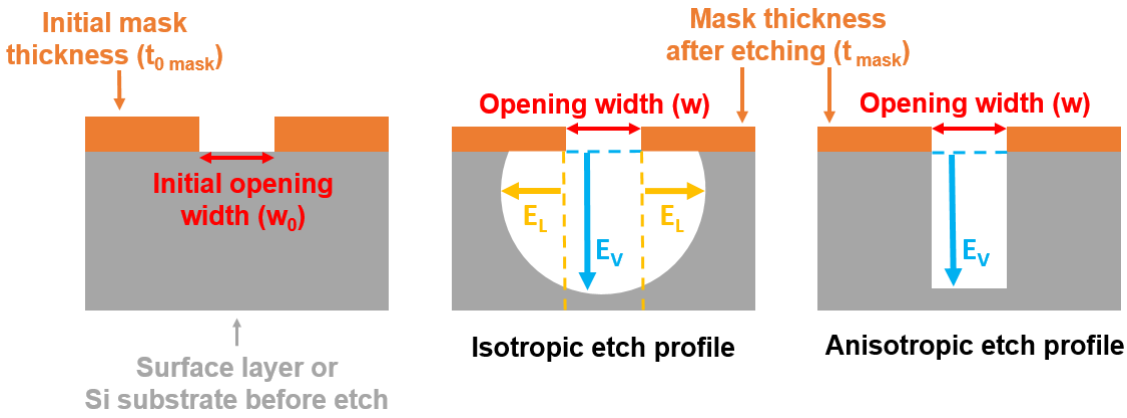

Figure I.9: Main dimensions characterizing an etch profile

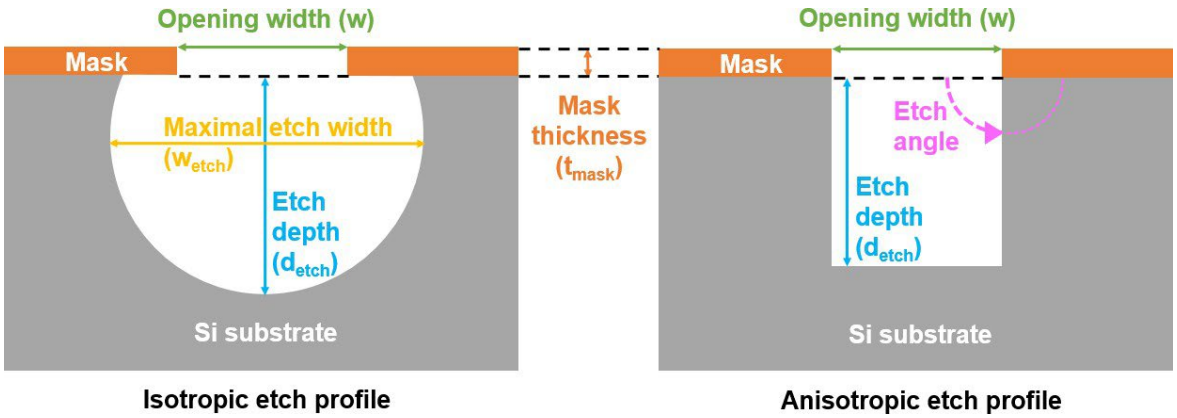

Equation I.1: Degree of anisotropy equations

$$Degree\ of\ anisotropy\ (A) = 1 - \frac{E_L}{E_v}$$

Consecutively to these measurements, the aspect ratio (AR) of an anisotropic etch trench can also be determined. This ratio evaluates the etch depth (d_{etch}) obtained compared to the initial opening width

(w_0) of the etch pattern as shown in **equation I.2**. Numerous products require high aspect ratio etchings ($AR > 10$) such as high-capacity memories where they can go up to 100:1 [46,87]. An illustration showing different anisotropic etch profiles with the same etch depths but with different aspect ratios is shown in **figure I.10**.

Equation I.2: Aspect ratio equation

$$Aspect\ ratio\ (AR) = \frac{d_{etch}}{w_0}$$

Figure I.10: Illustration of etching profiles with different aspect ratios

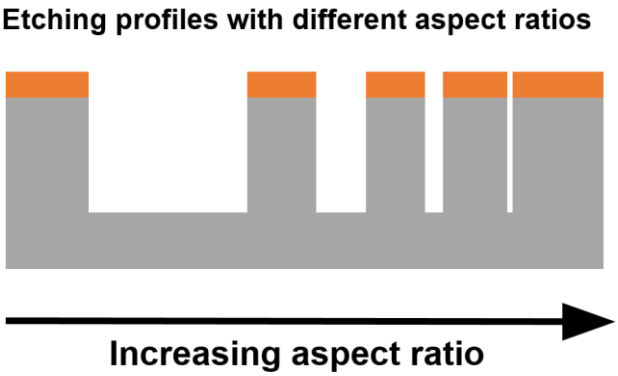

1.4.2 Etch rate

The etch rate describes the quantity of material that is removed from a wafer surface for a specific process. It is always related to a specific etched pattern or sample and is defined by the etch depth that is achieved in relation to the duration of the process. It is defined by **equation I.3.** For cyclical or pulsed processes, such as ALE, the etch rate can also be expressed in terms of quantity etched per process cycle also called etch per cycle (EPC). It is defined by **equation I.4.** Given that the etch rate of a process on a given sample can vary through time, it is important to differentiate the etch rate obtained after a specific duration and the global etching rate of a process.

Equation I.3: Etch rate equation

$$Etch\ rate = \frac{Maximal\ etch\ depth}{Process\ duration}$$

Equation I.4: Etch per cycle equation

$$Etch\ per\ cycle\ (EPC) = \frac{Etch\ depth\ measured\ for\ x\ cycles}{Number\ of\ cycles\ (x)\ considered}$$

Usually, the etch rate is expressed in nm/s for thin etching processes such as atomic layer etching and in µm/s for deep etching processes such as Bosch process.

1.4.3 Etching selectivity

As mentioned before, the selectivity of an etching process is also an important parameter to consider. It characterizes the ability of an etching process to remove a specific material compared to another. Therefore, it is necessary to identify a mask material that is significantly more resistant to a plasma process than the etched material, in order to achieve high etch depths while conserving the lithography pattern and minimizing the quantity of mask material that is needed. For typical lithography resists, the silicon to mask material etching selectivity can reach up to 100:1 for common plasma etching processes [70]. In other words, silicon is typically etched up to 100 times more easily and rapidly than the mask material. This calculation also enables to estimate the maximal process duration that can be applied on the sample before etching the whole mask layer in order to reach a maximal etch depth without damaging the sample.

In instance, the etch rate obtained for the same process on two different materials is sufficient to evaluate its etching selectivity, as is shown in **figure I.11** and detailed in **equation I.5** [83]. In the case of a multilayer stack composed of different materials, the etching selectivity of the plasma process applied to etch the surface material selectively to the underlying layer material should be as high as possible. High etching selectivities allow to limit eventual over-etching defects than can occur at the interface with the underlying layer as described in **figure I.12.c.**

Figure I.11: Illustration of etching selectivity

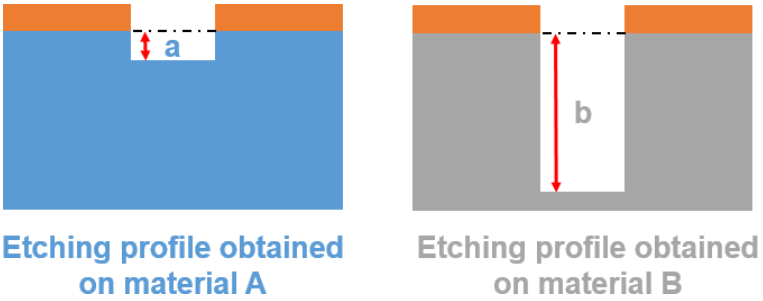

Equation I.5: Etch selectivity

$$Etch\ selectivity\ (B{:}A) = \frac{Etch\ rate\ (B)}{Etch\ rate\ (A)}$$

In the case of **figure I.12.a**, no over-etching is observed. The anisotropic etch trench is neat and no etching of the underlying material occurred. In the case of **figure I.12.b**, the notching defect is depicted. This type of defect can occur in the case of a highly selective etching process which was extended for a too long time. Once the surface layer is etched, the reactive species contained in the plasma and the local etching mechanisms of this top layer can change once the underlying layer is reached. Charging effects accumulated inside the etch trench during the etching of the surface material can also influence the trajectory of incoming ions once a new material layer is reached which

will lead to the etching of the sidewalls at the vicinity of the interface.

In the case of **figure I.12.c**, over-etching is observed. This defect can be due to an extended process time or to an insufficiently selective etching process which etches preferably the underlying layer material.

Figure I.12: Illustration of potential over-etching defects

1.4.4 Etching uniformity

The etching uniformity of a process describes its capacity to etch a specific pattern in the same way throughout the entire wafer surface. Nowadays, most semiconductor manufacturers are processing 300 mm diameter wafers where all the surface is used for chip production. Center to edge differences which can occur in the plasma medium during etching processes have to be limited as much as possible to guarantee an identical etching result throughout the wafer surface. Uniformity is controlled regularly on a wafer throughout the entire fabrication steps. After an etching process, the etch depth of specific identical patterns are controlled at several points of the wafer using techniques such as ellipsometry. Different calculations can be done to assess the etching uniformity of a process. They usually take into account the maximum etch rate difference that is measured over a single wafer or batch [83]. Different tolerances can be applied depending on the product. **Figure I.13** represents different etching uniformity scenarios that can be observed.

In the case of a uniform etching process (**figure I.13.a**) all the patterns are etched in the same way throughout the wafer surface with similar etch depths. However, if the plasma process is not uniform enough, important center to edge discrepancies can appear such as in **figure I.13.b** where reactive species are more concentrated in the center. Other scenarios of non-uniformity issues are typically depicted in **figure I.13.c** where the etch trenches have a certain tilted angle near the edges. These types of defects are frequently due to an irregular angular ion bombardment phenomenon or to electrical discontinuities due to the bending plasma sheath on the edge of the wafer during the etching process [88,89]. Moreover, sidewall passivation or etch rate may not be uniform across the wafer due to thermal and chemical discontinuities which can be inherent to the substrate holder nature and architecture [88].

Figure I.13: Illustration of etching uniformity common issues

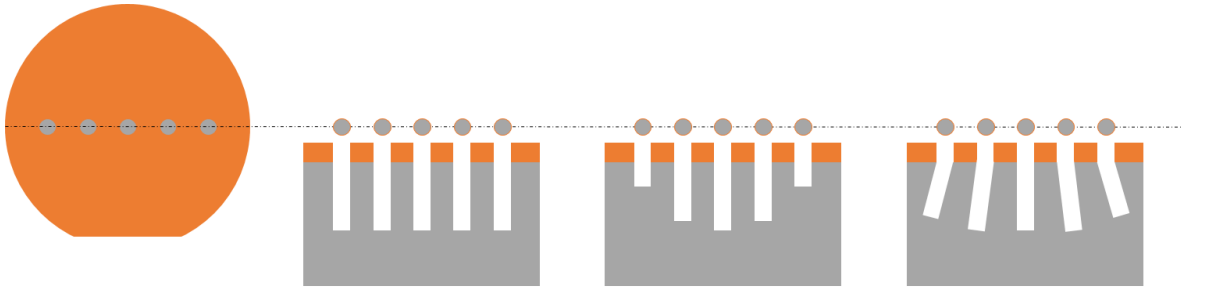

.

1.4.5 Description of anisotropic etch sidewall defects

Numerous defects can affect the trench sidewalls concerning anisotropic etch profiles [83]. Ideally, these should be as straight as possible with an etch angle of 90° as shown in **figure I.14.b.** In this figure, common sidewall etching defects are displayed in comparison to this ideal anisotropic etch profile. It is important to note that several combinations of these particular etching defects can also occur due to multiple factors.

Figure I.14: Sidewall characterization of etching profiles

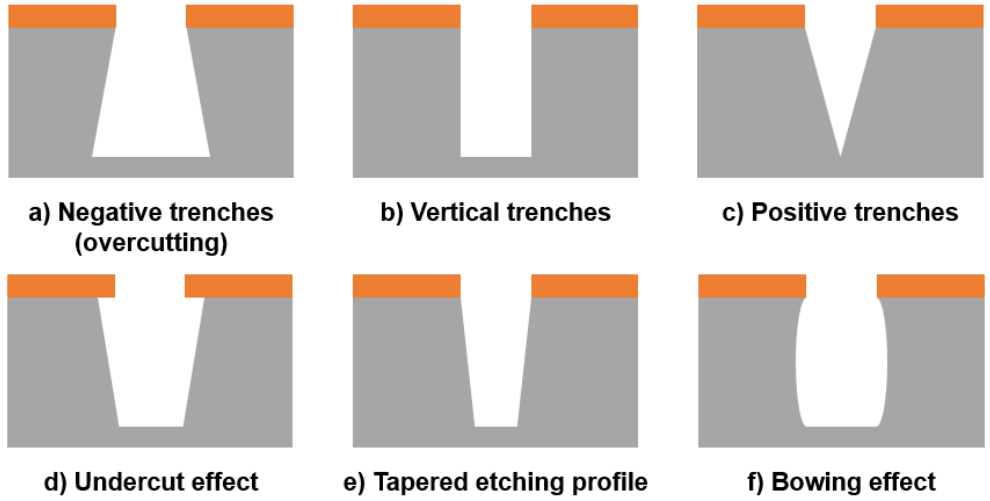

Negative trench (Figure I.14.a): A negative etch profile is characterized by symmetrical sidewalls which both have an etch angle which is superior to 90.0°. In this case, sidewall passivation was insufficient during the plasma etching process. The sidewalls near the mask layer are more protected comparatively to the bottom of the trench as they are less subject to ion bombardment.

Positive trench / Tapered etching profile (**Figure I.14.c / Figure I.14.e**): A positive etch profile is characterized by symmetrical sidewalls which both have an etch angle which is inferior to 90.0°. In this case, sidewall passivation was too important during the plasma etching process which eventually passivates the bottom of the trench and does not allow further etching.

Undercut defect (**Figure I.14.d**): Undercutting corresponds to etching that occurs under the mask layer. In this case an undercut length can be measured on each side of the etch trench between the etch sidewall and the mask opening. In this case sidewall passivation was insufficient to limit isotropic etching effects which occurred during the plasma etching process.

Bowing defect (**Figure I.14.f**): Bowing defect corresponds to convex shape trench sidewalls. Numerous reasons can lead to the apparition of this kind of defect such as angular ion bombardment, charging effects which occur gradually on the passivated sidewalls or to the reduced ion flux in deep aspect ratio features. This defect can also be caused due to a tapered angle of the mask layer which reflects energetic ions towards the trench sidewalls as it shown in **figure I.15** where another case scenario of localized sidewalls defects is also depicted due to this reason.

Figure I.15: Illustration of localized sidewall defects due to tapered mask angle

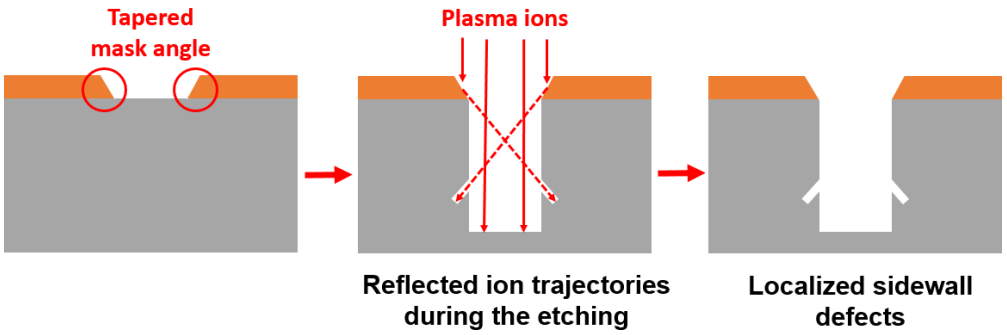

Sidewall smoothness: Another aspect that describes the trench sidewalls is their smoothness and roughness. Smooth sidewalls are easily obtained through the optimization of a continuous plasma process whereas pulsed or cyclical processes may lead to the formation of discontinuities also referred to as scalloping marks due to the succession of isotropic etching and sidewall passivation steps. These types of defects are illustrated in **figure I.16** where the case of extended scalloping is also shown. This particular defect is characterized by pronounced scalloping marks under the mask layer [90]. In general, scalloping marks tend to gradually disappear as the etch trench gets deeper. It is possible to minimize them by shortening the process steps which generate these marks and therefore increasing the pulsing frequency [58,90–92]. Post-process treatments can also be done to smooth the trench sidewalls following a pulsed etching process [93,94]. Striation defects can also occur on the etch trench sidewalls. This type of defect is illustrated in **figure I.17** and corresponds to the formation of irregular straight-line defects along the axis of the etched trench [95]. They are the direct consequence of mask patterning imperfections which are transmitted to the substrate due to anisotropic plasma etching.

Figure I.16: Illustration of sidewall defects occurring during cyclic etching processes

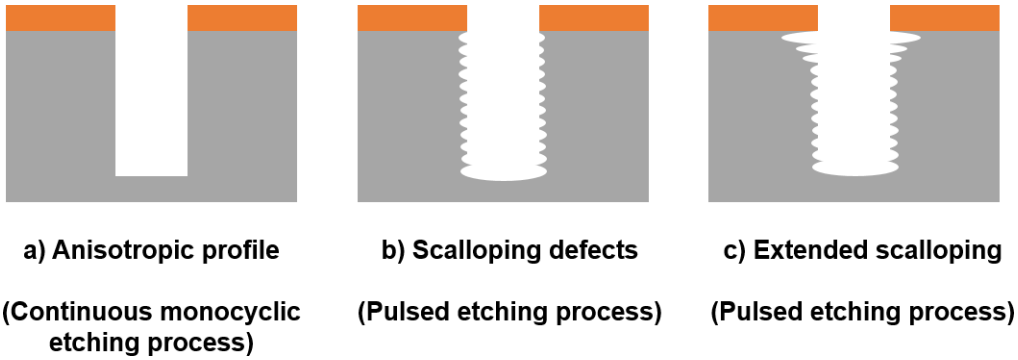

Figure I.17: Illustration of striation etching defects

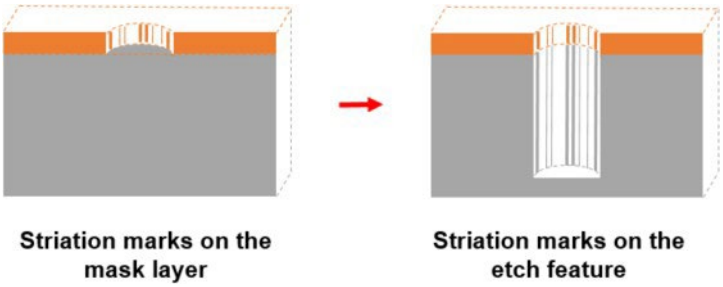

1.4.6 Description of bottom trench defects

Numerous defects can also affect the trench bottom concerning anisotropic etch profiles [83]. Common examples are shown in **figure I.18**.

Micrograssing defect (**Figure I.18.a**): Micrograssing or micromasking defect is characterized by the formation of micro-column structures at the bottom of the etch profile. Different factors may cause this phenomenon such as the sputtering caused by ion bombardment which increases the surface roughness of the bottom trench. Another cause may be the formation of black-silicon on the bottom trench. It is a specific surface modification of silicon marked by the formation of micro-needles of roughly 10 µm in length and less than 1µm in diameter which can be observed in many etching processes where passivation reactions are too predominant (over-passivation) [96–98].

Loading defect (**Figure I.18.b**): Loading defect corresponds to a convexly shaped bottom trench where the etch depth is relatively more important at the center of the etch profile. It is mainly due to ion bombardment which is not sufficiently directional and that will preferably etch the center rather than the sides due to sidewall reflections.

Microtrenching defect (Figure I.18.c): Microtrenching effect corresponds to a concavely shaped bottom trench where the etch depth is relatively more important near the sidewalls. It is also due to ion bombardment which is not sufficiently directional and that will preferably etch the edges of the bottom trench rather than the center due to sidewall reflections.

Figure I.18: Common bottom trench defects affecting etching profiles

a) Micrograssing effect b) Loading effect c) Microtrenching effect

Concerning deep aspect ratio features, bending (also called tilting) and twisting defects can occur at the bottom of the etch profile. These particular distortion defects are shown in **figure I.19**. The cause of these types of defects can be numerous. They include mask pattern dependencies, the randomness of reactive fluxes and their trajectories to reach the bottom of the trench as well as charging effects due to neighboring features and their spatial disposition [46,87,99].

Figure I.19: Illustrations of bending and twisting defects

a) Bending defect b) Twisting defect

1.4.7 Aspect ratio dependent etching (ARDE) phenomenon

Aspect ratio dependent etching (ARDE), also called microloading defect or positive RIE lag is an etching phenomenon which is frequently encountered in reactive ion etching. It is characterized by an increased etch rate for larger features as is shown in **figure I.20.a**. This phenomenon is quite problematic concerning the microfabrication of electronic components because etchings are realized on multistacks composed of homogenous films. Frequently, the etch features need to go through a complete layer of material to enable an electric contact with the underlying layer. Therefore, for a process which is prone to ARDE, etch features with the highest aspect ratio need a longer time to reach the desired etch depth compared to features with lower aspect ratios. As a result, these processes need to be highly selective in order to limit the over-etch which will first concern the larger etch features as they will reach the underlying material first due to a higher etch rate.

Several mechanisms may explain this phenomenon. Neutral and ion shadowing is enhanced for higher aspect ratio features causing incident particles to be reflected more easily before reaching the bottom of the etch feature. Differential charging along the etch sidewalls can also explain this phenomenon. Indeed, a slight potential difference is gradually formed along the trench sidewalls during the etching process. Negative charges preferentially build up at the top of the feature, near the mask area, due to the isotropic electron flux that occurs on the surface with the periodical RF plasma and sheath oscillations. However, positive charges build up at the bottom of the feature due to the isotropic electron flux due to ion bombardment. As a result, the trajectory of incident positive ions will be slightly deflected and they will lose energy as they enter the feature, especially near the sidewalls. This phenomenon is greatly enhanced for higher aspect ratios. Knudsen transport of neutrals to the bottom of the etch feature can also explain ARDE phenomenon as well as diffusion mechanisms [100,101].

On the contrary, inverse ARDE or negative RIE lag has been reported in some rare cases with processes including fluorocarbon plasmas [102,103]. This is shown in **figure I.20.b**. It is explained by the preferential formation of thicker CF_x polymer layers in the larger features which inhibits etching reactions.

Figure I.20: Illustration of the aspect ratio dependent etching (ARDE) phenomenon

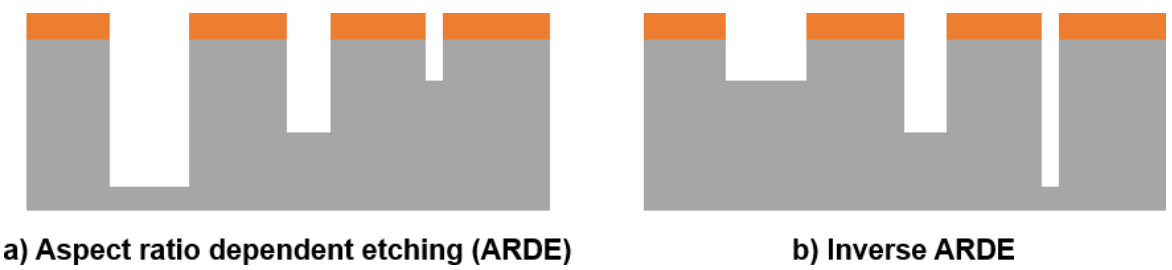

a) Aspect ratio dependent etching (ARDE) **b) Inverse ARDE**

1.4.8 Other etching characteristics or defects

Other specific etching defects or phenomenon can also arise due to the nature of the sample or the plasma chemistry.

Necking and clogging defects: These types of defects affect the surface area at the top of the etch feature at the mask level or just underneath it due to the formation or deposition of an unwanted product, usually polymer related [46,104]. An illustration of these defects is shown in **figure I.21**. They are particularly detrimental to the etching process as they heavily deviate, hinder (**figure I.21.a**) or even completely block (**figure I.21.b**) the penetration of reactive species. In consequence, the underlying etch profile will often present significant defects as well.

Figure I.21: Illustration of the necking and clogging defects

Crystallographic defects: Geometric defects can be observed in the etch trench depending on the crystallographic nature of the etched material [105–107]. Indeed, depending on its crystalline structure, plane and orientation, various atomic densities and bond lengths can be observed as a function of the crystalline direction that is considered. As a result, crystallographic etching can occur if the ion energy of the plasma process lies between different sputtering threshold energies of the etched material according to the crystallographic plane. Different examples of crystallographic etching defects described in references [105–107] are shown in **figure I.22**.

Figure I.22: Illustration of crystallographic etching defects

Etching defects due to the crystallographic nature of the substrate

1.5 Principle plasma processes used for deep silicon etching

1.5.1 Introduction

Multiple etching processes have been developed since the emergence of semiconductor manufacturing. These include a variety of techniques which can be first categorized as either dry or wet etching processes. Wet etching processes include liquid state etchants such as acids (HF, HCl, HNO_3, H_3PO_4, acetic acid, …) which etch the substrate through chemical reactions. They were mainly used for pattern transfer in the early days of microfabrication. They usually enabled high etch rates but were isotropic and lacked etching selectivity for several material stackings in some cases [70,108]. Dry-etching processes includes the use of gaseous products and do not necessarily involve plasma media or low-pressures. They progressively rose to prominence to replace wet-etching processes for an increasing number of etching applications since the 1960s.

Among them, ion beam etching (IBE) is a non-plasma dry etching process which involves energetic ions (usually argon) which are bombarded towards the substrate [109–111]. Therefore, the etching mechanism is purely physical but only allows etch rates under 100 nm/min. Other gaseous products can be added such as Cl_2 or CF_4 in an alternative process called reactive ion beam etching (RIBE) to enhance the etch rate through chemical reactions yet physical etching is predominant. Other non-plasma dry etching processes have also been developed and are based on very reactive gaseous chemicals such as XeF_2, ClF_3, BF_3 with silicon substrates or (HF/methanol) vapor with SiO_2 substrates [110–115]. Several etching chemical mechanisms involved with these processes are listed below.

Silicon etching using gaseous xenon difluoride [110]**:**
$Si\ (s) + 2\ XeF_2\ (g) \rightarrow SiF_4\ (g) + 2\ Xe\ (g)$

Silicon dioxide using (HF/methanol) vapor [110]:
$SiO_2\ (s) + 2\ HF_2^-\ (ads) + 2\ MH^+\ (ads) \rightarrow SiF_4\ (ads) + H_2O\ (ads) + 2\ M\ (ads) \rightarrow SiF_4\ (g)$

The development of plasma processes which now take a predominant place in dry etching processes first followed two different directions according to their application, physical etching and chemical etching, before eventually merging together [108,116]. Plasma physical etching also referred to as sputtering processes were developed to ensure anisotropic features when wet etching was not possible notably through the use of Ar ions (Ar^+). They were first realized in the 1960s in RF sputter chambers where the wafer was placed on an electrode which was capacitively coupled with an RF generator with a negative bias voltage to accelerate Ar ions [108,117].

On the other hand, chemical plasma processes were developed to replace wet etching processes in certain applications where high selectivities were required [108,109]. It was first developed for photoresist stripping using O_2 plasmas notably by *Irving et al* [118]. Subsequently, it was discovered that fluorine and chlorine plasmas could have selective etching applications between SiO_2, Si_3N_4 and aluminum substrates notably through the work of *Irving et al* and R.A.H Heinecke in the 1970s [119–

121]. However, these processes were typically developed in different types of chambers such as barrel or Reinberg reactors as well as downstream microwave plasma etchers where the substrates were not negatively biased which only allowed isotropic chemical etching reactions [108,109,119,122].

The idea of merging both aspects of physical and chemical etching in a plasma process was introduced by *Hosokawa et al* in 1974 who tested fluorine and chlorine type gases in an RF plasma sputtering reactor which enabled an increase in the etch rates of various types of substrates [123]. The emergence and improvements of these types of techniques, now referred to as reactive ion etching (RIE) or energetic ion-enhanced etching processes, rapidly took over in the manufacturing industry due to their higher etch rates, anisotropy and precision [108–111,116,124,125].

1.5.2 Principle of Reactive Ion Etching (RIE)

Reactive ion etching processes regroup plasma etching processes which etch substrate materials both through physical and chemical reactions [109–111]. They involve various reactive species including ions, radicals and neutrals which can generate different etching and passivation mechanisms. The main plasma chemistries used for RIE include fluorine, chlorine, bromine based gases due to the etch byproducts they generate through chemical reactions with different substrates such as SiF_4, $SiCl_4$, $SiBr_4$, WF_6, $AlCl_3$. Their volatility depends upon the substrate temperature during the process. Other gases such as Ar, O_2, H_2, N_2 and He can be added to modify the plasma chemistry and enhance species or passivation reactions with the substrate. The chemical etching mechanism between fluorine and chlorine species with silicon are listed below.

Fluorine plasma etching of silicon [110,114]**:**

$Si\ (s) + 4\ F\ (g) \rightarrow SiF_4\ (g)$

$3\ Si\ (s) + 2\ SF_6\ (g) + 2\ O_2\ (g) \rightarrow 3\ SiF_4\ (g) + 2\ SO_2\ (g)$

Chlorine plasma etching of silicon [109,110]**:**

$Si\ (s) + 4\ Cl\ (g) \rightarrow SiCl_4\ (g)$

$Si\ (s) + 2\ Cl_2\ (g) \rightarrow SiCl_4\ (g)$

A summary table of several RIE plasma chemistries and their potential chemical reactions with a silicon substrate is shown in **table I.2**. The main radicals which contribute to chemical etching are listed as well as the passivation agents they can generate [109,126].

By extension, deep reactive ion etching (DRIE) processes enable high etch rates with the use of a second RF generator placed on the substrate holder to independently control plasma generation (source generator) and ion bombardment through the application of a bias voltage (bias generator) [110,111].

Table I.2: Main RIE etching chemistries with silicon (taken and adapted from [109] and [126])

Process gas	Plasma radicals	Si etching byproducts / Boiling point at P = 1 atm (°C)	Passivation agents
NF_3	F ; NF_x	SiF_4 / -86°C	$Si_xN_yF_z$
SF_6	F ; SF_x	SiF_4 / -86°C	$Si_xS_yF_z$
C_xF_y	F ; CF_x	SiF_4 / -86°C	$Si_xC_yF_z$
CH_xF_y	F ; H ; CF_x	SiF_4 / -86°C	$Si_xC_yF_z$
Br_2	Br_x	$SiBr_4$ / 154°C	Br_2
Cl_2	Cl_x	$SiCl_4$ / 57.6°C	Cl_2
SiF_4	F ; SiF_x	SiF_4 / -86°C	Si_xF_y
$C_xF_y + O_2$	F ; O ; CF_x	SiF_4 / -86°C	$Si_xO_yF_z$
$C_xF_y + H_2$	F ; H ; CF_x	SiF_4 / -86°C	$Si_xC_yF_z$
$SF_6 + O_2$	F ; O ; SF_x	SiF_4 / -86°C	$Si_xO_yF_z$
$SF_6 + H_2$	F ; H ; SF_x	SiF_4 / -86°C	$Si_xS_yF_z$
$SiF_4 + O_2$	F ; O ; SiF_x	SiF_4 / -86°C	$Si_xO_yF_z$

1.5.3 Bosch process

The Bosch process is the main DRIE process used for deep-Si etching in the semiconductor industry. It was patented by F. Laermer and A. Schilp from Robert Bosch GmbH in 1996 and was rapidly implemented to the manufacturing scale [127]. It has been used over the last 30 years especially towards applications such as MEMS, TSV or DRAM devices where deep aspect ratio features are needed [110,111,127–132]. It is based on the pulsed repetition of a plasma etching step using SF_6 plasma followed by a passivation step using C_4F_8 plasma which enables avoiding lateral etching through the deposition of fluorocarbon polymer. A descriptive illustration of this process is shown in **figure I.23**.

It is performed at the ambient temperature range and the careful balance of these two steps enables reaching anisotropic etching. This is explained by the fact that the ion bombardment which occurs during the SF_6 plasma is preferentially directed towards the bottom of the trench with the application of a negative bias voltage. The fluorine cations dispose of a sufficient kinetic energy to break the CF_x polymer barrier and sputter the underlying silicon material on the surface plane. However, CF_x passivation remains on the trench sidewalls because impacting ions lose their initial kinetic energy as they are reflected from the trench bottom (surface plane) to the sidewalls. Chemical etching is also important during the Bosch process mostly due to the presence of fluorine radicals which react with the silicon substrate to form volatile SiF_4 etching byproducts. High etch rates above 5.0 µm/min can generally be achieved with the Bosch process using ICP reactors [110].

Due to its pulsating nature, it generates scalloping marks on the trench sidewalls which can be more or less pronounced and present different kind of defects depending on the process parameters as well as the reactor capabilities [91,92,110]. However, the cyclic repetition of passivating and etching steps also allows a greater process robustness. Several studies point out that the careful dosing of fluorocarbon steps interspersed with etching steps offer more control and synergistic effects over the etching result than a continuous plasma process [55,133–135]. Indeed, continuous processing with fixed parameters

may have a variable etching impact depending on several independent factors such as aspect ratio dependence and offers no corrective flexibility.

Figure I.23: Schematization of the Bosch process

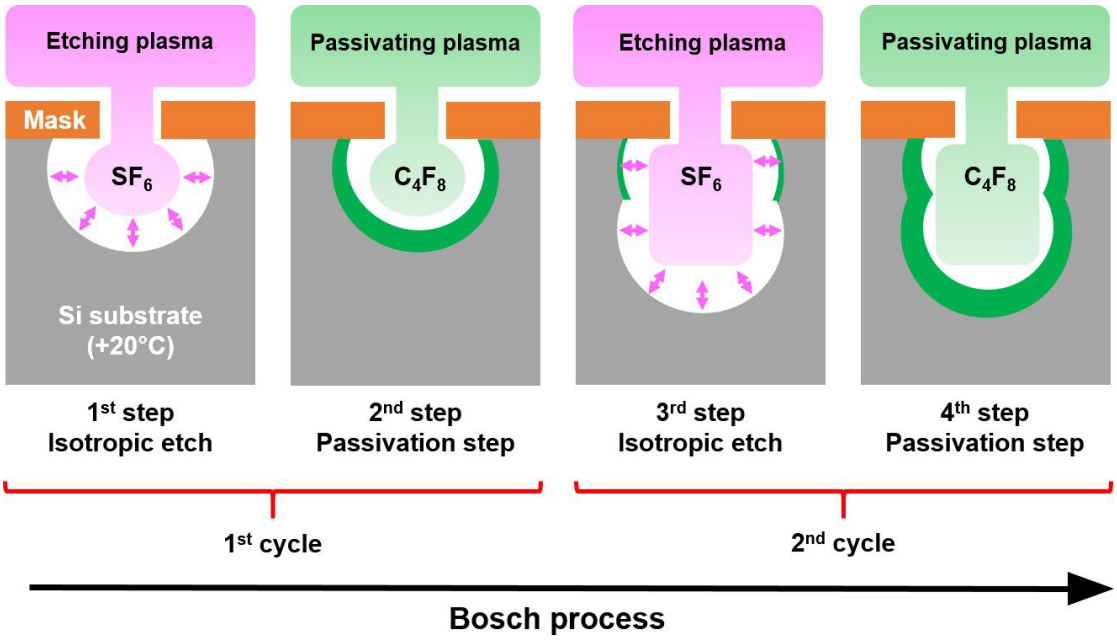

To that matter, the comprehension of fluorocarbon passivation mechanisms is key to implement stable Bosch processes. The passivating steps should be optimized to reverse and correct the potential defects which are caused by the SF_6 plasma etching steps such as aspect ratio dependent etching. Numerous publications have been realized concerning the influence of process parameters on the fluorocarbon passivation step [136–138]. Their impact on the plasma parameters and the resulting fluorocarbon passivation layer are generally well known yet no study was found in the literature concerning their performance at cryogenic temperatures.

Nevertheless, one of the main drawbacks of the Bosch process is the gradual accumulation of fluorocarbon contamination on the reactor sidewalls [139–141]. As a result, fluorocarbon species are gradually released back into the chamber which affects the process equilibrium that continuously drifts to an over-passivating regime and an etch rate decrease. Quite regularly, plasma cleanings or even manual cleanings of the chamber are necessary to retrieve and initialize a satisfactory chamber condition which is adequate to enhance process stability and uniformity [139,142,143]. Different pathways are studied to extend the process stability and reduce the occurrence of reactor sidewall cleanings. One of the solutions that was developed is the introduction of heating liners on the reactor walls which thermalizes the sidewalls above the condensation temperature of C_xF_y polymer species (up to +160°C) [140,141]. As a result, fluorocarbon deposition is reduced yet still occurring which leads to the search for alternative solutions to extend the process throughput.

In the context of this research project, the Bosch process as well as fluorocarbon plasma passivation processes were studied at cryogenic temperatures. To that matter, no significant data was found in the scientific literature. The main objectives were to evaluate their temperature dependence and establish whether lower flow rates of fluorocarbon gas could be used to achieve similar passivation effects in the cryogenic temperature range compared to ambient temperature processing. Various parametric studies and in-situ characterizations were realized to study the impact of process parameters on fluorocarbon passivation and Bosch etching.

1.5.4 Cryogenic etching (standard cryoetching process)

Cryogenic etching processes were introduced by *Tachi et al* at Hitachi Ltd after patenting the cryogenic etching concept in 1985 [54,144]. In this study, the idea was to favorize anisotropic physical etching due to ions and inhibit chemical etching due to radicals by cooling the substrate. Using a CCP and a microwave reactor, it was observed using a pure SF_6 plasma that the cooling of a silicon substrate at temperatures between -70°C and -140°C enhanced etching anisotropy as well as $Si:SiO_2$ etching selectivity and enabled higher etch rates. Below -140°C, no etching was observed due to SF_6 condensation on the substrate. Following these observations, *Tachi et al* studied the etching rate of silicon in relation to substrate temperature for different plasma chemistries (SF_6, NF_3, Cl_2, CF_4 and $CBrF_3$) [145]. It turned out that SF_6 was the gas which delivered a much higher etch rate between - 133°C and +20°C. Moreover, it was observed that the Si etch rate for all gases varied in relation to substrate temperature.

Since then, further studies were realized concerning its application to other type of reactors, especially ICP and helicon type sources with higher plasma densities [96,106,135,146,147]. Among them, Bartha *et al* pointed out the need to add an oxygen source in the plasma to enhance passivation on the sidewalls to maintain anisotropy while achieving higher etch rates [146]. It was argued that the presence of oxygen contamination sources during SF_6 plasma processing (such as a fused silica clamping ring in the chamber) may explain the first observations of etching anisotropy in pure SF_6 obtained by *Tachi et al* and reported in other publications [54,145,147]. SF_6/O_2 plasma chemistry had already been reported in the past for ambient temperature processing as an alternative to CF_4/O_2 plasma chemistry by *d'Agostino et al* [148]. However, the amount of necessary oxygen feed in the plasma mixture to achieve anisotropic etching is considerably reduced at cryogenic temperatures (usually less than 10% compared to roughly 40% at ambient temperature) [46,149].

Nevertheless, standard cryogenic etching now refers to the (SF_6+O_2) plasma process which is performed at cryogenic temperatures [55,110,111]. It is one of the main DRIE processes that was developed for deep-Si etching alongside Bosch etching for the same applications (MEMS, TSV, …) but also for the etching of nanostructures where scalloping is undesirable. However, it was not implemented in the manufacturing industry on the same scale. The reasons behind this are due to its lower robustness which is attributed to the temperature instability of the SiO_xF_y passivation layer as well as the extra costs

that represent cryogenic infrastructures [55,133,134]. Unlike Bosch etching, it is a polymer-free process where chamber wall contamination is extremely reduced. Indeed, the reactive species will mainly deposit on the cooled substrate surface due to its very low temperature. Moreover, it is a continuous plasma process where the plasma chemistry and process parameters have to be perfectly balanced to achieve anisotropic etching. Therefore, it produces etch features with smooth sidewalls without scalloping marks. High etch rates above 5.0 µm/min can also be reached with standard cryoetching [55,133]. It relies on the formation of a SiO_xF_y passivation layer on the sidewalls which is only stable at cryogenic temperatures. The formation of this layer is key to prevent lateral etching caused by fluorine radicals. A descriptive illustration of the process etching mechanisms involved during standard cryoetching is depicted in **figure I.24**.

As a result, the process is quite sensitive to substrate temperature and oxygen feed which have a direct impact on the formation of SiO_xF_y inhibitors. Indeed, black-silicon (b-Si) columnar microstructures (micro-grassing defects) can be generated in a slightly over-passivating regime where oxygen species are predominant [55,96,135,149]. These structures are typically generated when SiO_xF_y formation is too important and passivates slightly on the silicon interface at the bottom trench. If the ion flux and energy of SF_x ions are too low, anisotropic etching will only occur in the areas which are not sufficiently passivated and generate these characteristic microcolumnar structures. As a result, black-silicon will inevitably hold the etching reaction and lead to a failure of the etching process. Therefore, bias voltage has also an essential role as it will influence the angle and energy of bombarding ions which should be directed towards the trench bottom and not on the passivated sidewalls to preserve SiO_xF_y inhibitors.

Several studies using in-situ characterization methods have been realized concerning SiO_xF_y passivation and desorption reactions which are not yet fully understood [55,150–153]. It was observed that this passivation layer is generated through the adsorption of SiF_x radicals which react with oxygen atoms on the silicon surface. SiF_x radicals are generated through volatile SiF_4 etching byproducts due to chemical etching of the silicon substrate with fluorine radicals at the trench bottom. These byproducts react in the plasma medium near the silicon interface and redeposit in the form of SiF_x preferably on the sidewalls which are slightly cooler than the trench bottom which is subject to ion bombardment. By reacting with oxygen atoms, SiO_xF_y inhibitors are then preferentially generated on the trench sidewalls which allows gradual anisotropic etching. Through MD simulation calculations, *Tinck et al* also determined that the physisorption and residence time of SiF_x species is considerably enhanced on a silicon surface at cryogenic temperatures [66].

This SiF_x redeposition mechanism also explains why the formation of black-silicon and its characteristic structure is also dependent of the aspect ratio feature. Indeed, it was observed that the density and diameter of these microcolumnar structures varied in relation to the aspect ratio of the etch feature [152]. Smaller and denser black-silicon structures are preferentially generated in smaller aspect ratio features (larger features where the silicon interface with the plasma is greater). It is explained by the fact that the redeposition of SiF_x species and their reaction with oxygen atoms at the trench bottom is facilitated in these areas. Therefore, over-passivation reactions are more likely to occur on the surface. Moreover, they will initiate and preserve b-Si columnar structures because they will also passivate the

b-Si structure sidewalls more easily due to the greater accessibility that they dispose in these smaller aspect ratio areas.

At -100°C, the SiO_xF_y passivation stoichiometry evaluated by in-situ XPS after a (SF_6+O_2) plasma process is fluorine rich and close to $SiOF_3$ [153]. Through thermal desorption studies at low pressure using also mass spectrometry and in-situ ellipsometry, it is shown that this passivation layer desorbs at a low rate between -110°C and -70°C mostly in the form of SO_xF_y and SF_x species. Most of the SiO_xF_y passivation layer desorbs above -70°C in the form of SiF_4 in a continuous manner until ambient temperature is reached [151–153]. No SiO_2 is detected on the sidewalls by ex-situ XPS once the SiO_xF_y passivation layer has fully desorbed [150]. However, the oxygen content of the passivation layer seems not to be significantly altered during the desorption process by in-situ XPS analysis [153]. It supposes that fluorine diffusion and recombination occur in the SiO_xF_y layer through thermal heating to form SiF_4 volatile products which desorb continuously as they are formed.

Figure I.24: Schematization of the standard cryoetching process (taken and adapted from [55])

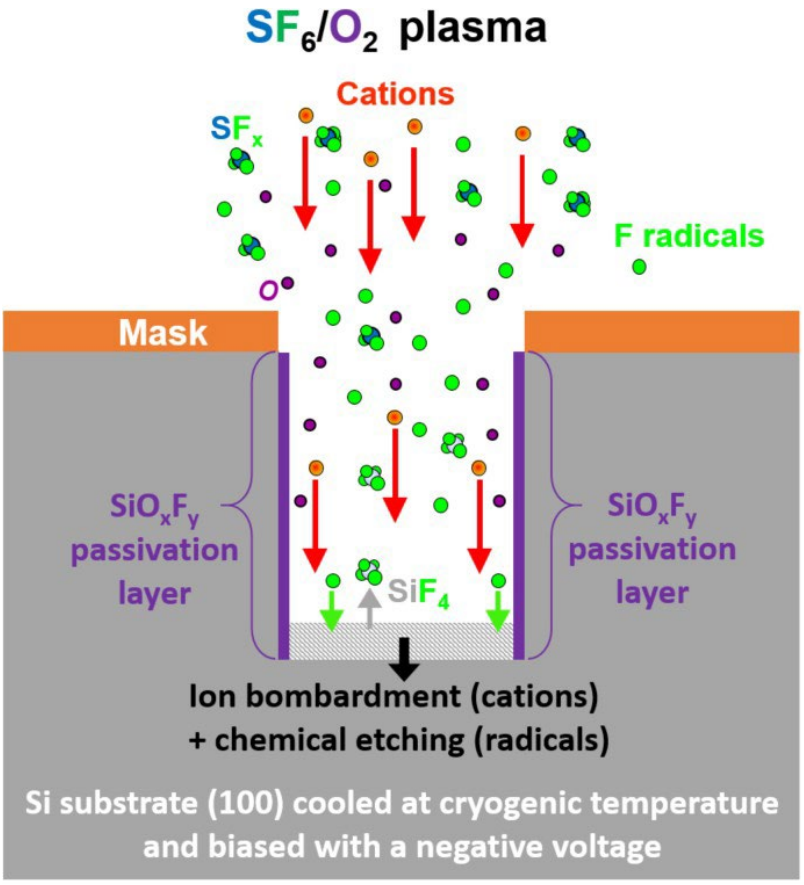

1.5.5 STiGer process

Since the development of the standard cryogenic process, numerous alternatives have been investigated to increase its robustness [55,133]. Amongst possible areas of optimization, one alternative was the implementation of pulsed processes using similar plasma chemistry. The idea of pulsed processing or process chopping was suggested by *Tsujimoto et al*, also at Hitachi Ltd in 1986, thus before the development of cryogenic and Bosch processing [154]. However, this concept only became popular after the development of the Bosch process in 1996. As a result, alternative pulsed processes were developed including SF_6 or SF_6+O_2 plasma etching steps interspersed with plasma passivation steps of CCl_4, O_2 or gases such as TEOS (tetra-ethyl-ortho-siloxane) or OMCTS (octa- methyl-cyclo-tetra-siloxane) [55,133,154,155]. Moreover, as it was found that SiO_xF_y sidewall passivation was generated through the redeposition of SiF_x species during (SF_6+O_2) plasma etching, rising interest was brought to the use of SiF_4 as a process gas, mostly for passivation purposes using also O_2 [155]. It was to that matter and towards the realization of deep aspect ratio features, that the STiGer process was instigated in 2006 and patented in 2011 by GREMI laboratory and ST Microelectronics [156].

This etching technique is based on the same principle as the Bosch process where SF_6 plasma etching steps are interspersed with a SiF_4/O_2 plasma passivation steps to passivate the profile sidewalls. This process is performed at cryogenic temperatures, typically -100°C, where SiF_4/O_2 passivation is effective [90,157–159]. Compared to Bosch etching, the STiGer process presents similar etching characteristics. It is a robust process and can achieve high etch rates above 5 µm/min [58,67,134]. It also generates scalloping etch marks on the profile sidewalls which can be reduced by increasing the pulse frequency of the process [58,90]. Although liquid nitrogen is mandatory when operating the STiGer process, it uses generally lower gas flows to achieve sidewall passivation compared to the Bosch process where C_4F_8 gas flows tend to be more important. Indeed, SiF_4/O_2 passivation is facilitated at very low temperatures and the necessary gases are only pulsed during the passivating steps. In comparison, industrial Bosch processes usually involve a constant flow of C_4F_8 even during the etching steps to maintain an acceptable chamber pressure during the cyclic repetition of passivating and etching steps. This high consumption of c-C_4F_8 gas can be quite costly and it is also a severe greenhouse gas just as SF_6 with a high global warming potential (GWP) [41,160,161]. In comparison, lower flow rates of SiF_4 are used during STiGer processing [58,90,134] and it is presumed to have a lower GWP than c-C_4F_8 although no substantial data on that point was found in the scientific literature. A descriptive illustration of the STiGer process is given in **figure I.25**.

Figure I.25: Schematization of the STiGer process

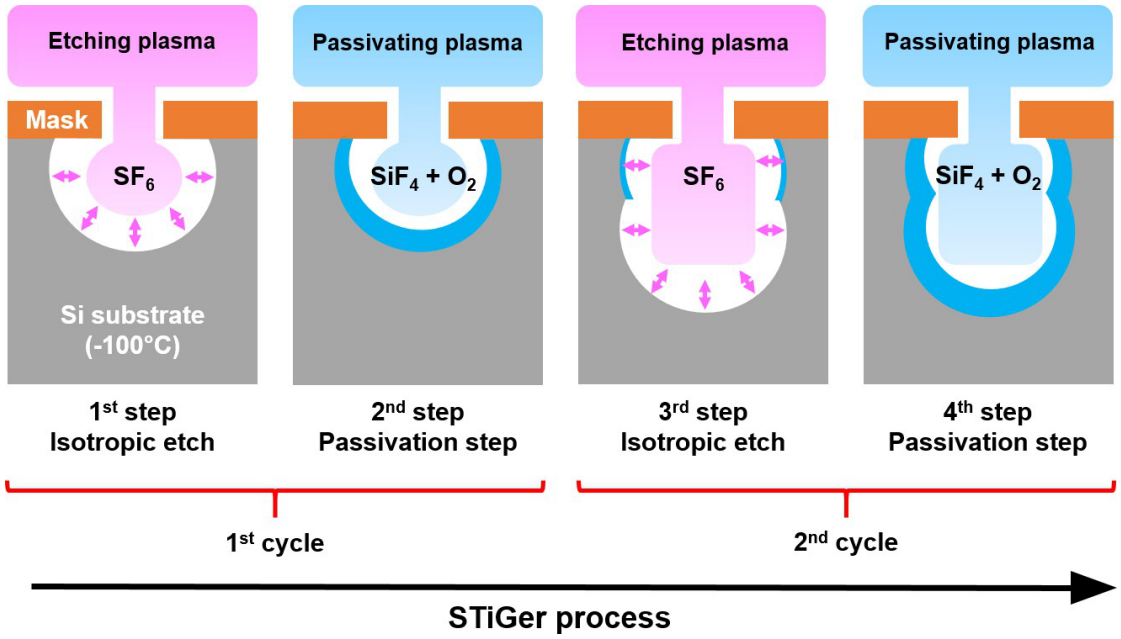

1.5.6 Fluorocarbon RIE plasma chemistries for selective silicon etching applications

Since the emergence of RIE processes, many plasma chemistries have been tested in order to achieve high etching selectivities between different materials of interest. It is mainly achieved through chemical etching where the nature of plasma species (mainly radicals and ions) can have a significant influence on their reactivity with different substrates. Therefore, several RIE processes were developed from previous plasma chemistries developed for chemical plasma processes. To that matter, Heinecke as well as Coburn & Winters notably demonstrated that fluorocarbon plasma chemistry can be effective to achieve SiO_2:Si as well as Si_3N_4:Si selective etching [114,120] at room temperature range.

Indeed, Heinecke showed in 1975 that SiO_2:Si selectivity could be increased in fluorine deficient fluorocarbon plasmas. It was first found that the addition of hydrogen to CF_4 plasma allows to scavenge fluorine etching species by forming HF molecules which decreases the etch rate of silicon. Secondly, it was found that a C_3F_8 plasma process enabled to achieve a SiO_2:Si selectivity of 5:1 whereas a selectivity of 1:10 was found in a pure CF_4 plasma [120]. It must be noted that for the same C_3F_8 plasma process, a Si_3N_4:SiO_2 etching selectivity of 18:1 was found. Consecutively, Ephrath managed to show that CF_4/H_2 RIE plasma chemistry allows reaching a SiO_2:Si selectivity of 35:1 with a hydrogen content of 40% [162]. However, no etching occurred on Si and SiO_2 substrates due to fluorocarbon polymerization once a hydrogen content of 42% was reached.

Additionally, it was found through *Hosokawa et al* that increasing oxygen content in fluorocarbon plasmas enables to enhance silicon etch rate until a certain threshold value is reached where it continuously decreases until it results in Si passivation [123]. This oxygen threshold value varies in relation to the fluorocarbon gas and other process parameters but was evaluated to 5% in CF_4 plasmas. As a result, SiO_2:Si etching selectivity could be significantly enhanced according to oxygen content in the fluorocarbon plasma mixture.

By reviewing fluorocarbon plasma etching publications in 1979, *Coburn & Winters* pointed out the importance of the fluorine-to-carbon (F/C) ratio of the fluorocarbon process gas as well as the applied bias voltage to determine whether a plasma process will either polymerize (deposit) or etch a given surface [114]. Hydrogen and oxygen content as well as the etched material area (loading effect) can shift the etching or polymerizing capacity of a fluorocarbon gas in a plasma process. They also noted that SiO_2:Si etching selectivity can generally be obtained when the fluorocarbon plasma parameters are close to the boundary conditions between polymerization and etching.

Since then, several studies have been carried out concerning silicon etching selectivity mechanisms in fluorocarbon plasmas. To that matter, it was found in numerous publications that a steady state fluorocarbon film is formed on Si, SiO_2 and Si_3N_4 substrates during fluorocarbon plasma etching [163–169]. *Schaepkens et al* notably found that SiO_2 > Si_3N_4 > Si selective etching results could be obtained with four fluorocarbon ICP plasma chemistries (C_2F_6 ; C_3F_6 ; CHF_3 and C_3F_6/H_2) [167]. A maximal SiO_2:Si_3N_4 etching selectivity of nearly 6:1 was obtained with C_3F_6/H_2 plasma at high bias voltages (>150 V) where a SiO_2 etch rate of nearly 600 nm/min was obtained. By characterizing the fluorocarbon interface films obtained through ellipsometry and XPS, it was found that the film thickness had a significant influence on the resulting etch rates that were observed during the fluorocarbon plasma processes independently of the substrate nature. Indeed, relatively thin fluorocarbon films were found on SiO_2 substrates whereas intermediate and thick films were generally found respectively on Si_3N_4 and Si substrates.

The thickness of the fluorocarbon film is both dependent on the fluorocarbon gas chemistry and the substrate material. Indeed, SiO_2 has a stronger affinity than Si_3N_4 and Si to react with carbon species. As a result, volatile CO, CO_2 and COF_2 volatile byproducts are generated more rapidly in the case of SiO_2 than CNF volatile byproducts in the case of Si_3N_4. In the case of a silicon substrate, no volatile byproducts can be generated with carbon species. Only volatile SiF_4 byproducts are formed through the diffusion of fluorine in the fluorocarbon interface layer as described by *Standaert et al* [166].

The increasing thickness of the fluorocarbon interfacial layer acts as a double barrier for the etching of the underlying material. The incoming ions will lose their energy in the fluorocarbon layer and contribute less to physical etching of the substrate. Moreover, thicker steady-state fluorocarbon films consume greater amounts of fluorine atoms to conserve their thickness during the plasma process. Therefore, fluorine atoms which are continuously generated during the process contribute less to the chemical etching of the underlying substrate material. A descriptive illustration of these etching mechanisms involved during fluorocarbon plasma processing of Si, SiO_2 and Si_3N_4 substrates is described in **figure I.26.**

Figure I.26: Schematization of incoming and outgoing fluxes of volatile chemical species during hydrofluorocarbon plasma etching of Si, SiO_2 and Si_3N_4 substrates (taken and adapted from [167])

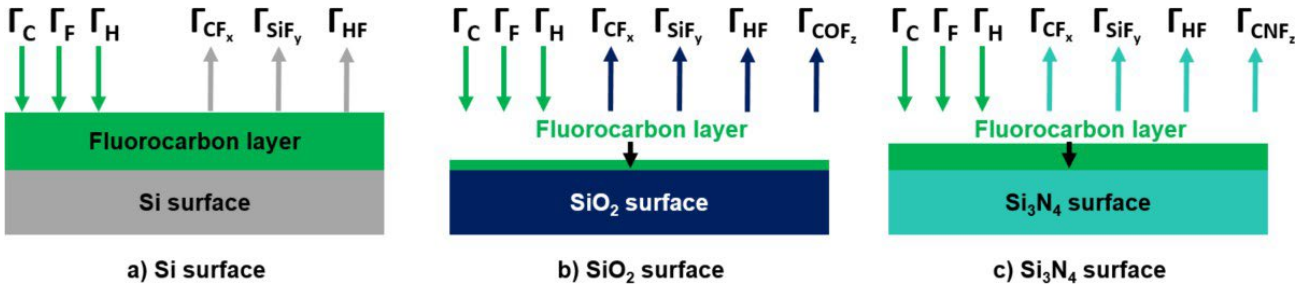

Conversely, also in 1999, it was found through *Kastenmeier et al* that Si_3N_4:SiO_2 and Si_3N_4:Si selective etching could be achieved through O_2/N_2 chemistry with additions of either CF_4 or NF_3 in a chemical plasma etching process (not RIE) [170]. This mechanism is explained by the presence of NO species which enhances silicon nitride etching compared to SiO_2 or Si surfaces. Moreover, high oxygen content allows to oxidize Si surfaces to make them less reactive to fluorine etching. Fluorine density is also greatly reduced in this plasma chemistry which reduces Si and SiO_2 etch rates. The same year, Reyes-*Betanzo et al* also achieved selective Si_3N_4 etching over Si and SiO_2 in a $N_2/SF_6/CH_4/O_2$ RIE plasma chemistry with a maximal Si_3N_4:SiO_2 selectivity of 4:1 and a Si_3N_4 etch rate of roughly 40 nm/min [171].

Further studies concerning selective silicon nitride etching in RIE fluorocarbon plasmas also pointed out the interest of adding oxygen to the fluorocarbon plasma mixture. Indeed, *Lee et al* showed that mild oxygen addition to CF_4 or C_2F_6 plasmas (high F/C ratio) enhances silicon nitride etching due to the formation of NO reactive species [172]. However, once a certain threshold value is reached, the addition of oxygen contributes to a decrease of NO species due to the effective reduction of O species in the plasma. A maximal Si_3N_4:SiO_2 selectivity value of 13.2:1 was obtained with CF_4/O_2 plasma mixture with a Si_3N_4 etch rate of 306 nm/min.

Furthermore, it was also shown by *Chen et al* that oxygen addition to hydrofluorocarbonated plasmas (CHF_3, CH_2F_2, CH_3F) allows to increase hydrogen density and silicon nitride selective etching [173]. This mechanism is explained by the fact that O addition reduces the density of CF_x etchants by forming CO, CO_2 and COF_2 volatile byproducts in the plasma which reduces SiO_2 etch rate. Moreover, the increase of H density which is induced by these mechanisms reacts favorably with CN involatile byproducts in the fluorocarbon interface layer above the Si_3N_4 substrate during the etching process. The accelerated formation of HCN volatile byproducts will allow a reduction in the fluorocarbon interface thickness with the silicon nitride substrate material which will both enhance chemical and physical etching reactions. A maximal Si_3N_4:SiO_2 value above 10:1 was obtained in CH_3F/O_2 plasma with an O_2 content of 80% where the Si_3N_4 etch was nearly equal to 120 nm/min.

More recently, a chemical plasma etching process (using a remote plasma source) was reported by Jung *et al* to achieve very high Si_3N_4:SiO_2 etching selectivities [174]. A maximal selectivity of nearly

400:1 was obtained in a $NF_3/N_2/O_2/H_2$ plasma mixture yet the Si_3N_4 etch rate was only 6 nm/min due to the absence of bombarding ions.

1.5.7 Influence of substrate temperature on RIE etching selectivity and surface roughness

Research and development of plasma etching chemistries which allow high etch rates, important etching selectivities and reduced surface damage always took an important part in semiconductor fabrication. As it can be seen, most RIE chemistries were first developed for Si, SiO_2 and Si_3N_4 materials in the ambient temperature range before being implemented for other materials of interest. However, the introduction of cryogenic and high-temperature chucks also progressively enabled the study of etching mechanisms in relation to substrate temperature. More and more, plasma chemistries were evaluated in relation to this parameter which can significantly affect etching selectivity and surface roughness.

Indeed, as it was seen at the birth of cryogenic etching, *Tachi et al* found that the decrease of substrate temperature allowed to enhance $Si:SiO_2$ as well as Si to photoresist etching selectivity using SF_6 plasma [54]. Further studies using different gases (Cl_2, NF_3, $CBrF_3$, CF_4) showed that their Si etch rate could also vary in relation to substrate temperature although it was less impressive than with SF_6 where the etch rate increases significantly between +30°C and –130°C before over-passivation is observed at -140°C [54,145]. Moreover, it was shown that fluorocarbon deposition rates could be significantly enhanced at low temperatures with the example of CHF_3 [145].

Since then, several studies have been reported concerning the effect of substrate temperature on the etching selectivity of a plasma process chemistry. In instance, *Lee and Lee* observed that the etch rate of CoFe and PtMn magnetic films was significantly enhanced using a CH_3OH ICP plasma process at 120°C rather than at 20°C whereas the etching of Ta and W metallic films slightly decreases with substrate temperature [175]. More recently, it was found by *Hsiao et al* that SiN PECVD films showed opposite etch rate variations in relation to substrate temperature using CF_4/H_2 plasma [176]. Indeed, depending on the nature of their main hydrogen impurities, N-H rich SiN substrates were etched more rapidly by increasing temperature whereas Si-H rich SiN substrates showed the opposite tendency.

Additionally, it was rapidly spotted that cryogenic etching allowed reducing significantly plasma induced damage on silicon substrate surfaces. This observation was reported by *Konuma et al* for Si etching using NF_3 plasma in 1989 as well as *Mizutani et al* for Ne plasma etching of SiO_2/Si interfaces in 1990 [177,178]. It was notably shown by *Mizutani et al* that cryogenic etching also reduces surface defects induced by VUV photons irradiation due to the reduced hole mobility in the substrate material which limits their propagation from the SiO_2 surface to the SiO_2/Si interface [178]. However, this point was later tempered by *Lopaev et al* in 2017 who studied the impact of F atoms and VUV photons independently and in a combined manner in a Xe/SF_6 plasma mixture on SiOCH low-k samples. They showed that VUV photons induced damage was rather independent to substrate temperature whereas

damage due to F atoms decreased significantly between 15°C and -60°C. Both of these components seem to have a synergistic effect on global SiOCH surface damage during the etching process even though it decreases with lower substrate temperatures.

Nevertheless, cryogenic etching processes were successfully developed for the precise etching of new materials of interest such as porous OSGs (organosilicate glasses) [179–181]. It was notably demonstrated by *Chanson et al* that cryogenic etching between -55°C and -35°C using SF_6/HBPO (High boiling point fluorocarbon etch gas) plasma mixture allowed to etch accordingly the low-k OSG material with low damage due to the condensation of HBPO gas in the pores [181]. Moreover, *Clericò et al* reported the use of an SF_6/Ar plasma process at -110°C to precisely etch graphene nanoconstrictions with very low surface roughness [182].

1.6 Summary of chapter I (English):

The semiconductor industry and microelectronics technology have undergone prodigious innovation since the invention of the point-contact transistor in 1947. The ongoing development of microfabrication processes enabled the constant miniaturization of electronic components. In 2024, the critical size of the most advanced transistors has reached 3 nm and their downscaling is set to continue in a fierce battle between major semiconductor companies. Among these microfabrication steps, plasma etching processes are of utmost importance. These processes must be increasingly precise in order to obtain high aspect ratio features with limited etching defects with error margins that can reach the order of few atomic layers. Amongst these plasma processes, cryogenic etching processes are regaining interest in the semiconductor research sector. They consist in etching materials at very low temperature, typically around -100°C using liquid nitrogen which enhances passivation mechanisms on the cooled substrate and limits chemical etching reactions on the feature sidewalls. These processes also allow to reduce plasma induced damage on the etched surface and to limit reactor wall contamination thus avoiding process drifts.

The first cryogenic etching process was introduced by *Tachi et al* in 1988 for deep silicon etching applications. It is now referred to as standard cryoetching and uses a SF_6/O_2 plasma to generate a protective SiO_xF_y passivation layer on the sidewalls which is only efficient at cryogenic temperatures. Currently, cryogenic etching plasma processes are being studied with diverse chemistries for thin etching applications but also for the etching of new materials of interest such as 2D materials (MoS_2, graphene), low-k materials or porous materials where high selectivity and low induced damage are needed. However, extensive understanding of the passivation mechanisms including SiO_xF_y, C_xF_y and other chemistries at very low temperature is not yet fully established. Their exact stoichiometry as well as their precise thermal desorption mechanisms also remain quite uncertain. More generally, plasma-surface interactions in relation to the substrate temperature need to be further studied for the understanding of cryogenic processes. It implies the characterization of quantitative data at very low temperature such as sticking probabilities, thermal desorption and surface diffusion rates as well as sputtering yields which are often not fully available or insufficiently known. Coupled with the determination of plasma properties during the performance of these processes, these parameters are crucial for a full understanding and to enable the modelization of cryo-etching mechanisms. However, they are difficult to obtain experimentally, as they have to be characterized in-situ and at cryogenic temperature, which can be complex depending of the characterization techniques.

It is within this context that this research project was carried out. It aims at better understanding mechanisms involved in multiple cryogenic etching processes on silicon-based materials (p-Si, SiO_2, Si_3N_4). A significant part of this manuscript will focus on the study of fluorocarbon plasma processes in relation to the substrate temperature. Experimental results will be used to feed molecular dynamics simulation models currently being developed by the LTM laboratory in collaboration with this research project. This first chapter covered the general aspects of microfabrication processes and introduced the interest and specificities of cryogenic etching processes. The second chapter will present the experimental set-up and characterization methods that were used for this research project.

The third chapter will focus on the study of deep cryo-etching processes, in particular Bosch etching test results obtained at cryogenic temperature. The fourth chapter will focus more precisely on the fluorocarbon (C_4F_8) plasma passivation step in relation to substrate temperature. The physical adsorption properties of c-C_4F_8 gas will also be experimentally analyzed as a function of temperature and pressure. The fifth chapter will present the results obtained from the analysis of optical emission spectroscopy (OES) acquisitions using a CF_4 plasma in relation to substrate temperature to evaluate the density of CF and CF_2 radicals near the substrate surface. The second part will concentrate on the implementation a Bosch-type process using CF_4 as a passivation gas. A general conclusion will summarize the main results obtained during this research study concerning fluorocarbon plasma-based cryo-etching processes.

1.7 Résumé du chapitre I (français) :

L'industrie des semi-conducteurs et la microélectronique ont connu des innovations prodigieuses depuis l'invention du transistor bipolaire en 1947. Les progrès réalisés dans les procédés de microfabrication ont permis la miniaturisation des composants électroniques dans leur ensemble. En 2024, la taille critique des transistors les plus aboutis atteignent 3 nm et leur réduction est amené à se poursuivre dans une lutte acharnée que se livrent les entreprises du secteur. Parmi les étapes de fabrication, la gravure de ces composants se fait pour la plupart par procédés plasma. Ces procédés doivent être de plus en plus précis afin d'obtenir des rapports d'aspect maximal avec peu de défauts et une marge d'erreur qui peut atteindre l'ordre de quelques couches atomique. Ils doivent aussi être robustes et répétitifs tout en permettant une productivité maximale. Aujourd'hui, les procédés de fabrication industriels sont tenus aussi de réduire leurs consommations et les émissions en gaz fluorocarbonés qui sont toujours très utilisés afin de diminuer leur impact environnemental. Pour l'ensemble de ces raisons, les procédés de cryogravure regagnent en intérêt dans le milieu de la recherche. Ils consistent à refroidir le substrat aux alentours de -100°C avec de l'azote liquide ce qui favorise les mécanismes de passivation de surface tout en limitant certaines réactions de gravure par voie chimique. Cela permet de limiter les défauts de gravure sur les parois et la surface du substrat en général et de réduire la contamination des parois du réacteur pour une meilleure stabilité du procédé.

Le premier procédé de gravure cryogénique, maintenant appelé cryogravure standard, a été introduit par *Tachi et al* en 1988 pour la gravure profonde du silicium. Ce procédé utilise un plasma SF_6/O_2 pour créer une couche de passivation SiO_xF_y qui se forme uniquement à basse température. Actuellement, des procédés de gravure plasma cryogéniques aux chimies diverses sont à l'étude pour certaines applications de gravures fines ou pour la gravure de nouveaux matériaux (matériaux 2D, low-k, poreux, …) afin de limiter les défauts de gravure et assurer des sélectivités plus importantes. Cependant, la compréhension approfondie des mécanismes de passivation SiO_xF_y, C_xF_y ainsi que pour d'autres types de chimie n'est pas complètement établie concernant ces procédés à très basse température. Leurs stœchiométries exactes demeurent incertaines et il en est de même pour les mécanismes précis de désorption thermique concernant ces couches de passivation. Les informations quantitatives sur les probabilités de collage, les taux de désorption thermique, les vitesses de diffusion de surface ou taux de pulvérisation ne sont souvent pas disponibles ou insuffisamment connus à cette gamme de température. Ces données couplées aux paramètres plasma en jeu durant ces procédés sont d'une importance cruciale pour comprendre pleinement les mécanismes de cryogravure. Elles sont difficiles à obtenir expérimentalement car elles doivent être caractérisées in-situ et à température cryogénique ce qui peut s'avérer complexe pour certaines techniques d'analyses.

C'est dans ce cadre que s'inscrit ce projet de recherche qui vise à mieux comprendre les mécanismes associés aux procédés de gravure cryogénique sur des substrats à base silicium (p-Si, SiO_2 et Si_3N_4). Ce manuscrit portera majoritairement sur l'étude de procédés plasmas fluorocarbonés en fonction de la température du porte-substrat. Les résultats expérimentaux permettront d'alimenter des modèles de simulation de dynamique moléculaire en cours d'élaboration au sein du laboratoire LTM en collaboration

sur ce projet de recherche. Dans ce manuscrit, ce premier chapitre a permis d'introduire les principaux procédés de microfabrication et d'exposer les principaux procédés de gravure et de cryogravure par plasma. Le deuxième chapitre présentera le dispositif expérimental et les méthodes de caractérisation qui ont été utilisés pour ces travaux de recherche. Le troisième chapitre se concentrera sur les essais de gravure Bosch à température cryogénique en variant l'apport du gaz de passivation C_4F_8. L'étape de passivation par plasma C_4F_8 et ses propriétés en fonction de la température du porte-substrat sera étudié au sein du chapitre 4. Les propriétés physiques d'adsorption du gaz c-C_4F_8 seront également analysées expérimentalement en fonction de la température et de la pression.

Le cinquième chapitre présentera les résultats obtenus à partir de l'analyse des acquisitions de spectroscopie optique utilisant un plasma CF_4 en fonction de la température du substrat pour évaluer la densité des radicaux CF et CF_2 près de la surface du substrat. La deuxième partie se concentrera sur la mise en œuvre d'un procédé de type Bosch utilisant le CF_4 comme gaz de passivation. Une conclusion générale résumera les principaux résultats obtenus au cours de cette étude de recherche concernant les procédés de cryogravure à base de plasmas fluorocarbonés.

2 Chapter II: Experimental equipment and techniques

2.1 Introduction

This chapter aims to describe the characteristics of the tools and techniques used for the study of cryoetching processes during this research study. The characteristics of the etching reactor as well as its global operation and precautions needed for the implementation of cryoetching processes will first be described. Subsequently, the different samples that were used will be presented with their general structure and preparation method. The surface characterization tools will then be presented followed by the plasma characterization tools. Their working principle will be presented as well as the methodology and acquisition parameters that were used for data analysis.

2.2 ICP etching reactor

2.2.1 General characteristics and dimensions

The experiments were carried out using an Oxford Instrument Plasma Pro 100 Cobra etching equipment [183,184], referred to hereafter in this work as the Oxford Cobra ICP reactor. A detailed schematic of the reactor is provided in **figure II.1** which is not to scale. A schematized picture of the tool is also shown in **figure II.2**. Most of the main components as well as the in-situ characterization tools are listed. The principal dimensions of the chamber are listed in **table II.1**. The available processing gases and injection options are listed in **table II.2** and its main processing characteristics are listed **table II.3**. It consists of an inductively coupled plasma (ICP) reactor with a 2.0 MHz radio frequency (RF) source generator with a maximal power of 3,000 W and a 13.56 MHz RF bias generator with a maximal power of 300 W. The source generator was an Advanced Energy 0230 400V model [185,186]. The bias generator was an Advanced Energy Hilight 133 model [185]. The reactor source contains an alumina tube which acts as a dielectric barrier between the ICP coil consisting of five revolutions around the alumina tube and the plasma volume inside the source. The rest of the chamber (top of the source and the diffusion chamber) is made in aluminum. The chamber walls in the diffusion chamber are connected to the mass.

The total chamber volume is 57 liters. It is sub-divided into two zones. The source is situated at the top where the plasma is struck. The diffusion chamber is situated underneath where the substrate holder is placed. The chamber can be manually opened at the level where what will be referred to as the top and bottom diffusion chambers separate. A schematized picture of the open chamber is shown in **figure II.1.3**. The chamber volume above the substrate holder is approximately 37.4 liters without subtracting the volume that occupies the clamping crown and the gas-ring. Most of the chamber volume under the wafer height is occupied by the substrate holder. The vertical distance between the bottom of the source and the substrate is roughly 27 cm. For gas injections through the source, the

vertical distance is approximately 42 cm from the wafer. Concerning gas injections through the gas-ring, the gas is spread uniformly out of the ring through holes that are placed precisely to that matter at a vertical distance of roughly 12 cm above the wafer level. The exact measurements of the bottom diffusion chamber beneath the substrate holder could not be ascertained due to the difficulty of access.

Figure II.1: Schematic of the Oxford Instruments Plasma Pro 100 Cobra ICP reactor

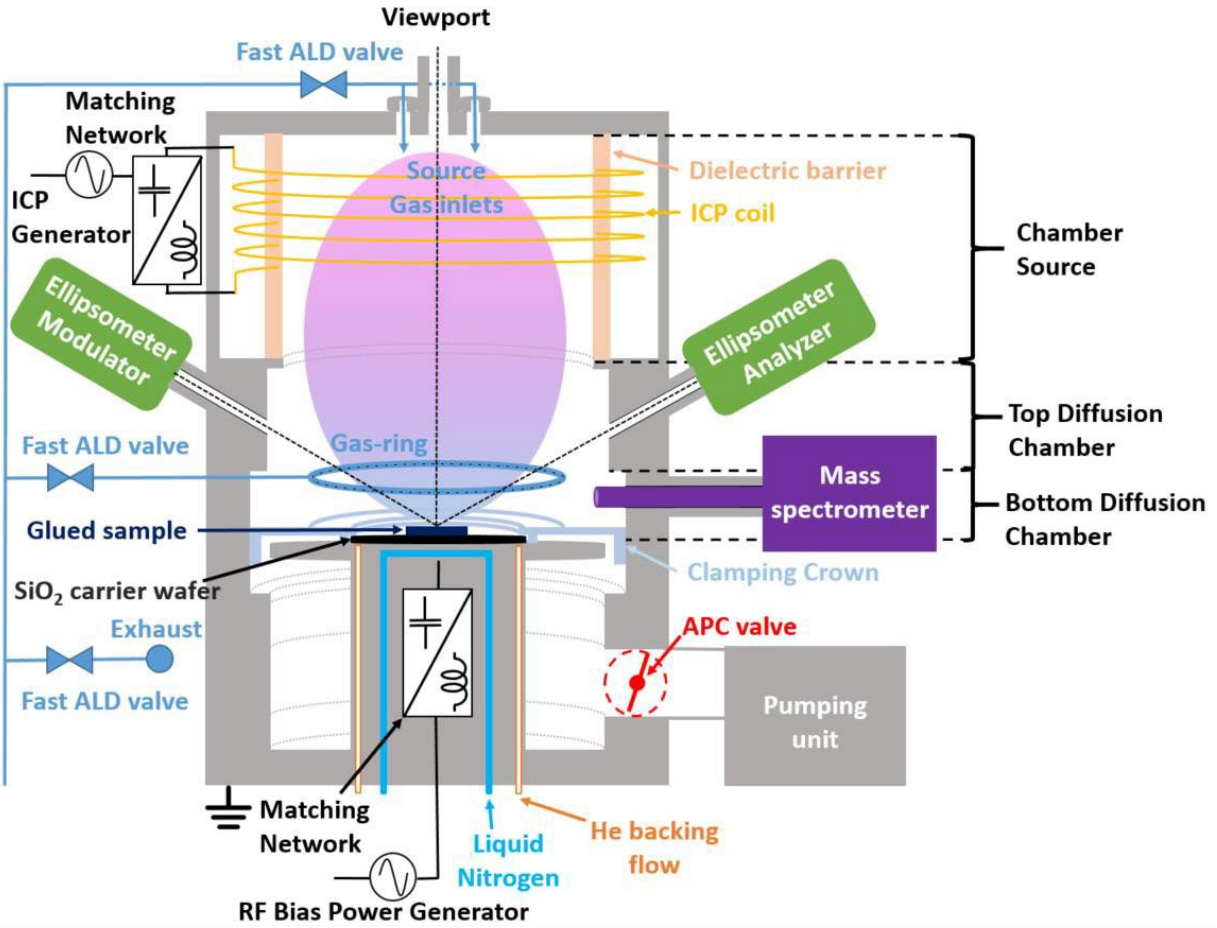

One of the main characteristics of this ICP reactor compared to conventional reactors is the presence of a gas-ring for gas injections. Indeed, it allows gas injections inside the diffusion chamber just above the wafer which offers numerous process possibilities compared to the single use of source injections. It is assumed that gases introduced through the gas-ring dissociate much less in the plasma before reaching the wafer compared to a situation where they are injected through the source in the same conditions. Process gases can also be directed straight to the exhaust (diverted to the foreline). This option enables initializing and/or maintaining a stable gas flow for the gases concerned before being introduced to the chamber in a subsequent process step (either through a source or a gas-ring injection). This option is very practical in the case of fast-pulsed processes with precise short gas injection steps whereas it typically takes one second for a mass flow to stabilize a precise gas flow set value. It is important to note that for all the gas lines concerned, the gas injection can only take place via one of

these channels during a single process step (source, gas-ring or divert). All the gas injection channels (source, gas-ring and divert) are governed by fast Swagelok ultrahigh-purity ALD valves with a response time of 10 ms [187]. These valves are specifically dedicated to the performance of fast pulsed processes such as Bosch, STiGer and ALE. They are each placed very close to the respective gas inlet they govern to enable precise gas injections. To that matter, their electronic controller unit and control air supplies are placed right next to them and are designed to enable fast switching capabilities.

Table II.1: Principal dimensions of the Oxford Plasma Pro 100 Cobra reactor

Dimension	Documentation information / Measurement
Total Chamber volume	57 liters
Chamber Source volume	≈ 10.4 liters
Diffusion chamber volume above the substrate holder	≈ 27.0 liters
Total Chamber volume above the substrate holder	≈ 37.4 liters
(Source - Substrate holder) vertical distance	273 mm
Chamber Source diameter	300 mm
Chamber Source height	147 mm
Top diffusion chamber diameter	334 mm
Top diffusion chamber height	153 mm
Bottom diffusion chamber diameter	380 mm
Bottom diffusion chamber height (until reaching the substrate holder level)	120 mm
(Gas-ring inlet – Substrate holder) vertical height	≈ 120 mm
(Source gas inlet – Substrate holder) vertical height	≈ 420 mm

The ICP reactor is equipped with a cryogenic chuck that enables the cooling down of the substrate holder using liquid nitrogen and can heat it up using thermal resistances. The substrate holder temperature window allowed for wafer processing ranges from -150°C (123.15 K) to +400°C (673.15 K). The substrate temperature measurement is made by a Pt100 sensor which is situated inside the metallic chuck at a distance of several centimeters underneath the wafer. Wafers are clamped with a mechanical clamping system with a helium backing flow which also allows a thermal transfer between the cryogenic chuck and the sample. The quartz crown which is fitted on a metallic clamping ring can be changed in order to process wafers of different sizes, in instance 4'' (100 mm), 6'' (150 mm) and 8'' (200 mm). Although several preliminary tests were carried out with 6'' wafers at the beginning of the research project, it was decided to manipulate exclusively with 4'' wafers subsequently for practical reasons and for compatibility with other research projects which involved the use of the ICP reactor.

The operating pressure of the reactor is situated from roughly 1.0 $x10^{-5}$ Pa to 13.33 Pa. The pressure is regulated through an automatic pressure controller (APC) rotating valve. It can be monitored either by a pressure order value (from 0.01 to 13.33 Pa) or an APC angle order position. At 0.0°, the APC valve is completely closed which stops the pumping. At 90.0°, the APC valve is completely open which allows maximal chamber pumping where a base pressure of roughly 1.0 $x10^{-5}$ Pa can be reached. The pressure inside the chamber is measured via a capacitance manometer gauge and a Penning gauge.

Figure II.2: Schematized picture of the Oxford Cobra ICP reactor tool

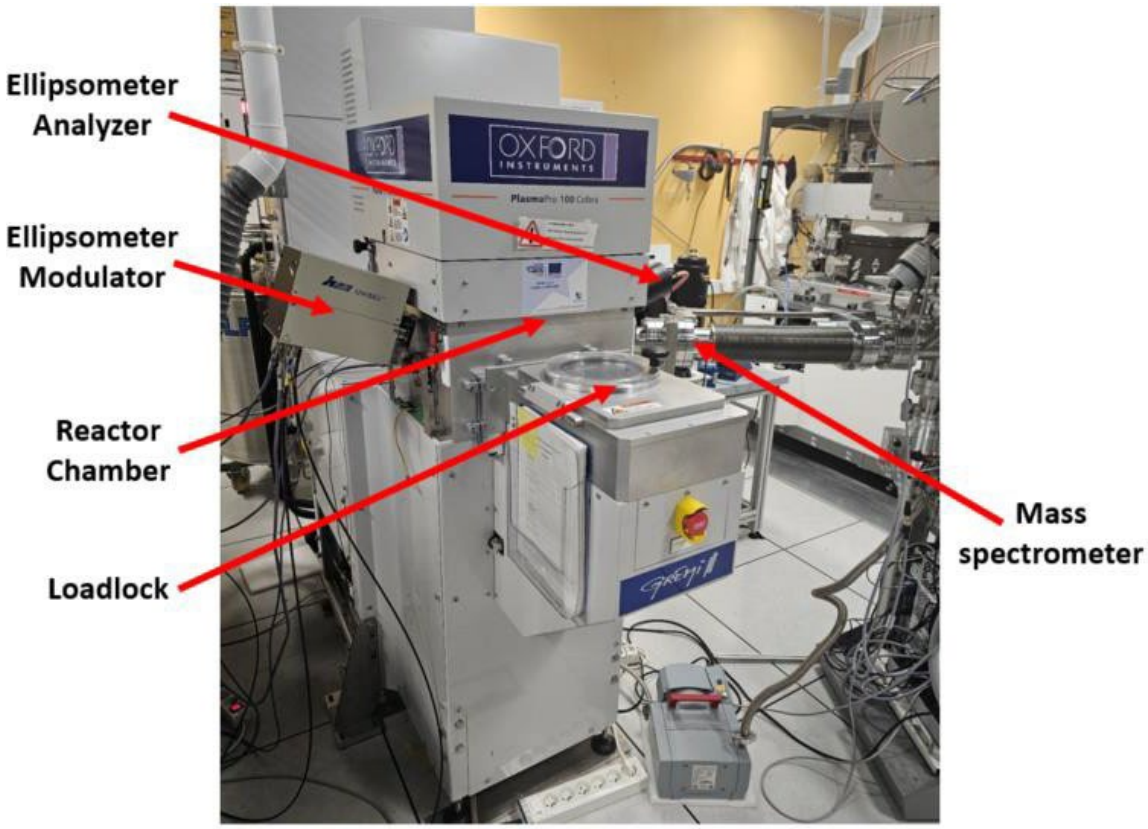

Figure II. 3: Schematized picture of the open Oxford Cobra ICP reactor chamber

Concerning the processing gases, the following gases were installed on the equipment: Ar, SF_6, O_2, CHF_3, CF_4, C_4F_8, SiF_4. The detail of the gas channels and injection channels available on the ICP reactor is presented in **table II.2** and **figure II.4**. It can be noted that Ar and SF_6 were both installed on two separate gas-lines. This was done in order to have the possibility of injecting these gases either through the source at high flows (gas-lines n°1 and n°2) or through the gas-ring at lower flows (gas-lines n°6 and n°12). The gases installed on lines 6 to 12 can be either injected through the source or through the gas-ring or can be directed at the exhaust. One gas injection channel can be used for each process step for all the gas-lines from n°6 to n°12 which are mixed in the same channel line that is selected. All gas lines dispose of a digital MKS mass flow controller (MFC) which uses nitrogen as calibrating gas [188]. They were calibrated accordingly to the working gas of their respective gas-line. The digital calibration allows a 1% setpoint accuracy on the injected gas flow. The settling time of these MFCs are inferior to 750 ms and their control range is accurate from 2% to 100% of their calibrated full scale (maximal flow).

Automated matching units (AMU) are placed on the RF circuits of the source and bias power generators in order to match the impedance between the RF powers they deliver and the plasma. They consist in a resonant resistance-inductance–capacitance (RLC) network. One adjustable capacitor is placed in series (Tune capacitor) with an inductor and another adjustable capacitor is placed in parallel (Load capacitor). The reflection coefficient that is obtained by the setting of these capacitors is a complex number with a real and an imaginary part. Their adjustment allows to maximize the power transfer and minimize the reflected power that RF generators receive back from the plasma which preserves their lifespan and enhances the plasma process. In this case, the starting position and variation of these matching parameters during the plasma process can be controlled by servomotors which are automated by the AMUs. The user can set the initial load (Magnitude C1) and tune (Phase C2) matching parameters for each generator manually during a process step. Concerning the variation of these parameters during a plasma step process, the user can choose to either block the initial values or let them evolve during the process step according to different available options.

Table II.2: List and detail of the process gas lines available on the Oxford ICP reactor

Gas-line number	Gas	Maximal flow	Possible injection modes
1	**Ar**	200 sccm	Source
2	**SF_6**	500 sccm	Source
6	**O_2**	100 sccm	Source / Gas-ring / Divert
7	**Ar**	200 sccm	Source / Gas-ring / Divert
8	**CHF_3**	100 sccm	Source / Gas-ring / Divert
9	**CF_4**	100 sccm	Source / Gas-ring / Divert
10	**C_4F_8**	100 sccm	Source / Gas-ring / Divert
11	**SiF_4**	100 sccm	Source / Gas-ring / Divert
12	**SF_6**	100 sccm	Source / Gas-ring / Divert

The samples are transferred to the chamber from a loadlock which is pumped with a primary pump. The loadlock wafer support is not heated. It is composed of positioning pins that are fitted according to the wafer size in order to place the wafer flat spot at an accurate position. The transfer airlock is vented with

nitrogen gas to reach atmospheric pressure and is pumped down to approximately 1.0 Pa before the slit valve separating the two chambers is opened to enable the transfer. The transfer is ensured with a transfer arm which translates axially the wafer. A lifting pin situated at the center of the substrate holder raises the wafer in order to retract the transfer arm before lowering it at the substrate holder level. The clamping crown is then finally brought down to the wafer level on the substrate holder at the end of the wafer transfer process. Subsequently, a helium backing flow is introduced to allow the thermal contact and clamping of the wafer with the substrate holder during the process.

Figure II.4: Schematic of the process gas lines and associated gas injection channels available on the Oxford ICP reactor

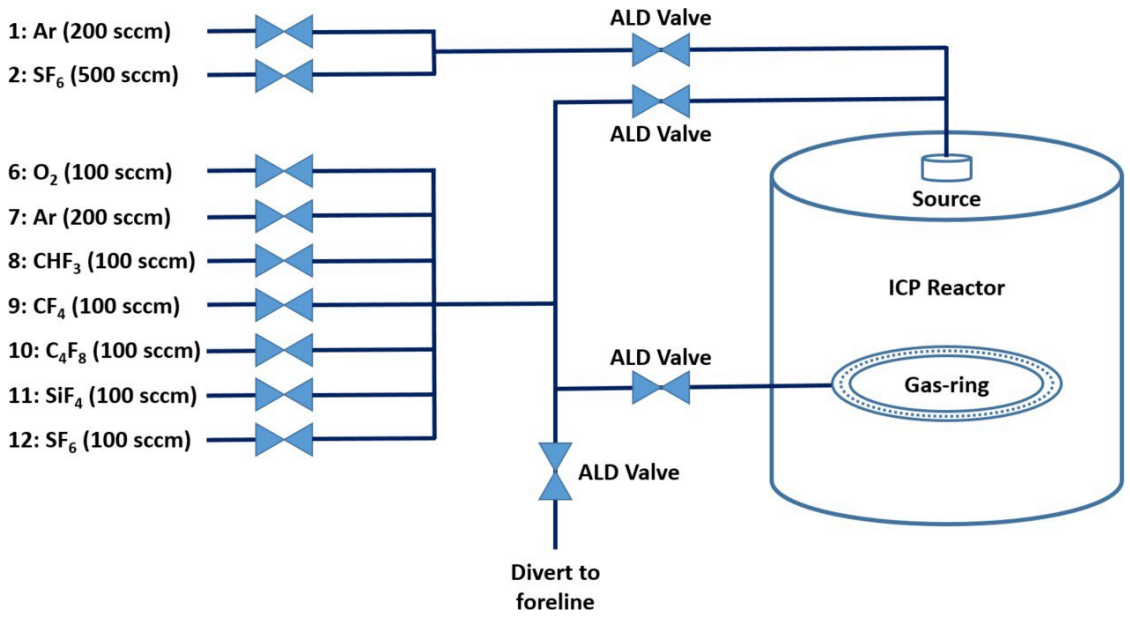

Table II.3: Principal characteristics of the Oxford ICP reactor

Dimension	Documentation information / Measurement
Operating pressure range (APC Pressure setting)	1.0 x10^{-5} to 13.33 Pa
APC valve positioning (APC Position setting)	0,0° (fully closed) to 90,0° (fully open)
Maximal Source Power	3,000 W
Maximal Bias Power	300 W
Operating Gases installed	Ar, SF_6, O_2, CHF_3, CF_4, C_4F_8, SiF_4
Gas injection modes available	Source gas inlet / Gas-ring inlet / Exhaust
Clamping System	Mechanical chuck with He backing flow
Compatible wafer sizes	4'' (100 mm) ; 6'' (150 mm) ; 8'' (200 mm)
Substrate Temperature	-150°C to +400°C
Chamber walls temperature	≈ +40°C
Minimal process step time	10 ms (fast mode) / 1 s (slow mode)
Leak rate	< 5.0 x10^{-3} Pa.min^{-1}

The chamber is pumped using a primary pump and a turbopump. The turbopump is a Pfeiffer ATH 1600 MT (DN 200 ISO-F) model with a pumping speed of up to 1,360 $l.s^{-1}$ for nitrogen [189]. It is a magnetically levitated turbopump that is cooled with water. The chamber can also be vented with nitrogen in order to open it to perform manual operations such as the installation of characterization tools. The RF source generator as well as the auxiliary RF circuits are also cooled with water. The RF antenna located at the top of the chamber source as well as the RF bias generator are cooled using compressed air. An aeration is located near the bias electric relays and automated matching unit (AMU) but it was decided to fit in a fan in this area to enhance cooling. Regular leak rate tests of the chamber were carried out to verify the value was under 5.0 $x10^{-3}$ $Pa.min^{-1}$. Maintenance work to detect and repair the origin of the leaks was carried out if ever the leak rate was above this value.

2.2.2 Chamber Openings and placement of in-situ characterization tools

The ICP reactor disposes of ten windows or viewports for the installation of various in-situ characterization tools as well as giving an access to the gas-ring. The characterization tools than can be mounted on the ICP reactor include mass spectrometry, ellipsometry, absorption spectroscopy, electrostatic probes as well as etch depth monitoring using reflectometry and interferometry. Fuller details of the different openings on the reactor and their function are shown in **figure II.5**.

Openings n°1 and n°2 are located at the rear side of the reactor, in opposition to the slit valve where the wafer is transferred to the chamber. Opening n°1 was originally used by the gas-ring injection channel. However, it was decided to dismantle the gas-ring system and reinstall it on opening n°2 because opening n°1 offered a preferential position to perform plasma probe measurements. Indeed, it is aligned with center of the substrate holder with a vertical height of 7.2 cm above the substrate holder level. This operation did not modify significantly the position of the gas-ring inside the chamber, only adding approximately 1 cm of vertical distance compared to the substrate holder. As a result, a glass viewport was placed by default on opening n°1 which was only replaced to fit the plasma characterization probes when needed.

Opening n°7 was used for mass spectrometry acquisitions. The center of this opening is located 4.85 cm above the substrate holder level. It allows the mass spectrometry head to be approached at a horizontal distance of roughly 2 cm from the edge of the clamping crown.

The in-situ ellipsometer openings (n°4 and n°8) are face to face but are inclined to allow an angle of incidence (AOI) of 70° for the incident and reflected polarized beams which are aimed at the exact center of the substrate holder.

Figure II.5: Picture of the different chamber openings available on the Oxford Instruments Plasma Pro 100 Cobra reactor

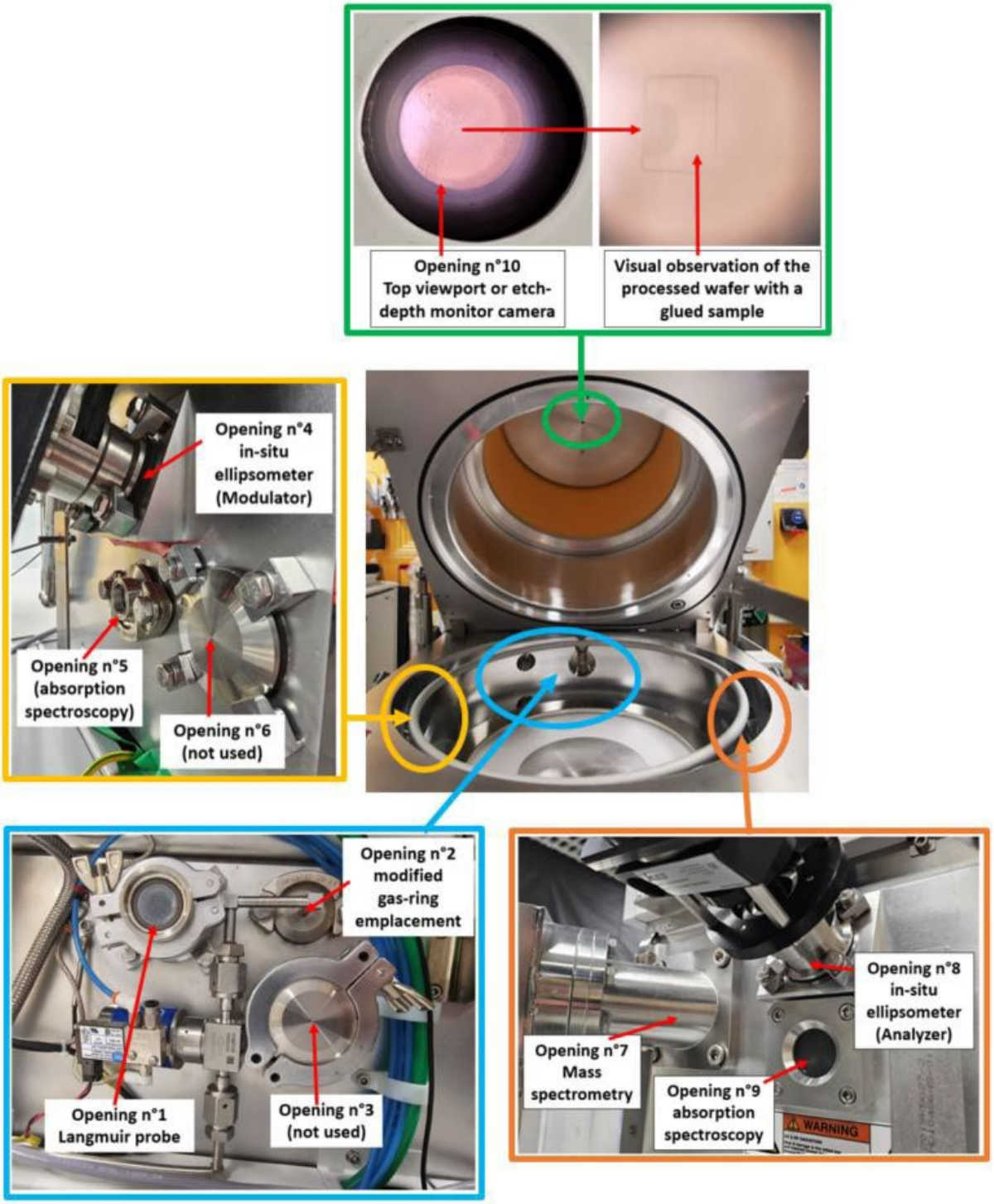

The absorption spectroscopy openings (n°5 and n°9) are also placed face to face. The exact center of these openings is located approximately 1.25 cm above the substrate holder level. As a result, the clamping crown had to be removed in order to not obstruct the optical signal during the acquisitions.

The top viewport (opening n°10) is located on top of the source. The center of this opening is vertically aligned to the center of the substrate holder. Although it is meant to host an etch-depth monitor camera which was used on rare occasions, it was mostly used as a viewport to visualize the position and aspect of the samples being processed. Its preferential location prevented plasma from gradually etching and obstructing this window in comparison to the other windows situated in the diffusion chamber.

The chamber windows n°3 and n°6 were always sealed and never used throughout this research study. Their normal axis is not aligned with the center of the substrate holder and they do not dispose of a complementary opposite window. In general, only the openings n°4 and n°8 (in-situ ellipsometry), n°7 (mass spectrometry) and n°2 (gas-ring injection) were constantly in use. Glass viewports were placed on chamber windows n°5 and n°9 (absorption spectroscopy) as well as n°1 (Plasma probes) when these characterization tools were not used. However, these were partially etched or covered with plasma deposited species which did not allow a clear visual observation of the processed wafer. Only plasma light could be distinguished.

2.2.3 Process editing, optimization and acquisition settings

2.2.3.1 Bias voltage setting

The bias voltage could only be set during a process step by applying an order bias power value on the generator. Therefore, preliminary testing was necessary to determine the input power to retrieve an adequate bias voltage. This operation had to be done using a dummy wafer that was the same type as the wafer holder used for the subsequent process tests (Si or SiO_2). Indeed, the bias voltage measurement is sensitive to the material which undergoes a plasma process.

Towards the precise application of bias power, the equipment disposes of two electrical relays in the bias power circuitry. One of them is solicited when the bias power order value is above 10% of the maximal power output of the generator (in this case ≥ 30 Wb). In the other case (bias power order value < 30 Wb), where the power delivery from the generator may not be optimal, the other electrical relay is activated. In this case, the programmable logic controller (PLC) orders a bias power 10 times more important to the bias generator which passes through a 10 dB attenuator to retrieve a more precise bias power output. As a result, high frequency pulsed processes had to be realized in a way where both ordered bias powers for the passivation and etching steps had to be either below or above 30 W. This precaution was taken in order to preserve the switch from being over-solicited.

2.2.3.2 Gas injections

To prevent gas mixing as much as possible during processes involving the gas-ring, it was in most cases decided to inject etching gases (Ar or SF_6) through the source by soliciting gas-lines n°1 and n°2. The passivating gases (O_2, CHF_3, CF_4, C_4F_8 and SiF_4) would then only be injected through the gas-ring. Usually the exhaust option (divert) was only used before gas-injection steps (1 to 5 seconds) for fast pulsed processes or cryo-ALE processes. This was done in order to activate the mass-flow of the gas-line and achieve a stable gas flow before switching the injection mode towards the source gas inlet or gas-ring inlet. It prevented the observation of gas over-flows at the beginning of gas injection steps. Moreover, it allowed the recordings of gas-flows to better respect a square-type shape with rapid and precise responses in relation to the order value which is important notably for ALE processes. In the same way, it was also used sometimes at the end of gas injection steps. The objective was to purge the source or gas-ring inlet channels as much as possible before introducing another gas of different nature.

2.2.3.3 Temperature settings and wafer clamping

The substrate temperature is stabilized using two proportional integral derivative (PID) systems which either inject liquid nitrogen to cooldown the sample (cooling table) or induces heating of the chuck through resistances (heating table). The operation frequency and intensity of these tables depend on the setting of the PID systems which induce temperature fluctuations due to the activation of the necessary table determined by the measured chuck temperature. The PID values (Kp, Tn and Tv) for both the heating table and the cooling table were evaluated and optimized to maintain cryogenic temperatures with a precision of usually ± 1°C for a substrate temperature comprised between -130°C and -70°C. At maximal cryogenic temperatures (-150°C to -130°C) and minimal cryogenic temperatures (-70°C to 0°C), the chuck temperature maintenance was a bit less sensitive with a precision of usually ± 2°C.

In general, 20 to 25 minutes were necessary to cooldown the substrate holder from +20°C to cryogenic temperatures (typically -100°C). A supplemental period of 5 minutes was necessary in order to stabilize the chuck to the desired temperature. The chamber walls are heated with heating liners and the temperature is maintained at +40°C. However, it is important to note that the cooling channels inside the cryogenic chuck are not insulated from the rest of the total volume and are not heated by thermal resistances except at the top area where the wafer is clamped. Several other cryogenic chucks choose to insulate the channels by vacuum pumping. As a result, it is likely that the outer walls of the substrate holder might be thermalized at a colder temperature than the temperature value which is measured by the Pt100 sensor at the level of the wafer during cryogenic processes. In this case, it is presumed that condensation and physisorption reactions might be enhanced in this area during cryogenic processing compared to the top surface of the substrate holder where the wafer is placed.

The temperature mentioned in the experimental conditions corresponds to the set point temperature of the chuck. Therefore, a minimal thermalization time of 5 minutes was given at the beginning of each

cryogenic test which involved the introduction of a new sample coming from the exterior atmosphere at a temperature of roughly +20°C. The wafer was systematically clamped at 1,300 Pa (9.75 Torr) using a helium backing pressure to maintain a constant pressure for 5 minutes at the beginning of the processes. The helium backing gas flow value was monitored during the thermalization time to check if it was stable and under 5 sccm in order to ensure a satisfactory thermal contact.

2.2.3.4 Plasma striking and impedance matching

The reactor was installed and preliminary process testing occurred at the beginning of the research project. The reactor initially had a Faraday shield placed around the source between the alumina cylinder and the antenna to prevent capacitive coupling during the plasma strike. However, it was observed that low source power argon plasmas could not be struck without a minimal bias power (usually 5 W), which is not wanted in most ALE processes. Therefore, it was decided to take it off in order to perform plasma strikes at 0 W to prevent any form of sputtering of the substrate, especially during cryo-ALE process tests.

The equipment supports two process execution modes which are referred to as slow and fast modes. In slow mode, the process steps have to exceed 1 s. This allows the user to pause, skip or extend a process step during the execution of a process. In fast mode, the process steps can go down to 10ms. However, the PLC is solicited in a way which prevents the user from skipping, pausing or extending a process during the execution of the process. This mode usually allows a better plasma impedance matching efficiency between etching and passivation steps for fast-pulsed processes. Most of the processes presented in this manuscript were carried out in slow mode.

Plasma impedance matching parameters applied to the RF source and bias powers were systematically optimized during the implementation of etching or deposition processes. Their starting positions were chosen for each necessary process step so as to enable rapid plasma striking and efficient holding in order to rapidly decrease the reflected powers. During the processes, the evolution of the matching parameters was always controlled by the AMU. Their values were closely monitored during the process tests to verify their stability and to ensure that they did not drift towards extreme positions (0 or 100%) where the matching becomes inefficient. The associated reflected powers were also monitored during the process tests.

2.2.3.5 Plasma and manual cleanings of the chamber

Plasma cleaning processes were always carried out in the reactor before, in between and after process tests. The objective was to decontaminate the chamber walls as much as possible and ensure that these were in clean condition at the beginning of each process test. The realization of plasma cleanings enables enhancing process repeatability. As a result, significant chemical contamination which could

arise from previous tests was excluded in the analysis of process results. All these cleaning processes were realized with dummy Si or SiO_2 wafers.

In general, an O_2 plasma was used to clean the chamber (50 sccm O_2 ; source injection: 2.5 Pa ; 1500 W source power ; 50 W bias power ; 1300 Pa clamping pressure) for at least 5 minutes. The use of O_2 creates oxygen radicals in the plasma which will react chemically with any fluorocarbon contaminants. The high source and bias energies used in this process also allows physical sputtering of contaminants. The bias power was sometimes reduced or not used depending on results of previous plasma process tests. In some cases, the chamber pressure was manually modified several times during the cleaning processes (10 Pa, 2.5 Pa, 1 Pa) so that the plasma could be localized and therefore more efficient at different heights of the chamber (source, diffusion chamber, substrate holder). Occasionally, an Ar cleaning plasma was used (50 sccm; source injection; 2.5 Pa; 1,500 W source power ; 50 W bias power ; 1,300 Pa clamping pressure). In very rare occasions, such as the appearance of thick black silicon on a wafer a process test, the ICP reactor was opened to perform manual cleanings. This was done with dedicated clean wipes wet with isopropyl alcohol (IPA) or distilled water. On these occasions, the clamping crown was dismantled to access it from underneath and the substrate holder was sometimes scrubbed with Scotch-Brite also wet with IPA or distilled water.

2.2.3.6 Realization of process tests and parametric studies

Particular precautions were taken during the implementation and realization of processes as well as the elaboration of parametric studies. During the elaboration of a reference test, a dummy wafer with the same characteristics as the subsequent tested samples was used. Every process step was evaluated and optimized especially for plasma striking rapidity, plasma holding and repeatability. The necessary bias power to retrieve a desired bias voltage was investigated for each necessary step. For continuous plasma or fast-pulsed processes, the plasma strike was verified and the evolution of the impedance matching parameters and bias stability were monitored for the rest of the time the plasma was held. For cyclic processes, the plasma strike rapidity as well as its maintenance, impedance matching and bias voltage were evaluated for each cycle repetition.

For process steps involving pressure governed by an APC position setting, the valve angle was precisely fixed in order to rapidly achieve a required pressure which was fairly stable in time. For fast-pulsed processes involving different APC angles for the etching and passivation steps, the positions were chosen in order to maintain repeatable pressure measurements throughout the process duration. The preparation of reference tests for the realization of parametric studies was always implemented with intermediate parameters. When a particular parameter was studied, the process tests were usually realized by starting with the reference process and then varying the parameter following a specified random order or alternating order. Frequently, the reference test was repeated several times during the realization of the parametric study to evaluate the process repeatability and assess that the chamber conditioning is roughly the same at the beginning of each test.

2.2.3.7 Acquisition and analysis of process parameters

The ICP reactor software allowed the recording of the process parameters that could be carried out with a sampling rate defined by the user. Depending on the duration of a process step, a sampling rate between 250 ms and 1 s was chosen in order to accumulate a sufficient number of points for each step. The software allowed the plotting of multiple parameters in relation to time on the same graphs which was helpful towards the optimization and analysis of plasma processes during their implementation. Moreover, these process recordings were exported when necessary to compare with in-situ characterization recordings that took place at the same time (in-situ ellipsometry, mass spectrometry).

All the data needed to be reprocessed and synchronized in time in order to match each other. Indeed, the recordings were taken with different software and were launched at different time intervals with various sampling rates. As a result, it was possible to plot the deposition or etching rate of a sample obtained by in-situ ellipsometry as well as the intensity of species detected in the chamber by mass spectrometry in relation to process parameters recorded by the ICP reactor such as the gas-flow injections, chamber pressure etc. The analysis of this data was helpful in the understanding of plasma-surface interactions involved during cryogenic processes.

2.3 Samples and sample preparation

Plasma processes were mostly performed on sample coupons which were glued with a specific thermal glue on 4'' or 6'' (100 mm or 150 mm) silicon or silicon dioxide wafer carriers depending on the experiment and the reactor configuration. The thermal glue which was used is specifically designed for cryogenic process studies. It liquifies at around 60°C and allows the glued coupon sample to stick on the wafer carrier with a limited thickness between them. It has a high heat transfer coefficient which allows the glued sample to rapidly reach the same temperature as the carrier wafer. The use of these sample coupons was privileged due to the nature of this research project. The goal was to focus more on the main etching or deposition characteristics that could be observed through quantitative parametric studies rather than optimizing etching process uniformity. This solution prevented the waste of entire patterned wafers which were rather cleaved in several coupons of roughly 3x3 cm^2 maximum in size. These coupons were glued systematically at the exact center of the carrier wafers in the case where a single coupon was studied for a process experiment. This is mainly due to the fact that the in-situ ellipsometer light beam was situated at this position on the carrier wafer.

In some cases, one or two other sample coupons were glued onto a single carrier wafer. They were glued with a minimal distance of 1 cm from the edges of the wafer in order not to damage the quartz crown which clamps the carrier wafer on its borders on the top surface. For example, some deep-etching tests involved the use of two coupon samples (such as SF_6 and Alcatel trenches samples) which had different patterns, in order to compare a greater variety of etching profiles in a single process. A second example consisted in the study of the etching or deposition selectivity of a process by gluing three different coupons on a single carrier wafer (p-Si, SiO_2, Si_3N_4). The coupon sample glued at the center, in these cases, was usually studied by in-situ ellipsometry during the process whereas the two other coupons were characterized by ex-situ ellipsometry before and after the process test.

Concerning the preparation of the coupon samples, they were first cleaved from their respective wafers and then glued to the carrier wafer. To do so, the glue contained in a syringe was softened by a heating lamp and a volume of roughly 8.0 $x10^{-3}$ cm^3 cylinder of 0.5 mm radius and 1 cm in length) was manually injected at each spot where a coupon sample was placed on the carrier wafer. The carrier wafer was then placed on a hotplate at 60°C to liquify the glue completely which flattened and fitted the area of the coupon sample above it. The carrier wafer was then placed on a flat support at ambient temperature to allow the thermal glue to solidify again and maintain the position of the coupon samples on the carrier wafer. As a result, the exact thickness of glue separating the coupon and the carrier wafer always varied depending on the size of the coupon sample and the volume of glue that was used. After the process test, the glued coupon samples were detached manually with tweezers from their support carrier wafer by placing them on a heated table again at 60°C. The excess of glue on the back side of the coupon sample was then swept away using a tissue wet with isopropyl alcohol. It was done very carefully so as not to interfere with the front-side where the etching took place, in

order to avoid any contamination issues due to the adhesive. The deep-etching process tests were realized with “Trench Via Trench” (TVT) coupon samples whereas thin etching and thin deposition tests were realized with thin film p-Si, SiO_2 and Si_3N_4 samples. The detailed characteristics of these samples are explained below.

2.3.1 Trench Via Trench (TVT) samples

Trench via trench (TVT) samples consisted of a silicon substrate with a SiO_2 hard mask with a thickness of 1.2 µm which was patterned with an array of parallel trenches from 2 to 10 µm in width and roughly 2 mm in length. A single array consisted of 2 trenches of 2 µm in width, 4 trenches of 4 µm in width, 6 trenches of 6 µm in width, 8 trenches of 8 µm in width and 10 trenches of 10 µm in width. Every trench of the same width is separated by roughly 100 µm from each other and every series of identical trenches was separated by 300 µm. A scanning electron microscope observation of a pristine single face TVT sample is shown in **figure II.6**

Figure II.6: SEM image of a pristine TVT sample (6 µm trench)

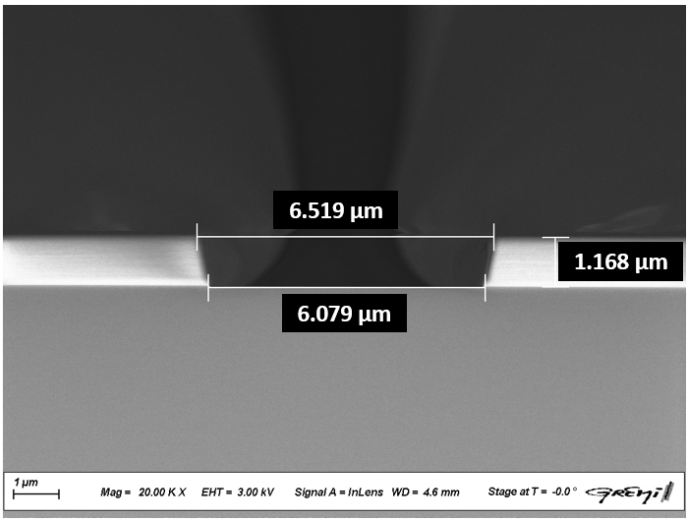

2.3.2 Thin film p-Si, SiO_2 and Si_3N_4 samples

Thin film samples were used to characterize thin etching process tests as well as deposition tests which were both monitored through in-situ ellipsometry. They consisted in blanket samples with thin layers of different nature deposited on a Si substrate. Polycrystalline silicon (p-Si) samples consisted of a 150 ± 5 nm thick p-Si layer deposited by plasma-enhanced chemical vapor deposition (PECVD) on a 100 ± 5 nm layer of thermal SiO_2 grown on a 300 mm (100) silicon wafer. Silicon oxide (SiO_2) samples consisted of a 100 ± 5 nm thick layer of thermal SiO_2 grown on a 300 mm (100) silicon wafer. Silicon nitride (Si_3N_4) samples consisted of a 250 ± 13 nm thick layer of silicon nitride deposited by

low-pressure chemical vapor deposition (LPCVD) on a 300 nm (100) silicon wafer. All these individual samples were cleaved from 12'' wafers which were provided by TEL to the GREMI laboratory for a previous PhD thesis project.

An example of 3 coupon samples (Si_3N_4, p-Si and SiO_2) glued on a 100 mm SiO_2 carrier wafer for an etching test is shown in **figure II.7**. An unscaled stacking schematic of these 3 samples is detailed in **figure II.8**.

Figure II.7: Image of a 100mm SiO_2 carrier wafer with 3 glued samples (Si_3N_4, a-Si, SiO_2)

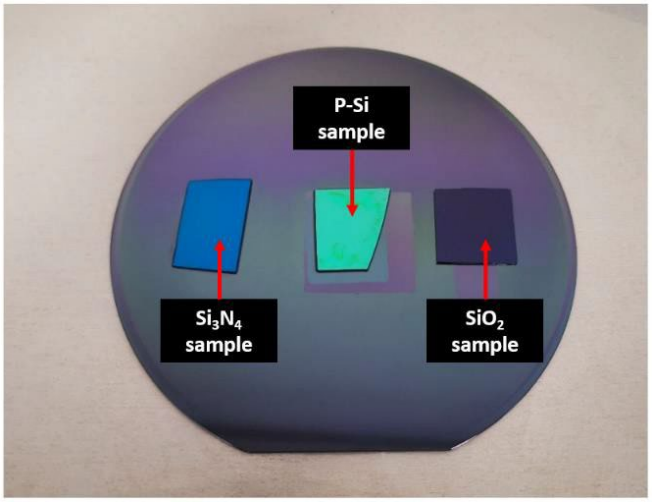

Figure II.8: Stacking schematic of Si_3N_4, p-Si and SiO_2 samples (not to scale)

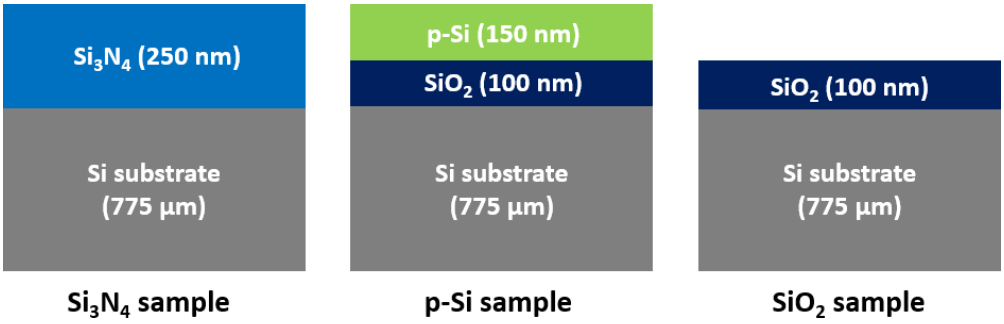

2.4 Sample characterization techniques

2.4.1 Spectroscopic ellipsometry

2.4.1.1 General ellipsometry theory

Spectroscopic ellipsometry is an optical non-destructive technique which is based on light polarization [190,191]. Ellipsometry spectra are realized by measuring the polarization modification over a range of light beams which are reflected or transmitted from a sample surface. Subsequently, the acquisitions need to be fitted to an ellipsometry model which accurately respects the nature of the sample surface to retrieve the thin-layer thicknesses and their respective optical index. It can also be used to estimate the composition, roughness, crystallinity and electrical conductivity of a sample surface material.

This technique is frequently used to analyze thin-layer thicknesses from the atomic scale to several microns. It is often used in the semiconductor industry to evaluate the wafer homogeneity after an etching or deposition process. During the acquisition, the incident light beam is considered as a plane progressive harmonic wave. Its polarization state represents the electric field component of the electromagnetic wave. The polarization state of the incident light beam is described by the sum of its two components, E_p^i and E_s^i which are respectively the parallel and perpendicular components to the plane of incidence.

A schematic is shown in **figure II.9** to illustrate the reflection of a polarized light beam from a sample surface. Usually, the incident light beam is first linearly polarized through a polarizer before reaching the sample surface. Once the light beam hits the sample surface, the reflected light beam will shift from a linear to an elliptical polarization state depending on the dielectric properties of the surface material. The resulting parallel and perpendicular polarization components of the reflected beam, respectively E_p^r and E_s^r will have a complex nature with real and imaginary parts. Therefore, the reflection can be characterized by two complex coefficients, r_p and r_s, also called the Fresnel coefficients which are obtained with the following equations (**equation II.1**):

Equation II.1: Fresnel coefficient equations

$$r_p = \frac{E_p^r}{E_p^i} = |r_p|.e^{i\delta p} \qquad r_s = \frac{E_s^r}{E_s^i} = |r_s|.e^{i\delta s}$$

In these equations, $|r_p|$ and $|r_s|$ represent the magnitude of the reflection coefficients, respectively in the parallel and perpendicular planes whereas δp and δs correspond to their argument values, representing in this case the phase shifts for the reflection coefficients in the parallel and perpendicular planes. The relation between r_p and r_s is given by the fundamental equation of ellipsometry (**equation II.2**) which introduces two values, ψ and Δ.

Equation II.2: Fundamental equation of ellipsometry

$$\rho = \frac{r_p}{r_s} = \tan(\psi).e^{i\Delta}$$

$\tan(\psi) = \frac{|r_p|}{|r_s|}$ where 0° < ψ < 90° corresponds to the variation of the $\frac{|r_p|}{|r_s|}$ amplitudes ratio

$\Delta = \delta_p - \delta_s$ where 0° < Δ < 360° corresponds to the variation of the phase shift between r_p and r_s

Both ψ and Δ values are determined by the ellipsometer based on the polarization measurement of the reflected beam using a photoelastic modulator. From these values, it is possible to retrieve the refractive index of the sample surface N_2 using the Snell-Descartes equation (**equation II.3**) and the Fresnel equations (**equation II.4**).

Figure II.9: Spectroscopic ellipsometry principle (adapted from [190])

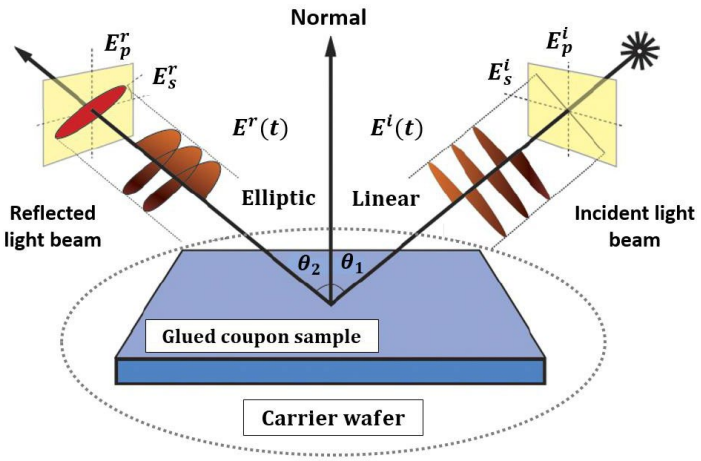

Equation II.3: Snell-Descartes equation

$$N_1.sin(\theta_1) = N_2.sin(\theta_2)$$

Equation II.4: Fresnel equations

$$r_p = \frac{N_2.\cos(\theta_1) - N_1.\cos(\theta_2)}{N_2.\cos(\theta_1) + N_1.\cos(\theta_2)} \qquad r_s = \frac{N_1.\cos(\theta_1) - N_2.\cos(\theta_2)}{N_1.\cos(\theta_1) + N_2.\cos(\theta_2)}$$

In these equations, θ_1 and θ_2 are respectively the complex angles of incidence and refraction of the light beam on the sample surface. N_i corresponds to the complex refractive index of the medium. In the case of air (transparent medium): $N_1 = n_1 = 1$

For the substrate or the sample surface material, which is an absorbing medium, the complex refractive index N_2 is calculated using n_2 and k_2 which correspond respectively to the refraction index and extinction coefficient of the medium: $N_2 = n_2 + ik_2$

The refractive index defines the phase velocity of light in the medium whereas the extinction coefficient describes the decrease of light intensity through the medium due to absorption reactions. For an absorbing medium, the decrease in intensity of an incident light beam I is described by the Beer-Bouguer-Lambert extinction law in **equation II.5**.

Equation II.5: Beer-Bouguer-Lambert extinction law

$$I = I_0 . e^{(-\alpha . z)}$$

In this equation, I_0 corresponds to the intensity of the incident light beam, α corresponds to the absorption coefficient which is defined by **equation II.6** whereas z corresponds to the penetration distance of the light beam in the medium.

Equation II.6: Absorption coefficient formula

$$\alpha = \frac{4\pi . k}{\lambda}$$

In this equation, k corresponds to the extinction coefficient of the medium at the specific λ wavelength.

There are mostly three types of reactions which are responsible for light absorption inside a material: electronic transitions, molecular or lattice vibrations and free carrier absorptions. These reactions occur only at quantified energy levels. Therefore, depending on the nature of the dielectric material, its dispersion law which characterizes the refractive index in function of the incident wavelength will vary significantly. As a result, different types of equations and models were developed to approximate the dispersion laws of materials given their chemical and structural properties. For absorbing materials, their dispersion law will depend mostly on their dielectric permittivity ε which is also a complex function with a real part ε' and an imaginary part ε'' which is detailed in **equation II.7**. They depend on the light beam angular frequency ω (**equation II.8**).

Equation II.7: Complex permittivity formula

$$\varepsilon\,(\omega) = \varepsilon'(\omega) - i\varepsilon''(\omega)$$

Equation II.8: Angular frequency formula

$$\omega = 2\pi . f = \frac{2\pi . v}{\lambda}$$

In these equations, v corresponds to the phase velocity of the wave propagation in the medium which is wavelength dependent in dispersive media. Therefore, once the dispersion law of a material has been correctly approximated, it is possible to determine its dielectric properties as well as its thickness by mathematically interpreting the acquired ellipsometry spectrum in relation to its dispersive characteristics. In the case of a single isotropic thin layer deposited uniformly on a substrate material, the thickness d of the thin layer m can be calculated by determining the reflected coefficients and using the Airy formula (**equation II.9**).

Equation II.9: Airy formula for the determination of $r_{1\,s,p}$ and $r_{2\,s,p}$ complex reflection coefficients

$$r_{s,p} = \frac{r_{1\,s,p} + r_{2\,s,p} \,.\, e^{-2ib}}{1 + r_{1\,s,p} \,.\, r_{2\,s,p} \,.\, e^{-2ib}} \quad where\ b = \frac{2\pi . d . N_m . \cos(\theta_m)}{\lambda}$$

In this equation, $r_{1\,s,p}$ corresponds to the complex reflection coefficients associated with the air to thin layer interaction whereas $r_{2\,s,p}$ corresponds to the complex reflection coefficients associated with the thin layer to substrate interaction. N_m is the complex refractive index of thin layer and θ_m is the complex angle within the thin layer. λ corresponds to the wavelength of the incident monochromatic light beam.

For more complicated sample stackings, the reflections can be determined using matrix methods which enables the characterization of the different dielectric material properties and associated thin layer thicknesses. The matrix calculations can extend to more complicated computations if the thin-layers are not isotropic or possess certain specificities such as the presence of porosities, interaction layers or gradients of the refractive index. Therefore, it is important to determine an appropriate model which accurately describes the sample stacking to avoid misinterpretations during ellipsometry model fittings.

2.4.1.2 Equipment

Spectroscopic ellipsometry (SE) was the main surface characterization technique used in this research project to determine the thin surface layer thicknesses of relevant samples. This technique was used for thin-etching process tests such as cryo-ALE or during deposition tests such as C_4F_8 adsorption tests or (SiF_4+O_2) passivation tests.

For that matter, two UVISEL-1 model spectroscopic ellipsometers from Horiba Jobin-Yvon were used [192]. The first was an in-situ device which was attached to the ICP reactor to monitor the thickness

of the surface thin film and the evolution of its dielectric properties during the plasma processes. The second was an ex-situ model which is available in the clean room. The ex-situ ellipsometer was only used in rare cases for sample preparation or as a back-up when the in-situ was temporarily out of service or for verification matters.

Both of these ellipsometers are polarization modulation ellipsometers (PME). The light source consists of a xenon arc lamp which has a spectral range from the near-UV area to the near-IR area. UV optical fibers were used to convey the light beam from the source to the analyzer and from the modulator to the monochromator and multiwavelength units. UV fibers cover a spectral range for the light beam it transports from 190 nm (≈ 6,53 eV) to 880 nm (≈ 1,41 eV). The conversion from the photon wavelength to its associated energy is defined by the Planck-Einstein relation (**equation II.10**).

Equation II.10: Planck-Einstein relation

$$\lambda = \frac{h.c}{E} \qquad and\ with\ 1\ eV\ \approx 1.602\ \text{x}10^{-19}\ J \qquad \lambda = \frac{1.24\ \text{x}10^{-6}}{E\ (eV)}$$

During a spectroscopic ellipsometry acquisition, the generated light beam travels through an optical fiber towards the analyzer unit where a mirror network, different filters and more importantly a polarizer allows to polarize the light linearly. The polarized light beam is then directed to the sample surface at an angle of 70°. Depending on the surface nature and the sample stacking, the light beam will be reflected and transmitted through the different thin layers of material which will modify its polarization. The reflected signal is acquired by a modulator unit. It first reaches a photoelastic modulator (PEM) which will modulate the polarization state in function of time using a piezoelectric birefringent silica bar which oscillates at a resonance frequency of 50 kHz. The phase retardation which is caused by the PEM between the 2 components of the electric field is defined by **equation II.11**.

Equation II.11: Phase retardation in a birefringent material

$$\delta(t) = A.\sin(\Omega.t) \quad with\ f = \frac{\Omega}{2\pi} \quad and\ A = \frac{2\pi.d(n_1 - n_0)}{\lambda}$$

In these equations, d corresponds to the thickness of the birefringent bar ; n_1 and n_0 correspond to the two refractive indices of the birefringent material. The oscillations are regulated via a modulation voltage which enables maintaining a constant modulation amplitude for every wavelength. The modulated signal is then conveyed to a polarizer analyzer which will measure the polarization states in function of time. The signal is then either directed to the monochromator unit or to the multiwavelength unit in function of the acquisition mode. The monochromator unit will sort the light signal in function of the adequate wavelength before it reaches the detector which will analyze the signal in the UV-visible

range using photomultipliers and the signal in the IR spectral range using an InGaAs detector. Concerning the multiwavelength unit, the light signal is decomposed and analyzed by 32 photomultipliers. Each detects the signal at a specified wavelength between 1.517 and 4.993 eV. A schematic of the different components of the in-situ ellipsometer is detailed in **figure II.10**. Ellipsometry data analysis was realized through the dedicated software called DeltaPsi2 provided with the equipment [193].

Figure II.10: Schematic of the Horiba Jobin Yvon UVISEL-1 in-situ characterization tool (adapted from [190])

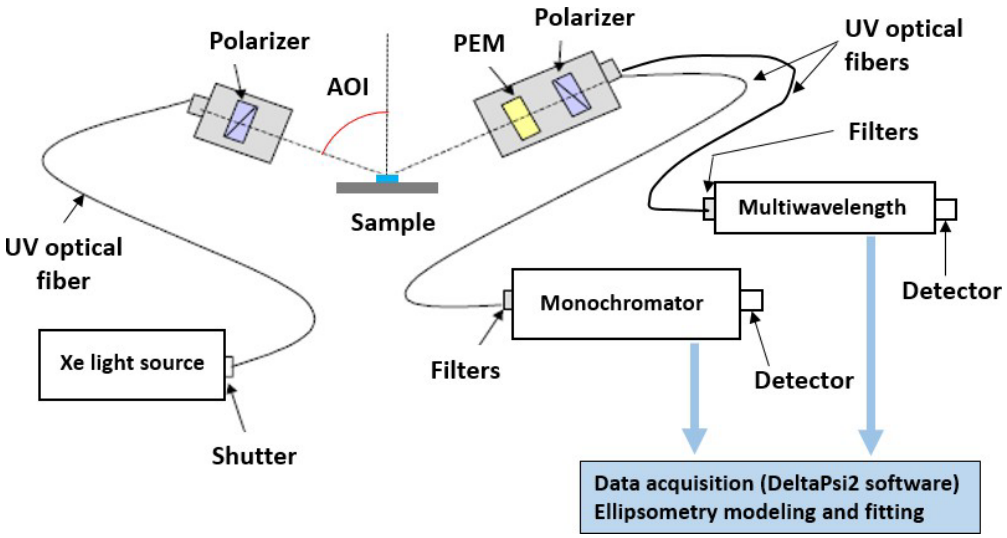

2.4.1.3 Acquisition parameters

Amongst several acquisition modes that are available, the three main modes that were used on the in-situ ellipsometer are the spectroscopic monochromatic acquisition mode (Mono), the spectroscopic multiwavelength acquisition mode (MWL) and kinetic multiwavelength acquisition mode (kinetic).

Using the Mono mode, a single ellipsometry spectrum is acquired with the monochromator unit which will analyze the reflected light signal from the sample at precise wavelengths. A spectral range from 1.5 to 5.0 eV was used and the sampling interval was typically 0.05 eV which enabled the acquisition of precise ellipsometry spectra with at least 90 points. Each point was measured four times with an integration time of 50 ms each.

Using the MWL mode, a single ellipsometry spectrum is rapidly acquired between 1.517 eV and 4.993 eV. The integration time for this specific acquisition was set to 800 ms which resulted in a reduced acquisition time but with only 32 points acquired for each spectrum.

The kinetic mode allows performing successions of single MWL acquisitions in real time. This enables following the evolution of a sample surface ellipsometry spectrum during an etching or deposition test.

An integration time of 500 ms and sampling rate of 1 s was used for these acquisitions. The kinetic acquisitions covered the duration of the entire process timings from the thermalization step until the end of the final pumping step.

The UVISEL-1 allows three different configurations which correspond to three different sets of angles concerning the analyzer (A) and the modulator (M) during the ellipsometry acquisition:

For Configuration I: M= 0° and A= 0°

For Configuration II: M= 0° or 90° and A= ± 45°

For Configuration III: M= ± 45° and A= ± 45°

Configuration I was used to calibrate the 0° angle positions for the analyzer and modulator using an aluminum coated wafer specifically dedicated to that purpose.

Configuration II was the only configuration that was used for ellipsometry acquisitions in this research project. This configuration allows to determine Δ on the whole range between 0° and 360° except around 45°. Using this configuration, the ellipsometer plots I_s and I_c parameters in relation to the wavelength during the ellipsometry spectrum acquisition. The ellipsometry parameters ψ and Δ can then be obtained using the following equations (**equations II.12**).

Equations II.12: Ellipsometry relation using Horiba Jobin-Yvon UVISEL-1 ellipsometer in configuration II

$$I_s = sin(2\psi).sin(\Delta)$$

$$I_c = sin(2\psi).cos(\Delta)$$

In general, a single ellipsometry acquisition was done for each sample before a process test (Mono or/and MWL). A kinetic acquisition was then acquired during the whole duration of the plasma process. Subsequently, a single ellipsometry acquisition was realized after the test (Mono or/and MWL). An additional acquisition was sometime realized after venting the processed sample with N_2 in the loadlock.

2.4.1.4 Ellipsometry modeling and analysis

2.4.1.4.1 Introduction

Once an ellipsometry spectrum of a sample surface is acquired, the determination of its dielectric surface properties can only be approached through ellipsometry modeling. This is typically done by creating an ellipsometry model corresponding to the ideal composition of the sample surface. The model is composed of the vertical layers of material that compose the stacking with their associated

thicknesses. It can be seen that the underlying substrate material is considered to have an infinite thickness and every layer of material is represented above, in the order and arrangement that respects the stacking. Every layer refers to a material file which contains the dispersion law with the expressions of n and k in relation to the photon energy as well as its associated dielectric constants.

By defining a stacking model, the user can then specify on which parameters the model can be fitted to retrieve the parameters which best match the experimental file obtained. As a result, the quality of the ellipsometry model depends on the exact knowledge that the user has of the sample stacking as well as the fitting criteria that are used to fit the model to the ellipsometry acquisition data. According to the material optical properties, different dispersion formulae can be tested for model fitting. Surface roughness and porosities can also be modeled within a material layer. The user can also choose to fit the model according to a specific range of wavelengths or by fitting the angle of incidence (AOI) of the polarized beam to better match the experimental spectrum. DeltaPsi2 disposes of numerous other fitting options and techniques that can be used towards the fitting of ellipsometry models with each individual acquisition file. For the analysis of the fitting quality, a χ^2-residue parameter is calculated by the software. It corresponds to the minimization of I_s and I_c values obtained by fitting a model on the desired parameters, compared to the values acquired on the experimental spectrum.

Therefore, the strategy was to create a model for each type of thin-layer sample described in **section II.2.2.** The goal was to find a model sample structure which best matched the experimental acquisition with a minimal χ^2 value. Once the adequate structure was found, the model was fixed and the number of fitting parameters for the analysis of experimental acquisitions was usually reduced to the surface layer thickness and eventually its specific dielectric parameters. This model was then used to determine the exact thickness for each sample before a process test. These values were then compared to those obtained on the same sample using the same model after an etching process. For the analysis of deposition processes, a specific model was created for each sample type with a supplemental surface layer corresponding to the deposition process. In the same way, a kinetic model was created for each sample type and specific etching or deposition process.

For the realization of in-situ ellipsometry models and data analysis, the first fitting parameter which had to be fixed was the angle of incidence (AOI). In theory, the chamber openings of the ICP reactor for the in-situ ellipsometer is 70.00°. However, this angle is only valid for a clamped wafer without a glued sample. Given the fact that all the samples analyzed by ellipsometry were glued on a carrier wafer, it was decided to quantify and fix the AOI for ellipsometry data analysis and model fittings. Therefore, multiple calibration tests were realized with glued samples to determine the AOI which best fitted in the analysis of spectrums obtained with a monochromatic acquisition mode. The same was done to identify the AOI which best fitted the analysis of spectrums obtained with the multiwavelength acquisition modes (MWL and kinetic). As a result, an AOI position of 70.08° was fixed for Mono models and 70.18° for kinetic and MWL models.

The acquisition of a single spectroscopic ellipsometry spectrum (Mono or MWL modes) or a series of single MWL acquisitions (kinetic mode) generate different types of acquisition files. They need to be analyzed with two different types of ellipsometry models, the simple model and the kinetic model

respectively. A simple model simulates the stacking of a sample surface at the precise moment when the single acquisition is acquired. A kinetic model takes over the same stacking structure described in a simple model yet it includes an additional kinetic layer which will simulate the evolution of the sample surface during the entire kinetic acquisition.

If the model describes a deposition process, a deposition layer is inserted in the stacking usually underneath an additional surface material layer which will correspond to the material being gradually deposited during the plasma process and kinetic ellipsometry acquisition. An initial thickness and theoretical deposition rate amongst several other fitting parameters need to be provided for the deposited layer. Conversely, if the model describes an etching process, an etching layer is inserted usually underneath the top surface layer of the stacking model. An etching rate amongst other fittings needs to be provided for the model. The choice can also be made to fit the thickness and material dielectric properties of the underlaying thin layers during the kinetic ellipsometry acquisition. Once the fitting of a kinetic file is launched on a kinetic model, the software will fit the evolution of the desired parameters by incrementing each single MWL acquisition acquired during the sampling period. It is up to the user to fix the fitting parameters which best match the surface evolution of the sample during the process and to determine whether a kinetic fit is relevant or not.

2.4.1.4.2 Modeling of SiO_2, p-Si and Si_3N_4 samples

The main samples that were used to characterize thin-etching and deposition processes are the SiO_2, p-Si and Si_3N_4 samples presented in **section II.2.2.** These samples were used for ellipsometry analysis due to their precise stacking knowledge and their thin surface layer which were realized through industrial deposition processes at a high precision. These 3 samples were defined into Mono and MWL models by realizing a precise Mono acquisition with a step of 0.05 eV. Subsequently the thickness of the surface layer as well as their respective optical properties were fitted which allowed saving the material file. The sample stacking structures which were modeled for the ellipsometry fittings and analysis of SiO_2, p-Si and Si_3N_4 samples are respectively illustrated in **tables II.4, II.6 and II.8**. The substrate material used for all the ellipsometry models is c-Si_HJY.ref. It is accessible in the materials library provided with the DeltaPsi2 software. The ellipsometry spectrum of this substrate material was described by *Jellison* [194] and complemented by Horiba Jobin Yvon.

2.4.1.4.2.1 Silicon dioxide:

Table II.4: Stacking structure used for the modeling of SiO_2 samples

Layer Order	Thickness (nm)	Thickness fitting (F)	Material	Material fitting (F)
n°1 (Surface layer)	100.0	Yes	SiO2-fit sample.dsp (Classic Dispersion law)	Yes
Substrate	Infinite	No	Polycristalline silicon (c-Si_HJY.ref)	No

The SiO_2 material which was used was updated from an original material file called SiO2.dsp accessible in the materials library of DeltaPsi2. The updated material called SiO2-fit sample.dsp was fitted on a reference SiO_2 sample. The dielectric constants of these materials are listed in **table II.5**.

Table II.5: Dielectric constants of SiO_2 materials used for ellipsometry modeling

SiO2.dsp	
ε_∞	1.00
ε_s	2.12
ω_t	12.0

SiO2-fit sample.dsp	
ε_∞	1.00
ε_s	2.10
ω_t	13.04

Both of these materials follow a classical dispersion formula [195] including four oscillator models which are detailed in the following equation (**equation II.13**).

Equation II.13: Classical dispersion model including four oscillators used for the spectroscopic ellipsometry fitting of SiO_2 and SiO_xF_y material

$$\varepsilon = \varepsilon_\infty + \frac{(\varepsilon_s - \varepsilon_\infty){\omega_t}^2}{{\omega_t}^2 - \omega^2 + i\Gamma_0\omega} + \frac{{\omega_p}^2}{-\omega^2 + i\Gamma_D\omega} + \sum_{j=1}^{2} \frac{f_j {\omega_0}_j^2}{{\omega_0}_j^2 - \omega^2 + i\gamma_j\omega}$$

$\frac{(\varepsilon_s-\varepsilon_\infty){\omega_t}^2}{{\omega_t}^2-\omega^2+i\Gamma_0\omega}$ corresponds to the Lorentz single oscillator. In this expression, ε_∞ represents the high frequency dielectric constant, ε_s is the static dielectric constant at a zero frequency, ω_t is the resonant frequency of the Lorentz oscillator and Γ_0 is the broadening of the Lorentz oscillator also called the damping factor.

$\frac{{\omega_p}^2}{-\omega^2+i\Gamma_D\omega}$ corresponds to the Drude term, also called Drude oscillator. In this expression, ω_p corresponds to the plasma frequency where $\varepsilon'(\omega) \approx 0$ and Γ_D is the collision frequency.

$\sum_{j=1}^{2} \frac{f_j {\omega_0}_j^2}{{\omega_0}_j^2-\omega^2+i\gamma_j\omega}$ corresponds to the double oscillator. In this expression, f_j corresponds to the strength of oscillator j ; ${\omega_0}_j$ is the resonant (peak) of energy of oscillator j and γ_j is the broadening parameter of the peak energy of the oscillator j .

However, only the parameters associated with the single Lorentz oscillator were retained during the fitting of the SiO2-fit sample.dsp material to facilitate the modeling. An example of an ellipsometry fit using the SiO_2 model which is described in **table II.4** is shown in **figure II.11**. In this example, a monochromatic acquisition (Mono mode) was realized on a SiO_2 thin film sample (**chapter II.3**) before a process test.

Figure II.11: Example of an ellipsometry fit applied on a pristine thin film SiO_2 sample acquisition using the predefined SiO_2 model (Table II.4)

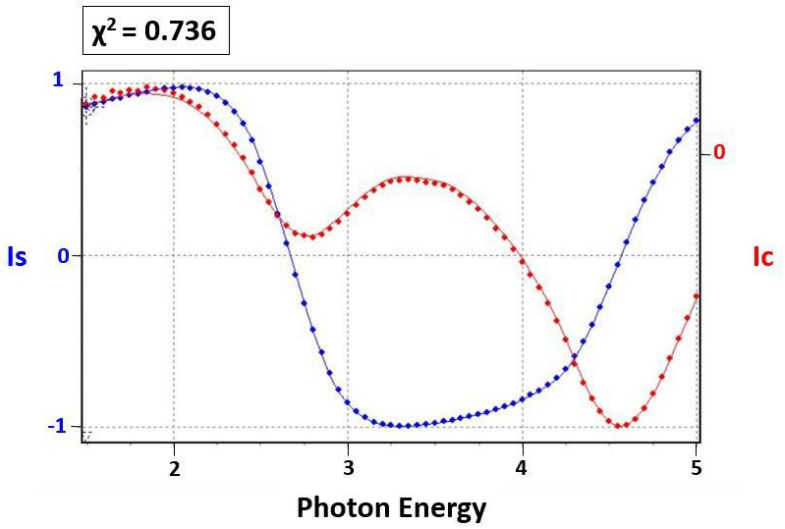

2.4.1.4.2.2 Polycrystalline silicon (p-Si):

The p-Si material which was used was updated from an original material file called p-Si_nam.dsp accessible in the materials library of DeltaPsi2. The updated material called p-Si_nam fit sample.dsp which was fitted on a reference p-Si sample. The dielectric constants of these materials are listed in **table II.7**. For both these models, a surface roughness layer was introduced to improve the fitting quality. It consisted of a layer of 5 nm of p-Si material with a porosity of 50%.

Table II.6: Stacking structure used for the modeling of p-Si samples

Layer Order	Thickness (nm)	Thickness fitting (F)	Material	Material fitting (F)
n°3 (Surface layer)	5.0	Yes	p-Si roughness (50% porosity) 50% p-Si_nam fit sample.dsp + 50% void.ref	Yes
n°2	150.0	Yes	p-Si_nam fit sample.dsp (New Amorphous Dispersion law)	Yes
n°1	100.0	No	SiO2.dsp (Classic Dispersion law)	No
Substrate	Infinite	No	Polycristalline silicon (c-Si_HJY.ref)	No

Table II.7: Dielectric constants of p-Si materials used for ellipsometry modeling

p-Si_nam.dsp	
n_∞	1.82
ω_g	0.99
f_j	0.86
ω_j	3.56
Γ_j	1.49

p-Si_nam fit sample.dsp	
n_∞	1.89
ω_g	1.16
f_j	0.39
ω_j	4.20
Γ_j	1.05

Both of these materials follow a new amorphous dispersion formula [196] with a single oscillator model. It was derived on the basis of Forouhi-Bloomer [197] formulation by Horiba Jobin Yvon for its application on the DeltaPsi2 software. The absorption coefficient $k(\omega)$ and the refractive index $n(\omega)$ are given by the following equations (**Equations II.14**).

Equations II.14: New amorphous dispersion model used for the spectroscopic ellipsometry fitting of p-Si, Si_3N_4 and CF_x materials

$$n(\omega) = n_\infty + \frac{B_j(\omega - \omega_j) + C_j}{(\omega - \omega_j)^2 + \Gamma_j^2} \quad ; \quad B_j = \frac{f_j}{\Gamma_j}\left[\Gamma_j^2 - (\omega_j - \omega_g)^2\right] \quad ; \quad C_j = 2.f_j.\Gamma_j.(\omega_j - \omega_g)$$

$$k\left(\omega > \omega_g\right) = \frac{f_j(\omega - \omega_g)^2}{(\omega - \omega_j)^2 + \Gamma_j^2} \quad ; \quad k\left(\omega \leq \omega_g\right) = 0$$

In these equations, f_j is related to the amplitude of the extinction coefficient, Γ_j is the broadening term associated to the absorption peak, ω_j is the energy where the extinction peak is maximal and ω_g is the energy bandgap.

2.4.1.4.2.3 Silicon nitride (Si_3N_4):

Table II.8: Stacking structure used for the modeling of Si_3N_4 samples

Layer Order	Thickness (nm)	Thickness fitting (F)	Material	Material fitting (F)
n°2 (Surface layer)	5.0	Yes	Si_3N_4 roughness (50% porosity) Si_3N_4_nam fit sample.dsp + 50% void.ref	Yes
n°1	250.0	Yes	Si_3N_4_nam fit sample.dsp (New Amorphous Dispersion law)	Yes
Substrate	Infinite	No	Polycristalline silicon (c-Si_HJY.ref)	No

The Si_3N_4 material which was used was updated from an original material file called SiNx_nam.dsp accessible in the materials library of DeltaPsi2. The updated material called Si_3N_4_nam fit sample.dsp which was fitted on a reference Si_3N_4 sample. The dielectric constants of these materials are listed in **table II.9** For both of these models, a surface roughness layer was introduced to improve the fitting quality. It consisted of a layer of 5 nm of Si_3N_4 material with a porosity of 50%. Both of these materials follow a new amorphous dispersion law.

Table II.9: Dielectric constants of Si_3N_4 materials used for ellipsometry modeling

SiNx_nam.dsp	
n_∞	1.75
ω_g	3.42
f_j	0.16
ω_j	7.31
Γ_j	1.70

Si3N4_nam fit sample.dsp	
n_∞	1.85
ω_g	3.91
f_j	0.12
ω_j	6.60
Γ_j	1.15

2.4.1.4.3 Modeling of a fluorocarbonated (CF_x) deposited layer

For the ellipsometry modeling of plasma deposition processes involving a fluorocarbon gas (C_4F_8, CF_4 and CHF_3), a specific fluorocarbon material was used and referred to as CFx_nam.dsp. This material is accessible in the application library of DeltaPsi2 and follows a new amorphous dispersion law. Its dielectric constants are listed in **table II.10**. The modeling and ellipsometry analysis of this material will often be referred to as CF_x in the following results sections. It was usually added as a surface layer for the implementation of single and kinetic ellipsometry models based on the stackings presented in the previous sections (SiO_2, a-Si and Si_3N_4 samples). The thickness of this fluorocarbon layer was determined using a multiguess fitting choice for both spectroscopic and kinetic acquisitions. In some cases, the refractive index n of the CF_x layer material was calculated in function of the photon energy for the analysis of process tests to evaluate density variations in relation to process parameters. In these cases, the refractive index value at 2 eV was retained. An example of an ellipsometry fit using a specific model including a CF_x material (described in **table II.10)** on the sample surface is shown in **figure II.12**. In this example, a monochromatic acquisition (Mono mode) was realized on a SiO_2 thin film sample (**chapter II.3**) after a process test where C_4F_8 plasma was performed during 30 seconds at a substrate temperature of -40°C using the source gas inlet (**chapter IV.1.2.2**).

Table II.10: Dielectric constants of the fluorocarbon (CF_x) material used for ellipsometry modeling

Parameter	CFx_nam material
n_∞	1.361
ω_g	2.108
f_j	0.023
ω_j	4.299
Γ_j	1.186

Figure I.12: Example of an ellipsometry fit applied on a SiO_2 sample acquisition after a C_4F_8 plasma exposition process using a specific model including a surface CF_x layer

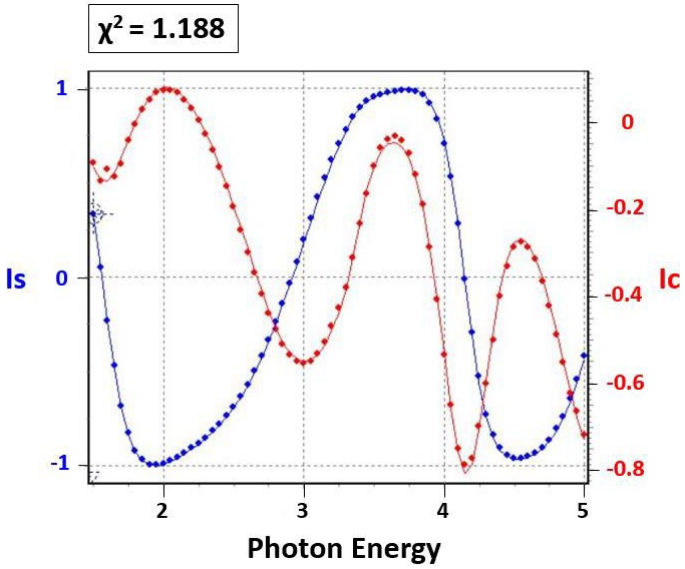

2.4.2 Scanning Electron Microscopy

The etching profiles were observed using a Zeiss SUPRA−40 field emission scanning electron microscope (SEM).

For the deep-etching tests where the etching profiles had to be characterized by SEM, the coupons were then cleaved in a perpendicular direction and approximately in the middle of the array of trenches. The same procedure was realized for thick deposition tests (on p-Si and SiO_2 samples) where the coupon samples were cleaved roughly in the middle. No sample metallization was used for the observation of deep-etching profiles. For thick fluorocarbon deposition tests that were observed post-process by SEM, the samples were metallized with a standard 4 nm platinum layer.

All samples were mounted on a specific wafer section stub for SEM characterization. All the SEM pictures were taken using the same detector (InLens) with an electron high voltage of usually 3 keV and using no tilt (0.0°). The working distance used to observe the samples with this detector was usually varied from 4 µm to 6 µm. Different measurements of the etching profiles were realized with the Zeiss SmartSEM software measurement tools, in instance and in order of priority: etch depth; trench width at the surface; the remaining SiO_2 hard-mask layer thickness; etch trench angles; trench width at the bottom of the profile; trench width at different heights of the profile and etching undercut width.

The average etch trench angles were also recalculated in some cases by taking the trench width at the surface and at the bottom of the trench using trigonometry calculations (**equations II.15**) which are also detailed in **figure II.13**.

Equations II.15: Set of equations used to calculate the etch angle of various etch profiles previously observed through SEM

$$Trench\ opposite\ side = \frac{|Etch\ width\ at\ surface - Etch\ width\ at\ trench\ bottom|}{2}$$

$$Trench\ hypothenuse = \sqrt{(\text{Etch depth})^2 + (\text{Trench opposite side})^2}$$

For a positive trench (Etch width at surface > Etch width at bottom):

$$Etch\ angle = 90° - \arccos\left(\frac{Etch\ depth}{Trench\ hypothenuse}\right)$$

For a negative trench (Etch width at surface < Etch width at bottom):

$$Etch\ angle = 90° + \arccos\left(\frac{Etch\ depth}{Trench\ hypothenuse}\right)$$

Figure II.13: Schematized illustration of the etch angle calculation based on trigonometry

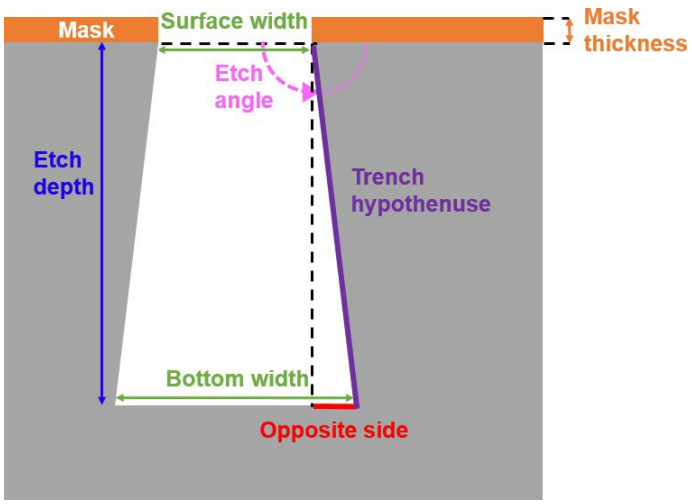

Concerning the calculation of the (Si:SiO_2 hard-mask) etching selectivity, the following equation was used (**equation II.16**).

Equation II.16: (Si:SiO_2 hard-mask) etching selectivity formula used for the analysis of SEM etch profiles

$$Etching\ selectivity = \frac{Etch\ depth}{(Original\ SiO_2\ hardmask\ thickness - Remaining\ \ SiO_2\ hardmask\ thickness}$$

Additional images were taken to focus on the observation of etching specificities depending on the profiles obtained such as the formation of black-silicon at the bottom of the trenches or the scalloping marks on the trench sidewalls for pulsed processes.

2.5 Process characterization techniques

2.5.1 Mass Spectrometry

The mass spectrometer that was used is an electrostatic quadrupole plasma (EQP) mass spectrometer (QMS) series 1000 model from Hiden Analytical. It was used to detect gas phase species, in instance neutrals and radicals, in the reactor according to their mass and charge during the etching and deposition processes.

The mass spectrometry unit was placed on a mobile rack which allowed fixing the vertical position of the column and to insert or retract the probe inside the reactor (see **figure II.2**). A manual gate valve was fixed on the chamber orifice in order to isolate the QMS when not in use and could only be closed when the probe was retracted. The system was differentially pumped with a Pfeiffer HiPace 80 turbopump with a pumping speed of up to 67 l/s for N_2. As a result, the QMS column vacuum pressure was typically equal to 1.0 $x10^{-6}$ Pa (1.0 $x10^{-8}$ mbar). During operation, the column pressure was monitored and the acquisition was systematically stopped if it exceeded 1.5 $x10^{-4}$ Pa (1.5 $x10^{-6}$ mbar). This was done in order to preserve the detector which can only withstand a maximal amount of 5.0 $x10^{6}$ counts per second without damage. It also preserves an adequate mean free path for species not to collide with each other inside the mass spectrometer.

The center of the mass spectrometry probe was positioned at a height of 4.85 cm above the substrate holder level and a horizontal distance of roughly 19 cm from the center of the wafer. As a result, it was positioned at total distance of approximately 19.6 cm. The sampling orifice of the probe is 0.1 mm. The EQP mass spectrometer disposes of an array of electrodes and lenses in order to dissociate and filter the volatile species it collects according to their mass-to-charge (m/z) ratio. A schematic of the Hiden Analytical EQP mass spectrometer is detailed in **figure II.14** which was adapted from the operator's manual provided with the tool [198].

In order to characterize the neutral volatile gas phase species in the reactor (residual gas analysis mode), they are first collected through the orifice where they travel by diffusion to the extraction unit which can be set in order to attract or reject ions back to the chamber according to the acquisition mode. The particles then reach the ionization source which consists of two filaments of oxide coated iridium with a radially symmetrical cage [199]. Electrons are produced from the filaments by thermionic emission and accelerated to the cage with an energy that can be set by the user. The energetic electrons will consequently dissociate and ionize the collected species. The ionized species then reach the 45° energy sector analyzer. The setting of its associated electrodes induces an electromagnetic field which allows to deflect and filter the ions inside the 45° pathway according to their energy and characterize the ion energy distribution.

The ions are then directed through the electrostatic quadrupole which consists of four parallel electrode rods with a diameter of 9 mm which enables mass filtering. All the rods are charged with the same RF alternative voltage component, yet the opposite electrodes are electrically charged with the same direct

component voltage sign whereas the juxtaposed rods are charged with the opposite component voltage sign. The resulting quadrupolar electrical field through which the ions travel will expose them to an oscillatory regime where their amplitude will depend on their (m/z) ratio. In consequence, a particle with a high (m/z) ratio will be more affected by the alternative voltage component inside the quadrupole, whereas a particle with a low (m/z) ratio will be more affected by the direct voltage component. Therefore, depending on the quadrupole voltage setting, only the ions with a certain (m/z) ratio will be maintained inside the quadrupole and make their way towards the detector, whereas the others will hit the rods and be expelled from the quadrupole. By tuning the direct and alternative voltage settings of the quadrupole, it is possible to modify its ion mass-to charge ratio acceptance towards the detector.

Figure II.14: Schematic of the electrostatic quadrupole plasma (EQP) mass spectrometer (adapted from [198])

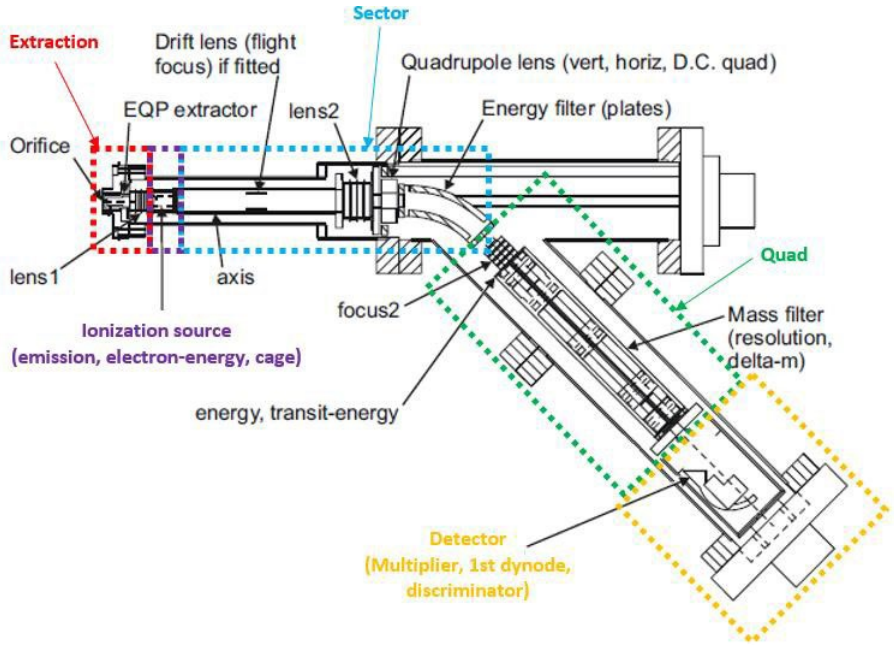

Finally, the selected ions reach the secondary electron pulse-counting multiplier detector. They are attracted to the 1st dynode which is set at a negative voltage. By hitting this dynode, the ions release secondary electrons which will then be attracted to the detector using a positive voltage. As a result, the detector records the number of secondary electrons counts for selected incident ions of a particular (m/z) ratio.

Concerning the standard acquisition parameters and settings, the mass range of species that can detect the system can be set from 0.4 to 510 amu. The multiplier voltage in the detector was usually set to 2,200 V and the electron energy range used to dissociate the species in the quadrupole was set to 70 eV. The main parameters used for mass spectrometry acquisitions are listed in **table II.11**.

Two types of mass spectrometry scans can be realized [198,200]. The first is residual gas analysis (RGA) mode and the second is secondary ion mass spectrometry (SIMS). RGA mode allows the detection of radicals and neutral species whereas SIMS mode allows the detection of ions. Only the

residual gas analysis (RGA) acquisition mode was used in this research study as it was preferred to characterize the ion species using a Langmuir probe. During the RGA scans, two types of acquisitions could be realized. The profile mode allows scanning a range of masses with a mass interval and incrementation which is set by the user. The multiple ion detection mode (MID) allows monitoring the ion peak intensity of several specific masses chosen by the user with a certain sensitivity versus time. The resulting sampling rate depends on the number of masses that are followed and the sampling parameters.

The mass spectrometry acquisitions were configured and collected using the dedicated MASsoft software provided by Hiden Analytical. The acquired data was often extracted and retreated in order to be synchronized with the process parameters recorded by the ICP reactor and the in-situ ellipsometry monitoring of the sample surface during the surface. In practice, for every use of the EQP, several profile mode mass spectra of the chamber were completed with a clamped wafer. The goal was to verify the chamber condition and the repeatability of mass spectra before launching process test characterizations. The realization of these reference mass spectra allowed removing the excess water present in the QMS column with the stabilization of the H_2O peak intensity (18 amu) and allowed eventually to proceed to filament degassing when necessary.

Table II.11: Principal acquisition parameters used for mass spectrometry

Scanning mode	RGA
Acquisition modes	MID or Profile
Mass range	0.4 – 510 amu
Increment value (Profile acquisition)	0.01 to 0.1 amu
Sampling interval (MID acquisition)	100 ms to 1,500 ms
MID Relative Sensitivity	1 amu
1st dynode (detector)	-4,000 V
Multiplier (detector)	2,200 V
Background delay (extraction)	0.1 µs
Foreground delay (extraction)	0.1 µs
Lens 1 (extraction)	0 V
Flight focus	-76 V
Focus 2 (Quad)	-360 V
Transit energy (Quad)	3 V
D.C quad (Sector)	26%
Energy (Sector)	2.7 V
Lens 2 (Sector)	-116 V
Plates (Sector)	7.27 V
Electron energy (Source)	70 V
Source focus	-232 V
CRV range	7 c/s
CRV resolution	6 bits
Gating	Off

When a new plasma step process was studied, continuous profile mass spectrum acquisitions were generally carried out over a large mass range (at least from 0 to 200 amu). The principal peaks observed in these preliminary profile acquisitions were then identified using the data provided in **annex I** and according to the gases that were used in the plasma step of interest.

After the identification and selection of the principal and relevant peaks, the process tests involving the same plasma chemistries were followed by continuous MID type mass spectra on the peaks of interest. The objective was to study the evolution of the principal peaks during the processes by monitoring their intensity in relation to time. This characterization technique was used to characterize the principal species present in the different plasma processes involved in this research project. Moreover, it was used to study the adsorption and desorption of c-C_4F_8 on SiO_2 substrates.

2.5.2 Langmuir and capacitive probe characterizations

2.5.2.1 Introduction

As part of the PSICRYO research program, several plasma chemistries of interest were characterized by Langmuir probe and by capacitive probe to determine their main electrical parameters which are necessary as inputs for the implementation and understanding of numerical simulations. These include the plasma potential (V_p), the floating potential (V_f), the electronic temperature (T_e) as well as the electron and ion densities (respectively N_e and N_i). The study of these plasma parameters and their evolution in relation to process parameters such as pressure, source and bias powers was done mainly in Ar plasma and tested roughly in SF_6 plasma and SF_6+O_2 plasma. In the context of this manuscript which focuses mainly on the study of fluorocarbon plasmas and Bosch-type processes, only capacitive probe measurement results obtained in SF_6, c-C_4F_8 and CF_4 plasmas will be presented.

2.5.2.2 Equipment

The Langmuir probe used for this study was an Impedans cylindrical single probe with an integrated DC compensation reference probe [201–204]. The Langmuir probe measurement technique consists in an electrostatic probe which measures the local plasma current by varying the electric potential on its tip to measure a voltage-current characteristic. Probe tips can also be flat or spherical depending on the applications [201–206], but in this case, a cylindrical probe tip was used. It consisted of a conductive platinum wire of known dimensions which sticks out of an insulating ceramic tube that is enclosed in an alumina tube to protect them from the rest of the bulk plasma. The whole tip is then connected to a ceramic shaft. The DC reference tip is built in the same manner and sticks out of the shaft in a retracted position from the measurement tip. The measuring tungsten filament is enclosed through RF compensation inductors which have resonance frequency covering the RF plasma frequency and an impedance superior to 100 kΩ to couple the exposed filament and the surrounding plasma and allow accurate measurements [204]. The probe was mounted and sealed on the rear opening of the ICP reactor and connected to its complimentary electronics unit.

The capacitive probe which was used for this study was a Plato probe™ provided by Impedans [207,208]. This probe measurement technique was co-developed by *Braithwaite et al* in 1996 [209] and subsequently patented by *Booth et al* in 2012 [210]. This characterization technique was mainly used to evaluate the ion fluxes near the substrate area for the plasma processes of interest. This technique was designed in order to characterize plasma parameters such as plasma density, ion current density, electron temperature even while operating plasma deposition processes such as PECVD where a standard Langmuir probe is not suitable. It is composed of a ceramic shaft to which is attached a replaceable planar probe tip. Unlike standard Langmuir probes, the system is biased with an AC signal through a blocking capacitor which allows the probe to float even in the presence of an insulating layer deposited through the plasma process. The AC bias signal is applied at two frequencies run in sequence (100 kHz and 200 kHz) in order to obtain a corrected I-V probe if ever plasma deposition occurs on the probe tip. It is generated by the data acquisition unit and coupled to the probe interface which consists of a capacitance sensor to collect the voltage and an induction sensor to collect the current. The data acquisition and analysis are realized through the dedicated Plato System software. A schematic representing the Plato probe™ sensor equivalent circuit is shown in **figure II.15**.

Figure II.15: Plato probe™ sensor equivalent circuit schematic (taken and adapted from [207,208])

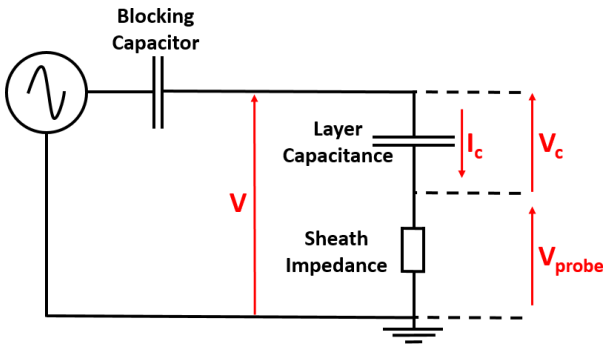

In this schematic, V corresponds to the measured voltage, I_c the current across the deposited layer, V_c the voltage drop across the deposited layer and V_{probe} the probe voltage. During the dual measurement of the I-V characteristic (at 100 kHz and 200 kHz), the plasma deposited layer is considered as a pure capacitance with an impedance equal to $(1/\omega C)$. The floating point of the I-V curve is used as a reference point as the real component of the probe current is zero. The sheath resistance tends to infinity and so the equivalent circuit contains only the series layer capacitance and sheath capacitance. The zero crossing of the I-V curve occurs at two different voltages for the two different frequencies if a layer is deposited on the probe tip. The true I-V characteristic is determined by plotting the calculated real current versus the measured voltage subtracted by the voltage drop on the layer capacitance.

For these specific complimentary measurements, the Plato probe was fixed on the ICP reactor opening n°9 (**figure II.5**). As a result, the probe tip was placed at a height of approximately 1.25 cm from the chuck level at a radial distance of roughly 1.25 cm from the exact center. The quartz clamping crown

was removed and the measurements were realized without any sample on the bare aluminum chuck as was the case for the standard Langmuir and RFEA probe measurements.

2.5.2.3 Langmuir probe theory

During a Langmuir probe characterization, the probe tip is biased at a potential which is swept such that the collected current yields an I-V characteristic. A typical (I-V) characteristic acquired with a single cylindrical probe configuration is shown below (**figure II.16**). It contains three characteristic zones: the ion region (ion collection region), the exponential region (or electron transition or retardation region) and the electron region (electron collection region).

Figure II.16: Graph representing a typical I-V characteristic obtained by Langmuir probe measurement of an Ar plasma in the Oxford Cobra ICP reactor chamber (cylindrical single probe with DC reference configuration): a) Full I-V characteristic ; b) Closer view around the plasma potential V_p

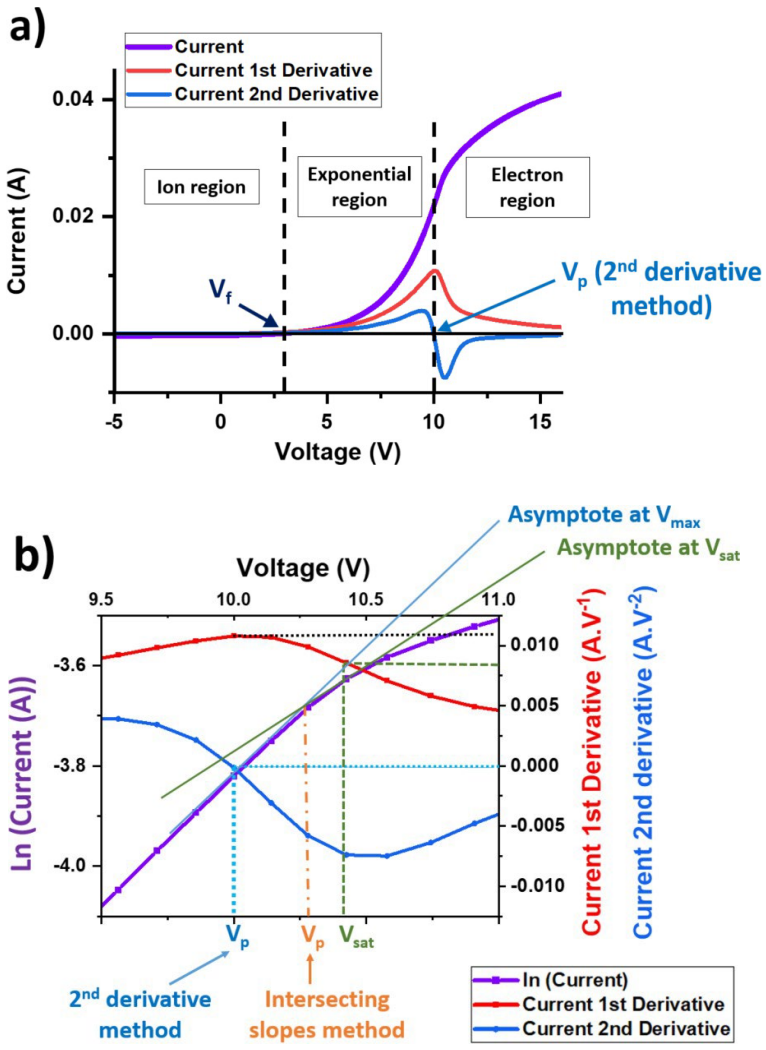

The figure also indicates how to determine graphically several plasma properties such as the floating potential (V_f) as well as the plasma potential (V_p) with the 2nd derivative and intersecting slopes methods. It is important to note that the intersecting slopes method should be determined graphically using the logarithmic scale for the Y-axis as it is shown in **figure II.16.b** [201,205,206].

In the ion region, the probe potential is inferior to V_f which attracts positive ions and repels most of the electrons. In the exponential region, delimited by V_f and V_p, the electron current is collected more easily by the probe as the potential approaches V_p. The electron collection region starts at higher potentials than V_p .

After the I-V acquisition, the Impedans Langmuir probe software calculates the following plasma properties as detailed below in the different sections. These equations are valid and used specifically in a single probe measurement configuration. The software also takes into account several physical inputs that have to be entered by the user which are intrinsic to the experiment such as the gas temperature, the gas pressure, the exact probe dimensions and the ion mass. Moreover, it is important to consider the results obtained in relation to the exact position of the Langmuir probe inside the chamber during the measurements.

2.5.2.3.1 Theory concerning the collection of ions by a single Langmuir probe

The total current collected by a single Langmuir probe is described by several theories that coexist and can be applied notably in function of the probe shape as well as the chamber pressure and the collisions occurring in the plasma sheath before reaching the probe. The comparison and application of these theories were analyzed in many publications, notably by *Godyak et al* [211] and *Chen* [212,213].

The orbital motion limit theory (abbreviated OML or OMT) was introduced by *Mott-Smith* and *Langmuir* [214] which assumes quasi-infinite plasma sheaths compared to the probe radius ($\lambda_D >> r_p$) and suggests the conservation of ion energies and orbital motion (angular momentum) of ions as they are attracted to the probe. This theory was later refined by *Bernstein and Rabinowitz* [215] who applied these suggestions to a finite plasma sheath for both cylindrical and spherical probes for monoenergetic ions. It was then refined subsequently by *Laframboise* [216] to a Maxwellian distribution of ion energies. This extension of the OML theory is often referred and abbreviated to BRL theory according to its authors.

The radial motion theory (RMT but also abbreviated ABR) was introduced by *Allen, Boyd and Reynolds* [217] for spherical probes which assumes finite plasma sheath lengths ($\lambda_D \geq r_p$) and neglects the orbital motion of ions at the approach of the probe. Ions have a radial trajectory in the sheath, which can model sheaths with collisions. This theory was later supplemented by *Chen* [218] notably for its application to cylindrical probes. The following equations detailed below are used to determine the plasma parameters.

First of all, in order to use the most appropriate theory to account for the ion current measurement during the acquisition of the I-V characteristic, the Langmuir probe software performs the following calculations to determine the ion mean free path (λ_i) and estimates the number of collisions (X_l) occurring in the sheath thickness (s) before reaching the probe (**equations II.17**). It is considered that the main type of collisions occurring at working pressures are ion-neutral momentum transfer collisions [201].

Equations II.17: Ion mean free path (λ_i) equation and number of collisions (X_l) equation

$$\lambda_i = \frac{k_B . T_g}{P . \sigma_{i-N}}$$

$$X_l = \frac{s}{\lambda_i}$$

k_B is the Boltzmann constant, T_g is the gas neutral temperature, P is the neutral gas pressure and σ_{i-N} is the ion-neutral momentum transfer cross-section.

2.5.2.3.2 Plasma potential (V_p):

The plasma potential corresponds to the potential of the space that occupies the bulk plasma in the reactor chamber. It corresponds to the potential which separates the electron transition zone with the electron saturation zone in the I-V characteristic. It is usually positive compared to the chamber walls. In order to approximate the plasma potential from an I-V curve, two methods are available with the Impedans software, the 2nd derivative method or the intersecting slopes method. The graphical application of these methods is displayed in **figure II.16.b**.

2.5.2.3.2.1 2nd derivative method:

The second derivative method considers that V_p is reached at the potential where the value of 2nd derivative of the (I-V) curve is equal to zero (**equation II.18**).

Equation II.18: 2nd Derivative method used for the estimation of the plasma potential V_p

$$\frac{d^2 I}{dV^2} = 0$$

2.5.2.3.2.2 Intersecting slopes:

The intersecting slopes method considers that V_p is reached at the potential where the asymptote of the I-V curve at the V_{max} potential in the electron transition zone intersects the asymptote of the I-V curve at the end of the electron-current saturation zone at the saturation potential (V_{sat}). It is better done by replotting the natural logarithm of the current collected by the probe between V_f and $Vsat$ (**equation II.19**). By default, V_{sat} is set by the software as the potential where the first derivative has

dropped by 20% after reaching its peak value at V_{max}. This method is applied automatically by the Langmuir probe software. This method accounts for the sheath expansion that occurs during the voltage sweeping of the Langmuir probe during the measurement according to Laframboise theory [201,216].

Equation II.19: Intersection slopes method used for the estimation of the plasma potential V_p

$$V_p = \frac{-b + \ln\left(I(V_{max})\right) - \frac{V_{max}}{kT_e}}{a - \frac{1}{kT_e}}$$

In this equation, V_p is the potential at the intersection of these 2 asymptotes. The asymptote of the (I-V) curve at V_{sat} is considered to have a slope equal to a and Y-axis intercept value of b. Concerning the asymptote of the electron transition zone, it intercepts the (I-V) curve at V_{max} which is the potential value where the 1st derivative of the (I-V) curve is maximal. In this case it does not correspond to V_p. For this asymptote, the slope is equal to the inverse of kT_e and its Y-axis intercept is equal to the term $\ln\left(I(V_{max})\right) - \frac{V_{max}}{kT_e}$.

2.5.2.3.3 Floating potential (V_f)

The floating potential V_f corresponds to the potential where the ion current is equal to the electron retarding current. It is situated at the boundary of the ion current saturation zone and the electron transition zone in the (I-V) characteristic. This is the potential at which an electrically isolated material will float when placed in the bulk plasma.

2.5.2.3.4 Electron temperature (T_e) and average electron energy $\langle \varepsilon \rangle$:

The electron temperature (Te) of a plasma is usually expressed by convenience in electron-volts (eV). The conversion of an electron temperature in kelvins (which is abbreviated as kT_e) to an electron temperature in electron-volts (which is abbreviated as T_e) is expressed below (**equation II.20**).

Equation II.20: Electron temperature conversion temperature

$$T[K] = \frac{e}{k_B}.T[eV]$$

In this equation, k_B is the Boltzmann constant which is abbreviated as k in the expression of kT_e whereas e corresponds to the elementary charge. The electron temperature is derived by supposing that the collisions between particles inside a plasma and thus, their velocities, follow a Maxwell-Boltzmann distribution, expressed below (**equation II.21**).

Equation II.21: Maxwell-Boltzmann distribution function

$$f(v) = 4.\pi.v^2.n.\left(\frac{m}{2.\pi.k_B.T}\right)^{\frac{3}{2}}.\ e^{\left(-\frac{m.v^2}{2.k_B.T}\right)}$$

In this equation, v corresponds to the velocity, n is the density of particles and m is the particle mass. From the distribution of particle velocities, the determination of the root mean square speed (v_{RMS}) allows to retrieve the temperature of particles (**equation II.22**).

Equation II.22: Root mean square speed of gas molecules according to the kinetic theory of gases

$$v_{RMS} = \left(\overline{v^2}\right)^{\frac{1}{2}} = \left(\frac{3.k_B.T}{m}\right)^{\frac{1}{2}}$$

From this value, it is possible to estimate the average electron energy $\langle\varepsilon\rangle$ which is intrinsically linked to kT_e as described below (**equation II.23**).

Equation II.23: Average electron energy $\langle\varepsilon\rangle$ formula

$$\langle\varepsilon\rangle = \frac{1}{2}.m.{v_{RMS}}^2 = \frac{3}{2}.k_B.T = \frac{3}{2}.kT_e$$

To determine kT_e from an (I-V) characteristic, it is necessary to focus on the exponential region, below Vp, where the probe potential retards the collection of electrons according to the Boltzmann relation. In this area, the electron current follows an exponential slope which enables to determine kT_e as detailed below (**equation II.24**). For better precision in the calculation of kT_e, the current measured coming from the ions has to be isolated and subtracted from the total current.

Equation II.24: Electron temperature (T_e) formula

$$\frac{1}{kT_e} = \frac{I\ (V_p)}{\int_{Vf}^{Vp} I_e(V).dV}$$

$I\ (Vp)$ corresponds to the electron current measured at the plasma potential Vp and $\int_{Vf}^{Vp} I_e(V).dV$

corresponds to the integral of the I-V curve between the floating potential Vf and the plasma potential Vp .

2.5.2.3.5 Electron density (N_e) and electron flux (J_e):

The electron density (N_e) is obtained by taking the current collected by the probe at a potential just above V_p, at the neighborhood between the electron current saturation zone and the electron transition zone. This the point where the plasma sheath disappears between the probe and the bulk plasma which allows an accurate measurement of the electron current which has to be divided by the probe area to obtain N_e (**equation II.25**).

Equation II.25: Electron density (N_e)

$$N_e = \frac{I\,(V_p)}{A_p} \cdot \sqrt{\frac{2.\pi.m_e}{e^2.kT_e}}$$

In this equation, A_p corresponds to the cylindrical probe area, m_e is the mass of the electron and e is the elementary charge.

The electron flux (J_e) is determined by taking the ion current collected by the probe at V_p and by dividing this value by the probe area (**equation II.26**).

Equation II.26: Electron flux equation (J_e)

$$J_e = \frac{I(V_p)}{A_p}$$

2.5.2.3.6 Ion density (N_i) and ion flux (J_i):

The ion density (N_i) is determined from the ion flux at the sheath edge (I_0) which is itself a corrected value obtained from the probe current collected in the ion region which is referred to as the ion current (I_i) region. The expression of I_0 can be derived by different expressions which depend on the collisions occurring in the plasma sheath (collisionless or collisional models), the probe geometry as well as the theory which is considered for ion collection (OML or ABR) [201]. The estimation of I_0 allows to calculate the ion density (N_i) through the following equation (**equation II.27**).

Equation II.27: Ion density (N_i) equation

$$N_i = \frac{I_0}{A_p} \cdot \sqrt{\frac{2.\pi.m_i}{e^2.kT_e}}$$

For this calculation, the Impedans measurement tool software considers that I_0 corresponds to the ion flux at the plasma sheath edge defined by the Bohm sheath criterion. Usually, it is assimilated to the ion current collected by the probe at a potential of -80 V (or another negative potential defined by the user) which is then affined by dividing this value by a factor which depends notably of the probe dimensions entered manually by the user and the Debye length of the plasma sheath. This factor accounts for the number of ion collisions in the plasma sheath before reaching the probe according to the Bohm criterion [201]. Additionally, m_i is the mass of the dominant ions.

The ion flux (J_i) is determined by taking the calculation of the affined ion current I_0 collected by the probe in the ion current saturation zone and by dividing this value by the probe area (**equation II.28**).

Equation II.28: Ion flux (J_i) equation

$$J_i = \frac{I_0}{A_p}$$

2.5.2.4 Capacitive probe acquisition parameters

The I-V characteristics were acquired with the Plato probe™ using the time averaged mode with 2,000 accumulations and 20 scans per acquisition run. The probe tip dimensions that were used for these acquisitions include a probe radius of 3.3 x10^{-3} m and a holder radius of 4.5 x10^{-3} m. For the characterization of argon plasmas, an ion-neutral collision cross section of 8.8 x10^{-19} m^2 was used and an electron-neutral collision cross section of 4.14 x10^{-20} m^2 was used. The plasma sheath expansion generates a linear increase of the probe current in the ion region. As a result, a linear fit is made in this region by the Impedans measurement tool software and is extrapolated back to the Y-axis to correct the I-V characteristic and determine the ion saturation current $(-I_{sat})$ [207].

The electron temperature (kT_e) is then determined using the same method which is used through Langmuir probe characterization (**equation II.24**).

The ion density (Ni) is then determined through the following equation where A_p corresponds to the probe area, e to the elementary charge and m_i to the ion mass (**equation II.29**).

Equation II.29: Ion density (Ni) calculation through capacitive probe characterization

$$N_i = \frac{I_{sat}}{A_p . e . \sqrt{\frac{kT_e}{m_i}}}$$

The ion current density (J_i) is determined by assuming its conservation in the sheath area through current continuity with the following expression (**equation II.30**).

Equation II.30: Ion current density (J_i) calculation through capacitive probe characterization

$$J_i = e . N_i . u_s$$

In this expression, u_s corresponds to the ion velocity at the sheath edge. It is related to the Bohm velocity (u_B), the Debye length (λ_D) and the ion mean free path (λ_i) with the following equations (**equations II.31**) [207].

Equations II.31: Ion velocity at the sheath edge (u_s) , Bohm velocity (u_B) and Debye length (λ_D) equations

$$u_s = u_B . \frac{1}{1 + \left(\frac{5\lambda_D}{\lambda_i}\right)}$$

$$u_B = \sqrt{\frac{kT_e}{m_i}}$$

$$\lambda_D = \sqrt{\frac{\varepsilon_0 . T_e}{N_i . e}}$$

In these equations, ε_0 corresponds to the vacuum permittivity and T_e to the electron temperature (in eV). The calculation of the ion mean free path (λ_i) is realized through the entry parameters (pressure P, gas temperature T_g and the gas ion–neutral charge exchange collision cross section σ_g) defined by the user in the Plato system software using **equation II.17**.

2.5.3 RFEA probe characterization

2.5.3.1 Equipment

In order to measure the ion energy and ion fluxes involved in the different plasma process steps developed in this research project, a retarding field energy analyzer (RFEA) was used (Impedans Semion single button probe) [219–221]. The system is designed to collect and detect the plasma ions using a sensor which faces the plasma. The button probe sensor contains four independently biased grids through which an array of 37 orifices (approximately 800 µm diameter holes on the top RFEA chassis) are fitted in a hexagonal area of roughly 1 cm^2 [219,222]. A collector electrode is placed at the bottom of the button probe to collect ions which make their way through the orifices. A schematic representing the RFEA button probe sensor structure through a single orifice is shown in **figure II.17**.

Figure II.17: RFEA sensor structure schematic

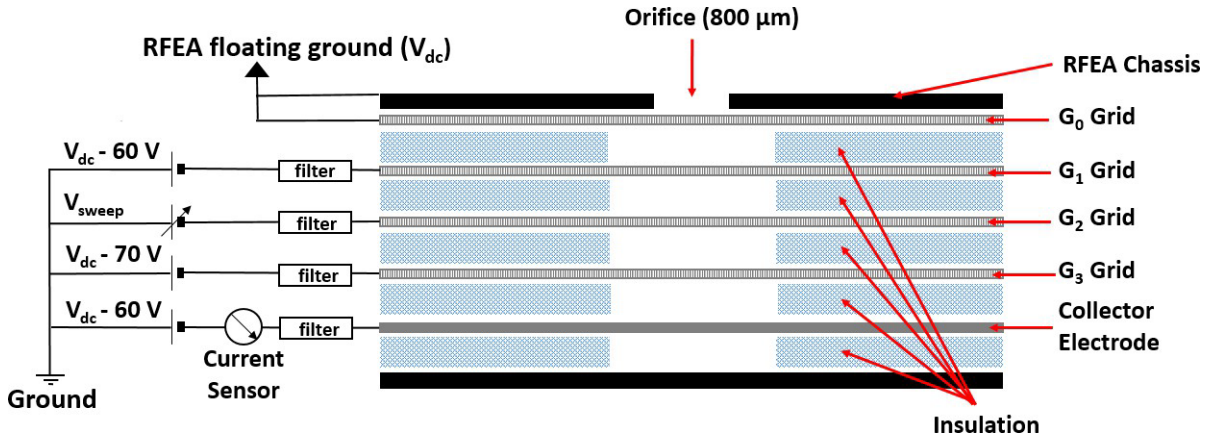

Beneath the top RFEA chassis, all four grids share the same size and design. They consist of nickel grids of 4 µm in thickness with an array of square-shaped apertures. All the grids are separated by mica insulators and the collector electrode is made of copper. The top grid G_0 as well as the RFEA chassis are meant to float at the DC component of the applied bias signal. However, the bottom grids (G_1, G_2,

G_3) as well as the electrode collector are equipped with high impedance low-pass filters which protect the probe electronics and enables them to float at the AC component of the applied bias signal [223]. The vertical distance between the G_0 grid and the electrode collector is meant to be 0.6 mm [223].

The button probe sensor which was used is 32 mm in diameter and 4 mm in thickness and was placed in a compatible button probe holder of 70 mm in diameter and 5 mm in thickness. The housing material of the button probe sensor was made of anodized aluminum which is compatible with mild and aggressive etching plasma chemistries. The probe holder was wire connected to a control unit which was mounted and sealed on the rear opening of the reactor. In theory and according to the Impedans manual concerning the Semion RFEA button probe, each grid should have a transmission of 50% and contain apertures of 20 µm [219].

The first grid (G_0) is designed to prevent plasma from directly entering through the orifice and occupying the volume inside the sensor. With the array of 30 µm apertures, it reduces the sampling orifice down to less than the plasma Debye length. The second grid (G_1), also called the suppression grid is intended to repel the plasma electrons by applying a negative bias, generally of -60 V_{DC} in comparison of G_0. The third grid (G_2) is designed to discriminate the positive ions during the RFEA measurement. The potential applied to G_2 is varied during the RFEA acquisition to create a retarding electric potential (V_2) between G_0 and G_2, in order to gradually collect the incident positive ions on the electrode collector. Only the ions which have a kinetic energy superior to $q.V_2$ (q being the ion charge) during the voltage sweeping will make their way to the collector.

The fourth grid (G_3) is intended to prevent secondary electrons from escaping the collector electrode. It is usually biased negatively in comparison with the collector electrode by generally 10 V. This potential is meant to create a retarding field which traps the secondary electrons that are emitted when the surface of the collector electrode is hit by energetic ions. The recollection of these secondary electrons back to the collector electrode is key to acquire a relevant ion-current characteristic.

The underlying collector electrode (C) detects and records the ion current in function of the different potential voltages applied to G_2 during the RFEA acquisition, which gives the I-V characteristic. To that purpose, it is set with a negative potential which is usually the same potential applied for G_1.

The ion energy distribution function (IEDF) is then determined by differentiating the I-V characteristic. The ion flux is obtained by measuring the ion current when V_2 is minimal ($V_2 < 0V$) and when V_2 is maximal (higher than E_{max} being the highest ion energy measured during the voltage sweeping). At $V_2 < 0$ V, all the positive ions are collected, and the current is maximal. At $V_2 > E_{max}$, all the positive ions are meant to be forced out of the RFEA probe. At this potential, the measured current should be insignificant and correspond to the current leakage which is inherent to the system. This current offset is then retracted to the maximal ion current measured at $V_2 < 0$ V. This total ion current is then divided by the surface area and the ion charge to obtain the ion flux. However, many assumptions made in this final calculation are contested and will be further explained.

The RF bias that is eventually applied to the substrate holder during the plasma characterizations is measured by the RFEA sensor which displays the measured bias value. The measured DC potential is

automatically taken into account during the data acquisition where G_0 and G_2 starting values are adapted to this value by the system which will then display the corrected ion energy distribution for this measured bias voltage. The RFEA sensor, the control unit as well as the acquisitions were controlled using a dedicated software provided by Impedans called Semion. The control unit records the ion current for each potential applied to G_2 during the acquisition. The software displays and records the resulting current-voltage characteristic and subsequent ion energy distribution function. It also displays the average energy of the measured distribution function as well as the ion flux which is estimated by integrating the measured IEDF.

The single button probe sensor was placed in the center of the substrate holders of the ICP reactor. Following the recommendations given by Impedans, the mounting of the RFEA probe was done by respecting the following precautions. The four connectors of the button probe sensor were checked to verify that they were all at the same height. The button probe sensor was then inserted in the probe holder by carefully aligning the four sensor connectors with their respective tab positions inside the holder. The button probe holder was then tested electrically with a multimeter to check any false contacts and to verify the electric connections between the ten screw wires on the bottom part of the probe holder and the six wires on the top side of the button probe sensor.

Thereafter, the bottom part of the probe holder was covered by three pieces of dual-sided copper adhesive to enhance electric contact with the reactor substrate holder. These copper adhesives were carefully placed in order to recover, level and precisely connect several screw wires together. Additionally, single side aluminum scotch was placed evenly in four positions on the top of the sensor and along the reactor substrate holder to fix and maintain the position of the RFEA probe during the experiments. The clamping crown of the substrate holder was detached for these acquisitions to prevent any wire damage due to an eventual error or misuse of the reactor during the tests.

2.5.3.2 RFEA theory

The ion energy distribution function is derived and affined from the ion-voltage characteristic acquired during the RFEA measurement using the following formula (**equation II.32**).

Equation II.32: Ion energy distribution function $f(x_i)$ calculation

$$f(x_i) = \frac{\sum_{j=1}^{n} y_{i+j} - \sum_{j=1}^{n} y_{i-j}}{\sum_{j=1}^{n} x_{i+j} + \sum_{j=1}^{n} x_{i-j}}$$

The user can then choose a linearization level or method to calculate and display the IEDF using the Semion software. The most linear IEDF correction is obtained with method (n= 5) whereas the least linear IEDF correction is obtained with method (n= 1).

For all the RFEA acquisitions that were carried out the IED functions and their derived values were obtained and treated with the second linearization method (n= 2).

It is supposed at this point that the ion mean free path (λi) must be inferior to the distance between G_0 and C in order to acknowledge that the ion energies are not considerably affected by collisions inside the RFEA button probe [222]. By calculating the ion mean free path for Ar^+ ions, it can be estimated that the experimental Impedans RFEA probe can measure IEDFs accurately as long as the pressure is under 13.8 Pa. This value was calculated by fixing λ_i to 0.6 mm (distance between G_0 and C) and supposing that the gas temperature T_g was 300 K using **equation II.17** (Langmuir probe characterization section). The argon ion–neutral charge exchange collision cross section σ_{Ar} that was retained for this calculation was 5.0 x10^{-19} m^2 [224,225]. The average ion energy (E_i) is calculated by the Semion software using the following equation (**equation II.33**).

Equation II.33: Average ion energy (E_i) calculation obtained through RFEA acquisition

$$E_i = \frac{\int_{Emin}^{Emax} E.f(E).dE}{\int_{Emin}^{Emax} f(E).dE}$$

The ion flux (Ji) is also calculated by Semion after the acquisition of the ion voltage characteristic following the equation shown below (**equation II.34**).

Equation II.34: Ion flux (J_i) calculation obtained through RFEA acquisition

$$J_i = \frac{\int_{Emin}^{Emax} IED.dE}{q.A.T}$$

At the denominator, q corresponds to the ion charge. It is assumed that the outstanding majority of collected ions are positive single charges (Ar+ ions in the case of Ar plasma), therefore, q is equal to 1 [226,227].

The term A corresponds to the total area through which the positive ions can penetrate to reach the collector. Therefore, it is assimilated to the area occupied by the 37 orifices of the RFEA button probe (**equation II.35**).

Equation II.35: Calculation of the total area A occupied by the orifices of the RFEA button probe

$$A = \pi.r^2 * 37 = 1.86\,\text{x}10^{-5}\ m^2$$

T corresponds to the total ion transmittance of the sensor which is equivalent to the ratio of the number of ions that actually reach the collector to the total number of incident ions. However, there has been an ongoing debate concerning the calibration of RFEA probes towards the measurement of the ion flux. This is due to the fact that the determination of T for a specific RFEA probe system is not completely straightforward.

This value actually varies importantly in relation to the probe system itself as well as the plasma process conditions such as pressure and ion energies to which it is exposed thereafter. Several calibration methods have been proposed to approximate the value of the total ion transmittance of a RFEA sensor [222,224,226–230]. They all show that the ion flux measurement is sensitive and depends on several factors which need to be evaluated and referenced in the first place for a reliable measurement. Moreover, they suggest that the ion energy, the chamber pressure as well as the pressure-dependent ion angular distribution do have an influence on the resulting transmittance of the RFEA probe itself and the measurement of the ion flux [222,224,226,228].

Additionally, it must be noted that all these calibration techniques were realized using Ar plasma. This implies that complementary calibrations should be done when characterizing a plasma of a different nature with ions of different masses as suggested by *J.W. Buiter* [227]. Therefore, given the uncertainty of the exact value of the total transmittance of the system, it was decided that the analysis of the RFEA plasma acquisitions will mainly focus on the IEDF and average ion energy results. The ion flux value obtained will be compared with those obtained with other techniques (Langmuir probe, Plato probe) in the same process conditions.

2.5.3.3 Acquisition parameters

After carrying out several preliminary measurements on argon plasma, the RFEA acquisition parameters were optimized and clearly defined. Subsequently, the RFEA characterizations were performed using the acquisition parameters and software functions detailed in **table II.12**.

The energy range which was used during the acquisitions depended on the plasma nature and process parameters. It varied from 40 to 200 eV.

For each RFEA acquisition, the plasma was ignited and maintained for several seconds at the desired process conditions in order to verify that the plasma source and RF matching were adequate and to minimize the reflected RF plasma power. The substrate holder was continuously thermalized at +20°C using liquid nitrogen. The bias voltage measurement provided by the Oxford ICP tool was noted as well as the electrode voltage measured by the RFEA sensor before and during each acquisition. These two values were always in accordance before each acquisition which suggests that the probe was mounted adequately [223]. During the RFEA acquisition, the electrode voltage measured by the sensor always decreased in absolute value by roughly 1 or 2 V in general compared to the original value displayed in volts before the acquisition.

Table II.12: RFEA acquisition parameters and software options used for plasma characterization

Measurement Mode	Standard mode (Quick measurement mode)
Scan Type	Time Averaged / Single Scan
Traces per Scan	5 or 10 depending on the plasma chemistry and stability
Electrode Voltage	Use Measured option
Ion Energy Range	40 to 200 eV
Energy Resolution	1 to 2 eV (1% of the Ion Energy Range)
Sensor current ranges	60 µA
G_1 Grid Voltage	(Measured Electrode Voltage - 60 V)
G_2 Grid Voltage Start	(Measured Electrode Voltage - 2 V)
G_2 Grid Voltage End	(Measured Electrode Voltage + Ion Energy Range + 20 V)
G_2 Grid Voltage Step	1 V
G_3 Grid Voltage	(Measured Electrode Voltage - 70 V)
Collector Electrode Voltage	(Measured Electrode Voltage - 60 V)
Timing 1 (Bias grid settling time for the end of previous scan)	100 ms
Timing 2 (Bias grid settling time from the end of the previous scan)	200 µs
Timing 3 (IV accumulation)	2,000 µs
Ion Flux Factor (Single button probe sensor)	637,000
IEDF integration calculation method	2^{nd} derivative method (n=2)

Additionally, several plasma experiments were realized in the same process conditions without the RFEA probe (with and without a Si or SiO_2 wafer) to compare the bias voltage values measured by the ICP reactor during the RFEA characterizations and during standard processing configurations with a silicon wafer. It was observed that the presence of the RFEA probe did influence the measured bias voltage at identical process conditions involving the same bias powers. This is due to the reactor configuration concerning the RF bias setting which can only be adjusted with a bias power that is delivered by the generator to the sample. Therefore, the resultant bias voltage that is measured depends on the nature of the sample and its impedance. The low pass RF filters that are connected to the RFEA grids are composed of high input impedance elements with an inductor-resistor-capacitor (LRC) configuration [223] which makes the RFEA probe much more resistant than a silicon wafer when exposed to a plasma with a given RF bias. As a result, the RFEA results obtained in these conditions should only be analyzed in relation to the bias voltage measured by the ICP equipment rather than the bias power applied during the acquisitions.

2.5.4 Broadband UV-visible absorption spectroscopy

2.5.4.1 Introduction

Broadband UV-visible absorption spectroscopy acquisitions were realized on the Oxford ICP tool to evaluate the density of fluorocarbon radical species (CF and CF_2) present in a CF_4 plasma in relation to the chuck temperature. It is a widely used technique to identify and approximate the relative as well as absolute concentrations of small polyatomic radicals present in a specific plasma [231–242].

At first, the idea was to determine the absolute density of CF and CF_2 radicals in c-C_4F_8 plasmas using the same input parameters which were applied during Bosch process tests for the fluorocarbon deposition steps. However, the extended acquisition time necessary for the determination of a relevant absorbance spectra would have led to considerable fluorocarbon deposition on the substrate and reactor walls due to the long c-C_4F_8 plasma exposure time. As a result, it was decided to perform this study using CF_4 plasma which is known to polymerize much less than c-C_4F_8 [[243]]. It enabled to repeat spectroscopic acquisitions using the same range of input process parameters without having to repeat long and time-consuming plasma cleaning procedures after each test run.

2.5.4.2 Equipment

To perform absorption spectroscopy characterizations on the Oxford ICP reactor, a Hamamatsu Energetiq ED-99X-FC-S laser-driven light source (LDLS™) [244] was used. It consists of a plasma source obtained in a Xe gas filled bulb which is sustained by a laser beam which emits a quasi-flat signal and covers a spectral range from 170 nm to 2,500 nm. The emitting light signal was then conveyed through an optical fiber to a Thorlabs S120-SMA optical system where an adjustable 25 mm focal point optical lens was fixed and placed in line with a manual shutter device. This optical system was attached to a custom designed vacuum deportation tube with a silica porthole to ensure maximal signal transmittivity. As a result, the input light signal was collimated and conveyed through the ICP reactor porthole n°9 (**figure II.5**) which is placed at vertical distance of 1.25 cm above the substrate holder level inside the chamber. The output signal is collected with a reverse assembly which is connected to the reactor porthole n°5 (**figure II.5**). At this level, the reactor diameter is equal to 38.0 cm. However, external vacuum tubes were added on the reactor openings to limit fluorocarbon plasma deposition on the quartz portholes and maintain an adequate optical signal during the experimental study. The total length of both vacuum tubes amounted to 25.0 cm and their internal diameter was equal to 1.0 cm. The output signal is then conveyed to a Princeton Instruments Acton Spectra Pro SP 2750 spectrometer [245] equipped with a Pylon-400B CCD detector [246]. The focal length of the spectrometer is 750 mm and it disposes of a triple grating imaging system which can achieve up to 1800 grooves/mm gratings. The detector has a resolution of 1340x400 pixels of 20x20 µm and its vacuum window disposes of a standard MgF_2 anti-reflection coating which enables a transmission above 90%

from 200 to 1,050 nm. A schematized illustration of the experimental setup which was used for the absorption spectroscopy acquisitions is shown in **figure II.18**.

Figure II.18: Schematized illustration of the absorption spectroscopy experimental setup

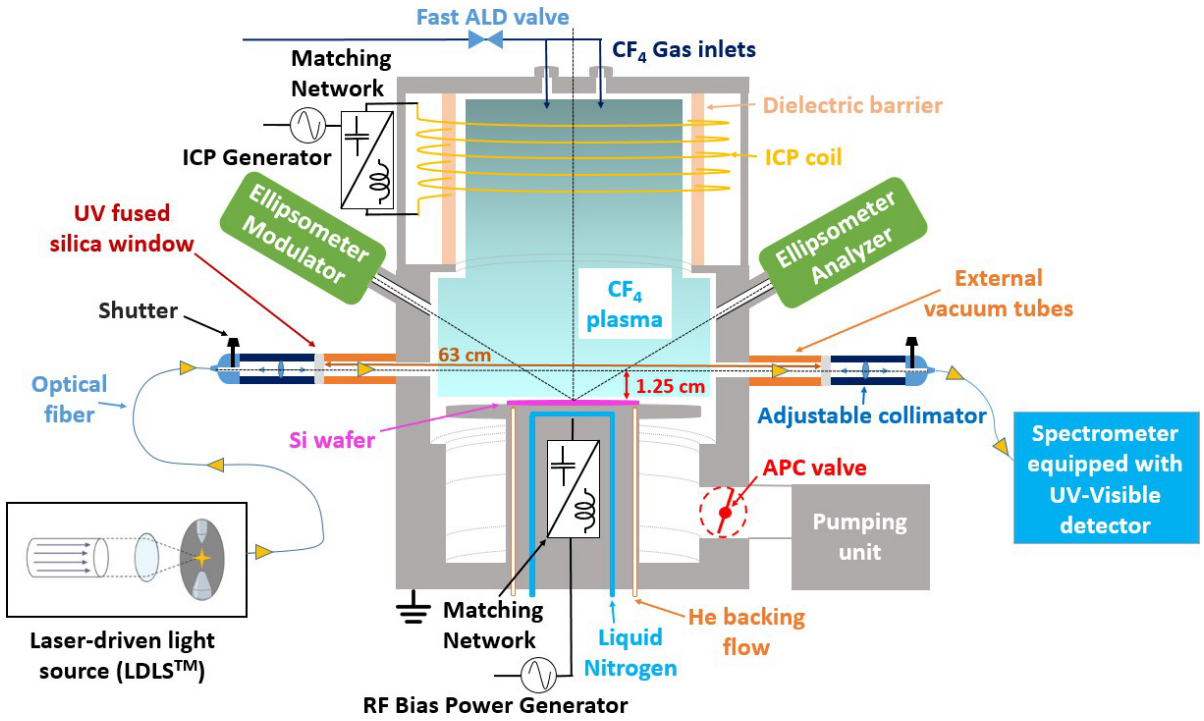

2.5.4.3 Acquisition method

To determine the absorbance spectra (A) of a single plasma medium, four necessary spectrum acquisitions have to be acquired:

1) $I_L(\lambda)$: Light-source spectrum (plasma off and light source on)
2) $I_{LP}(\lambda)$: Plasma and light source spectrum (plasma on and light source on)
3) $I_P(\lambda)$: Plasma emission spectrum (plasma on and light source off using a shutter)
4) $I_{BG}(\lambda)$: Background signal spectrum (plasma off and light source off)

Every single acquisition had to be realized in stable conditions to ensure a reliable absorbance spectra. Therefore, it supposes a stable plasma process throughout the acquisition and a stable monochromator source.

During these acquisitions, the clamping crown device had to be removed from the ICP chamber in order to avoid optical beam vignetting during absorption spectroscopy experiments. As a result, plasma process characterizations were realized with a 150 mm diameter Si wafer which was fixed on the substrate holder using kapton tape. It surrounded entirely the sample edges and a He clamping pressure of 500 Pa was fixed during these tests to enable thermal transfer at cryogenic temperatures. The resulting He backing flow monitored during the acquisitions was equal to 0.0 sccm most of the time, interspersed with regular He flow injections up to 1.3 sccm.

During a single acquisition series, the four necessary spectrum acquisitions were performed in the same order. The light-source $L_0(\lambda)$ and plasma emission $P_0(\lambda)$ spectra were taken twice during the same acquisition series to reduce drift errors and an average spectrum was determined for each of them. Before launching the series of acquisitions, a stabilization period of roughly 30 seconds was respected to ensure the stability of the plasma process where the minimal reflected power value (1 W) was reached.

For a single CF_4 plasma process, at a given substrate temperature, at least 3 acquisition series were realized in order to account for eventual fluctuations and to refine baseline treatments. UV absorption spectra were first realized in the 210 nm to 285 nm spectral region before focusing on the acquisition of specific spectra which were restricted to the associated absorption domains of CF (between 221.5 nm and 225 nm) and CF_2 radicals (between 235 nm and 270 nm).

2.5.4.4 Analysis

The absorbance spectra A of the plasma medium is determined from the Beer-Lambert law which is expressed below (**equation II.36**).

Equation II.36: Beer-Lambert law applied to absorption spectroscopy

$$-ln\left(\frac{I_{LP}-I_P}{I_L-I_{BG}}\right) = -ln\left(\frac{I_T}{I_0}\right) = A = \sigma.n.L$$

In this equation, I_T corresponds to the transmittance spectra and I_0 to the incidence spectra. L corresponds to the absorption medium path. Moreover, n corresponds to the relative density of absorbing species whereas σ corresponds to the absorption cross section. These 3 parameters have to be carefully evaluated depending on the experiment setup and the nature of the radical species which are monitored. The absolute density of absorbing species N can then be deduced by integrating $A(\lambda)$ over a rovibronic transition λ_0 through the following equation (**equation II.37**) where $f_{v'v''}$ corresponds to the oscillator strength.

Equation II.37: Integration of the absorbance spectra $A(\lambda)$ over a rovibronic transition λ_0

$$\int \frac{I_0 - I_T}{I_0} . d\lambda = 8.85 \, \mathrm{x10}^{-20} . {\lambda_0}^2 . f_{v'v''} . N . L$$

Every single absorption spectrum (A) has to be retreated independently according to its respective background signal and light-source spectra in order to evaluate a baseline noise level. The baseline noise level typically depends on the stability of the light source, acquisition method and sampling environment. Once it is evaluated, it allows to better identify and characterize the absorption peak intensities which are characteristic of the radical species.

Following the baseline treatments and integration of the absorbance spectra obtained, the calculation of the absolute CF and CF_2 radical densities was realized in relation to the substrate temperature for identical CF_4 plasma processes.

2.6 Summary of chapter II (English):

The study of cryoetching processes was realized with an Oxford Instruments Plasma Pro 100 Cobra reactor. It is an inductive coupled plasma (ICP) reactor. The reactor disposes of a cryogenic chuck that can thermalize wafers down to -150°C using liquid nitrogen with a precision of roughly ± 1°C around the order value during cryogenic processes. The wafer is mechanically clamped to a quartz crown using a backing He flow which ensures a clamping pressure of 1,300 Pa. Before the execution of cryogenic tests, the wafer was systematically thermalized at the process temperature for at least 5 minutes. The following process gases were installed on the tool: SF_6, Ar, O_2, CHF_3, CF_4, C_4F_8 and SiF_4 . All the gas lines disposed of a MKS mass flow controller which was calibrated to its respective gas. The gases can be injected inside the chamber at two different locations, either through the source or through the gas-ring which is situated inside the diffusion chamber above the wafer. Fast ALD Swagelok valves with an actuation time of 10 ms regulate the injection of gases inside the chamber via these two channels. The chamber pressure is regulated with an automated pressure control (APC) valve which can be set to a certain pressure (0.00 Pa to 13.33 Pa) or to a certain position (0.0° to 90.0°). The reactor is equipped with a source RF generator with a frequency of 2 MHz and a maximal power output of 3,000 W. It is also equipped with a bias RF generator with a frequency of 13.56 MHz with a maximal power output of 300 W. The application of bias could only be set with a power value.

Deep etching tests (standard cryo-etching, STiGer or Bosch) were carried out mainly on a single type of sample, which consisted of a silicon substrate coated with a 1.2 µm SiO_2 hard mask layer with a pattern composed of a series of trenches from 2 to 10 µm thick. Thin-etching or deposition studies were carried out with blanket samples consisting of silicon substrates with thin surface layers of polycrystalline silicon (p-Si), SiO_2 or Si_3N_4 from 100 to 250 nm thick. For each process test, a coupon of roughly 3x3 cm^2 was cleaved with an array of patterns was cleaved from the sample wafer and glued on a 4-inch Si or SiO_2 carrier wafer with a specific thermal glue which enables a convenient heat transfer during the cryogenic process tests. The etch profiles of deep-etching process tests were characterized by scanning electron microscopy (SEM) to evaluate their general aspect and determine the etching rate. Thin-etching processes were analyzed by in-situ ellipsometry using a Horiba Jobin Yvon UVISEL-1 model. The thickness of the surface layer as well as its dielectric properties were characterized before, during and after each process test. This technique was also used to monitor the deposition of thick layers of adsorbed molecules and their subsequent desorption during gas injection tests at cryogenic temperatures. An electrostatic quadrupole plasma (EQP) mass spectrometer series 1000 model provided by Hiden Analytical was used to characterize the volatile species present in the chamber during process tests. These processes were also characterized using plasma probes, including Langmuir probe, RFEA probe and Plato probe all provided by Impedans. These diagnostics allowed to determine key plasma properties such as the plasma potential, the ion energy distribution function (IEDF) as well as the ion and electronic densities. An absorption spectroscopy study was also carried out to estimate the density of CF and CF_2 radical species during a CF_4 plasma in relation to the substrate temperature.

2.7 Résumé du chapitre II (français) :

L'étude des différents procédés de gravure cryogénique a été réalisée sur un réacteur Oxford Instruments Plasma Pro 100 Cobra. Il s'agit d'un réacteur plasma à couplage inductif (ICP). Le réacteur est doté d'un porte-substrat cryogénique permettant de thermaliser des échantillons jusqu'à -150°C avec de l'azote liquide et une précision de ± 1 °C autour de la valeur de consigne. La plaquette est fixée par clampage mécanique et thermalisée avec un débit d'hélium apporté en face arrière permettant son maintien sur une couronne en quartz avec une pression de 1300 Pa tout en assurant le transfert thermique. Le temps de thermalisation des échantillons était au minimum de 5 minutes lors des essais de procédés plasma à température cryogénique (T<0°C). Les gaz à disposition (SF_6, Ar, O_2, CHF_3, CF_4, C_4F_8 et SiF_4) pour l'étude des procédés pouvaient être injectés soit au niveau de la source ou au niveau d'un anneau situé dans la chambre de diffusion appelé gas-ring. L'injection des gaz est assurée par des vannes rapides de type ALD (Swagelok) avec un temps de réponse de 10 ms. Chaque ligne de gaz est dotée d'un régulateur de débit massique MKS calibré pour leur utilisation. La pression au sein de la chambre est régulée par une vanne de laminage qui peut être réglée soit avec une consigne de pression (0,0 à 13,33 Pa) ou de position (0,0° à 90,0°). Le générateur RF en source de fréquence 2 MHz dispose d'une puissance maximale de 3000 W alors que le générateur RF au niveau du porte-substrat de fréquence 13,56 MHz dispose d'une puissance maximale de 300 W. Le réglage de la tension d'autopolarisation au niveau porte-substrat se fait uniquement en puissance et non en tension.

Les essais de gravure profonde (cryogravure standard, STiGer ou Bosch) ont été réalisés principalement sur un seul type d'échantillon qui consistait en un substrat de silicium recouvert d'un masque dur SiO_2 de 1,2 µm avec un motif composé d'une série de tranchées de 2 à 10 µm d'épaisseur. Des études complémentaires ont été réalisées avec des échantillons composés de substrats de silicium avec des dépôts minces de silicium polycristallin (p-Si), SiO_2 ou Si_3N_4 de 100 à 250 nm d'épaisseur. Chacun de ces échantillons étaient clivés en morceaux d'environ 3x3 cm^2 et collés sur des plaquettes support en Si ou SiO_2 de 100 mm avec une colle spécifique assurant le transfert thermique. Pour l'étude des procédés de gravure profonde, les profils ont pu être observés au MEB pour déterminer l'aspect général et la vitesse de gravure associée. Les essais de gravures fines ont pu être suivis par un ellipsomètre in-situ Horiba Jobin Yvon de type UVISEL-1. Cette technique a aussi été utilisée pour caractériser des dépôts épais de gaz adsorbés sans plasma et leurs désorptions successives. La nature des différentes espèces chimiques volatiles contenues au sein de la chambre lors des essais de procédés a pu être caractérisée par un spectromètre de masse Hiden Analytical de type EQP Series 1000. La caractérisation des propriétés des plasmas étudiés a pu être réalisée par sonde RFEA et sonde capacitive fournies par Impedans. Cela a permis notamment de déterminer le potentiel plasma, l'énergie des ions ainsi que les densités électronique et ionique. Une étude de spectroscopie d'absorption a aussi été réalisée afin d'évaluer la densité de radicaux CF et CF_2 dans un plasma CF_4 en fonction de la température du porte-substrat.

3 Chapter III: Evaluation of Bosch processing using c-C_4F_8 as a passivation gas in relation to substrate temperature for deep silicon etching

3.1 Introduction

As seen in **chapter I**, Bosch processing is the main technique used in the industry for deep Si etching. However, its major drawback is the gradual accumulation of fluorocarbon contamination on the reactor sidewalls which leads to process drifts. As a result, regular interventions are necessary to retrieve an ideal etch rate [247,140,248–251]. The main technical solution which was implemented to limit the occurrence of these cleaning interventions was the installation of heating liners around the chamber which can take various forms [140,247,248]. Their role is to thermalize the chamber sidewalls above the condensation temperature of C_xF_y polymers which is typically above +150°C [140,247]. Indeed, various studies demonstrate that the temperature of chamber walls can influence fluorocarbon plasma processes which can result in modified etch rates and etching selectivities [249,251,252]. In the case of Bosch processing, high temperature chamber walls limits fluorocarbon contamination [249]. As a result, fluorocarbon deposition is enhanced on the wafer surface that is cooled at ambient temperature which reduces Si etch rate and can enhance SiO_2 or Si_3N_4 selective etching if the process parameters are not refined. However, heating chamber liners do not completely resolve the issue of chamber wall contamination and can be quite energetic.

Within the scope of this research project, no significant data in the scientific literature was found concerning the global performance of the Bosch process at cryogenic temperatures despite the fact that it is a widely used process for deep Si etching. As a result, it was decided to carry out a series of experiments in order to evaluate its global temperature sensitivity. Amongst the different fluorocarbon gases available on the etching tool (C_4F_8, CHF_3 and CF_4), it was decided to use C_4F_8 (c-C_4F_8) as a passivating gas because it is the most widely used for Bosch processing in general [128,253]. The secondary goal was to evaluate whether the C_4F_8 passivating gas feed could be reduced at lower temperatures while achieving similar etch profiles at ambient temperature. Therefore, various process tests were implemented to verify the hypothesis that cryogenic cooling of the Si substrate actually enhances fluorocarbon deposition. To that matter, it was first decided to perform etch tests with an identical set of Bosch process parameters at +20°C and -100°C where just the C_4F_8 passivating gas feed was varied. The comparison of the etching profiles obtained allowed to determine the minimal amounts of C_4F_8 needed to achieve anisotropic etching in each case. Subsequently, and in the same way, the impact of the injection mode concerning C_4F_8 passivation was also studied to evaluate whether major differences could be observed between source or gas-ring injections at +20°C and -100°C. Further process tests where the APC valve was blocked at the same position during both etching and passivation steps were also carried out. In this chapter, the Bosch process results will be presented and commented for each process configuration that was tested. Subsequently, a general

analysis will be presented where the results obtained for each configuration will be compared and discussed. High aspect ratio etch profiles will then be presented as well as the RFEA and capacitive probe characterizations of the SF_6 plasma that was used during these process tests. The main results disclosed in this chapter were published in the following article [254].

3.2 Comparison of C_4F_8/SF_6 Bosch etching profiles at -100°C and +20°C

To evaluate the influence of the substrate temperature on the etching profiles obtained during Bosch processing, preliminary tests were realized at ambient temperature using parameters obtained through bibliographic research and corrected according to the reactor capabilities [128,253,255–259]. Following the analysis of the first etch test results, it was decided to fix the set of process parameters listed in **table III.1**. The choice was made to carry out all the etching tests with TVT samples (**Chapter II** / Samples) glued onto SiO_2 carrier wafers.

The choice of 200 Bosch cycles was set to rapidly obtain etching profiles of sufficient depth to be observed and compared to each other by SEM. Following their observation, the principal etching characteristics could be differentiated and a relevant etch rate could be derived. The choice of the step durations, respectively 3 seconds for the etching step and 2 seconds for the passivation step, was done in a desire to take advantage of the fast-pulsing process capability of the ICP tool in order to limit the scalloping defect while still remaining in the same order of standard durations found in literature (5 to 15 seconds for each step) [259,92,260]. In consequence, it was decided to adjust the pressure of the process steps by fixing adequate APC valve angle positions rather than setting pressure order values. In the case of rapid pulses, this technique was preferred to enhance process stability. Therefore, preliminary testing was mandatory for each process involving a different C_4F_8 gas feed. Indeed, APC valve positions were fine- tuned to maintain a stable chamber pressure throughout the whole process.

Table III.1: Set of C_4F_8/SF_6 Bosch process parameters used to study the impact of substrate temperature on the etch profiles

Temperature (°C)	+20°C or -100°C	
Thermalization time	(30 s / 5 min) respectively for tests at (20°C / -100°C)	
Process duration	200 Bosch cycles (16 min 40 s)	
Process step	**Etching step**	**Passivation step**
Gas	SF_6	C_4F_8
Flow rate (sccm)	300 sccm	Variable flows tested (2 to 60 sccm)
Step time (s)	3 s	2 s
Pressure (Pa)	3.0 Pa (APC angle position)	2.0 Pa (APC angle position)
Source Power (W)	1,500 W	1,500 W
Bias Power (W)	15 W	15W
Equivalent Bias Voltage measured on a Si wafer (V)	≈ 135 V	≈ 90 V
Equivalent Bias Voltage measured on a SiO_2 wafer (V)	≈ 35 V	≈ 15 V

A stable source power of 1,500 W and stable bias power of 15 W were used for both the passivation and etching steps for all the Bosch processes tested in this particular study. Although most Bosch processes include different source and bias powers for the passivating and etching steps, the choice was to set a fixed value for both these parameters for process stability and plasma matching reasons.

Due to the rapid pulsing nature of the process and the insulating SiO_2 carrier wafer used for the tests, the bias voltage measurement on the ICP tool was quite erratic. To better approach the real bias voltages that occur during the process, each step was manually tested for extended durations to retrieve a stable measurement of the bias value. It resulted that for a dummy Si substrate, the measured bias values were approximately equal to 135 V for the SF_6 etching step and 90 V for the C_4F_8 passivation step (C_4F_8 flow rate of 12 sccm). For a SiO_2 dummy substrate, the bias voltages measured during the same manual tests were equal to roughly 35 V and 15 V respectively.

During the process, the SF_6 gas flow was only injected during the etching steps and brought down to 0 sccm during the passivation steps. However, the C_4F_8 gas flow was injected in the reactor only during the passivation steps and was diverted to the exhaust during the etching steps.

The first Bosch process tests were done by injecting the C_4F_8 passivating gas flow through the gas-ring which will be referred to as configuration A. Secondly, a series of tests were done by injecting the fluorocarbon gas through the source inlet and will be referred to as configuration B. For these two configurations, a different APC valve position was set for each process step to reach the desired chamber pressure value.

Consecutively, it was decided to carry out the same tests by fixing the APC valve position during the whole process. This position was determined according to the SF_6 etching steps where a pressure of 3.0 Pa was required. As a result, the chamber pressure monitored during C_4F_8 passivation steps was considerably lower than the initial order value of 2.0 Pa. The idea of performing Bosch process tests by fixing the APC valve comes from the belief that industrial processes prefer to limit its use for a longer service life. However, this technique implies the use of considerably higher C_4F_8 gas flows to maintain the desired chamber pressure value of 2.0 Pa during the passivation steps if all the other process parameters remain unchanged. Nevertheless, given the scope of this research study, which was designed to evaluate if the amount of C_4F_8 passivation gas can be reduced at cryogenic temperatures, it was decided to apply low C_4F_8 flow rates while sticking to the same process parameters fixed in **table III.1.** Therefore, the chamber pressure during the passivation steps was considerably reduced during these specific tests. The Bosch process tests carried out under these conditions in this condition with C_4F_8 gas-ring injections will be referred to as configuration C. Finally, configuration D involving C_4F_8 source injections with a fixed APC valve condition was briefly tested but the preliminary etching results obtained were inconclusive and were therefore not further explored.

A detailed schematic of the four different tested etching configurations is provided for a better understanding in **figure III.1**. The main results and etch profiles obtained for each configuration are resumed in the following sub-sections. In majority, the etch profiles presented concern those obtained with 6 µm trench mask openings to better compare them with each other.

Figure III.1: Schematic of the different configurations used for Bosch process tests

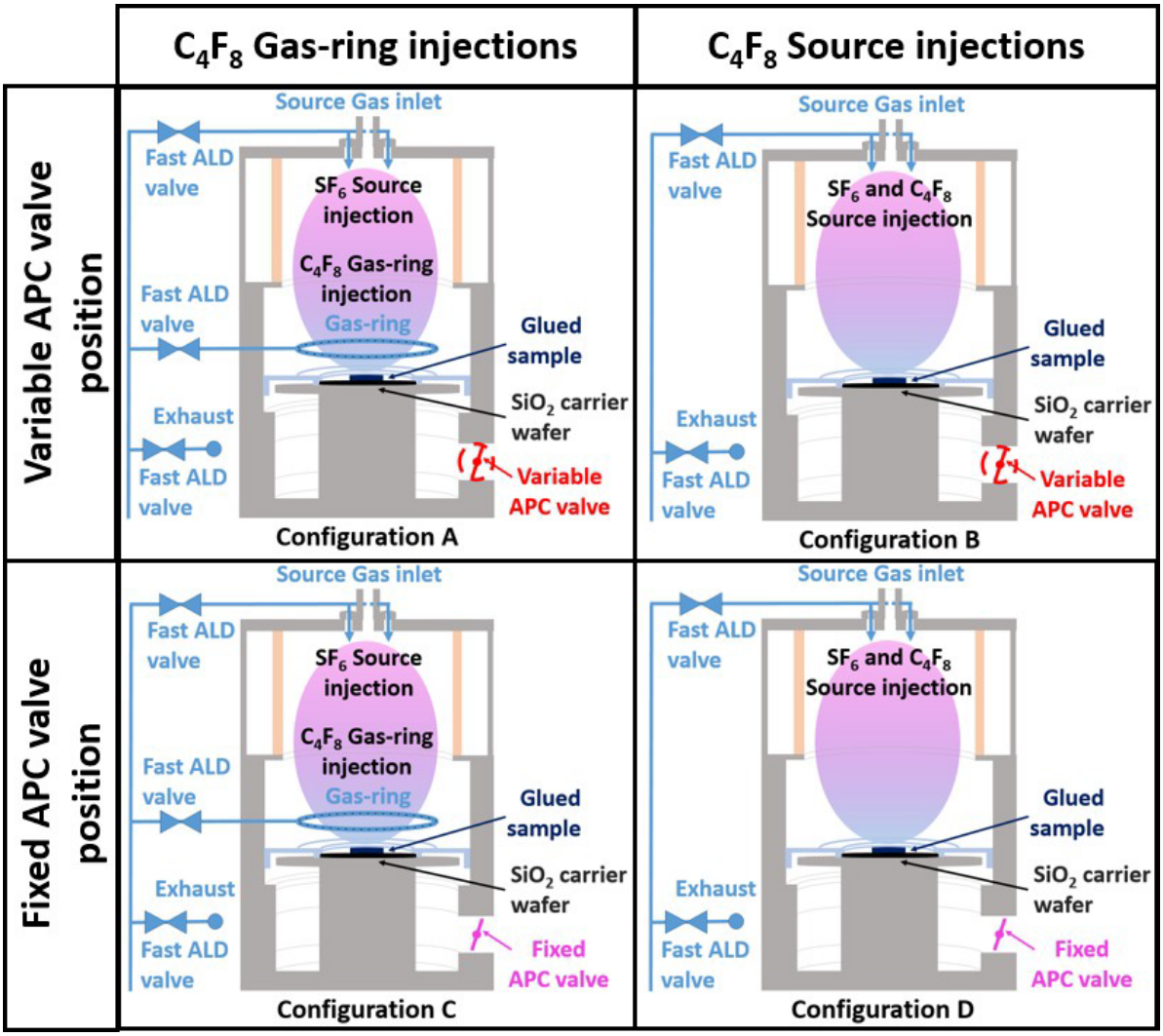

3.2.1 Configuration A (Variable APC configuration / Gas-ring C_4F_8 injections)

The following etch profiles obtained at a substrate temperature of -100°C are shown in **figure III.2**. They include C_4F_8 gas feeds from 4 to 16 sccm applied during the passivation steps.

At 4 sccm, the passivating gas flow is slightly insufficient and the etching profile obtained is slightly negative (around 91.2°). The equivalent etch rate is roughly equal to 5.1 µm/min without considering the thermalization time of 5 minutes.

At 8 sccm, an optimal anisotropic profile is achieved. The etch angle is approximately equal to 90.2° with an equivalent etch rate equal to 4.4 µm/min.

Above 8 sccm of C_4F_8 passivating gas flow, over-passivation features quickly appear on the etched trenches. At 12 sccm, an etched trench is observed but it is packed with over-passivated vertical columns where scalloping marks are visible on their sides. At 16 sccm, no etching is observed as

over-passivation is too significant to allow any subsequent SF_6 plasma etching. A fluorocarbon passivated layer of roughly 3.8 µm is clearly observable on top of the SiO_2 mask and the trench has not been etched.

Figure III.2: Comparison of etch profiles at -100°C in relation to the passivating C_4F_8 gas flow (6 µm wide trenches / Configuration A)

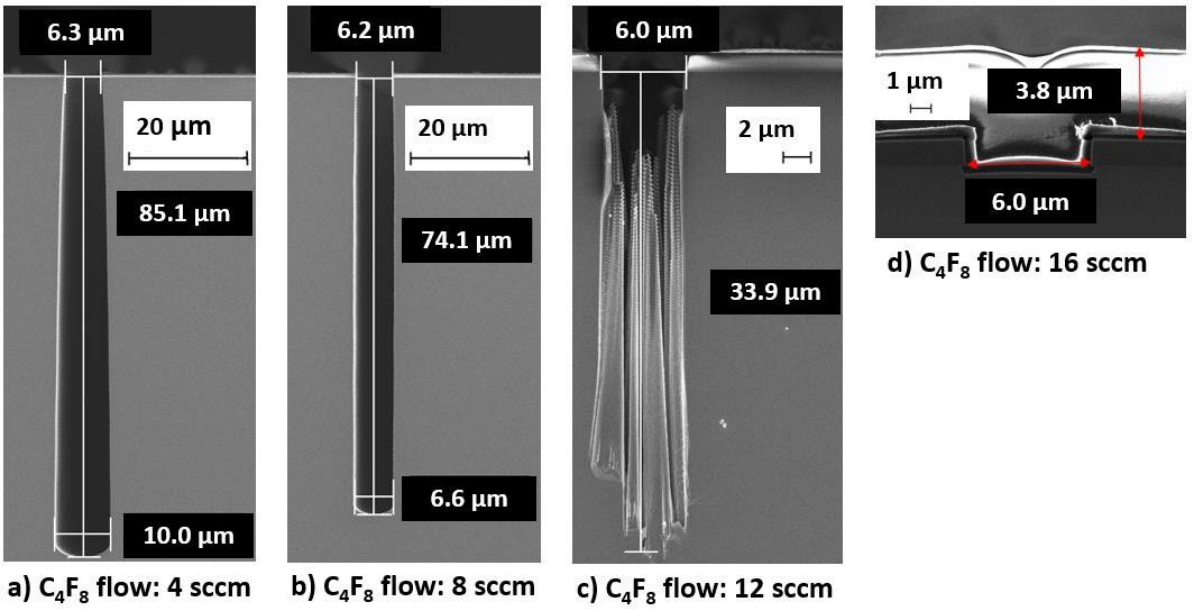

In comparison, the following etch profiles obtained at +20°C with the process parameters are listed in **figure III.3**. They include passivating C_4F_8 gas feeds from 8 to 20 sccm.

At ambient temperature, the etching profiles obtained are more uniform. At 8 sccm of C_4F_8 gas feed, the etched profile presents consistent lateral etching which means that the fluorocarbon passivation is clearly insufficient to prevent isotropic etching. As a result, the equivalent etch rate is significantly decreased down to 2.4 µm/min. Once a sufficient C_4F_8 gas feed is reached, starting at 12 sccm, the passivation is sufficient. The etching profiles obtained from 12 to 20 sccm all look quite alike with similar anisotropy and etched depths. At 12 sccm, the etch rate is the highest at 4.0 µm/min. By increasing the C_4F_8 flow, the etch rates slightly decrease as can be seen for the profiles at 16 sccm and 20 sccm.

By comparing the profiles obtained at -100°C and +20°C, respectively in **figures III.2** and **III.3**, it can be clearly observed that the Bosch process is temperature sensitive. The results show that the etching-to-passivating equilibrium slightly shifts in relation to the substrate temperature. The optimal anisotropic etching profile at -100°C is obtained with a C_4F_8 gas feed of 8 sccm. By performing the same process at +20°C, the profile obtained clearly lacks sidewall passivation and presents an etched depth reduced by nearly half. As a result, the gas feed has to be increased by 50% to 12 sccm to retrieve an anisotropic profile yet a lower etch rate (4.0 µm/min) is observed in comparison with the optimal profile obtained at -100°C (4.4 µm/min).

Figure III.3: Comparison of etch profiles at +20°C in relation to the passivating C_4F_8 gas flow (6 µm wide trenches / Configuration A)

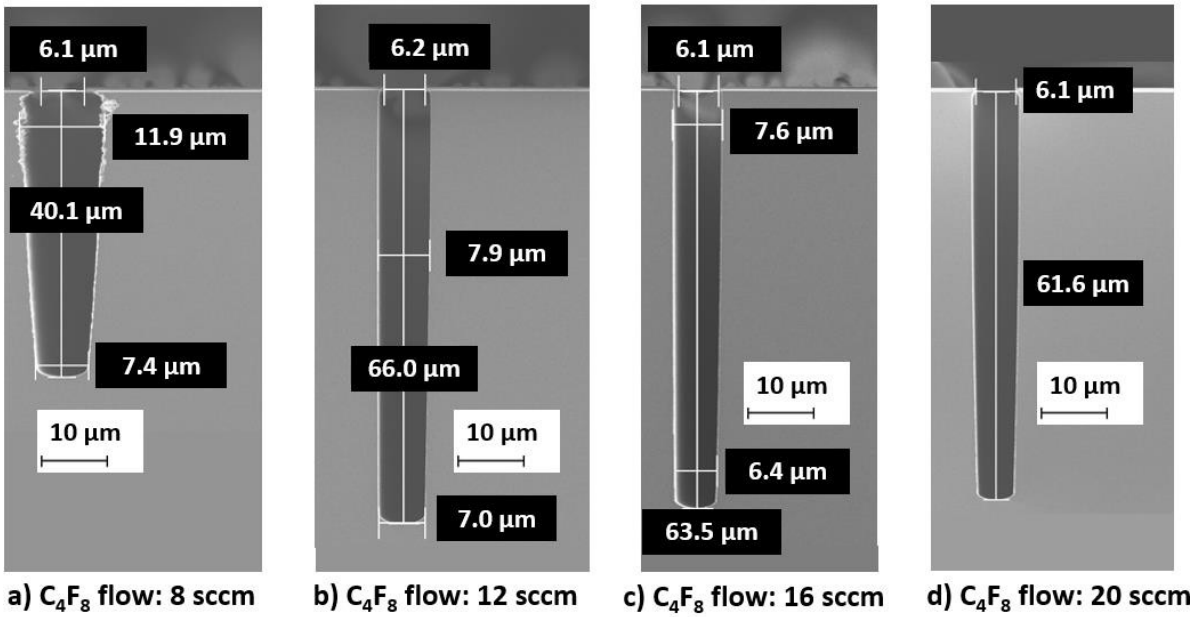

a) C_4F_8 flow: 8 sccm b) C_4F_8 flow: 12 sccm c) C_4F_8 flow: 16 sccm d) C_4F_8 flow: 20 sccm

By taking a closer look at optimal etching profiles obtained at -100°C and +20°C which is presented in **figure III.4**, it can be observed that the Si:SiO_2 etching selectivity is higher at -100°C than at ambient temperature. By calculating the amount of SiO_2 hard mask that was etched for both processes, the Si:SiO_2 selectivity is approximately equal to 135:1 at -100°C and 105:1 at +20°C. Additionally, a slight etching undercut of roughly 600 nm is observed on the etching profiles processed at +20°C. However, scalloping marks are more pronounced at -100°C compared to the profile obtained at ambient temperature where these marks are inexistent or barely noticeable.

Figure III.4: Close view of the anisotropic etch profiles obtained at -100°C and +20°C (6 µm trenches / Configuration A)

a) T = -100°C ; C_4F_8 flow: 8 sccm

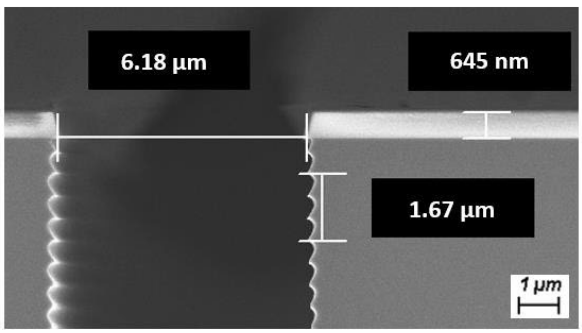

b) T = +20°C ; C_4F_8 flow: 12 sccm

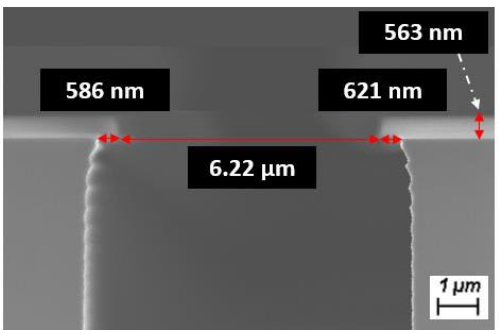

Globally, by comparing the etched depths obtained for each trench width which is plotted in **figure III.5**, it can be observed that cryo-Bosch etching allows a narrower process window for the achievement of anisotropic etch profiles than at ambient temperature. In general, the main observations made for profiles obtained with 6 µm trench openings apply also to profiles obtained with smaller and larger openings (2, 4, 8 and 10 µm). Only the etch depth is modified accordingly to the ARDE phenomenon. It can be observed through this same graph that ARDE effect is more pronounced at cryogenic temperatures than at ambient temperature.

Figure III.5: Etched depth in relation to the C_4F_8 gas flow at -100°C and +20°C (Configuration A)

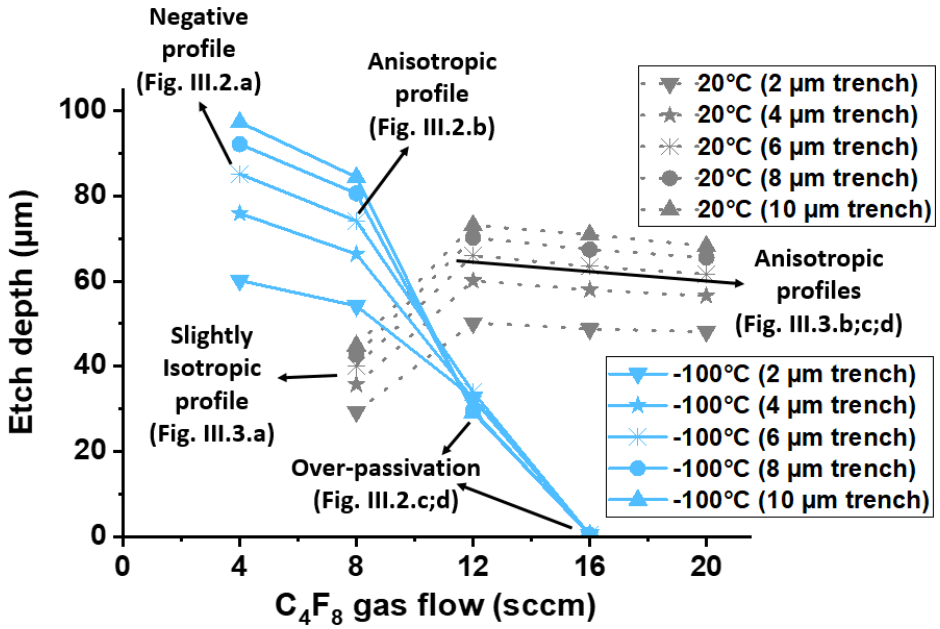

3.2.2 Configuration B (Variable APC configuration / Source C_4F_8 injections)

Concerning these second series of Bosch tests, only the gas injection mode for C_4F_8 passivation steps was switched from gas-ring to source injections. Quite surprisingly, the APC valve positions had to be slightly changed to satisfy chamber pressure requirements for each step during preliminary testing.

The etching profiles obtained at -100°C using this configuration are shown in **figure III.6**, they include source passivating C_4F_8 gas feeds from 2 to 10 sccm.

At 2 sccm of C_4F_8 gas feed, the etching profile obtained is clearly negative and sidewall etching defects are visible. The equivalent etch rate is equal to 5.2 µm/min.

At 4 sccm, the etching profile is slightly negative yet there are no sidewall etching defects. This particular sample presents defects on the surface due to cleaving mishandling. The equivalent etch rate is equal to 4.9 µm/min.

An optimal anisotropic profile is obtained with a C_4F_8 gas feed of 8 sccm where the associated etch rate is equal to 4.0 µm/min.

Over-passivation due to excess of fluorocarbon material occurs rapidly after this optimal point as no etching is observed with a 10 sccm gas feed. In these conditions, a thick fluorocarbon layer of roughly 300 nm is formed.

Figure III.6: Comparison of etch profiles at -100°C in relation to the passivating C_4F_8 gas flow (6 µm wide trenches / Configuration B)

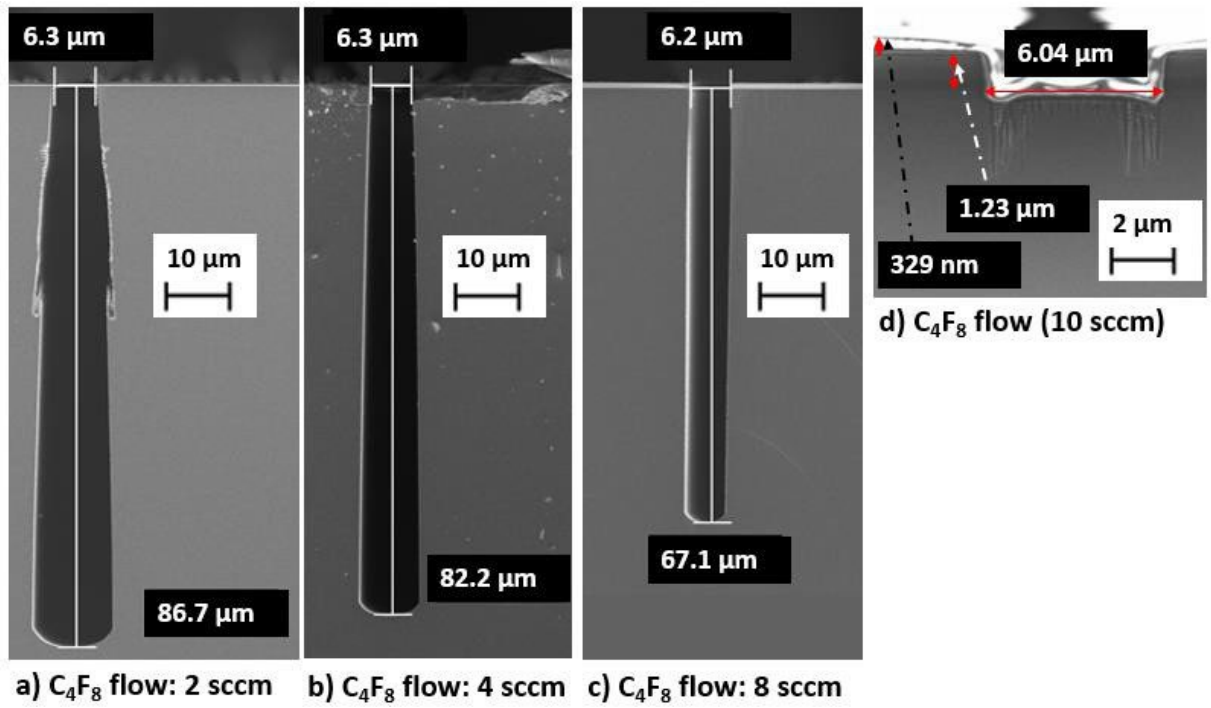

In general, the aspect and equivalent etch rates are similar to the ones obtained using gas-ring injections (configuration A) except that C_4F_8 source gas feed injections seem to have a stronger effect on fluorocarbon passivation. Indeed, by comparing the profiles obtained using source injections at -100°C to the ones obtained with gas-ring injections **(figure III.2)**, the associated etch rates obtained at 4 and 8 sccm of C_4F_8 gas feed are both slightly less important in the case of source injections. Moreover, over-passivation occurs at a lower C_4F_8 flow rate using source injections where a thick fluorocarbon layer is formed by applying a C_4F_8 gas flow of 10 sccm whereas a 16 sccm C_4F_8 flow was necessary using gas-ring injections in order to observe a similar result.

In comparison, the etching profiles obtained at +20°C are shown in **figure III.7** with source passivating C_4F_8 gas feeds from 4 to 12 sccm. In general, the same observations can be made in comparison with the etching profiles obtained at +20°C using gas-ring injections (**figure IV.3**).

Similar etch rates are achieved. They are estimated at 3.7, 3.8, 3.9 and 3.8 µm/min for C_4F_8 gas flow rates of respectively 4, 8, 10 and 12 sccm. Although all profiles are quite similar and fairly anisotropic,

the most optimal profile seems to be obtained at 10 sccm where the etch rate is maximal and seems to present a slightly lower bowing defect.

However, the main difference in comparison with **figure III.3** is that no lateral etching is observed using C_4F_8 source injections even at low flow rates (4 sccm) whereas it is observed at 8 sccm using gas-ring injections. This result also suggests that C_4F_8 source injections are more effective than gas-ring injections to passivate the trench sidewalls even at ambient temperature.

Figure III.7: Comparison of etch profiles at +20°C in relation to the passivating C_4F_8 gas flow (6 µm wide trenches / Configuration B)

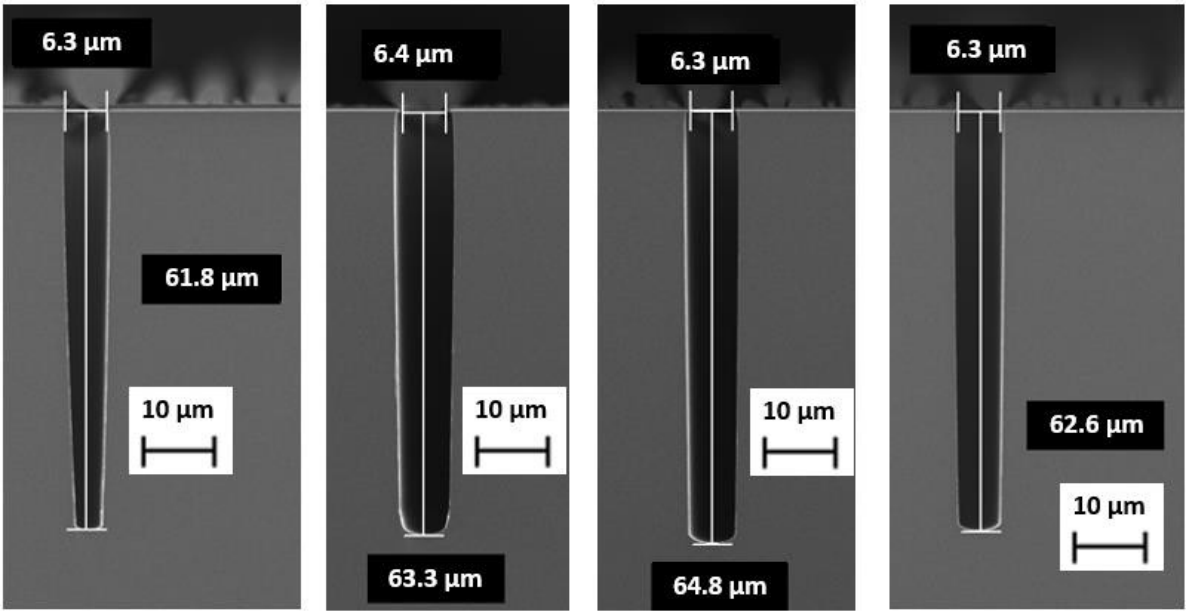

a) C_4F_8 flow: 4 sccm b) C_4F_8 flow 8 sccm c) C_4F_8 flow: 10 sccm d) C_4F_8 flow: 12 sccm

A zoom of the optimal anisotropic etching profiles obtained using C_4F_8 source injections at -100°C (8 sccm) and +20°C (10 sccm) are shown in **figure III.8**. Globally, the same observations can also be made concerning the Si:SiO_2 etching selectivity as well as the general aspect of the etchings in comparison with gas-ring injections. Indeed, at -100°C, Bosch processing also leads to the generation of scalloping marks which are much more pronounced than at +20°C where the sidewalls are quite smooth except at the near surface under the SiO_2 hard-mask. At ambient temperature, all the profiles appear to be slightly bonded and present an etching undercut of roughly 500 nm on each side whereas no undercut is observed on the etch profiles obtained at -100°C. For the etching profile obtained at -100°C with a C_4F_8 passivating gas-flow of 8 sccm, it can be seen that the scalloping marks obtained for the first cryo-Bosch cycles that the etch rate is approximately 0.5 µm/ cycle. For these two optimal profiles, the Si:SiO_2 etching selectivity is approximately equal to 165:1 at -100°C (C_4F_8 source gas flow: 8 sccm) and 85:1 at +20°C (C_4F_8 source gas flow: 10 sccm).

Figure III.8: Close view of the anisotropic etch profiles obtained at -100°C and +20°C (6 µm trenches / Configuration B)

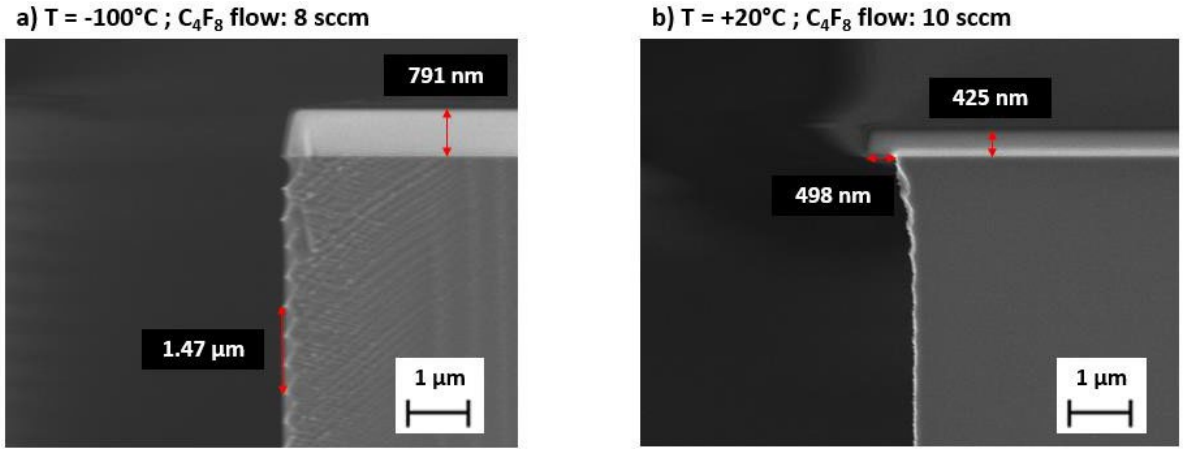

By comparing the etched depths obtained with C_4F_8 source injections for each trench width which is presented in **figure III.9**, it can be seen that ARDE is also more pronounced at cryogenic temperatures than at ambient temperature. Indeed, it is slightly more important at -100°C where the optimal profile is obtained at 8 sccm compared to the optimal profile obtained at +20°C (10 sccm). It becomes even more important at cryogenic temperatures when the C_4F_8 gas-flow is reduced where negative profiles are obtained. Once again, it can be said that the main observations realized for 6 µm wide trenches also apply globally to the other trench sizes (2 to 10 µm).

Figure III.9: Etched depth in relation to the C_4F_8 gas flow at -100°C and +20°C (Configuration B)

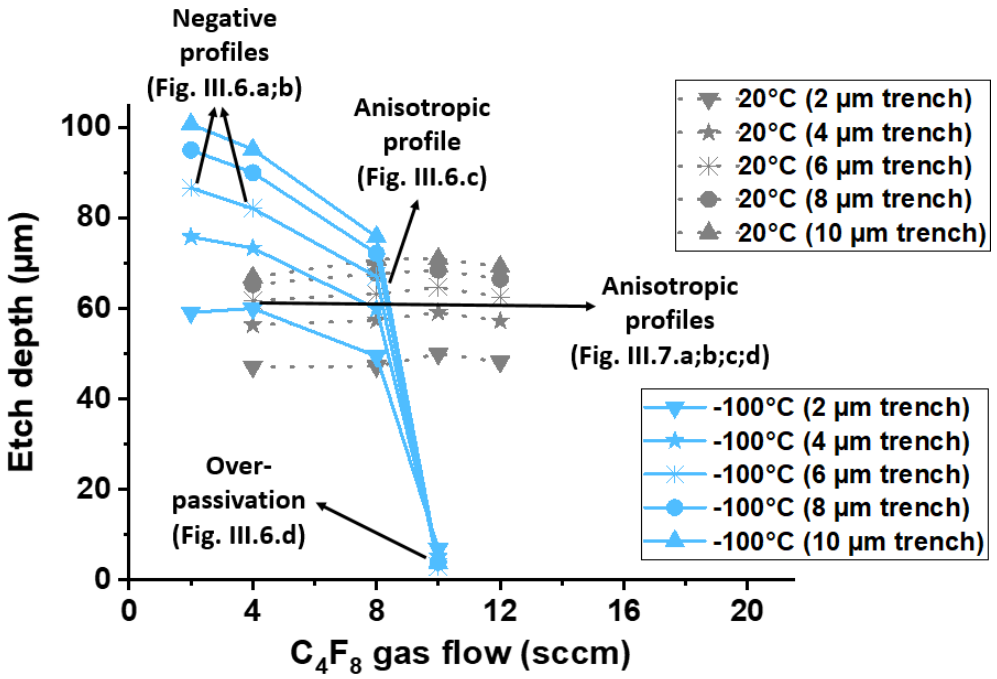

3.2.3 Configuration C (Fixed APC configuration / Gas-ring C_4F_8 injections)

For this specific configuration, the processes were implemented using C_4F_8 gas-ring injections by setting a fixed APC valve angle which corresponded to the most accurate position where the SF_6 etching steps reached a steady pressure of 3.0 Pa. Just like for the previous process tests, the APC valve angle position had to be tested and evaluated throughout the entire process to ensure that no significant pressure variations occurred.

As a result of this fixed valve position, the pressure during the passivation steps was significantly reduced compared to the chamber pressure of 2.0 Pa which was targeted for the two previous etching configurations where the valve position was adapted at a convenient position. Depending of the C_4F_8 gas flows and the substrate temperature that were tested in this configuration, the measured pressure during these C_4F_8 passivation steps did not exceed 0.34 Pa. The following etching profiles obtained with this specific configuration at -100°C are shown in **figure III.10**. They include C_4F_8 gas-ring flow rates from 2 to 8 sccm.

At 2 sccm, it can be observed that C_4F_8 passivation is insufficient as sidewall etching is important. The etch profile seems slightly negative with an equivalent etch rate of approximately 4.1 µm/min.

At 3 and 4 sccm, the profiles are clearly anisotropic and more optimal. However, small localized etching defects can be observed on the sidewalls which may be caused by the low pressure during the passivation steps that are intrinsic to the conditions imposed by the process configuration. The associated etch rate for these profiles are equal to 4.1 µm/min and etch 3.6 µm/min respectively.

At 6 and 8 sccm, over-passivation features gradually appear and the sidewalls are clearly positive due to enhanced passivation. The etch rates are considerably reduced with the increase of fluorocarbon gas feed. They reach respectively 2.3 and 1.1 µm/min.

Figure III.10: Comparison of etch profiles at -100°C in relation to the passivating C_4F_8 gas flow (6 µm wide trenches / Configuration C)

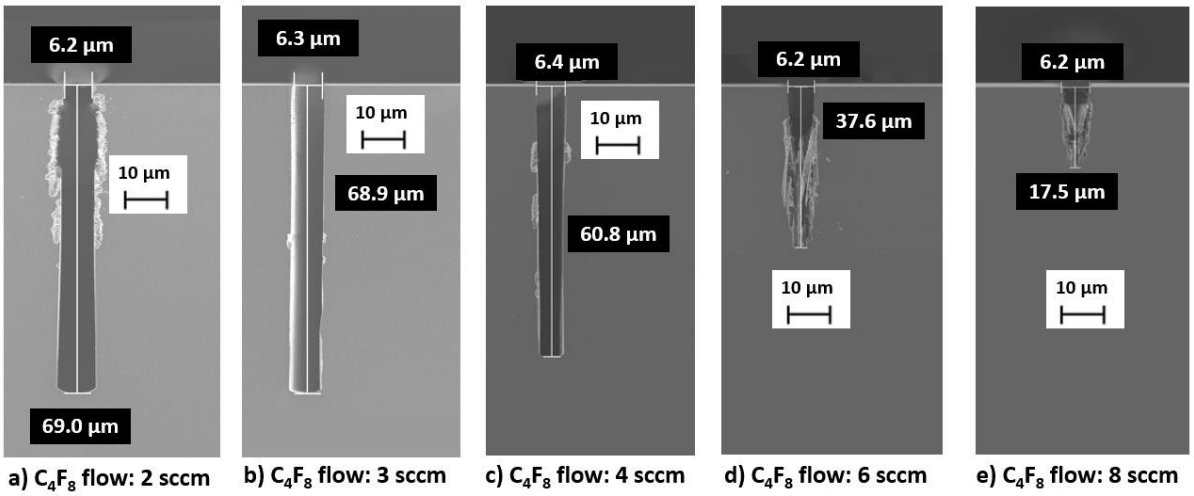

a) C_4F_8 flow: 2 sccm b) C_4F_8 flow: 3 sccm c) C_4F_8 flow: 4 sccm d) C_4F_8 flow: 6 sccm e) C_4F_8 flow: 8 sccm

Subsequently, in **figure III.11,** the following etch profile results were obtained with this specific configuration at +20°C. These etching profiles were obtained with C_4F_8 gas-ring flow rates from 4 to 16 sccm.

At 4 and 8 sccm, the fluorocarbon passivation is insufficient where sidewall etching and undercut are considerable. The equivalent etch rates obtained are equal to 2.6 and 2.9 µm/min respectively.

At 12 sccm, the etching is quite anisotropic and the etch rate is maximal yet small but continuous passivation defects are observed throughout the sidewalls. The associated etch rate of this profile is equal to 3.2 µm/min.

At 16 sccm, the C_4F_8 passivation seems optimal with no sidewall defects. The profile is anisotropic yet a slight bonding effect can be observed in the same proportions as the etching profiles obtained at +20°C in configurations A and B. The equivalent etch rate is equal to 2.8 µm/min.

Figure III.11: Comparison of etch profiles at +20°C in relation to the passivating C_4F_8 gas flow (6 µm wide trenches / Configuration C)

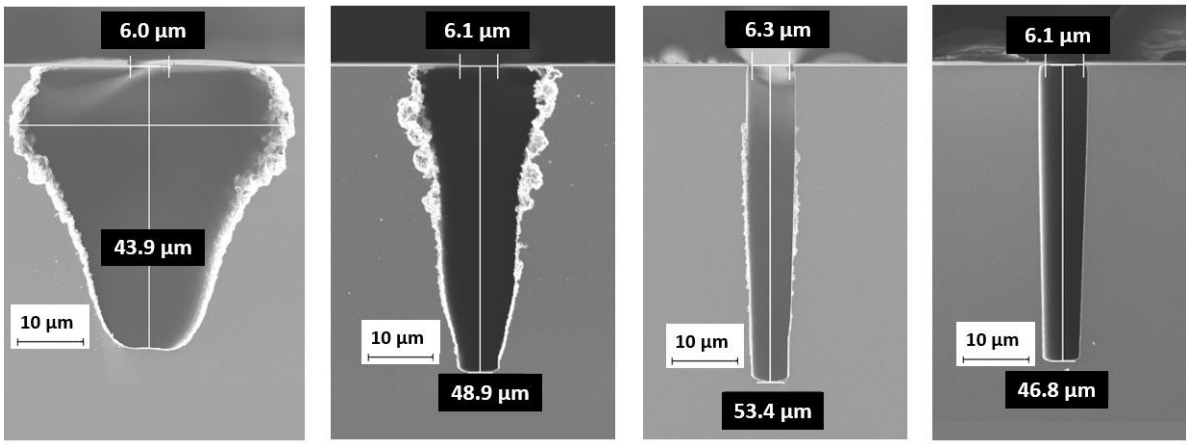

a) C_4F_8 flow: 4 sccm b) C_4F_8 flow: 8 sccm c) C_4F_8 flow: 12 sccm d) C_4F_8 flow: 16 sccm

Overall, it can be seen by comparing all the etch profiles obtained at -100°C that C_4F_8 passivation seems to be enhanced at -100°C in configuration C where the APC valve is fixed during the process. Indeed, etching anisotropy at -100°C is reached with C_4F_8 gas-ring feeds of 3 to 4 sccm whereas 8 sccm was needed to achieve etching anisotropy using also C_4F_8 gas-ring injections but with variable APC positions for each process step (Configuration A). Moreover, over-passivation features are achieved more rapidly in this configuration at -100°C where the etched trenches start to get obstructed at 6 sccm with the formation of over-passivation features whereas the observation of these specific features is made at 12 sccm in configuration A.

However, these observations are more likely to be due to the very low pressures and instabilities that are inherent with this configuration. Indeed, the lower pressures which are achieved at the end of each C_4F_8 passivation steps presumably affect the subsequent SF_6 etching steps, which never reach the

pressure obtained in configurations A and B. This would also explain the reduced etch rates observed in this particular configuration at -100°C and +20°C.

As an example, an etch depth of 60.8 µm is observed at -100°C for the most convenient profile (C_4F_8 gas-ring injection: 8 sccm) in configuration C. In comparison, an etch depth of 85.1 µm is achieved at -100°C for the most optimal profile obtained in configuration A (C_4F_8 gas-ring injection: 4 sccm). At ambient temperature, an etch depth of 46.8 µm is measured in configuration C for the most optimal profile (C_4F_8 gas-ring injection: 16 sccm) whereas it amounts to 63.5 µm for the best profile obtained in configuration A (C_4F_8 gas-ring injection: 12 sccm). They both correspond to an etch rate decrease of roughly 25% for configuration C compared to configuration A which cannot be explained just by the increase of necessary C_4F_8 flow in these cases as this tendency is observed by comparing all the profiles obtained with these configurations.

A close view of the optimal anisotropic etching profiles obtained at -100°C (C_4F_8 gas-ring injection: 3 sccm) and +20°C (C_4F_8 gas-ring injection: 16 sccm) is shown in **figure III.12**. Almost the same observations can be made in comparison with the two previous configurations that were studied where the APC valve position was varied. Again, all the profiles obtained at +20°C present an etching undercut of roughly 600 nm on each side and appear to be slightly bonded whereas no undercut is observed on the etch profiles obtained at -100°C.

Figure III.12: Close view of the anisotropic etch profiles obtained at -100°C and +20°C (6 µm trenches / Configuration C)

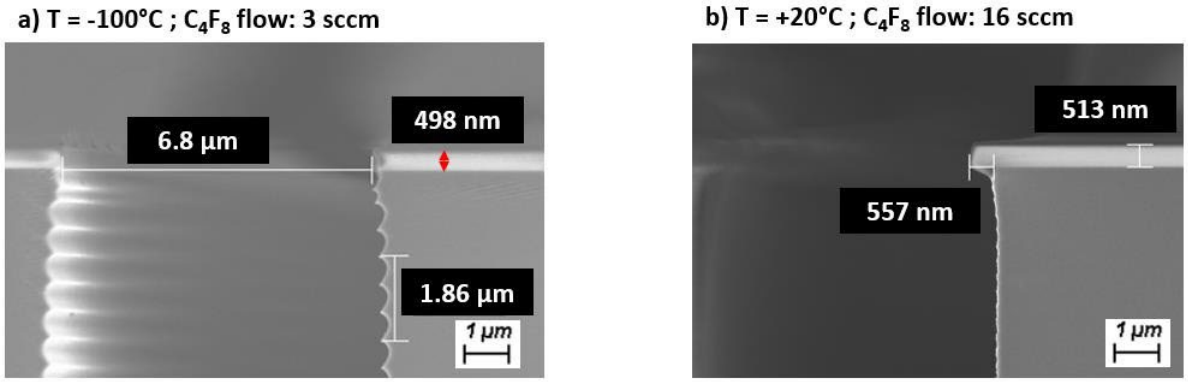

However, in this case, the Si:SiO_2 etching selectivity is reduced compared with what was observed before in configurations A and B. It is still more important at cryogenic temperatures where it is approximately equal to 100:1 (3 sccm of passivating gas flow) compared to 70:1 obtained at +20°C (16 sccm of passivating gas flow). This Si:SiO_2 selectivity decrease may be again due to the lower pressure during C_4F_8 passivation steps which are inherent with this configuration. As a result, the SF_6 etching step is also affected which leads to the observation of a lower etch rate and etching selectivity. Generally, it can be seen that the process parameters are not completely optimized in this case especially at -100°C where small localized etching defects can be observed on the sidewalls of the most anisotropic profiles at 3 and 4 sccm gas feeds. A closer view of these localized

under-passivated areas is shown in **figure III.13** concerning the 4 sccm etch profile. They suggest that the process parameters that were defined for this study and the overall objective of reducing the amount of necessary C_4F_8 gas flow to obtain anisotropic etching are not really compatible with the conditions that are imposed by fixed APC valve position processing.

Figure III.13: Close view of the passivation defects obtained at -100°C with a C_4F_8 passivating gas-slow of 4 sccm (6 µm trench / Configuration C)

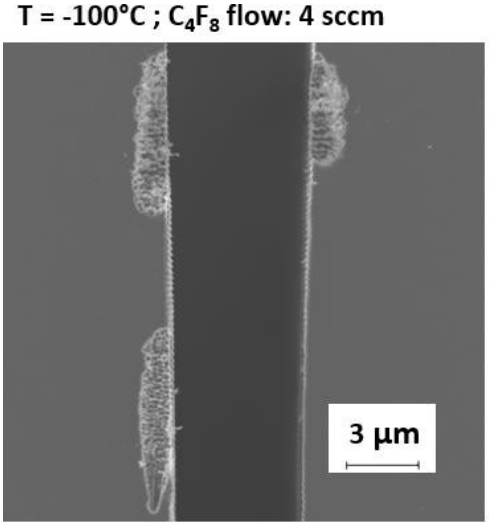

The etched thicknesses obtained with this configuration for each trench width are shown below in **figure III.14**. At -100°C, over-passivation actually starts to occur with a passivating gas-flow of 4 sccm where the wider trenches (8 and 10 µm) are first affected.

Figure III.14: Etched depth in relation to the C_4F_8 gas flow at -100°C and +20°C (Configuration C)

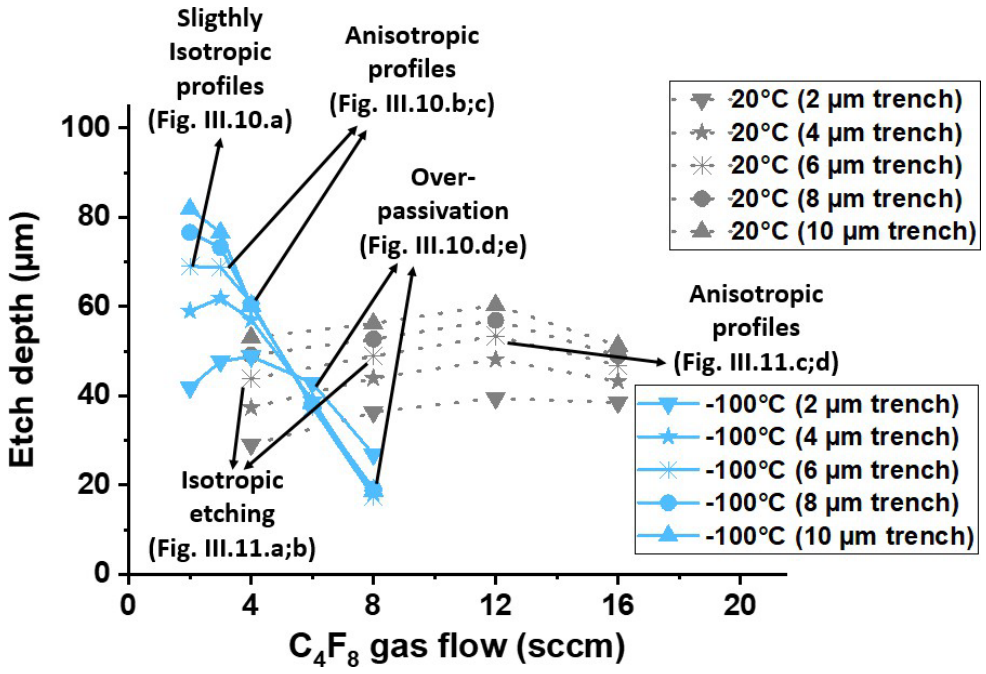

At higher passivating gas-flows, over-passivation features appear and propagate to the smaller trenches but still do not affect them as much as for the wider ones. Once again, ARDE is more pronounced at - 100°C for low passivating gas flows than for most of processes tested at +20°C where it is quite constant except at 16 sccm where it is reduced and an optimal anisotropic profile is reached.

3.2.4 Configuration D (Fixed APC configuration / Source C_4F_8 injections)

The fourth configuration (configuration D) which included C_4F_8 source injections with a fixed APC valve was briefly explored but not studied extensively due to timing reasons. Moreover, the preliminary etching profiles obtained both at +20°C and -100°C were not satisfactory and relevant. Following the same method that was used for process implementation in configuration C, the measured pressures during the C_4F_8 passivation steps were very low which probably explains the poor quality of the few etch profiles observed in this configuration. The pressure measurement during the C_4F_8 passivation steps went down to 0.12 Pa and 0.13 Pa for a 20 sccm C_4F_8 gas feed at -100°C and +20°C respectively. An example of etch profiles obtained at +20°C with this configuration are shown in **figure III.15**.

Figure III.15: Comparison of etch profiles at +20°C in relation to the passivating C_4F_8 gas flow (6 µm wide trenches / Configuration D)

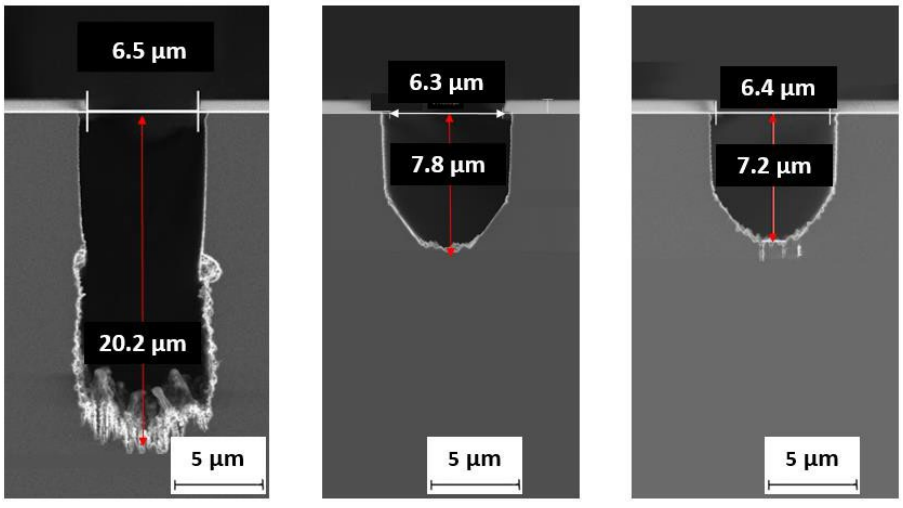

a) C_4F_8 flow: 20 sccm b) C_4F_8 flow: 30 sccm c) C_4F_8 flow: 40 sccm

3.3 Analysis

3.3.1 Synthesis of Bosch process test results

By synthetizing the results obtained with the fixed set of parameters that were applied and using four different process configurations at -100°C and +20°C, it can be observed that the Bosch process is effectively temperature dependent.

By just studying the impact of the variation of C_4F_8 flow, it can be seen that the fluorocarbon passivation is far more efficient at -100°C than at ambient temperature. The resulting reduction of C_4F_8 gas feed needed to achieve optimal profiles at -100°C is noticeable yet the proportions it can take greatly depends of the process configuration that is used compared to ambient temperature processing.

In general, cryogenic Bosch (cryo-Bosch) processing allows a narrower process window for anisotropic etching when it comes to C_4F_8 flow rate adjustment. Indeed, this parameter becomes more sensitive and the slight modification of the gas-flow during the passivation steps can easily lead to over-passivation or isotropic etching. Cryo-Bosch etching also results in a slight increase of the etch rate when comparing optimal etching profiles obtained at -100°C and +20°C. Silicon to silicon oxide ($Si:SiO_2$) etching selectivity is also increased by at least 29% at -100°C. However, the aspect-ratio dependent etching (ARDE) phenomenon is more important at lower process temperatures. A summary of the main results obtained with configurations A, B and C is presented in **table III.2**.

Table III.2: Summary of Bosch etching results obtained at +20°C and -100°C in configurations A, B and C:

Parameter	Configuration A	Configuration B	Configuration C
Fluorocarbon injection mode	Gas-ring	Source	Gas-ring
APC valve positioning	Variable	Variable	Fixed
Resulting pressure during C_4F_8 passivation step	≈ 2.0 Pa	≈ 2.0 Pa	≈ 0.25 Pa
Optimal profile at +20°C (C_4F_8 gas flow)	12 sccm	10 sccm	16 sccm
Optimal profile at -100°C (C_4F_8 gas flow)	8 sccm	8 sccm	3 sccm
No etching due to over-passivation at -100°C (C_4F_8 gas flow)	16 sccm	10 sccm	> 8 sccm
Reduction of necessary C_4F_8 gas flow to maintain an optimal profile at -100°C	≈ - 33%	≈ - 20%	≈ - 81%
Etch rate at +20°C (optimal profile)	4.0 µm/min	3.9 µm/min	2.8 µm/min
Etch rate at -100°C (optimal profile)	4.4 µm/min	4.0 µm/min	4.1 µm/min
Remaining SiO_2 mask layer at +20°C (optimal profile)	≈ 0.56 µm	≈ 0.43 µm	≈ 0.51 µm
Remaining SiO_2 mask layer at -100°C (optimal profile)	≈ 0.65 µm	≈ 0.79 µm	≈ 0.50 µm
$Si:SiO_2$ etching selectivity at +20°C (optimal profile)	≈ 105:1	≈ 85:1	≈ 70:1
$Si:SiO_2$ etching selectivity at -100°C (optimal profile)	≈ 135:1	≈ 165:1	≈ 100:1
Increase of $Si:SiO_2$ etching selectivity at -100°C (optimal profiles)	≈ + 29%	≈ + 94%	≈ + 43%

By comparing the results obtained according to the process configurations that were tested, it can be globally observed that the reduction of the necessary C_4F_8 gas to maintain an optimal profile at -100°C

is generally more important when gas-ring injections were used for passivation (configurations A and C). However, the increase in Si:SiO_2 etching selectivity at -100°C is more important when C_4F_8 source injections were used for passivation (configuration B). In terms of processing, the use of the gas-ring for C_4F_8 injections (configurations A and C) allows to completely separate the gas injection lines for the etching and passivation steps which can offer more flexibility for process optimization. It can be observed that the etch rate is more important using configuration A where the APC valve is varied accordingly at each step for pressure regulation. However, constant APC valve position switching can be detrimental for the proper operation of the valve. Therefore, fixing the APC valve position (configuration C) can also present some advantages. In this case, process optimization can be done by notably increasing the step durations and by adjusting the gas flow rates to ensure that the pressure between each step is not so disparate. Overall, none of the configurations A, B or C clearly stand out as the best for Bosch processing as they can all be optimized to maximize the benefits they might offer.

3.3.2 High Aspect Ratio Features

Although the etching tests were limited to 200 cycles, high aspect ratio features were obtained on the smaller trench openings (2 µm and 4 µm trench widths). A maximal anisotropic aspect ratio feature of approximately (25:1) was observed on the optimal profiles obtained at -100°C in configurations A and B (both using 8 sccm of C_4F_8 gas feed) on the mask trench openings of 2 µm. The SEM images of these particular profiles are presented in **figure III.16**. The results obtained suggest that deeper features could be easily achieved by increasing the number of cycles both at -100°C and +20°C.

Figure III.16: High aspect ratio profiles obtained at -100°C (8 sccm of C_4F_8 gas feed / 2 µm wide trenches / Configurations A and B)

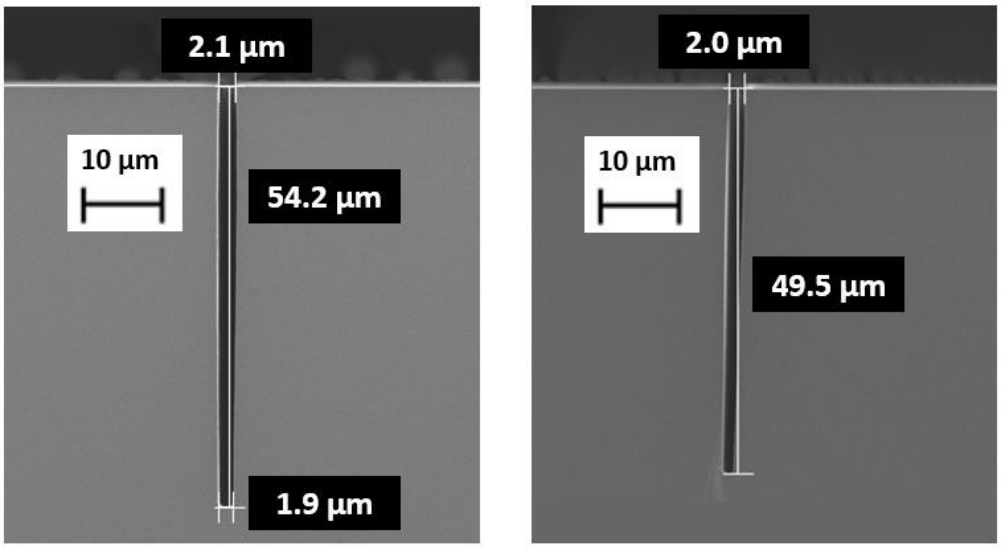

a) Configuration A
[-100°C ; C_4F_8 flow: 8 sccm]

b) Configuration B
[-100°C ; C_4F_8 flow: 8 sccm]

3.3.3 RFEA analysis of the SF_6 etching step during Bosch processing

Subsequent RFEA characterization of the SF_6 etching step was realized in the same process conditions at ambient temperature (SF_6 flow rate: 300 sccm ; ICP Source power: 1,500 W). Several acquisitions were realized at ambient temperature by varying the chamber pressure and bias power during the experiments. The ion energy distribution functions obtained by varying the bias power at a chamber pressure of 3.0 Pa are represented in **figure III.17**. The associated bias voltage values that were measured on the ICP tool by varying the bias power from 0 to 20 W during the RFEA experiments are disclosed. It must be noted that the negative components observed at low ion energies for the distribution functions obtained at 0 and 5 W of bias voltage should be ignored and considered to be equal to 0. They should correspond to the emission of secondary electrons which were not recollected by the RFEA probe (adjustment of grid n°3).

By comparing these values to the bias voltage measured in the same conditions with a Si or SiO_2 carrier wafer during the Bosch etching tests (respectively 135 V and 35 V obtained with a bias power of 15 W), it can be observed that they are not in accordance. Indeed, the bias voltage measured by the ICP tool at 15 W bias power with the RFEA probe is 63.2 V. For this particular RFEA acquisition, the average ion energy measured during the acquisition was 59.9 eV. However, by looking more carefully at the IEDF obtained with these process parameters, the real value of the average ion energy for this acquisition seems to lie between 65 and 70 eV.

Figure III.17: Ion energy distribution functions in relation to the bias power obtained during RFEA characterization of the SF_6 etching step

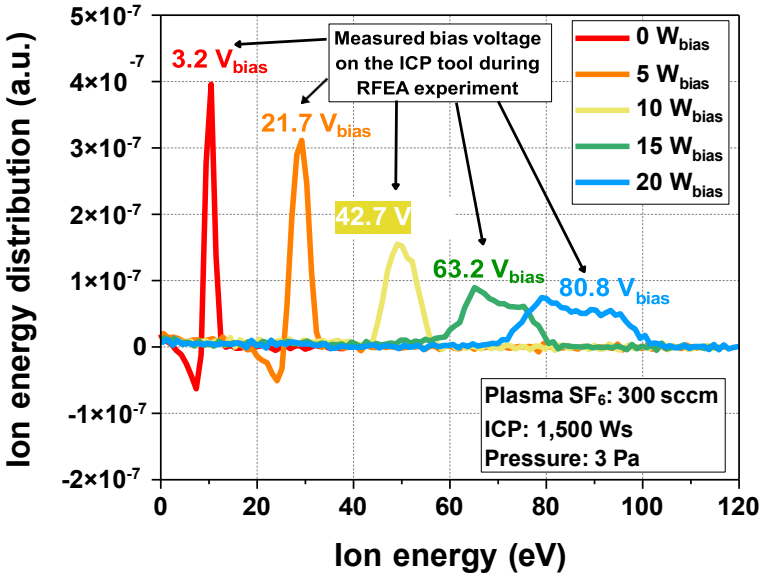

The different bias voltages observed when applying the same bias power of 15 W during these tests are due to the conductivity difference between the RFEA probe, the Si carrier wafer and the SiO_2 carrier wafer. Given the fact that the bias voltage measurement on the ICP tool is altered due to the insulating nature of the SiO_2 surface layer, the value of 135 V obtained with a Si carrier wafer at

15 W is more reliable for the estimation of the true IEDF that is involved concerning the results of the etching tests all presented above. Indeed, the etching occurs on a SF_6 coupon sample (**Chapter II** / Samples) which consists of silicon covered with a 1.2 µm SiO_2 hardmask. The coupon sample is glued to a SiO_2 carrier wafer which does not allow an accurate measurement of the bias voltage during the experiments.

However, the maximal bias voltage measured with the RFEA probe during the acquisitions in the same process conditions was equal to 80.8 V using a bias power of 20 W. It can be observed that at this point, the IEDF is already very broad with ion energies comprised between 70 eV to just above 100 eV compared to the IEDFs obtained with lower bias powers. Therefore, it can be assumed that the adequate IEDF which is representative of the bias voltage measurement of 135 V using a Si carrier wafer in the same etching conditions (SF_6 flow rate: 300 sccm ; Pressure: 3.0 Pa ; Bias power: 15 W) should be even broader with ion energies probably extending from at least 120 eV to 160 eV following a uniform distribution.

3.3.4 Capacitive probe analysis of the SF_6 etching step during Bosch processing

The capacitive probe characterization of the SF_6 etching step was realized by applying the same plasma parameters (**Table III.1**) without any sample on the substrate holder. Three independent acquisitions with the Impedans Plato probe (**Chapter II** / Capacitive probe characterization) were taken at a vertical height of 1.25 cm from the substrate holder where the clamping crown was removed. The acquisitions were launched once the plasma processes were stabilized with minimal reflected power. The bias voltage measured by the ICP tool was noted for every acquisition where a value of 77.7 V was found whereas a bias voltage of roughly 135 V is found with a clamped 4'' Si wafer in the same conditions. The corrected I-V characteristics of these acquisitions are shown in **figure III.18** between 30 V and 60 V. An averaged value of the electronic temperature (4.64 eV), ion density (1.73 x10^{16} m^{-3}) and ion flux (5.09 $A.m^{-2}$) for this particular process step were determined and are listed in **table III.3**. It must be noted that for these specific capacitive probe measurements, the main ion mass which was considered was the one of SF_5^+ (127 a.m.u).

Table III.3: Plasma parameters obtained from the (I-V) characteristics acquired during capacitive probe characterization of the SF_6 plasma etching step

Acquisition Reference	Electronic Temperature (eV)	Ion Flux ($A.m^{-2}$)	Ion Density (m^{-3})	Measured Bias Voltage (V)
Test 1	4.64	5.08	1.72 x 10^{16}	77.5
Test 2	4.63	5.11	1.74 x 10^{16}	77.7
Test 3	4.65	5.08	1.73 x 10^{16}	78.0
Average	4.64	5.09	1.73 x 10^{16}	77.7

Figure III.18: Current-voltage (I-V) characteristics between 30V and 60V obtained through capacitive probe acquisitions of the SF_6 plasma etching step

Process parameters: SF_6 flow rate: 300 sccm (Source injection) ; Pressure: 3.0 Pa ;
ICP Source power: 1,500 W ; Bias power: 15 W

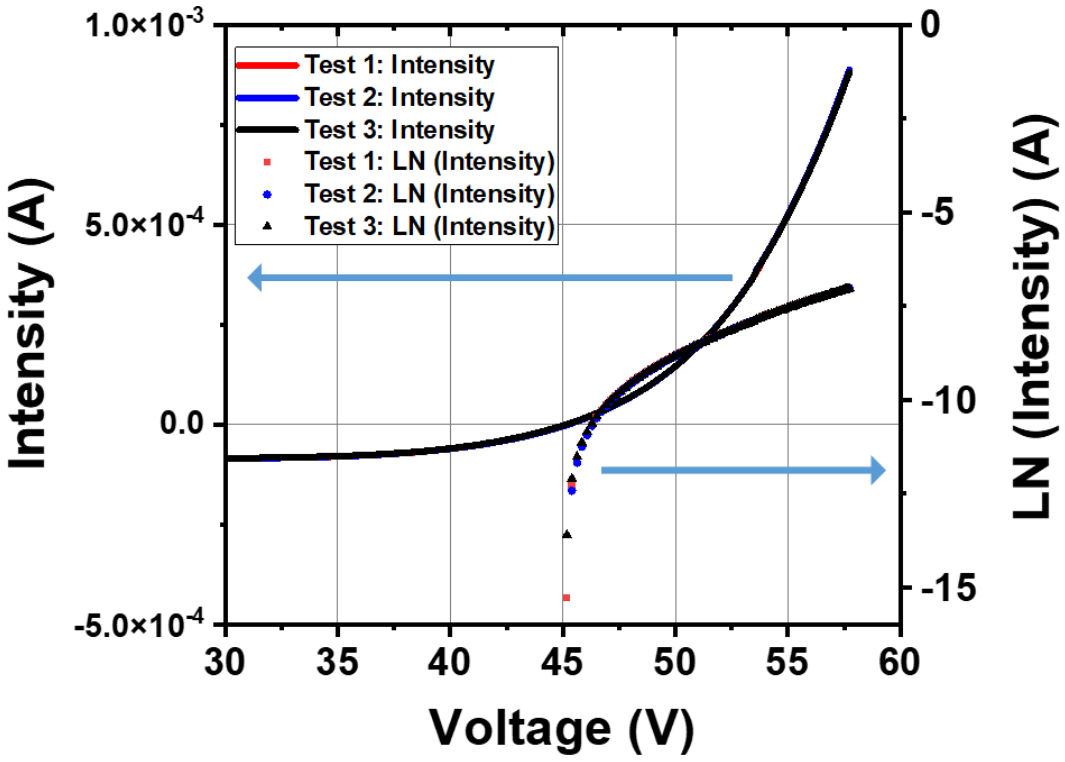

3.3.5 Summary of chapter III (English)

In this chapter, the traditional Bosch process using c-C_4F_8 as a passivation gas and normally performed in the ambient temperature range was studied at a substrate temperature of -100°C. To do so, a set of process parameters were tested using mainly 3 different configurations (A, B and C) at ambient temperature (+20°C) and at cryogenic temperature (-100°C) with variable C_4F_8 passivating gas-flows. A fourth configuration (D) was briefly explored but not extensively studied because it did not enable to produce satisfactory etch profiles due to the low pressure it generated during the passivation steps. The main goal was to evaluate whether the C_4F_8 gas supply could be reduced at cryogenic temperature while maintaining anisotropic profiles compared to ambient temperature processing. The second objective was to evaluate whether the gas injection channel (source or gas-ring inlets) has an influence on the passivation efficiency of C_4F_8 during Bosch processing. It was shown through these process tests that the Bosch process is effectively temperature dependent and that the necessary C_4F_8 passivating gas flow can be reduced to obtain similar anisotropic profiles at -100°C compared to the ambient temperature process. This tendency was observed for all three process configurations that were extensively tested (A, B and C). For example, using configuration A, a fluorocarbon gas-ring injection of 8 sccm is necessary to achieve an anisotropic etch profile at -100°C with an etch rate of 4.4 µm/min. However, the etch profile obtained at +20°C using the same process parameters presents lateral etching features with a reduced etch rate of 2.4 µm/min. Only the increase of the C_4F_8 flow up to 12 sccm in the same conditions allows to retrieve an anisotropic profile at ambient temperature with an etch rate of 4.0 µm/min.

It was globally observed that cryogenic Bosch (cryo-Bosch) processing is more sensitive when it comes to C_4F_8 dosing to achieve anisotropic etching. The slight modification of the gas-flow results in the equilibrium loss between SF_6 etching steps and C_4F_8 passivating steps leads to either over-passivation or isotropic etching. Cryo-Bosch etching also results in a slight increase of the etch rate in order to obtain similar anisotropic profiles. Silicon to silicon oxide (Si:SiO_2) etching selectivity increases significantly at -100°C with a gain of 29% to 94% depending on the process configurations that were tested. However, the aspect-ratio dependent etching (ARDE) phenomenon is more important at lower substrate temperatures. Scalloping marks on the near surface are also more pronounced for the profiles obtained at -100°C in comparison with the profiles obtained at +20°C where the sidewalls are smooth. Concerning the impact of the C_4F_8 gas injection channel (source or gas-ring inlets), several differences in the etch profiles were observed between configurations A and B. It was observed that C_4F_8 source injections are slightly more efficient to passivate the trench sidewalls using this exact set of process parameters. Nevertheless, none of the configurations A, B or C clearly stand out as the best for Bosch processing as they can all be optimized. Subsequently, the SF_6 plasma etching step which was used for these Bosch process experiments was characterized through RFEA and capacitive probe (Plato™ probe) acquisitions to estimate, among other properties, the ion energy distribution function and the ion flux near the wafer surface area.

3.3.6 Résumé du chapitre III (français) :

Ce chapitre a porté sur l'étude du procédé Bosch utilisant le C_4F_8 comme gaz de passivation à une température de -100°C alors que celui-ci est habituellement réalisé à une température minimale de 20°C. Pour ce faire, des essais de gravure ont été réalisés avec un même procédé où seul le flux de C_4F_8 a été varié à température ambiante et à -100°C sous 3 différentes configurations (A, B et C). Une 4ème configuration (D) a aussi été brièvement testée mais n'a pas été approfondie. Le but principal de ces essais était d'évaluer si le flux de C_4F_8 nécessaire à l'obtention de profils de gravure anisotropes peut être réduit à température cryogénique en utilisant le procédé Bosch. L'objectif secondaire était d'évaluer en fonction des configurations testées si l'injection de C_4F_8 nécessaire à la passivation était plus efficace lorsqu'il était injecté au niveau de la source ou bien au niveau du gas-ring. L'analyse des profils de gravure obtenus dans ces conditions ont permis de démontrer que le procédé Bosch est bien dépendant de la température du porte-substrat. La réalisation de ce procédé à température cryogénique (-100°C) permet de réduire le flux de gaz de passivation en C_4F_8 nécessaire à l'obtention de gravures anisotropes similaires à ceux qui sont obtenus à température ambiante (+20°C). Cela a été démontré pour toutes les configurations testées (A, B et C). Par exemple, pour la configuration A, un flux de C_4F_8 de 8 sccm est nécessaire pour obtenir un profil de gravure anisotrope à -100°C avec une vitesse de gravure de 4,4 µm/min. Le profil obtenu avec le même procédé à +20°C présente une importante gravure latérale avec une vitesse de gravure réduite à 2,4 µm/min. En conséquence, il est nécessaire d'augmenter le flux de C_4F_8 à 12 sccm pour obtenir un profil de gravure anisotrope similaire avec une vitesse de gravure de 4,0 µm/min.

D'une manière générale, il a été observé que la réalisation du procédé Bosch à température cryogénique (cryo-Bosch) réduit la marge de manœuvre concernant le dosage de C_4F_8 qui devient plus sensible. La gravure cryo-Bosch permet une vitesse de gravure légèrement plus élevée qu'à température ambiante pour la réalisation de profils anisotropes similaires. La sélectivité de gravure $Si:SiO_2$ est nettement plus importante avec une augmentation de 29% à 94% en fonction des configurations testées. En revanche, la présence du défaut de scalloping est plus marquée en surface pour les profils obtenus à -100°C par rapport à ceux obtenus à +20°C dans ces conditions de gravure. Le phénomène ARDE (aspect-ratio dependent etching) qui se caractérise par une gravure plus profonde pour les profils les plus larges est aussi plus important à température cryogénique. En ce qui concerne la voie d'injection pour le gaz de passivation C_4F_8, plusieurs différences ont été observés au niveau des profils de gravure obtenus avec les configurations A (gas-ring) et B (source). La passivation semble légèrement plus efficace lorsque le C_4F_8 est injecté en source dans ces conditions de gravure. Cependant, aucune des configurations testées (A, B et C) ne se détache comme étant la meilleure pour la réalisation du procédé Bosch car elles peuvent toutes être optimisées de manières différentes. Par la suite, des acquisitions par sonde RFEA et sonde capacitive (sonde Plato™) ont été réalisées au sein du plasma SF_6 maintenu avec les mêmes paramètres que ceux utilisés pendant les essais de procédé Bosch. Cela a permis d'estimer la fonction de distribution en énergie des ions ainsi que du flux d'ions au niveau de la surface du substrat lors de ce procédé.

4 Chapter IV: Study of c-C_4F_8 plasma passivation and adsorption at different temperatures

4.1 Introduction

Following the results obtained concerning the comparison of Bosch etching profiles using source and gas-ring C_4F_8 injections at -100°C and +20°C, it was decided to focus more precisely on the CF_x passivation layer thickness and its general properties in relation to substrate temperature. As a result, the C_4F_8 plasma passivation step was studied independently from the scope of Bosch processing. The growth of the fluorocarbon passivation layer was monitored on SiO_2 and p-Si substrates by in-situ ellipsometry. The idea was to compare the thicknesses obtained for an identical process step duration but at different substrate temperatures from +20°C to -150°C. In the same way, the impact of source and gas-ring injections of C_4F_8 on the fluorocarbon thickness layer were evaluated. To that matter, mass spectrometry acquisitions were also realized to determine whether the injection mode had any influence on the nature and concentration of fluorocarbon species in the plasma at the neighborhood of the substrate wafer. As it was mentioned in chapter II concerning the gas injection channels (**Chapter II.2: ICP etching reactor**), it is supposed that C_4F_8 should dissociate much less in the plasma when it is injected through the gas-ring inlet rather than through the source inlet. This chapter will summarize the main results that were obtained by varying process parameters on the C_4F_8 passivation step following this method. The main results disclosed in this chapter were published in the following article [254].

4.2 Analysis of c-C_4F_8 plasma passivation in relation to substrate temperature

4.2.1 Bibliography

Numerous publications have been published concerning the performance of fluorocarbon plasma processes for etching or deposition applications [167–169,243,261–266]. These include a great variety of fluorocarbon gases which can take many forms (c-C_4F_8, CF_4, C_2F_4, C_3F_6, C_4F_{10}, …). Although the thermodynamic nature of each species varies, they can be mainly subdivided depending on their fluorine-to-carbon (F/C) ratio when it comes to plasma processing [243]. Indeed, a fluorine rich gas (F/C ratio > 3) is more likely to etch a silicon surface due to the etching power of fluorine whereas a carbon rich gas (F/C ratio < 3) is more likely to polymerize on it independently of other process parameters at low bias conditions. By increasing the bias voltage, a fluorocarbon plasma process can switch from a polymerization regime to an etching regime due to the higher energy of fluorocarbon ion species. If it is

still insufficient, the addition of oxygen in the plasma mixture can contribute towards the accomplishment of an etching regime due to the oxidation of carbonated species which will inhibit polymerization. On the contrary, the addition of hydrogen to the plasma mixture will contribute to the achievement of a deposition regime as it will react with fluorinated species and therefore set back their etching potential. Within the scope of this research project and given the results obtained in the previous section, it is strongly believed that the decrease of the substrate temperature down to -100°C and further may considerably shift the etching-to-passivation equilibrium curve shown by *Coburn et al* towards higher (F/C) ratios [243]. All the properties concerning fluorocarbon plasma processing mentioned above are resumed in **figure IV.1 (**taken and adapted from [243]).

Figure IV.1: Evolution of the polymerization / etching regime boundary according to the F/C gas ratio and applied bias voltage during a fluorocarbon plasma process (taken and adapted from [243])

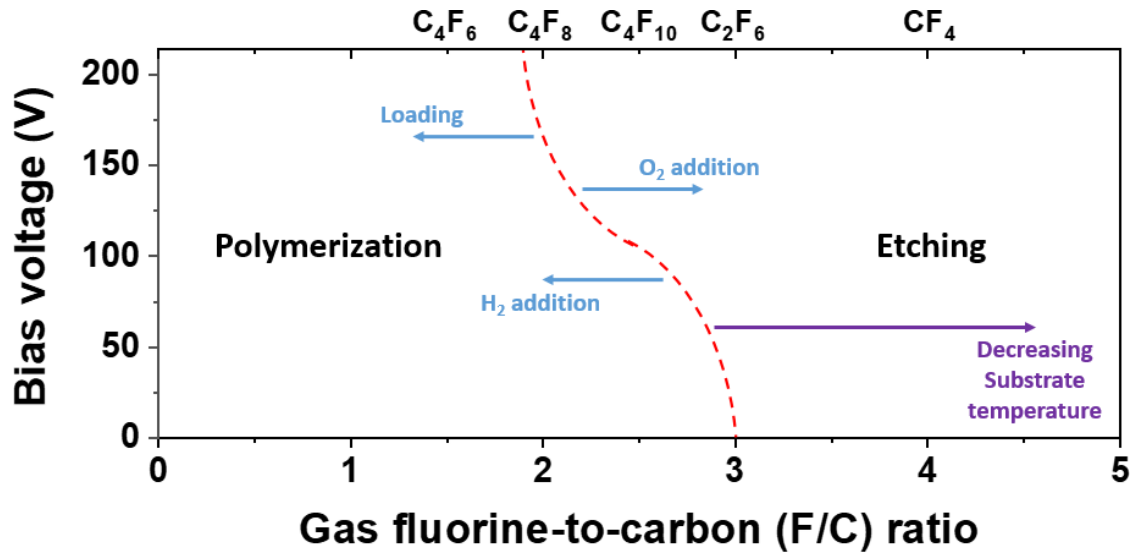

For etching applications, fluorocarbon plasmas are used especially for SiO_2 etching where high etch selectivities over Si_3N_4 and Si are needed [261,262,267]. During the process, a fluorocarbon interface layer is formed on the silicon substrate surface where the etching will depend on the layer thickness, fluorine content as well as the application of a sufficient bias power. A minimal bias power is also necessary to achieve SiO_2 etching with C_4F_8/Ar plasmas [268]. For thin etching of porous organosilicate glass, a cryogenic SF_6/C_4F_8 plasma process was developed by *Leroy et al* [180] at -120°C. In comparison with pure SF_6 plasma cryoetching, the addition of C_4F_8 to the plasma mixture allows to reduce plasma induced damage on the etched organosilicate glass layer.

Concerning the performance of C_4F_8 plasmas for deposition applications, several studies have been carried out to understand the impact of process parameters on the fluorocarbon passivation layer during Bosch processing. In their design of experiment using an ICP reactor, *Labelle et al* [269] showed that the fluorocarbon deposition rate is maximal at low pressure (1.33 Pa) and is reduced by roughly 25% once the chamber pressure is increased to 2.66 Pa using their processing conditions. It was argued that

higher pressures lead to higher concentrations of deposition species yet this phenomenon is countered more importantly by the decrease of the electron temperature which reduces the dissociation of C_4F_8 into smaller species that are likely deposited. It was also demonstrated that the deposition rate increases importantly with a higher source power due to the higher dissociation of C_4F_8 into smaller fluorocarbon species that are more likely to polymerize on the surface. It was also stated that the increase of C_4F_8 gas flow (from 60 to 110 sccm) or bias power (from 0 to 10 W) did not have a significant influence on the deposition rate. However, they observed that the increase of substrate temperature which was tested at +15°C, +25°C and +40°C decreases the deposition rate which they explained as a result of higher desorption rates concerning the deposited species. Moreover, it was argued that the temperature, the chamber pressure and the source power are not independent parameters as the decrease of substrate temperature will emphasize the effects of the two latter parameters.

Concerning the F/C ratio and the chemical content of the deposited fluorocarbon layer, it was shown that only the source power and chamber pressure have a significant yet opposite impact. Most of the deposited fluorocarbon layers had a F/C ratio ranging from 1.35 to 1.60 with a refractive index which varied between 1.365 and 1.385. However, fluorocarbon layers deposited at low source power coupled with high pressure conditions resulted in a lower F/C ratio (from 1.20 to 1.28) with a higher refractive index (from 1.40 to 1.42) despite leading in general to lower deposition rates. A graph illustrating the properties of the deposited fluorocarbon layers obtained with different input parameters during the C_4F_8 passivation step is shown in **figure IV.2** (taken from [269]).

Figure IV.2: Deposition rates and F/C ratios obtained for various deposited fluorocarbon layers using different input parameters during the C_4F_8 plasma passivation step (taken from [269])

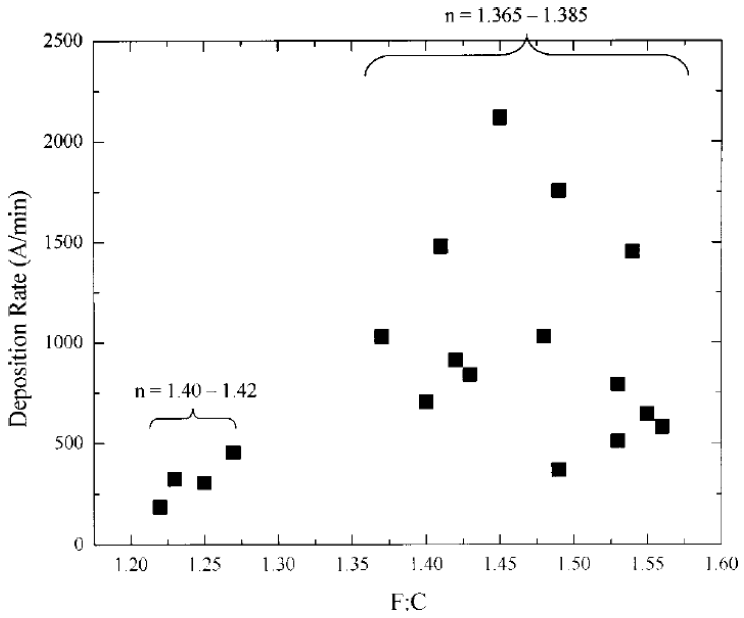

For further understanding, optical emission spectroscopy acquisitions were realized during the deposition processes and subsequent XPS acquisitions of the deposited layers after processing were realized. It was found that the coupling of low source power and high pressure results in a higher concentration of CF_2 species in the plasma yet a lower presence of CF_2 in the deposited layer which

had higher contents of other complex species (CF, CF_3 and C-$(CF_x)_y$). For all the other conditions that were tested, the exact opposite observation prevailed. The deposited layer was dominated by the presence of CF_2 species whereas the plasma presented higher contents of other fluorocarbon species (CF, CF_3 and C_2). It is argued by analyzing these observations that CF_2 has a much lower sticking coefficient than the other fluorocarbonated species mentioned previously. This characteristic is also specified in other publications [249,270–272].

Moreover, it was shown that the fluorocarbon layer deposited at low source power and high-pressure conditions was slightly more resistant to subsequent SF_6 plasma etching with a reduction of the etch rate close to 25% in comparison with CF_x layers deposited under other conditions. This increased resistivity is imputed to the relatively higher carbon content (lower F/C ratio). However, the considerably lower deposition rates that are generally associated to these particular poorly fluorinated CF_x layers counters this effect when it is applied in the consideration of an industrial Bosch process. Indeed, in this case, a high (SF_6 plasma resistivity / deposition rate) ratio is targeted for the optimization of the fluorocarbon passivation step.

In a previous study using a helicon-wave high-density plasma reactor, *Endo et al* [273] demonstrated that the increase of C_4F_8 flow rate and the resulting pressure have an influence on the F/C ratio of the PECVD deposited CF_x layer. In their experiment where the Si substrate was heated at +100°C, they showed through actinometry that the evolution of the radical densities of CF_2 and F in function of the C_4F_8 flow rate followed opposite behaviors. Indeed, CF_2 radical density tended to increase with increasing C_4F_8 flow rate (higher pressures) whereas F radical density tended to decrease. Through XPS analysis, they observed that the fluorocarbon films deposited at low C_4F_8 flow rates (low pressure) had a lower F/C ratio content. As a result, a slight decrease of the refractive index and dielectric constant was observed concerning the CF_x layers deposited with higher C_4F_8 flow rates. Consecutively, it was shown that the fluorocarbon layers which had a slightly lower F/C ratio content (deposited at low flow rate/ low pressure conditions) were considerably more thermal resistive. Although these results are mostly in opposition with *Labelle et al* [269], the F/C ratios obtained in these experimental PECVD conditions (ranging from 0.53 to 0.73) are radically different from those obtained using an ICP reactor (ranging from 1.20 to 1.60). It suggests that fluorocarbon dissociation mechanisms are completely different according to the plasma reactor type.

More recently, C_4F_8 has been used at low substrate temperatures concerning the cryo-ALE of SiO_2 [274,275]. It is simply injected in gas phase in the reactor where it physisorbs at the wafer surface without any plasma discharge (**Chapter I / Cryo-ALE**). In conformity with the equilibrium vapor pressure equation of C_4F_8, it was found that the substrate temperature as well as the chamber pressure have a crucial role concerning its physisorption, residence time and consequently its sticking coefficient. As a result, by fixing the adequate process parameters, the self-limiting nature of the cryo-ALE process was revealed at a temperature threshold of -120°C using a pressure of 3.0 Pa for the physisorption step. Although this particular study does not apply towards the optimization of a C_4F_8 plasma passivation step in a Bosch process, it is important to note that adsorption mechanisms may considerably influence a C_4F_8 plasma deposition step if it is performed near equilibrium vapor pressure conditions.

Concerning the desorption of CF_x layers deposited on Si and SiO_2, *Miyakawa et al* [276] studied the different species that preferentially desorb from each substrate through thermal desorption spectroscopy (TDS) coupled with mass spectrometry. The chemical content evolution of the remaining fluorocarbon layer deposited through a magneto-microwave C_4F_8 plasma process and then heated from +20°C to +800°C was monitored through temperature-programmed XPS (TP-XPS). The results obtained show that SiF_4 (SiF_3^+ ion) is the primary product which thermally desorbs from a CF_x layer deposited on a Si substrate. CF_4 (CF_3^+ ion) and CF_2 (CF_2^+ ion) are respectively the second and third desorption species monitored in order of intensity. Further analysis of the pyrograms obtained show that it is actually F species which contribute more than CF_2 and F_2 species inside the CF_x layer towards the reaction with the Si substrate and the formation of SiF_4. Concerning the products which desorb from a CF_x layer deposited on a SiO_2 substrate, the results obtained show that it is mainly CO (CO^+ and CO_2^+ ions) as well as SiF_4 (SiF_3^+ ion), CF_4 (CF_3^+ ion) and CF_2 (CF_2^+ ion) are also monitored at significantly lower intensities. Further analysis of the pyrograms also show that is available F species which are mainly responsible for the formation of SiF_4 desorption products more than CF_2 and F_2 whereas the formation of CO desorption products is mainly due to CF_2 which participate in the bond formation between C and O. The TP-XPS study of the remaining CF_x layer shows that its F/C ratio decreases drastically from approximately 1.6 to 0 as the temperature is increased from +20°C to +700°C. By analyzing the evolution of the C_{1s} XPS spectra components which were identified to be CF_3, CF_2, CF and C-CF_x ($x= 0 \leq x \leq 3$). Five thermal desorption regimes were identified as the substrate temperature was increased. The results obtained in this temperature range, from +20°C to +800°C, suggest that fluorocarbon desorption and subsequent desorption mechanisms may also be different for a Si and SiO_2 substrate in the cryogenic temperature range, from -150°C to ambient temperature.

Concerning the numerical simulation of fluorocarbon plasma processes, numerous models have been developed for the study of different applications such as deposition processes including the study of the C_4F_8 plasma passivation step [277–279] but also etching processes [280–285] Several models have also been developed towards the simulation of the Bosch process [286–290] yet no extensive data was found concerning the influence of substrate temperature or cryogenic processing.

Overall, by synthesizing the principal observations concerning fluorocarbon plasma processing and its passivation effects through bibliographic research [167,169,243], it can be noted that the gas nature (F/C ratio) and the bias voltage applied during fluorocarbon plasma processing are the two key parameters towards achieving a deposition or etching regime. In the case of a deposition regime, which is wanted in Bosch processing, C_4F_8 is much more likely to deposit at ambient temperature on a Si surface in comparison to CF_4 which explains the predominance of this particular gas for the passivation step. When it comes to the optimization of a fluorocarbon passivation process, the chamber pressure and source power are important parameters that can enable to influence slightly the fluorine content and the deposition rate of the CF_x layer. However, there is no exhaustive data concerning the impact of substrate temperature on the deposition properties of fluorocarbon. Therefore, it was decided to study the influence of this particular parameter on the fluorocarbon passivation step independently from a Bosch process.

4.2.2 Parametric study of the C_4F_8 passivation step in relation to temperature

An exhaustive parametric study of the C_4F_8 passivation step was realized where the influence of the C_4F_8 flow rate was first evaluated from 2 to 12 sccm for source injections at a substrate temperature of -100°C and +20°C on thin p-Si and SiO_2 blanket samples (**Chapter II / Samples**). Secondly the impact of substrate temperature was studied from 20°C down to -150°C on SiO_2 substrates where C_4F_8 gas was either injected through the source inlet or through the gas-ring inlet. For these first tests, it was decided not to apply any bias power to limit any form of etching from eventual fluorocarbon ions and mainly focus on the thickness of these deposited fluorocarbon layers. The impact of the bias power was subsequently studied on the fluorocarbon passivation layer from 0 W to 30 W at -100°C and +20°C using C_4F_8 source injections.

The impact of the C_4F_8 injection channel (source inlet or gas-ring inlet) was also studied more precisely. These tests were done to verify if the slight differences observed previously during the cryo-Bosch etching tests, especially between configurations A and B, could be explained from a difference in the deposition rates between these two injection modes during C_4F_8 plasma steps. Finally, it was decided to study the SF_6 plasma etching rate of thick fluorocarbon passivation layers previously deposited at -100°C either through a C_4F_8 source injection or through a gas-ring injection on p-Si and SiO_2 samples.

As a result, C_4F_8 plasma process tests were done using the same set of parameters used previously during the Bosch tests. However, a process duration of thirty seconds was fixed for each process test in order to achieve relatively thick fluorocarbon layers and to compare them with each other. The process parameters used for this parametric study are listed in **table IV.1**. The C_4F_8 plasma step was achieved by first igniting a short Ar plasma.

Table IV.1: Experimental conditions used for C_4F_8 plasma deposition tests

Parameters	C_4F_8 plasma deposition tests
Gas	C_4F_8
Flow rate (sccm)	Variable flows tested (2 to 12 sccm)
Gas injection mode	Source or Gas-ring
Plasma step time (s)	30 s
Pressure (Pa)	2.0 Pa
Source Power (W)	1,500 W
Bias Power (W)	0 W / 5 W / 15 W / 30 W
Temperature (°C)	+20°C / -40°C / -80°C / -100°C / -120°C / -150°C
Thermalization time	(30 s / 5 min) respectively for tests at (20°C / < 20°C)

4.2.2.1 Influence of C_4F_8 flow rate at +20°C and -100°C

The impact of C_4F_8 gas flow rate was first evaluated on p-Si and SiO_2 substrates at -100°C and +20°C using the source gas inlet to reproduce the fluorocarbon deposition conditions encountered in configuration B. The results obtained by in-situ ellipsometry are presented in **figure IV.3** and **table IV.2** which illustrate and list the measured CF_x thicknesses for different C_4F_8 passivating gas flows at +20°C

and -100°C. These tests were acquired on both p-Si and SiO_2 coupon samples that were glued on 100mm SiO_2 carrier wafers in order to facilitate ellipsometry modeling.

Figure IV.3: CF_x passivation layer thickness in relation to the C_4F_8 source gas-flow during C_4F_8 plasma deposition tests at +20°C and -100°C on p-Si and SiO_2 substrates

Process parameters: Variable C_4F_8 flow rate (Source injection channel); Pressure: 2.0 Pa; Source power: 1500 W; No bias power ; Step time: 30 s

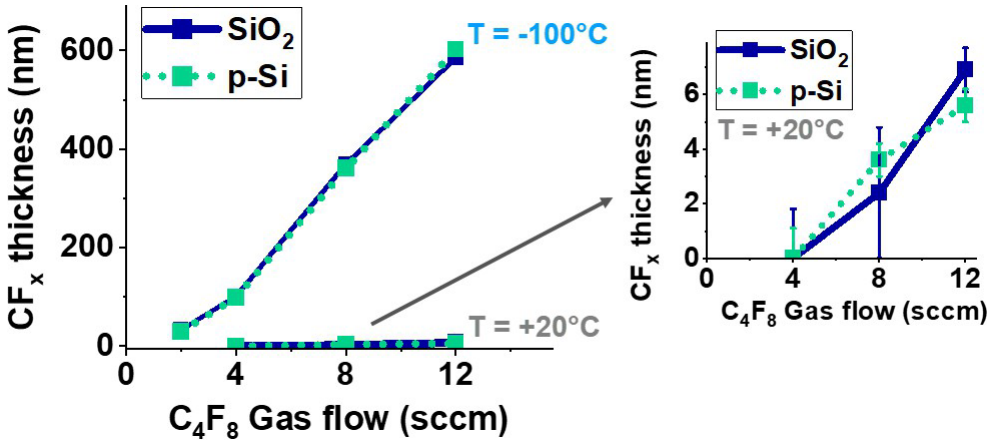

Table IV.2: CF_x passivation layer thicknesses and associated uncertainties determined by in-situ ellipsometry in relation to the C_4F_8 gas flow injected through the source inlet during C_4F_8 plasma deposition tests at +20°C and -100°C on p-Si and SiO_2 samples

Substrate Temperature (°C)	C_4F_8 flow rate (sccm)	CF_x layer thickness after plasma process on a p-Si substrate	CF_x layer thickness after plasma process on a SiO_2 substrate
-100°C	2 sccm	29.8 ± 1 nm	33.4 ± 0.4 nm
	4 sccm	99.0 ± 0.9 nm	101.3 ± 0.4 nm
	8 sccm	360.8 ± 9.9 nm	370.1 ± 4.0 nm
	12 sccm	602.1 ± 13.2 nm	586.6 ± 9.3 nm
+20°C	4 sccm	0.0 ± 1.1 nm	0.0 ± 1.8 nm
	8 sccm	3.6 ± 0.6 nm	2.4 ± 2.4 nm
	12 sccm	5.6 ± 0.6 nm	6.9 ± 0.8 nm

It can be observed that there is no particular difference on the measured fluorocarbon thickness layer after the process between p-Si and SiO_2 samples both at +20°C and -100°C. At ambient temperature, the CF_x layer which is formed is very thin and difficult to measure by ellipsometry. The thicknesses obtained for C_4F_8 gas flows of 4 and 8 sccm and their respective uncertainties seem to suggest that the deposited CF_x layer is not uniform or possibly inexistant with only a slight modification of the sample surface. At 12 sccm, the deposited fluorocarbon layer is clearly identified by ellipsometry and is approximately 6 µm thick. At -100°C, the fluorocarbon deposition rate is greatly enhanced. Depending on the C_4F_8 gas flow that was introduced, the deposition rate is roughly 100 times more important than at +20°C for identical process conditions. It is important to note that the uncertainty values given by the ellipsometry model fittings and associated to the thick CF_x layer thicknesses in **table IV.2** are generally very low to be considered as accurate.

In both cases, the thickness of the deposited fluorocarbon layer and the gas flow rate seem to be correlated, yet an offset for low passivating gas flow injections is observed. It can be supposed that fluorocarbon deposition conditions are not fully met when the gas flow is very low until achieving a threshold value which enables a stable deposition regime where the relation is quasi-linear. As a result. the SiO_2 samples which underwent the 12 sccm C_4F_8 source plasma deposition processes at +20°C and -100°C were analyzed by SEM and are shown in **figure IV.4**. Both samples were coated with a standard 4 nm platinum layer for a better observation of the deposited fluorocarbon layer. The observation of these two samples is in accordance with the thickness values determined via in-situ ellipsometry.

Figure IV.4: Fluorocarbon deposited layer profiles obtained after a C_4F_8 plasma process (2 Pa ; 12 sccm ; 30 s) at -100°C and +20°C observed by SEM on a SiO_2 blanket sample

Process parameters: Variable C_4F_8 flow rate (Source injection channel); Pressure: 2.0 Pa; Source power: 1500 W; No bias power ; Step time: 30 s

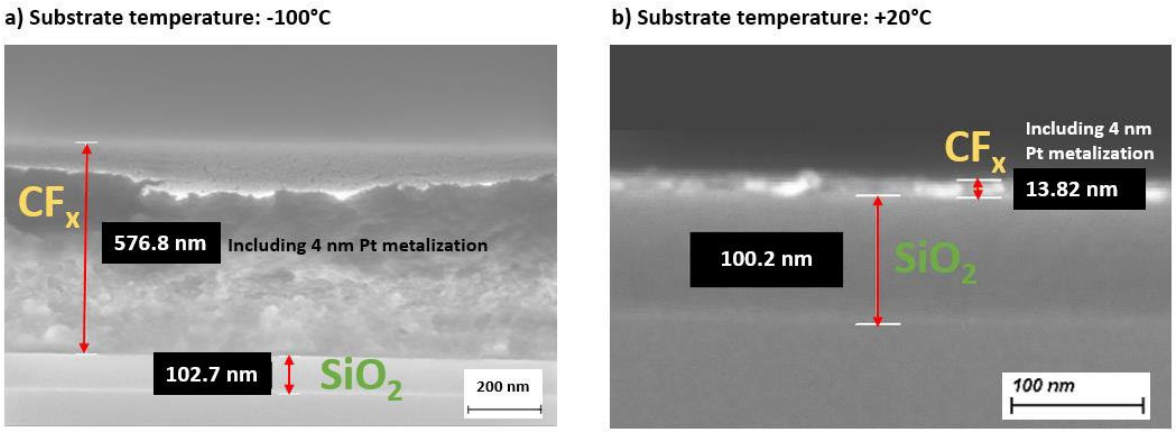

The measured fluorocarbon layer thickness for the SiO_2 sample which underwent the C_4F_8 plasma deposition process at -100°C was equal to 576.8 nm including the platinum metallization layer. For this sample, the CF_x layer thickness determined by ellipsometry modeling was equal to 587.4 nm. In comparison, the sample processed at +20°C was measured with a 13.8 nm CF_x layer thickness including the platinum metallization layer. For this sample, the CF_x layer thickness determined by ellipsometry modeling was equal to 5.8 nm. The CF_x layer of this particular sample seems to be quite inhomogeneous with the presence of sparse granular structures which seem to confirm the relatively high uncertainty values associated to the ellipsometry fitting results commented previously for C_4F_8 plasma deposition tests performed at +20°C. It must be noted that these particular samples were observed several days after the deposition process tests which testifies to the resistance of the fluorocarbon passivation layer obtained at cryogenic temperatures to atmospheric conditions re-exposure after the deposition process.

4.2.2.2 Influence of substrate temperature on fluorocarbon deposition

Consecutively, C_4F_8 plasma deposition was characterized at intermediate and more extreme cryogenic substrate temperatures either by injecting the C_4F_8 gas flow through the source or through the gas-ring. A fixed C_4F_8 flow rate of 12 sccm was chosen as it was observed that it corresponded to the minimal gas feed value where a distinctive fluorocarbon passivation layer could be determined at +20°C through in-situ ellipsometry in these process conditions. These tests were carried out only on SiO_2 substrates judging by the results obtained previously where no particular fluorocarbon thickness difference was observed between p-Si and SiO_2 substrates and to facilitate ellipsometry fitting. The ellipsometry fitting results obtained with these specific process tests are plotted in **figure IV.5**.

Figure IV.5: CF_x passivation layer thickness and refractive index in relation to the substrate temperature for C_4F_8 source or gas-ring injections during C_4F_8 plasma deposition tests on SiO_2 substrates

Process parameters: C_4F_8 flow rate: 12 sccm (Source or gas-ring injection channel) ; Pressure: 2.0 Pa ; Source power: 1500 W ; No bias power ; Step time: 30 s

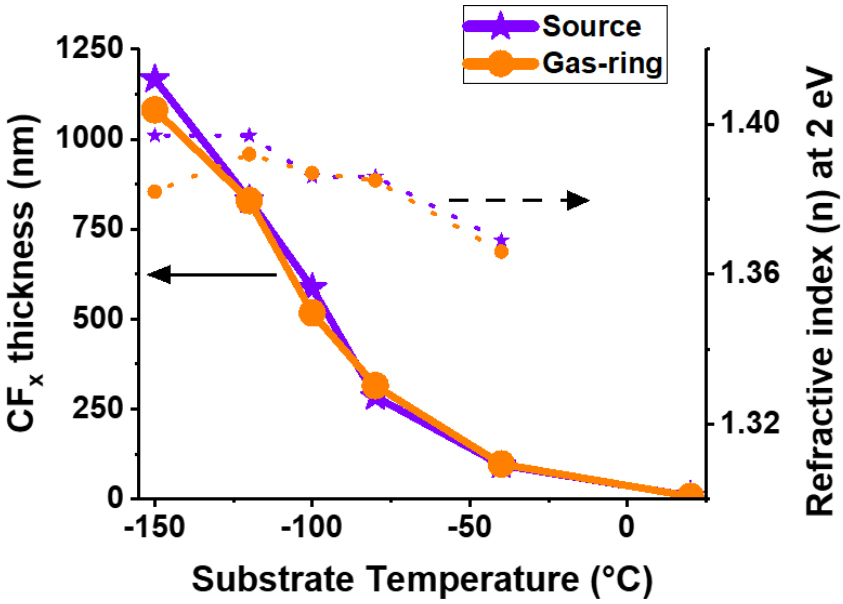

It can be observed that the C_4F_8 injection mode does not seem to have a significant influence on the fluorocarbon deposition rates. It can be seen that the fluorocarbon deposition rate is not linear in relation to the substrate temperature. It is quite low at +20°C at around 4 nm/min and then increases considerably as the substrate temperature is reduced to -100°C where it is superior to 1.0 µm/min. At -150°C, the fluorocarbon deposition rate reaches approximately 2.2 µm/min. Additionally, it can be seen that at very low temperatures, the CF_x layer thicknesses obtained with C_4F_8 source injections seem to be a bit more important compared to C_4F_8 gas-ring injections.

Concerning the ellipsometry modeling of the deposited fluorocarbon layers, the results obtained suggest that the refractive index (n) of the deposited CF_x layer slightly increases with decreasing substrate temperatures. The refractive indices of the fluorocarbon passivated layers obtained between -40°C and -100°C are nearly identical for both gas injection channels. However, below -120°C, the refractive index decreases in the case of gas-ring injections whereas it is stable for source injections. At -150°C, the refractive index of the CF_x layer at 2.0 eV is estimated at 1.397 for a source inlet C_4F_8 injection and 1.382 for a gas-ring injection. In comparison, the refractive indices of the deposited fluorocarbon layers evaluated at 2.0 eV are respectively equal to 1.292 and 1.185 at +20°C although the thicknesses obtained are too low and probably too inhomogeneous to take these values into consideration.

The process repeatability associated to the C_4F_8 deposition tests was evaluated three times each at -100°C in the case of source inlet and gas-ring injections. In the case of C_4F_8 source injections, the average CF_x layer thickness obtained was equal to 574.1 nm with a corrected sample standard deviation of 19.1 nm. The average refractive index associated to these CF_x passivation layers was 1.386 with a corrected sample standard deviation of 6.0×10^{-4}. Concerning C_4F_8 gas-ring injections, the average CF_x layer thickness obtained was equal to 523.1 nm with a corrected sample standard deviation of 8.1 nm. The average refractive index associated to these CF_x passivation layers was 1.386 with a corrected sample standard deviation of 2.0×10^{-3}. It can be noted that for each test, the deposited CF_x layers are slightly thicker for C_4F_8 gas source injections rather than gas-ring injections. This observation could explain why fluorocarbon passivation was more effective using C_4F_8 source injections during the previous cryo-Bosch etching tests.

4.2.2.3 Influence of bias power at +20°C and -100°C

Subsequently, the impact of bias power on the fluorocarbon deposition rate was evaluated at a substrate temperature of +20°C and -100°C on SiO_2 samples. Again, a fixed C_4F_8 gas flow rate of 12 sccm through the source inlet was chosen given the results obtained previously where a shallow fluorocarbon layer was obtained +20°C with a minimal flow of 12 sccm using no bias power. The process results obtained for this specific study are plotted in **figure IV.6**.

At ambient temperature, it was observed that the simple application of a bias power, in this case 5 W, is sufficient to switch from a fluorocarbon deposition regime to a SiO_2 etching regime. Using a bias power of 15 W, a SiO_2 etch rate of roughly 1.2 nm/s is observed. Although this result may sound surprising, given the anisotropic Bosch profiles obtained previously using a 15 W bias power during the passivation steps, it is important to note that these pulsed steps had a duration of two seconds. In comparison, the steady C_4F_8 passivation tests had a duration of 30 seconds in this case. Moreover, the passivation conditions which are studied in this experiment are more representative of what actually happens at the bottom of the etch trench rather than on the sidewalls. Indeed, the trench sidewalls are less exposed to ion bombardment where fluorocarbon passivation conditions are similar to the case where no bias power is used. Therefore, the C_4F_8 passivation step parameters used during Bosch process tests are sufficient

to passivate the trench sidewalls efficiently and should not cause further lateral etching, if ever the step duration was increased.

Figure IV.6: CF_x passivation layer thickness with associated refractive index at 2 eV or SiO_2 etch depth obtained by in-situ ellipsometry in relation to bias power after a C_4F_8 plasma deposition process at -100°C and +20°C on a SiO_2 substrate (Si substrate with a 100 nm SiO_2 thick layer)

Process parameters: C_4F_8 flow rate: 12 sccm (Source injection channel); Pressure: 2.0 Pa; Source power: 1500 W; Step time: 30 s

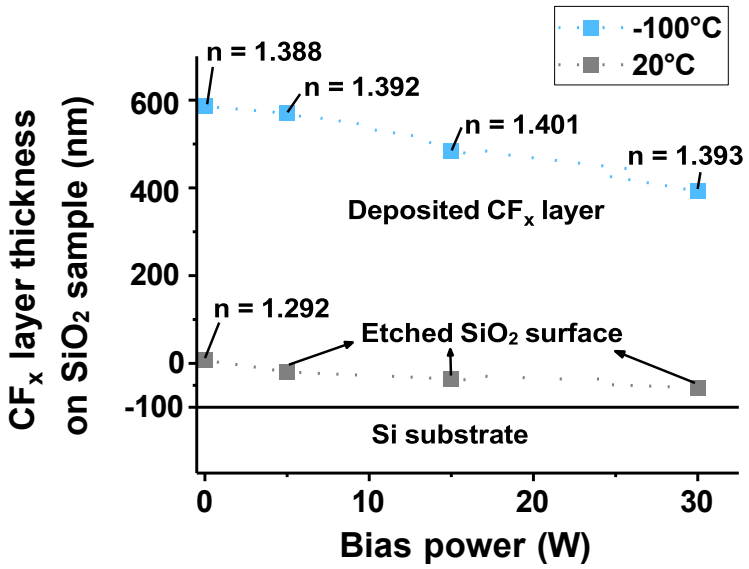

At -100°C, the increase of the bias power slightly inhibits the fluorocarbon deposition mechanism due to the fluorocarbon cations, which hit the surface with increasing energies. However, the condensation of fluorocarbon on the substrate is so significant that the process remains in a passivation regime even at higher bias powers. At 15 W, which corresponds to a bias voltage of roughly 90 V, the resulting CF_x passivation layer had a thickness of approximately 484.4 nm which is only slightly lower than the fluorocarbon layer deposited using no bias power (583.5 nm obtained after this specific test run). The analysis of the refractive indices associated to the CF_x passivation layers obtained at -100°C shows that the application of bias power does not have a significant influence on their refractive indices during the plasma deposition process.

4.2.2.4 Influence of the C_4F_8 gas injection channel

The analysis of fluorocarbon derived species contained in the plasma during passivation steps was also realized through mass spectrometry monitoring. High resolution multiple ion detection (MID) acquisitions were made during C_4F_8 deposition tests where C_4F_8 gas was injected either through the source inlet or through the gas-ring following the same conditions listed in **table IV.3** at ambient temperature with a C_4F_8 flow rate of 12 sccm and using no bias power. The ion peak intensities obtained for CF^+ (31 amu),

CF_3^+ (69 amu), $C_2F_4^+$ (100 amu) and $C_3F_5^+$ (131 amu) are plotted in **figure IV.7** where both tests are represented and synchronized in relation to time. The average intensities monitored during the acquisitions are specified and were rounded to the closest hundred.

Figure IV.7: Mass spectrometry MID acquisitions of C_4F_8 deposition plasmas realized with source passivating injection and with gas-ring passivating injection

Process parameters: C_4F_8 flow rate: 12 sccm; Pressure: 2.0 Pa; Substrate temperature: +20°C; Source power: 1500 W; No bias power; Step time: 30 s

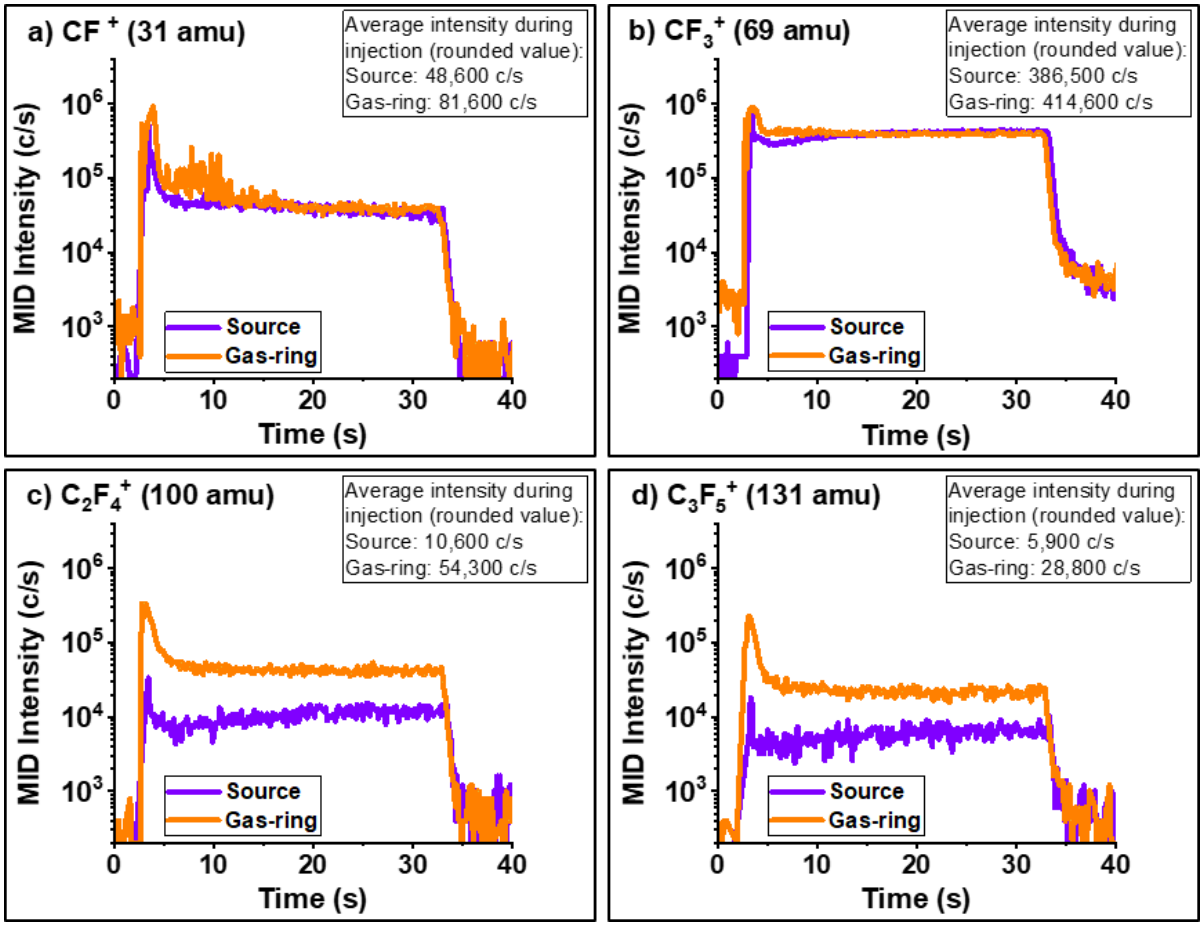

It can be observed that the four principal species derived from C_4F_8 plasma are all monitored in both source and gas-ring injection cases. In both cases, CF_3^+ and CF^+ are the main species detected by the mass spectrometer. For these ions, the rounded average intensities recorded throughout the whole process are relatively in the same range regardless of the C_4F_8 gas injection channel. For CF_3^+, an average rounded intensity of 386,500 counts per second (c/s) are measured for a source injection whereas 414,600 c/s are measured for a gas-ring injection. For CF^+, this value reached 48,600 c/s for a source injection and 81,600 c/s for a gas-ring injection.

However, the intensity monitored for $C_2F_4^+$ and $C_3F_5^+$ species varies more importantly according to the C_4F_8 gas injection channel. They are respectively third and fourth in orders of intensity predominance

for both injection modes. $C_2F_4^+$ is monitored with an intensity of roughly 54,300 counts per second and $C_3F_5^+$ at 28,800 counts per second in the case of gas-ring injections. However, they are measured with an intensity of roughly 10,600 counts/second and 5,900 counts/second respectively for source injections. Both of these relatively heavier and more carbonated species are detected approximately five times more by the mass spectrometer probe during gas-ring injections. This result is not surprising judging that the probe is situated much closer to the gas-ring than to the source gas inlet. However, it confirms the initial hypothesis which suggested that C_4F_8 dissociates less in the plasma medium when it is injected through the gas-ring rather than through the source inlet in these conditions.

To assess mass spectrometry fluorocarbon fragmentation reactions, a preliminary MID acquisition obtained in the gas phase using the same C_4F_8 source injection parameters was analyzed (Plasma Off / C_4F_8 Source injection). The main ion that is detected is also CF_3^+ with a monitored rounded average intensity of 62,000 counts per second. An intensity ratio was calculated for CF^+, $C_2F_4^+$ and $C_3F_5^+$ ions by weighting their respective intensities according to the maximal intensity monitored for CF_3^+ ion. Subsequently, intensity ratios of these ions were also calculated for the MID acquisitions presented in **figure IV.7** (Plasma On / Source injection & Plasma On / Gas-ring injection). The intensity ratios evaluated for CF^+, $C_2F_4^+$ and $C_3F_5^+$ ions for each C_4F_8 injection condition (Plasma Off / C_4F_8 Source injection ; Plasma On / Source injection & Plasma On / Gas-ring injection) are indicated in **table IV.3.** The lower intensity ratios obtained for $C_2F_4^+$ and $C_3F_5^+$ ions when the plasma is ignited in the case of source injections confirms the fact that they do not only result from fragmentation reactions occurring in the mass spectrometer. Therefore, the higher intensities monitored for these species during gas-ring injections when the plasma is ignited truly reflects a higher proportion of heavy undissociated fluorocarbon species in the reactor volume near the mass spectrometer probe.

Table IV.3: Intensity ratio of CF^+, $C_2F_4^+$ and $C_3F_5^+$ ions weighted according to CF_3^+ ion intensity during MID mass spectrometry acquisitions of a C_4F_8 gas injection process performed under different conditions (Plasma Off / C_4F_8 Source injection ; Plasma On / Source injection & Plasma On / Gas-ring injection)

Process parameters: C_4F_8 flow rate: 12 sccm; Pressure: 2.0 Pa; Substrate temperature: +20°C; Source power: 1500 W; No bias power; Step time: 30 s

Ion Species detected through MID monitoring (Intensity ratio weighted according to CF_3^+ ion)	**CF^+**	**CF_3^+**	**$C_2F_4^+$**	**$C_3F_5^+$**
Plasma Off / C_4F_8 Source injection	0.050	1	0.034	0.047
Plasma On / C_4F_8 Source injection (Source power: 1500 W; No bias power)	0.126	1	0.027	0.015
Plasma On / C_4F_8 Gas-ring injection (Source power: 1500 W; No bias power)	0.197	1	0.131	0.069

In another experiment, the thick fluorocarbon passivation layer resistance to subsequent SF_6 plasma etching was tested at -100°C using the same bias power (15 W) that was applied during the Bosch process tests. A thick fluorocarbon layer was first deposited using the same passivation step

parameters using either the source inlet or gas-ring injection channel. Consecutively, a five-minute chamber purge was maintained before the SF_6 plasma etching process. The tests were realized both on p-Si and SiO_2 sample surfaces. The results obtained are listed in **table IV.4** and demonstrate that the gas injection channel does not have a significant influence on the fluorocarbon passivation layer resistance to subsequent SF_6 plasma etching with bias power. Indeed, the etch rates obtained on these thick fluorocarbon layers are all similar at around 2.7 nm/s.

Table IV.4: CF_x passivation layer thicknesses with their associated refractive index and subsequent SF_6 plasma etching rate obtained through in-situ ellipsometry on p-Si and SiO_2 samples during C_4F_8 plasma deposition tests at -100°C using the source inlet or the gas-ring injection channels

Process parameters:
A) C_4F_8 plasma deposition step: C_4F_8 flow rate: 12 sccm; Pressure: 2.0 Pa;
Substrate temperature: -100°C; Source power: 1500 W; No bias power; Step time: 30 s

B) SF_6 plasma etching step: SF_6 flow rate: 300 sccm; Pressure: 3.0 Pa;
Substrate temperature: -100°C; Source power: 1500 W; Bias power: 15 W; Step time: 10 min

Substrate	Injection channel	CF_x deposited layer (nm)	Refractive index (n) at 2 eV	CF_x etch rate with a SF_6 plasma (nm/s)
SiO_2	Source	552.1	1.386	2.86
	Gas-ring	528.8	1.390	2.71
p-Si	Source	567.0	1.387	2.69
	Gas-ring	535.0	1.391	2.70

Therefore, it can be suggested that the higher concentration of heavily carbonated species detected in the vicinity of the substrate area during gas-ring injections do not take an important part in the deposition of the fluorocarbon passivation layer. Indeed, there are no substantial differences in the deposition rate, refractive index or subsequent etching rate in SF_6 plasma conditions concerning the deposited fluorocarbon layer in relation to the gas injection channel.

Nevertheless, it is presumed that the chemical composition of the CF_x layer might be substantially different depending on the gas injection channel, especially at the interfacial layer with the silicon substrate. Indeed, as it is shown by *Labelle et al* [269] who carried out an exhaustive parametric study of the C_4F_8 plasma passivation step, chamber pressure and source power have a significant influence on the dissociation of fluorocarbon species in the plasma. Subsequently, it was shown through XPS analysis that it significantly affected the composition of the deposited film. It is suggested that fluorocarbon plasma deposition follows a two-step mechanism where a carbon rich film is first deposited and is then gradually fluorinated by free F contained in the plasma. Therefore, the interfacial layer composition should strongly depend on the available species present in the plasma during the passivation step. In this case, it is shown in **figure IV.7** and **table IV.3** that the gas injection channel has an influence on the dissociation and concentration of fluorocarbon species near the substrate level. As a result, it should have an effect on the deposited film composition.

4.2.3 Capacitive probe analysis of the c-C_4F_8 plasma passivation process step

Using the same method described for the SF_6 plasma etching step, the capacitive probe characterization of the c-C_4F_8 passivation step was realized. Using the same process parameters listed in **table IV.1** for this step, five acquisitions were taken at a flow rate of 10 sccm (only source injections) to first evaluate process repeatability. The averaged plasma parameters determined through these acquisitions are listed in **table IV.5**. An average bias value of 22.5 V was measured by the ICP tool during these acquisitions whereas a bias voltage of approximately 90 V is found with a clamped 4'' Si wafer in roughly the same plasma conditions (C_4F_8 flow rate of 12 sccm in this case instead of 10 sccm during the capacitive probe acquisitions).

Table IV.5: Plasma parameters obtained from the (I-V) characteristics acquired during capacitive probe characterization of the c-C_4F_8 plasma passivation step

Process parameters: C_4F_8 flow rate: 10 sccm (Source injection) ; Pressure: 2.0 Pa ; ICP Source power: 1,500 W ; Bias power: 15 W

Acquisition Reference	Electronic Temperature (eV)	Ion Flux ($A.m^{-2}$)	Ion Density (m^{-3})	Measured Bias Voltage (V)
Test 1	3.24	11.32	4.05	22.8
Test 2	3.26	11.45	4.08	21.6
Test 3	3.27	11.48	4.08	22.5
Test 4	3.22	11.03	3.95	22.5
Test 5	3.23	11.31	4.05	23.1
Average	3.24	11.32	4.04	22.5

Subsequently, capacitive probe acquisitions were realized by varying the c-C_4F_8 flow rate from 4 to 50 sccm (only source injections). The corrected I-V characteristics obtained in relation to the c-C_4F_8 flow rate are shown in **figure IV.8** between 46 V and 56 V. The resulting plasma parameters obtained through this method are listed in **table IV.6**. For these specific capacitive probe measurements, the main ion mass which was considered was the one of CF_3^+ (69 a.m.u).

Table IV.6: Plasma parameters obtained from the (I-V) characteristics acquired during capacitive probe characterization of the c-C_4F_8 plasma passivation step by varying the gas flow rate

C_4F_8 flow rate (sccm)	Electronic Temperature (eV)	Ion Flux ($A.m^{-2}$)	Ion Density (m^{-3})	Measured Bias Voltage (V)
4 sccm	3.24	11.25	4.03×10^{16}	21.3
10 sccm	3.24	11.32	4.05×10^{16}	22.8
16 sccm	3.17	10.95	3.96×10^{16}	25.3
20 sccm	3.12	10.58	3.86×10^{16}	27.8
50 sccm	2.82	9.01	3.45×10^{16}	39.8

Figure IV.8: Current-voltage (I-V) characteristics between 46V and 56V obtained through capacitive probe acquisitions of the c-C_4F_8 plasma passivation step by varying the gas flow rate

Process parameters: C_4F_8 flow rate: 4 to 50 sccm (Source injection) ; Pressure: 2.0 Pa ; ICP Source power: 1,500 W ; Bias power: 15 W

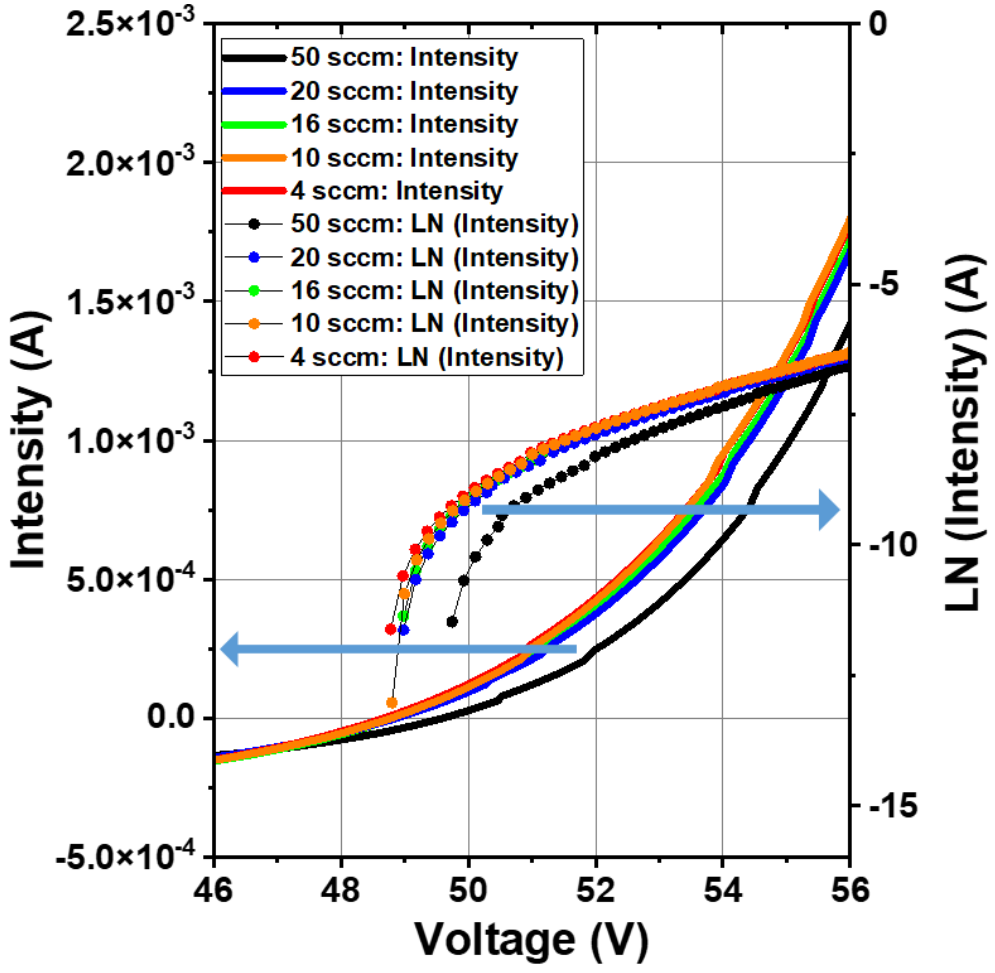

4.2.4 Global evaluation of c-C_4F_8 plasma passivation in relation to substrate temperature

The results obtained during this parametric study of the C_4F_8 passivation step show to what extent fluorocarbon plasma deposition on silicon substrates is temperature dependent. The CF_x layer thicknesses deposited at -100°C are roughly a hundred times thicker than at ambient temperature using the same C_4F_8 flow rate in these process conditions. However, it can be noticed that this considerable CF_x passivation thickness increase at -100°C only moderately affects the necessary C_4F_8 flow rate needed during the passivation steps during Bosch process to achieve anisotropic etching in these process conditions. It is believed that the short fluorocarbon deposition steps coupled with the application of a 15 W bias power were not optimal towards CF_x passivation in this case. The refinement

of these process parameters could further contribute to the reduction of the necessary C_4F_8 gas feed at -100°C compared to ambient temperature processing.

No significant difference was found concerning the fluorocarbon passivation layer whether C_4F_8 gas was injected through the source inlet or through the gas-ring apart from the layer thickness which is approximately 10% thicker for source injections at -100°C. However, this fails to explain the extent to which the passivation was enhanced through source injections during Bosch process tests. It is suggested that C_4F_8 gas species injected through the source inlet have a higher probability to dissociate into smaller fluorocarbon compounds before reaching the substrate in comparison with gas- ring injections.

This suggestion is partly confirmed through the mass spectrometry acquisitions resumed in **figure IV.7** despite the chemical fragmentation and ion recombination occurring during mass spectrometry analysis. It is supposed that C_4F_8 source injections may slightly enhance the presence of fluorine rich species in the plasma in comparison with gas-ring injections which would slightly enhance the presence of carbon rich species. However, the potential differences in the precise fluorocarbon chemical content of the passivated CF_x layers cannot be detected using in-situ ellipsometry. Nevertheless, the complementary SF_6 plasma etching experiments using bias power suggest that their resistance is relatively the same regardless of the gas injection channel that was used during the deposition process at -100°C. As a result, it is suggested that the enhanced fluorocarbon passivation observed using source injections could be explained by the chemical mechanisms involved in the formation of the CF_x interfacial layer with the Si substrate.

Although the fluorocarbon passivation layers have the same refractive index according to in-situ ellipsometry, it is supposed that the chemical composition of these layers, especially the thin interfacial layer with the Si substrate may be substantially different depending on the gas injection channel used for C_4F_8 plasma deposition. This hypothesis is compatible with the two-step mechanism proposed by *Labelle et al* [269] to describe the C_4F_8 plasma passivation on a silicon substrate. It is suggested that a carbon rich film is first deposited and is then gradually fluorinated by free F contained in the plasma. In this case, the higher dissociation of fluorocarbon compounds which is supposed to occur during source injections, and partly confirmed in **figure IV.7**, is expected to enhance the formation of a resistant interfacial CF_x film in comparison with gas-ring injections. This two-step mechanism would explain why both passivation films have roughly the same refractive index after thick deposition processes. However, the chemical composition of their thin carbon rich interfacial layers may be substantially different according to the gas injection channel. In this case, the interfacial layer deposited through C_4F_8 source injection is supposed to be slightly more resistant to SF_6 plasma etching than the one obtained through gas-ring injection judging by the etch results that were obtained. Only surface characterization techniques such as x-ray photoelectron spectroscopy (XPS) or perhaps energy dispersive x-ray (EDX) microanalysis would be able to assess this hypothesis.

4.3 Study of c-C_4F_8 adsorption on silicon substrates at cryogenic temperatures

4.3.1 Introduction to adsorption mechanisms

When it comes to plasma processing at cryogenic temperatures, it is important to evaluate the thermodynamic conditions in which the plasma species will evolve as they approach the substrate surface as well as the eventual byproducts which might be generated due to the etching chemistry taking place. An important aspect is the notion of physical adsorption also called physisorption which takes an increasing role with decreasing substrate temperatures in addition to chemisorption also referred to as chemical adsorption in the interaction between plasma species and substrate surfaces. Although most of the following considerations concern the surface atomic scale, thus affecting mostly thin-etching processes, they are also the basis of important mechanisms which can occur at the macroscopic scale during deep-etching processes.

4.3.1.1 Adsorption theory

Adsorption corresponds to the phenomenon where a fluid chemical compound (in gaseous or liquid state) called the adsorptive adheres to a solid surface called in this case the adsorbent [291–295]. The resulting substance which has undergone the adsorption process is referred to as the adsorbate. Adsorption must not be confused with absorption phenomenon where an absorbed chemical compound (in gaseous, liquid or solid form) penetrates into the bulk volume of an absorbent solid. It is strictly a surface phenomenon. A schematic representing the principal adsorption mechanisms is detailed in **figure IV.9**.

Figure IV.9: Representation of molecules involved in an adsorption process

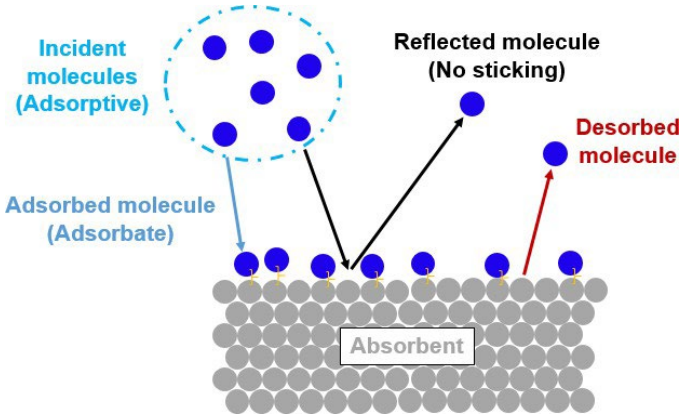

4.3.1.2 Adsorption mechanisms

4.3.1.2.1 Chemisorption

Chemisorption or chemical adsorption is a mechanism by which an adsorptive specie will adsorb on an adsorbent surface via a strong chemical bond such as a covalent bond or ionic bond with binding energies in the order of 1 to 10 eV [56,291,294]. As a result, the adsorbate is chemically changed and stable on the surface. Chemisorption reactions on a given surface are usually limited to a monolayer. Indeed, once all the surface sites are covered with chemisorbed species, no further chemisorption bonding can take place on this adsorbed monolayer.

4.3.1.2.2 Physisorption

Physical adsorption or physisorption is a mechanism by which adsorptive species will adsorb on an adsorbent surface through weak intermolecular forces called Van der Walls bonds with a low binding energy in the range of 10 to maximum 500 meV [56,292,294]. These attractions do not result from chemical electronic bonding but rather from molecular forces, in instance London, Debye and Keesom attraction forces [292,295]. At the time, these Van der Waals attraction forces were all included as a single term and opposed to the Pauli repulsion force in the famous Lennard-Jones potential (**equation IV.1**) which was first developed in 1924 to model the interaction of simple neutral atoms or molecules according to their relative distance [295–297].

Equation IV.1: Lennard-Jones (12, 6) potential equation

$$V(r) = 4.\varepsilon.\left[\left(\frac{\sigma}{r}\right)^{12} - \left(\frac{\sigma}{r}\right)^{6}\right]$$

In this equation, $V(r)$ corresponds to the potential energy of the two particles separated by a distance r whereas ε is the depth of the potential well (maximum binding energy) and σ is the distance at which $V(r)$ is equal to 0.

Physisorption mechanisms can be enhanced by specific surface properties such as higher surface areas, increased surface roughness, or the use of porous materials [295,298]. Depending on the adsorbate nature (polar or non-polar molecules), the surface chemical nature (also polar or non-polar) can also favor certain molecular reactions. Nevertheless, physisorption reactions greatly depend on the temperature and pressure conditions. They are easily reversible and should normally preserve the chemical nature of the adsorbate, meaning that a molecule which will physisorb will eventually desorb back with the same chemical composition [291,293,295]. They occur at a further distance from the surface than chemisorption reactions and can generally form multilayers. In the recent years, the study of physisorption of neutral species on semiconductor materials of interest has emerged for area-selective atomic layer deposition (AS-ALD) or atomic layer etching (ALE) applications [56,274,275,299].

4.3.1.2.3 Desorption

The reverse phenomenon of adsorption, where an adsorbate chemical compound is released from the adsorbent surface back into the surrounding phase (gas or liquid) is referred to as desorption [291–293,300–302]. Desorption reactions occur when the adsorbed compound receives a sufficient amount of energy (E_{Des}) to overcome the binding energy which keeps it held to the adsorbent surface. It concerns both physisorbed and chemisorbed adsorbates and can result from many factors which can be correlated such as the heating of the substrate (thermal energy), a pressure decrease or the exposition to photons and other energetic particles. Moreover, chemical reactions occurring on the surface may also trigger desorption reactions. The most common source of desorption reactions is due to thermal heating which is also referred to as thermal desorption.

The typical potential diagrams of physisorption and chemisorption are illustrated in **figure IV.10**. In this graph, ΔH_{phys} and ΔH_{chem} represent respectively the adsorption enthalpy for physisorption and chemisorption whereas ΔE_A represents the activation energy barrier between a physisorbed state and a chemisorbed state.

Figure IV.10: Potential energy in relation to the distance from the adsorbent surface involved for the physisorption or chemisorption of an adsorptive at constant pressure (taken and adapted from [293] and [303])

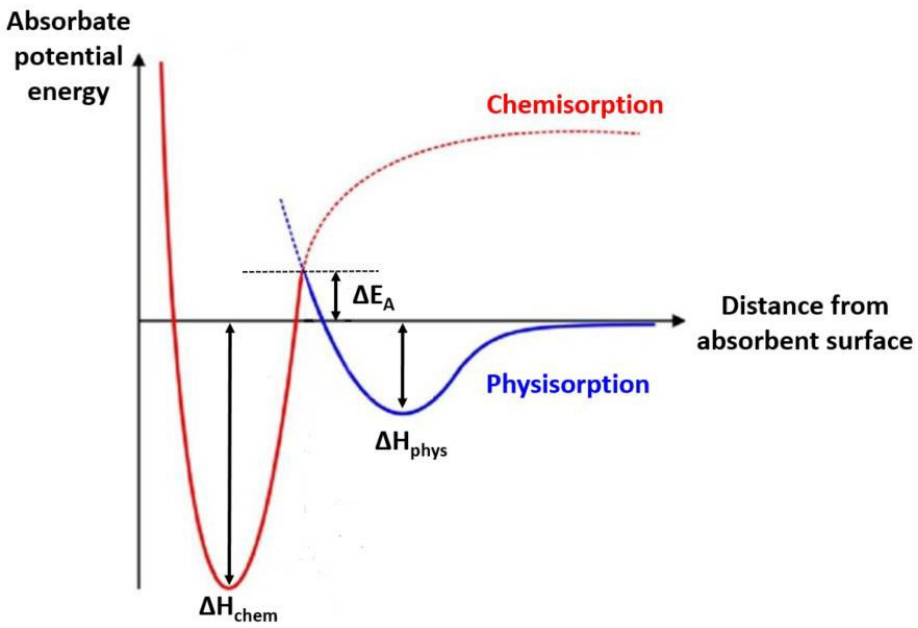

4.3.1.3 Physisorption parameters

The following section will focus on physisorption theory as it takes an increasing role in the case of cryogenic processing where absorbents are injected at low pressures on substrates which are thermalized at low temperatures. The main parameters which intervene will be presented in order to describe and characterize this mechanism towards process optimization.

4.3.1.3.1 Rate of incident molecules

The first notion that is needed to describe physisorption reactions is the rate of incident molecules or impingement rate (Φ) coming into contact with the sample surface. It is given in **equation IV.2** and is derived from the ideal gas law [304]. All these molecules represent potential adsorbate candidates and are expressed in molecules.m^{-2}.s^{-1}.

Equation IV.2: Impingement rate equation

$$\Phi = \frac{1}{4}.n.\bar{v}$$

In this equation, n corresponds to the density of gaseous species (expressed in molecules.m^{-3}) and $\bar{v}$ corresponds to the mean molecular speed (expressed in m.s^{-1}). The absolute pressure of gaseous species (P) is related to their density (n) through the ideal gas law given in **equation IV.3** whereas the mean molecular speed ($\bar{v}$) can be calculated using **equation IV.4** according to the kinetic theory of gases [304].

Equation IV.3: Ideal gas law

$$P = n.k_B.T$$

In this equation, P is expressed in Pa, k_B corresponds to the Boltzmann constant and T corresponds to the gas temperature in kelvins.

Equation IV.4: Mean molecular speed equation

$$\bar{v} = \sqrt{\frac{8.k_B.T}{\pi.m}}$$

In this equation, $\bar{v}$ s expressed in m.s^{-1} whereas m corresponds to the molecular mass expressed in kg.

4.3.1.3.2 Surface coverage

After determining the rate of incident molecules, the surface coverage (θ) corresponds to the ratio which describes the occupation rate of adsorbate molecules on an adsorbent surface within a monolayer [292].

It is expressed in **equation IV.5** and is valid both for chemisorption and physisorption mechanisms. The number of available sites on an adsorbent surface within a monolayer corresponds to Ns. The number of absorbate molecules Na can only be inferior to Ns within a monolayer or equal to Ns when full coverage of the monolayer is achieved ($\theta = 1$). Both Na and Ns are expressed in unit area of surface (m^{-2}).

Equation IV.5: Surface coverage equation

$$\theta = \frac{N_\alpha}{N_s}$$

Throughout time, the surface coverage of a sample surface evolves depending on the rate of incident molecules (m), the sticking probability (S) and the average residence time of absorbate molecules on the sample surface (t_{res}) [292]. The sticking probability is defined as the probability that has an incident molecule to adsorb on the sample surface. It can vary from 0 where all the incident molecules are reflected from the surface to 1 where all the incident molecules will adsorb on the surface. If the sticking probability of incident molecules is superior to 0, the notion of residence time comes into account as it is defined as the average time during which a physisorbed molecule will remain on the surface before desorbing back into the gas phase. Therefore, the evolution of surface coverage through time is expressed in **equation IV.6**.

Equation IV.6: Evolution of surface coverage in relation to time

$$\frac{d\theta}{dt} = \frac{S.P}{N_s.\sqrt{2\pi.m.k_B.T}} - \frac{\theta}{t_{res}}$$

4.3.1.3.3 Residence time on a sample surface

As mentioned previously, the average residence time (t_{res}) is defined as the average time where an adsorbate remains adsorbed on an adsorbent surface [292]. This value can be calculated using **equation IV.7**.

Equation IV.7: Average residence time of an adsorbate on an adsorbent surface

$$t_{res} = t_d^0.e^{\left(\frac{E_{Des}}{k_B.T}\right)}$$

In this equation, the pre-exponential factor t_d^0 is a time factor related to the vibration frequency of the adsorbed molecule. E_{Des} corresponds to the desorption activation energy needed for the adsorbate to escape the adsorbent surface whereas k_B and T respectively correspond to the Boltzmann constant and the adsorbent temperature.

4.3.1.3.4 Main adsorption models and isotherms

The study of various adsorption and subsequent desorption reactions amongst gaseous phase absorbates and solid phase adsorbents has led to the observation of different types of adsorption isotherms. The IUPAC classification of 1985 identifies 8 main adsorption isotherms which are illustrated in **figure IV.11** [298]. For these isotherms, the amount desorbed (Y-axis) corresponds to the quantity of desorbed absorptive from the adsorbent surface (usually expressed in moles per gram) in relation to the equilibrium relative pressure ($^{P}/_{P_{sat}}$) of the adsorptive (X-axis). This ratio corresponds to the partial pressure of the adsorptive (P) to its equilibrium vapor pressure (P^{sat}) at the same temperature. Both of these physical quantities are described in the following section.

Several adsorption models were developed from these absorption isotherms according to the physical properties of the adsorbates and adsorbents. Among them, the Langmuir adsorption model and its extension, the Brunauer-Emmett-Teller (BET) model are the most commonly used [291,292,302,304].

The Langmuir model **equation IV.8**, introduced by Irving Langmuir in 1918 [291,295,302,305], is mostly used to describe monolayer adsorptions which take place at lower pressures ($^{P}/_{P_{sat}} < 0.1$) until the surface is saturated allowing no further adsorption reactions ($0.1 < {}^{P}/_{P_{sat}} < 1$) [305,306]. This model supposes that the adsorbent surface is perfectly flat (no surface roughness) and that the adsorbate is an ideal gas at isothermal conditions. All the adsorption sites are presumed to be equivalent in energy and can accept only one adsorptive molecule. It also supposes no interaction between the adsorbed molecules which limits the surface coverage to a single monolayer.

Equation IV.8: Monolayer adsorption model (Langmuir adsorption model)

$$\theta = \frac{K.P}{1 + K.P}$$

In this equation, θ corresponds to the surface coverage fraction of occupied adsorption sites whereas K corresponds to the Langmuir adsorption equilibrium constant which is related to the binding energy between the adsorbate and the adsorbent. The term P corresponds to the absorptive partial pressure.

The Brunauer-Emmett-Teller (BET) model (**equation IV.9**) was introduced by Stephen Brunauer, Paul Hugh Emmett and Edward Teller in 1938 [291,295,298,302,306,307]. It supposes that gaseous molecules can adsorb on a solid surface infinitely by forming multilayers. Every single adsorbed molecule on a given multilayer can accept a subsequent adsorbent molecule on the following multilayer. The Langmuir model can be applied to each adsorption layer yet it does not require the saturation of an adsorption layer (x) before the formation of an upper adsorption layer ($x + 1$). The BET model assumes that the adsorption enthalpy of the adsorbent molecules is higher for the formation of the first monolayer and that it decreases for the subsequent adsorption multilayers. The uppermost adsorbed molecules are supposed to be in thermal equilibrium with the gas phase while the underlying adsorbed molecules are assumed as condensed species in the liquid state. This model is mostly used to describe multilayer

adsorptions at intermediate pressures ($0.05 < {}^{P}/_{P_{sat}} < 0.35$) [306]. Once the ($^{P}/_{P_{sat}}$) ratio exceeds 0.35 and approaches the saturation pressure (P_{sat}), the number of adsorption multilayers tends to infinity and the physisorption regime switches to a condensation regime where the model is not accurate.

Equation IV.9: Multilayer adsorption model (BET model)

$$\frac{{}^{P}/_{P_{sat}}}{n\left(1-{}^{P}/_{P_{sat}}\right)} = \frac{C-1}{n_m.C}.\left({}^{P}/_{P_{sat}}\right) + \frac{1}{n_m.C}$$

In this equation, n corresponds to the specific amount of gas adsorbed (typically expressed in mol/g), n_m is the specific monolayer capacity. The parameter C, also called the BET constant, is related to the monolayer adsorption energy of the adsorptive molecule.

Figure IV.11: Classification of physisorption isotherms (taken from [298])

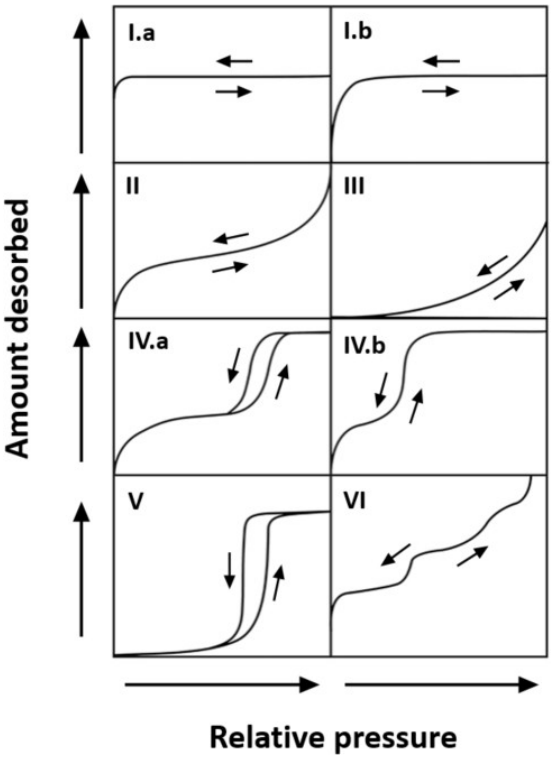

Type I isotherms (I.a and I.b) are also called Langmuir isotherms because they describe the Langmuir adsorption model. They are characterized by a steep initial region indicating strong adsorption at low pressures until a plateau is reached once the adsorption monolayer has been completed where all the adsorption sites have been filled with an adsorptive molecule. They describe the adsorption mechanisms which usually occur on microporous surfaces (with pore size diameters lower than 2 nm) such as activated carbon (charcoal) or zeolites.

Type II isotherms fit best the conditions of the BET adsorption model which mainly occurs on non-porous or macroporous materials (with pore size diameters over than 50 nm) such as silicon dioxide (silica gel) or metal surfaces with the formation of adsorption multilayers. It illustrates initial monolayer adsorption at low adsorptive partial pressure which is followed by multilayer adsorption at higher pressures.

Type III isotherms describe weak adsorption interactions between the adsorbate and the surface adsorbent which only take place at relatively high adsorptive partial pressures. An example of this type of isotherm can be obtained by studying the adsorption of water vapor with hydrophobic surfaces such as polyethylene.

Type IV isotherms (IV.a and IV.b) are similar to type II isotherms yet two plateau regions can be distinguished. They describe monolayer and multilayer adsorption followed by capillary condensation mechanisms which typically occur on mesoporous surfaces (with pore size diameters between 2 and 50 nm). Type IV.a isotherms are marked by a hysteresis loop which show a delay between the adsorption and desorption reactions due to capillary condensation effects as the partial pressure of the adsorptive is varied.

Type V isotherms are similar to type III as they describe weak adsorption interactions between the adsorbate and the surface adsorbent at low adsorptive partial pressures. However, they describe capillary condensation effects at higher pressures where a hysteresis loop is observed. This type of isotherm is obtained when studying the adsorption water vapor with hydrophobic mesoporous materials.

Type VI isotherms describe stepwise layer-by-layer adsorption mechanisms which are typically observed on uniform non-porous surfaces such as crystals or graphite especially at low temperature. One of the first examples of this type of isotherm was the study of argon adsorption on highly ordered pyrolytic graphite (HOPG) surfaces.

4.3.2 Introduction to condensation and deposition transition phases near the equilibrium vapor pressure

4.3.2.1 Introduction to condensation and deposition transition phases

Condensation refers to the thermodynamic process where a substance operates a phase transition from its vapor phase to its liquid phase [308]. The reverse phenomenon of condensation is referred to as vaporization (also referred to as evaporation). Condensation is usually triggered by the local cooling or compression of the gas phase above its equilibrium vapor pressure. The resulting loss of thermal energy will enable the vapor molecules to interact with each other and accumulate in a nucleation site which will enable them to operate their phase transition through the release of latent heat. Condensation reactions are favorably triggered on a foreign surface or particle in contact with the vapor phase as it usually lowers the energy barrier for nucleation. This mechanism is referred to as heterogenous nucleation whereas homogeneous nucleation occurs within the vapor phase without the help of an external element [309,310].

Deposition refers to the thermodynamic process where a substance operates a phase transition from its vapor phase directly to its solid phase without passing through its liquid phase [308]. This phase transition is even more exothermic than condensation and typically occurs at lower temperatures and/or high pressures where the thermodynamic conditions do not allow the substance to evolve in its liquid phase. The reverse phenomenon of deposition is referred to as sublimation.

4.3.2.2 Equilibrium vapor pressure

In order to evaluate the thermodynamic conditions where adsorptive molecules are prone to physisorb or condense on the adsorbent surface, the equilibrium vapor pressure of the adsorptive gas molecules has to be considered. Indeed, the equilibrium vapor pressure (or saturation vapor pressure) of a substance is defined as the pressure at which vaporized molecules are in thermodynamic equilibrium with their condensed phase (liquid or solid) at a given temperature in a closed system. As a result, when an adsorbent substrate is thermalized at a given temperature and the partial pressure of an adsorptive gas is equal to its equilibrium vapor pressure, the rate of adsorptive gas molecules which will condense (liquid phase) or deposit (solid phase) on the substrate is equal to the rate of adsorbate molecules which will desorb (vaporization or sublimation reaction) from the surface into the gaseous phase.

Therefore, if the partial pressure of a gaseous chemical is superior to its equilibrium vapor pressure, the condensation rate of adsorptive molecules will exceed the desorption rate of adsorbate molecules. In these conditions, multi-layer physisorption may occur and the residence time of physisorbing molecules will be considerably enhanced. It is important to note that physisorption reactions may occur even if the partial vapor pressure of a substance is under its equilibrium vapor pressure. However, the residence time of the adsorbate species will be very extremely short as desorption reactions prevail in these conditions.

The equilibrium vapor pressure of any pure substance increases non-linearly with temperature. The Clausius-Clapeyron equation defines the vapor-liquid phase transition (**equation IV.10**). It is derived from the Clapeyron equation (**equation IV.11**) for first-order phase transitions which can be applied in the case of an ideal gas ($P \leq P_{atm}$) at a temperature which is sufficiently distant from the critical point where the molar volume of the liquid phase is negligible to the molar volume of the gas phase. Previously and following the publication of this postulate, many empirical equations have been developed to fit with experimental data such as the Dalton equation, the Biot equation or Avogadro equation [311–313]. However, the Antoine equation has emerged as the most used empirical equation that was derived to that matter. Indeed, at first, a common equation which will be referred to as Dalton's empirical equation for vapor pressure was derived from the Clausius-Clapeyron equation. It aimed to approximate the relation between equilibrium vapor pressure of a pure substance and temperature using two empirical parameters (A and B) supposing that the enthalpy of vaporization is independent of temperature. However, it was found that this hypothesis was not valid over a wide range of temperatures. Therefore, this equation was not found reliable except on very short temperature ranges [314].

To overcome this issue, the Antoine equation was proposed by introducing a third empirical parameter (C) to describe the change in the enthalpy of vaporization of a pure substance over a wider range of temperatures (**equation IV.12**). This empirical relation was found to be quite reliable with a satisfactory precision in the determination of equilibrium vapor pressures at temperatures from the triple point to a reduced temperature of 0.75 from the critical point [314–316]. However, it is important to note that it remains an empirical equation which is not fully reliable if it is applied over wider temperature ranges. As a result, it is very common to find different sets of Antoine parameters for the same substance in the literature, as they account for the approximation of experimental data obtained over different temperature ranges. For practical reasons, the approximation of the equilibrium vapor pressure of a pure substance is usually expressed from the triple point to the critical point using at least two Antoine equations, one from the triple point to a reduced temperature of 0.75 followed by another one from this point to the critical point [314].

Since the introduction of the Antoine equation, other empirical equations have been proposed using 3 parameters or more [315,316] such as the Wagner equation [317] or the DIPPR 101 equation [318]. Although they were proven to be slightly more precise in the approximation of equilibrium vapor pressures of several substances, extensive data concerning their application to a large scale of chemicals are rarely encountered in the literature.

Saturating vapor pressures and other physicochemical properties such as the normal boiling temperature of pure substances have been determined experimentally for most chemicals using a variety of techniques, including calorimetry, ebulliometry or using an isoteniscope [319–321,316]. These techniques have been widely used near the atmospheric pressure range where the most accurate measurements are obtained close to the normal boiling point [319]. In general, vapor pressure data for most substances can be easily found in the scientific literature in the 5 kPa to 100 kPa pressure range. However, under 1 kPa, vapor pressure data is more difficult to find for various substances as it becomes increasingly difficult to measure this parameter in these low pressure conditions where they can be subject to significant systematic errors. Other techniques have been

developed to address this issue which include molecular effusion (Knudsen effusion technique) [322], gas-liquid chromatography [323], direct static measurement of vapor pressure [319,324]. Nevertheless, it was found that the equilibrium vapor pressures of most molecular substances remain complicated to find in the literature in these low-pressure conditions.

Equation IV.10: Clausius-Clapeyron equation (liquid-gaseous phase transition)

$$\left(\frac{dP_{sat}}{dT}\right) = \frac{P_{sat}.\Delta_{vap}H}{R.T^2}$$

In this equation, P_{sat} corresponds to the equilibrium vapor pressure (Pa), $\Delta_{vap}H$ corresponds to the enthalpy of vaporization of the pure substance, T to the temperature (K) and R to the molar gas constant.

Equation IV.11: Clapeyron equation

$$\left(\frac{dP_{a\to b}}{dT}\right) = \frac{\Delta_{a\to b}H}{T.\Delta_{a\to b}V}$$

In this equation, $P_{a\to b}$ corresponds to the phase transition pressure at a given temperature (Pa), $\Delta_{a\to b}H$ corresponds to the phase transition enthalpy of the pure substance from phase a to b at a given temperature ($J.mol^{-1}$), T to the temperature (K) and $\Delta_{a\to b}V$ to the phase transition volume from phase a to phase b ($m^3.mol^{-1}$).

Equation IV.12: Antoine equation

$$\log(P) = A - \frac{B}{T + C}$$

In this equation, P corresponds to the pressure (Pa), A, B and C correspond to the Antoine parameters for the given chemical compound and T to the temperature (K).

Although the Antoine equation takes into account the variation of the enthalpy of vaporization depending on the temperature to approximate the equilibrium vapor pressure over a wide range of temperatures, it does not adequately describe this phenomenon as is shown by W. Waring [315]. Therefore, the precise determination of equilibrium vapor pressures of substances at temperatures inferior to the triple point through the extrapolation of the Antoine equation is not entirely accurate [315,316]. Nevertheless, it was decided to use this technique to approximate the equilibrium vapor pressure curve of process gases which can be used with the ICP reactor as well as atmospheric gases such as H_2O and N_2. These conjectures can approximate whether these chemicals are likely or not to physisorb or deposit on the wafer surface in relation to the process parameters. Additionally, it is also interesting to approximate the equilibrium vapor pressure of eventual etching byproducts depending on the nature of the substrate which can be produced during plasma processing.

When analyzing and eventually extrapolating an equilibrium vapor pressure curve for a specific chemical, it is important to keep in mind its general phase diagram as well as its proper chemical properties notably its triple point and critical point. An example of a phase diagram is shown in

figure IV.12 with the simplified phase diagram of water (H_2O molecule) which represents the temperature and pressure (partial pressure) conditions of stability of its distinct phases when they are at equilibrium. The triple point and critical point are represented and are connected by the vapor-liquid equilibrium curve which specifies the pressure-temperature conditions at which this phase transition occurs.

Figure IV.12: Simplified phase diagram of H_2O molecule (taken and adapted from [325])

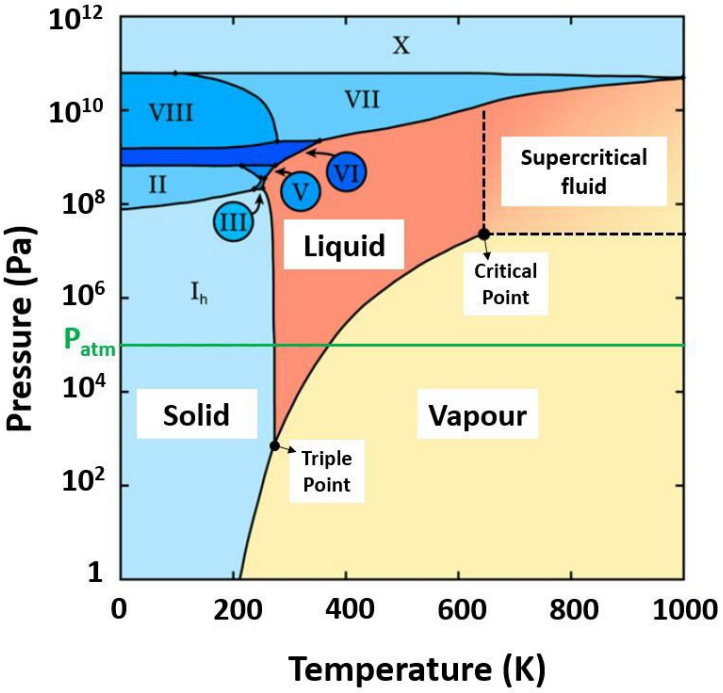

The triple point of a pure substance is defined as the temperature and pressure set where solid, liquid and vapor phases coexist and are in thermodynamic equilibrium. In the context of plotting the equilibrium vapor pressure of this substance, the identification of the triple point temperature (T_{triple}) delimits the temperature boundary where vaporized molecules will either be at thermodynamic equilibrium in liquid state and condense on the thermalized wafer or be at thermodynamic equilibrium in the solid state and deposit in a solid state.

The critical point of a substance or more precisely the liquid-vapor critical point refers to the highest temperature at which it can be in vapor-liquid equilibrium. At higher temperature and pressure conditions, the substance is considered to be in a supercritical fluid phase which is distinct from liquid and vapor phases as it will have both the properties of a gas and those of a liquid. At a higher temperature than the critical point ($T > T_c$) but lower pressure ($P < P_c$), the substance is considered to be in a gaseous state. As a result, it is important to identify the critical point of a specific substance when it comes to extrapolating equilibrium vapor pressure datasets found in the literature as the maximal equilibrium vapor pressure cannot exceed the critical pressure.

The equilibrium vapor pressure of a substance is closely related to its vaporization-condensation equilibrium (gaseous-liquid phase transition) followed by its sublimation-deposition equilibrium (gaseous-solid phase transition). However, the application of the Antoine equation for a given substance should be strictly restricted to the temperature range comprised between its triple point and critical point

where only the gaseous-liquid transition phase occurs. As a result, the approximation of the equilibrium vapor pressure in the gaseous-solid phase transition, in other words, from the triple point temperature (T_{tp}) to the absolute zero temperature (-273.15°C or 0 K) cannot be accurately described using an Antoine equation that was determined on another temperature range. In this region, the equilibrium vapor pressure can only be reliably approximated using experimental data which was proven to be difficult to find in the literature or which has not yet been established for several chemical compounds at these temperature and pressure conditions.

A focused phase diagram of H_2O in the neighborhood of the triple point is shown in **figure IV.13** where the slope shift which occurs between the vapor-liquid equilibrium curve and the vapor-slope equilibrium curve can be observed. Concerning the experimental approximation of the equilibrium vapor pressure of water, an example of two Antoine equations obtained over two temperature ranges is shown in **figure IV.14**. They correspond to two set of experimental results obtained independently to which Antoine parameters have been determined independently to best fit the data. Both of these references are found on the NIST database for water (H_2O molecule). The Antoine equation curves and their extrapolation between T_{triple} and T_c show to what extent the empirical Antoine equation should be applied and only on the temperature range that was determined. Indeed, it can be seen that at lower temperatures, the extrapolation of Antoine equations obtained over different temperature ranges can result in huge differences in the estimation of equilibrium vapor pressures. Therefore, the approximation of equilibrium vapor pressures at low pressure and low temperature conditions should only be attempted by extrapolating the Antoine equations obtained near the triple point for each gas of interest. As a result, for all the reasons detailed above, the equilibrium vapor pressure values obtained using this method should only be considered as an indication of the thermodynamic conditions which are necessary to enable the condensation of process gases on a thermalized wafer surface.

Figure IV.13: Phase diagram of H_2O molecule in the vicinity of the triple point (taken and adapted from [326])

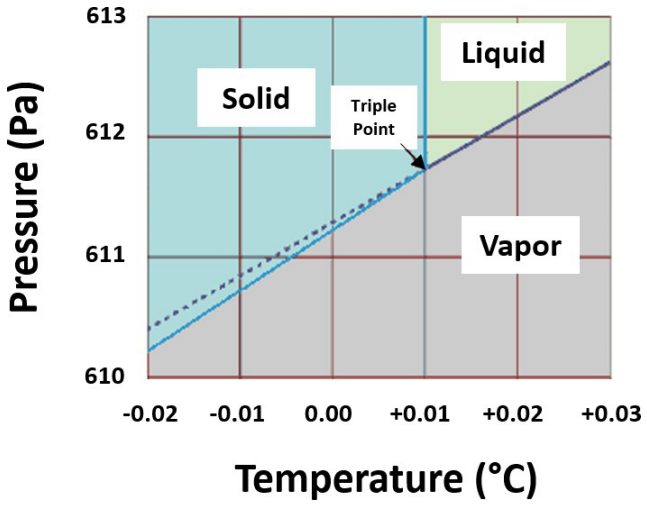

Figure IV.14: Plot of two Antoine equations and their respective extrapolation between T_{triple} and T_c describing H_2O experimental equilibrium vapor pressure data obtained over different temperature ranges (found on the NIST database [327])

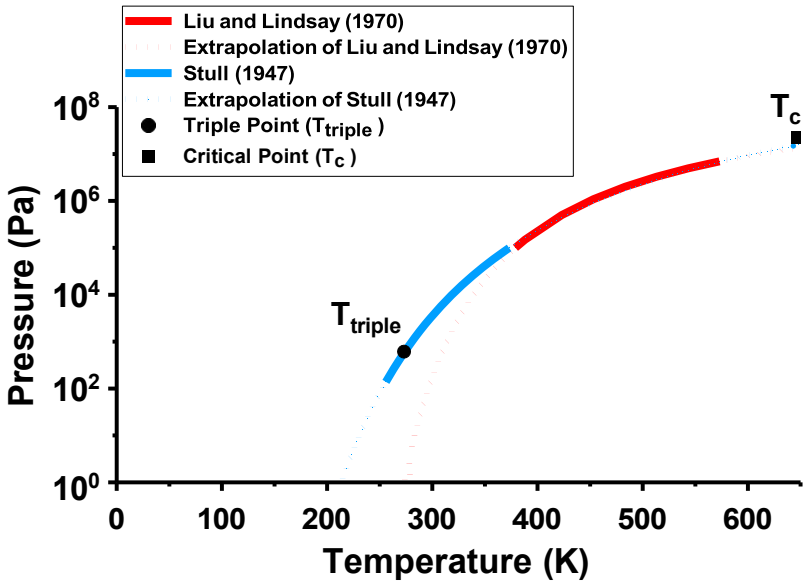

4.3.2.3 Extrapolation of the equilibrium vapor pressures of target substances of interest based on bibliographic data

For the interest of this research study, bibliographic research was realized to identify adequate Antoine parameters and other phase transition temperature properties of the process gases available on the ICP tool and eventual etching byproducts. The goal was to approximate the equilibrium vapor pressures of these chemical compounds in the pressure and substrate temperature conditions that can be applied using the ICP reactor during plasma processing. The data extracted from this bibliographic research is listed in **tables IV.7 and IV.8**. **Table IV.7** lists the data that was obtained concerning the ICP reactor process gases and other atmospheric gases whereas **table IV.8** lists the data obtained concerning eventual etching byproducts.

Table IV.7: List of Antoine equation parameters found in the scientific literature for the ICP reactor process gases and atmospheric gases with their associated triple point and critical point parameters

Gas chemical	c-C_4F_8	SF_6	SiF_4	CHF_3	CF_4
References	Kletskii / Krauss [328,329]	Linde*[1] / Solvay / Ohta / Lide (CRC) [23,330–332]	Stull / Pace / Booth [333–335]	Valentine / Ohgaki [336,337]	Smith/ Menzel / Altunin [338–340]
Parameter A	4.254	*[1] 4.47	7.10978	4.25548	0.62910
Parameter B	1007.399	*[1] 865.7045	1220.564	718.089	103.578
Parameter C	-30.205	*[1] -12.2389	-6.884	-22.013	-61.461
Experimental Minimum Temperature (°C)	-40.15	-145.00	-144.15	-127.79	-183.44
Experimental Maximum Temperature (°C)	115.22	45.00	-94.85	-81,96	-171.69
Triple point T (°C)	-40.19	-49.43	-86.8	-155.18	-183.6
Triple point P (Pa)	Not found	2,327 x10^5	2.23888 x10^5	Not found	Not found
Critical point T (°C)	115.31	45.573	-14.15	26.15	-45.65
Critical point P (Pa)	2.784 x10^6	3.77 x10^6	3.71457 x10^6	4.828 x10^6	3.745 x10^6

Gas chemical	H_2O	O_2	Ar	N_2	H_2	He
References	Stull / Sato [333,341]	Brower / Lide (CRC) [23,342]	Drii / Lide (CRC) [23,343]	Edejer / Lide (CRC) [23,344]	Lide (CRC)*[2] / [23]	Lide (CRC)*[3] / Angus[#] [23,345]
Parameter A	4.6543	3.9523	3.29555	3.7362	*[2] 3.0991	*[3] 2.2468
Parameter B	1435.264	340.024	215.24	264.651	*[2] 73.7007	*[3] 12.4463
Parameter C	-64.848	-4.144	-22.233	-6.788	*[2] 3.5558	*[3] 1.3386
Experimental Minimum Temperature (°C)	-17.25	-218.79	-189.37	-210.01	-259.15	-270.95
Experimental Maximum Temperature (°C)	99.85	-118.82	-122.43	-147.15	-240.65	-268.15
Triple point T (°C)	0.01	-218.7916	-189.3442	-209.99	-259.3467	[#] -270.978
Triple point P (Pa)	6.11 x10^2	1,463 x10^2	6.889 x10^4	1.252 x10^4	7,041 x10^3	[#] 5.04 x10^3
Critical point T (°C)	373.99	-118.569	-122.463	-146.958	-240.212	-267.949
Critical point P (Pa)	2.2064 x10^7	5.043 x10^6	4.863 x10^6	3.3958 x10^6	1.2858 x10^6	2.274 x10^5

*[1]Antoine parameters manually calculated for SF_6 using an equilibrium vapor pressure curve found in reference [330] using a regression software tool

*[21]Antoine parameters manually calculated for H_2 using an equilibrium vapor pressure curve found in reference [23] using a regression software tool

*[31]Antoine parameters manually calculated for He using an equilibrium vapor pressure curve found in reference [23] using a regression software tool

Lambda point of He (triple point between two He liquid phases (He I and He II) and Helium vapor phase) referenced in [345]

Table IV.8: List of Antoine equation parameters found in the scientific literature for eventual byproducts resulting from the application of a SF_6 or SF_6/H_2 plasma on a Si or SiO_2 substrate with their associated triple point and critical point parameters

Gas chemical	HF	SH_2	$SiHF_3$	SO_2	SOF_2
References	Stull / Lide (CRC) / [23,333,346]	Stull / Lide (CRC) [23,333]	Stull [333]	Stull / Giauque / Lide (CRC) [23,333,347]	Pace [348]
Parameter A	4.16129	4.43681	4.4464	3.48586	3.80303
Parameter B	1142.985	829.439	648.678	668.225	676.1
Parameter C	-17.993	-25.412	-32.493	-72.252	-50.852
Min T (°C)	-74.65	-134.35	-152.15	-95.45	-98.73
Max T (°C)	19.75	-60.35	-95.15	-10.15	-44.05
Triple point T (°C)	-83.39	-85.55	Not found	-75.51	Not found
Triple point P (Pa)	Not found	2.27×10^4	Not found	1.675×10^5	Not found
Critical point T (°C)	187.85	99.95	Not found	157.49	Not found
Critical point P (Pa)	6.48×10^6	9.00×10^6	Not found	7.884×10^6	Not found

Most of the data listed in these tables was found on the NIST database for each process gas of interest (Phase change data tab). In general, it resulted that for atomic elements, equilibrium vapor pressure datasets and associated Antoine parameters could be easily found and well defined over wide temperature ranges whereas it was not systematically the case for several molecular compounds of interest. Numerous publications, reviews and references were found where Antoine parameters of chemical compounds of interest are reported and approximated. When confronted to several sets of Antoine parameters for the same gas, the choice was decided to select the Antoine equation which was experimentally obtained at the temperature range which was the closest from the triple point. In some cases, the references found only disclosed the equilibrium vapor pressure curve of the substance in question without its Antoine parameters. In these cases, the Antoine parameters (A, B and C) were determined using a regression tool in order to best fit the equilibrium vapor curve and are shown with an asterisk prefix in **table IV.7**.

From these datasets, the equilibrium vapor pressure curves of process and atmospheric gases and their respective extrapolations were plotted in **figure IV.15** over a wide temperature range. An individual example concerning the c-C_4F_8 Antoine equation curve obtained from the equilibrium vapor pressure experimental data collected by *Kletskii et al* [328] and its extrapolation to lower temperatures is shown in **figure IV.16**. The area above the curve corresponds to thermodynamic conditions where condensation reactions are predominant on the surface, whereas the area underneath the curve corresponds to thermodynamic conditions where desorption reactions are prevalent.

Solid line curves correspond to the plot of the Antoine equation curves obtained in the experimental temperature dataset range which was used to determine them. The dotted lines correspond to the extrapolation of these curves at other temperatures ranges. The same method was used in **figures IV.17** to trace the equilibrium vapor pressures of several etching byproducts (HF, SH_2, $SiHF_3$, SO_2, SOF_2) which were found through bibliographic research (listed in **table IV.8**). Almost in every case, the

equilibrium vapor pressure databases and derived Antoine parameters had to be extrapolated to fit the wide substrate temperature range covered by the ICP tool during etching process tests (from -155°C to +25°C).

Figure IV.15: Extrapolation of equilibrium vapor pressure curves of gases available on the Oxford ICP tool

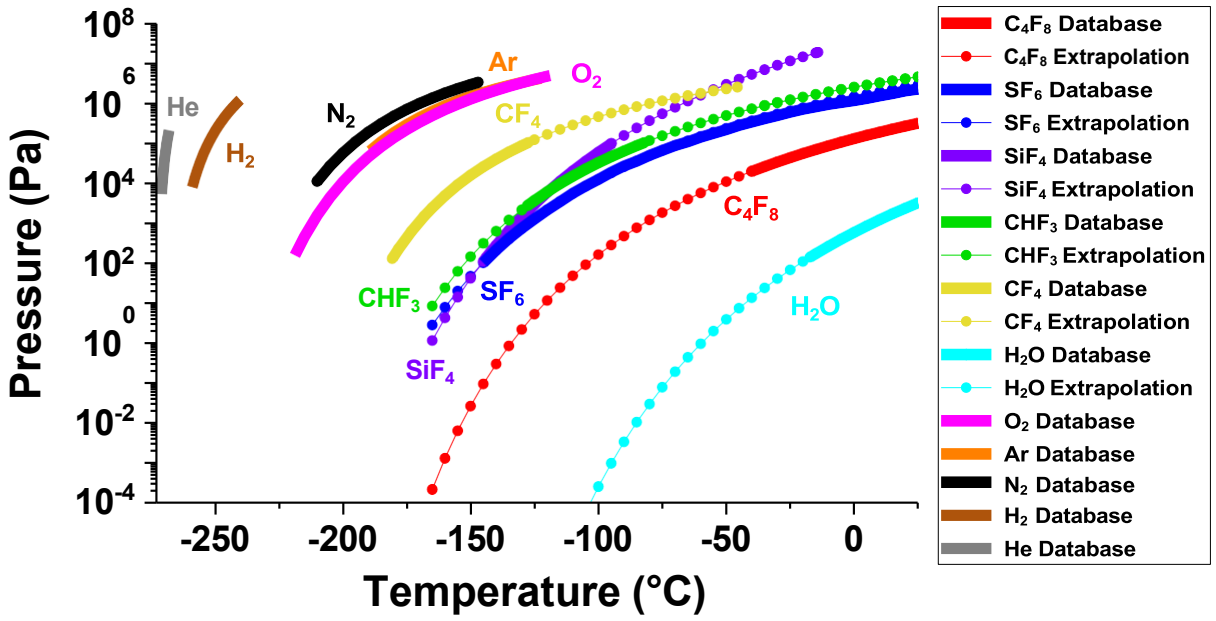

Figure IV.16: Extrapolation of c-C_4F_8 equilibrium vapor pressure curve

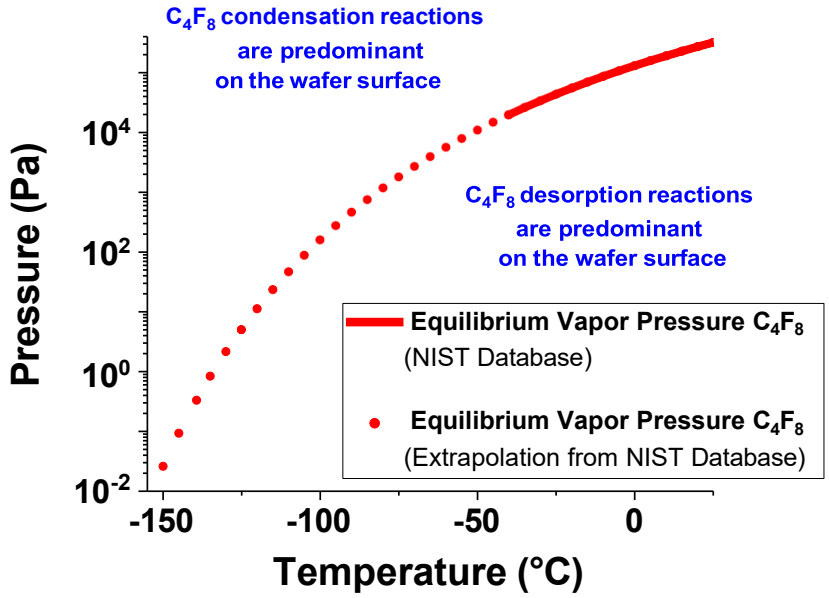

Through the extrapolation of equilibrium vapor pressures for the process gases available on the Oxford Cobra ICP tool, it was found that C_4F_8 and H_2O are the main gases which are prone to condense or at least physisorb at low substrate temperature and low pressure conditions using this reactor. This

statement is best illustrated in **figure IV.18** where the extrapolation of equilibrium vapor pressure curves of H_2O, C_4F_8, SiF_4, SF_6 and CHF_3 are shown between $1x10^{-8}$ and $1x10^{2}$ Pa. It is observed that C_4F_8 is expected to physisorb at a partial pressure of 1 Pa on a surface thermalized at around -134°C. Other process gases such as SF_6, CHF_3 and SiF_4 dispose of equilibrium vapor pressure curves which are very close to fit in the operational conditions of the reactor yet their saturation vapor pressures near -150°C appear to be slightly too high in theory (just above 10 Pa). It should be noted that the evaluation of water vapor (H_2O) condensation in these conditions is of upmost importance as it is inherently present in the chamber due to the reactor leakage (incoming atmospheric pressure to the vacuum space through its leaks) and outgassing sources (desorption of water vapor from the reactor walls) [304]. Moreover, H_2O has a relatively high equilibrium vapor pressure compared to the other process gases. Therefore, estimating its partial pressure in the reactor is crucial as the condensation of water vapor on substrate surfaces has a detrimental effect if it is too important during thin-layer deposition or etching processes [56,56,275,349].

Figure IV.17: Extrapolation of equilibrium vapor pressure curves of eventual byproduct gases generated by cryogenic etch processing using $SiF_4/H_2/O_2$ gases on the Oxford ICP tool

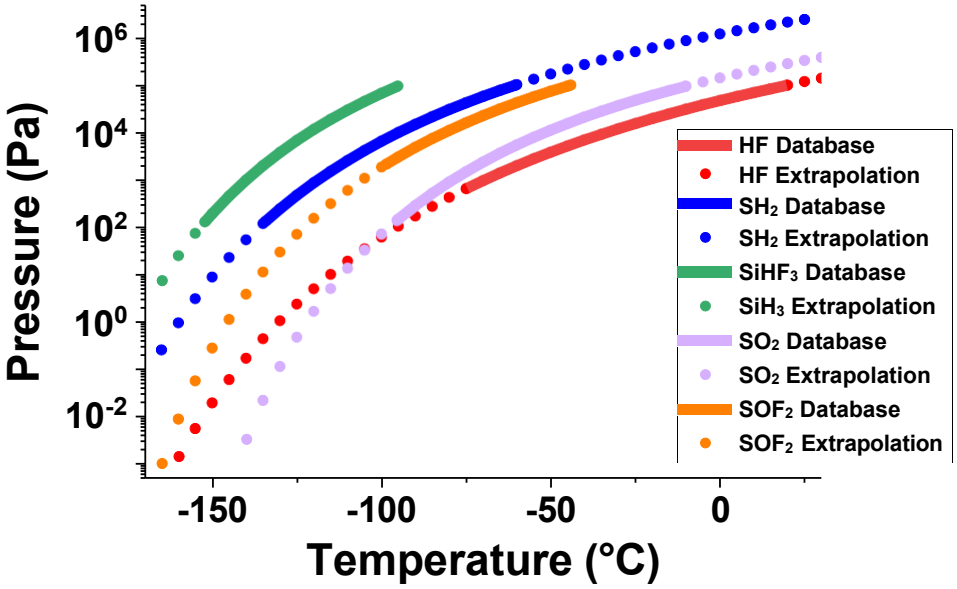

To evaluate the impact of water condensation in the operating experimental conditions of the Oxford ICP tool, the maximal leak rate ($5.0\ x10^{-3}$ Pa.min^{-1}) was taken into account and converted to a maximal air flow rate of $2.8\ x10^{-3}$ sccm using the reactor volume. At a base pressure of $1.0\ x10^{-5}$ Pa, the partial pressure of water vapor in the ICP reactor is approximately equal to $1.2\ x10^{-7}$ Pa (atmospheric temperature of 20°C with 50% humidity). In these thermodynamic conditions, H_2O is expected to condense on surfaces which are thermalized under -125°C (**see figure IV.18**).

As a result, the deposition rate (D_R) or condensation rate of H_2O was estimated in these conditions using **equation IV.2** to first determine a H_2O impingement rate (Φ) which was then converted to a deposition rate (or condensation rate) using **equation IV.13**. In this case, an H_2O impingement rate of

4.4 x10^{15} molecules.m^{-2}.s^{-1} was determined with a H_2O molecular mass of 2.99 x10^{-26} kg and a gas temperature of 20°C.

Figure IV.18: Extrapolation of equilibrium vapor pressure curves of interest gases in the processing pressure range available on the Oxford ICP tool

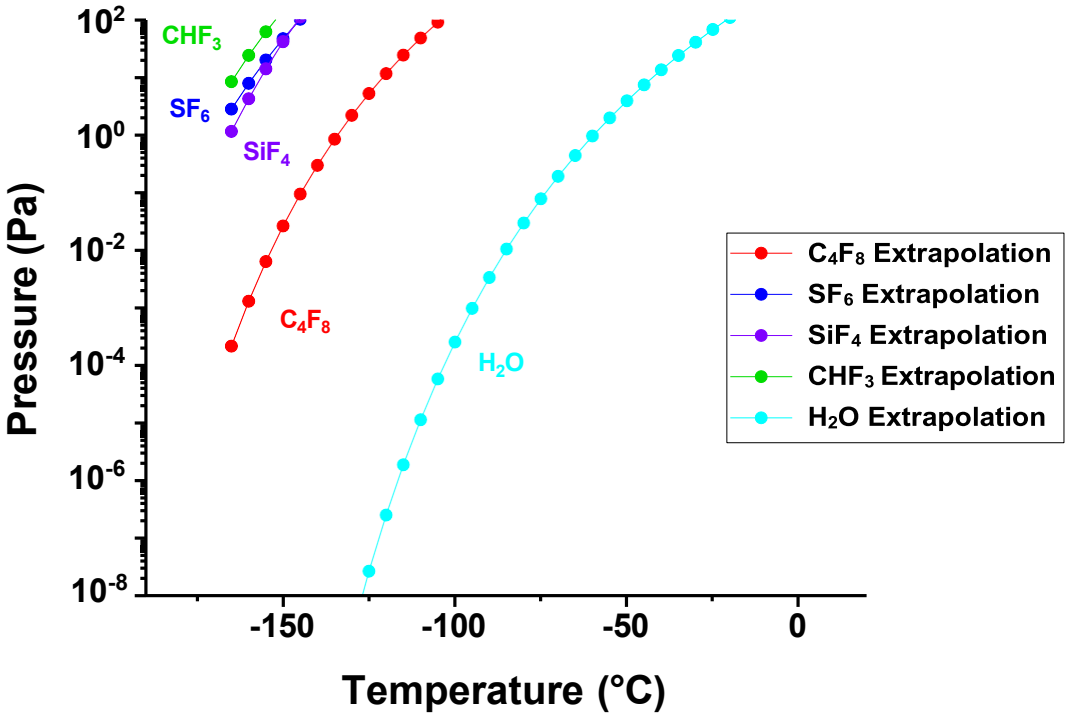

Equation IV.13: Deposition rate due to physisorption or condensation of incident molecules

$$D_R = \frac{\Phi . M . S}{N_A . \rho} \leftrightarrow S = \frac{D_R . N_A . \rho}{\Phi . M}$$

In this equation, M corresponds to the molar mass (expressed in kg.mol^{-1}), S to the sticking coefficient, N_A corresponds to the Avogadro constant ($\simeq$ 6.022 x10^{23} molecules.mol^{-1}) and ρ to the density of the condensed phase (expressed in kg.m^{-3}).

Therefore, a maximal H_2O condensation deposition rate of 1.3 x10^{-4} nm.s^{-1} was calculated in these experimental conditions. This approximation was realized by assuming a sticking coefficient equal to 1 as well as an infinite residence time. This relatively low H_2O condensation rate coincides with the experimental results obtained through the study of c-C_4F_8 physisorption in these conditions using the Oxford ICP reactor which will be presented hereafter (**section 4.3.3**). Indeed, no consistent H_2O physisorption or condensation is observed using in-situ ellipsometry at the surface of SiO_2 thin-layer samples at base pressure. During these experiments, c-C_4F_8 physisorption or condensation rates of up to 80 nm.s^{-1} were monitored during c-C_4F_8 (and argon) gas injections where the total chamber pressure was brought up to 1.2 x10^{-1} Pa.

4.3.3 Study of c-C_4F_8 adsorption on SiO_2 substrates in relation to substrate temperature

4.3.3.1 Introduction and experimental method

In the context of this research project, it was decided to study c-C_4F_8 adsorption on SiO_2 substrates at very low pressures in relation to temperature. Indeed, the physisorption properties of this gas were previously explored in similar conditions for the implementation and study of a cryogenic atomic layer etching process [274,275]. However, in this case, the goal was to assess the evolution of the sticking coefficient of c-C_4F_8 in relation to substrate temperature and estimate the impact of adsorption mechanisms which may take place during plasma etching processes performed in the same conditions in addition to chemisorption reactions with the substrate surface. As it was observed in **figures IV.15 and IV.18**, the extrapolation of its equilibrium vapor pressure curve shows that it should be the most eligible gas for this particular study among all other gases available on the etching tool given its hardware capabilities (pressure order value between 1.0 $x10^{-2}$ Pa and 13.33 Pa and minimal substrate temperature of -150°C).

Through preliminary experimentation, it was decided to focus on c-C_4F_8 adsorption at very low pressures with the APC valve fully open in order to reduce water condensation as much as possible and to extend the residence time of c-C_4F_8 adsorbed species on the substrate surfaces. This choice was preferred over closed APC valve experimentation because it enabled the study of adsorption and desorption reactions at relatively stable pressures and thereby to retrieve stable reaction rates. At first, the goal was to study very thin physisorbed layers (< 1 nm) but it was found to be too complicated and time consuming to implement from an experimental point of view. Indeed, the adsorption rates of C_4F_8 were found to be too important in these conditions once the saturation pressure was exceeded with C_4F_8 condensed layers reaching up to 2 µm. In this case, with C_4F_8 adsorbed layer thicknesses exceeding 10 monolayers (> 1 nm), it is more appropriate to refer to as capillary or film condensation rather than physisorption. Nevertheless, these two physical adsorption regimes will be englobed together in this particular study as the main focus was to evaluate the evolution of the sticking coefficient of incident c-C_4F_8 molecules in relation to the process parameters.

To assess the evolution of the condensation properties of C_4F_8 on SiO_2 in relation to the substrate temperature, a parametric study was implemented and is resumed in **table IV.9**. For this study, the substrate temperature was varied from -130°C to -150°C at an interval of 5°C where C_4F_8 was injected at two different flow rates (no plasma) which corresponded to two different partial pressures. The C_4F_8 flow rates (5 sccm, 20 sccm or 100 sccm), as well as the injection and pumping periods were defined at each substrate temperature through the analysis of preliminary test results. Indeed, it was found that the adsorption rate of c-C_4F_8 on SiO_2 (sticking coefficient) was very low in these conditions at -130°C and -135°C even for high C_4F_8 flow rates (low C_4F_8 partial pressure). However, the sticking and residence time of C_4F_8 species becomes relatively important at -140°C even at low C_4F_8 flow rates (low C_4F_8 partial pressure). Therefore, it was decided to test a common flow rate (20 sccm) and another flow

rates (5 sccm or 100 sccm) to either maximize or limit the residence time of C_4F_8 depending on the substrate temperature. For all of these tests, a continuous argon flow (20 sccm) was injected in the ICP reactor (through the source injection channel) in order to stabilize the base pressure during all these tests at a value of 7.2 $x10^{-2}$ Pa. For each test, a minimum of 3 adsorption and subsequent desorption cycles were repeated in order to assess process repeatability. A descriptive diagram of a C_4F_8 adsorption and subsequent desorption cycle is presented in **figure IV.19**. In this case, at -145°C, a C_4F_8 layer adsorbs on the SiO_2 surface as it is injected in the ICP reactor with a flow rate of 20 sccm over 30 seconds (orange zone corresponding to the C_4F_8 gas injection period). Once the C_4F_8 injection is stopped (green zone corresponding to the beginning of the pumping period), its partial pressure decreases under its saturation pressure which leads to C_4F_8 desorption from the SiO_2 surface at a stable rate until it has fully desorbed (blue zone corresponding to the end of the pumping period before a subsequent C_4F_8 injection period).

Table IV.9: List of process parameters used for the C_4F_8 adsorption study on SiO_2 substrates at cryogenic temperatures

Substrate temperature (°C)	c-C_4F_8 flow rate (sccm)	c-C_4F_8 injection period (s)	Pumping period (min)
-130°C	20 sccm	90 s	4 mins
	100 sccm	90 s	4 mins
-135°C	20 sccm	60 s	4 mins
	100 sccm	60 s	4 mins
-140°C	20 sccm	45 s	3.25 mins
	100 sccm	45 s	3.25 mins
-145°C	5 sccm	30 s	7 mins
	20 sccm	30 s	7 mins
-150°C	5 sccm	15 s	10 mins
	20 sccm	15 s	10 mins

For this study, SiO_2 thin film samples were chosen and glued to 4'' SiO_2 carrier wafers in order to monitor precisely the evolution of the C_4F_8 adsorbed layer using in-situ ellipsometry (represented in red in **figure IV.19**). In the meantime, MID mass spectrometry acquisitions were realized in order to monitor the presence of C_4F_8 in the ICP chamber during the tests ($C_2F_4^+$ MID intensity represented in black in **figure IV.19)**. Through preliminary testing, it was found that $C_2F_4^+$ (100 amu) was the main ion detected by the mass spectrometer in a continuous profile mode acquisition between 0 and 200 amu. In these C_4F_8 gas injection conditions, the other main fluorocarbon species detected were CF^+, CF_3^+ and $C_3F_5^+$ ions (respectively 31, 69 and 131 amu). Therefore, for this study, it was decided to monitor these fluorocarbon species as well as water (18 amu), argon (40 amu) and silicon (28 amu) by MID mass spectrometry at a sampling rate of 144 ms. The average $C_2F_4^+$ MID peak intensities during the C_4F_8 gas injections are given for each test in **table IV.10**. The average ion peak intensity percentages of the other species monitored through MID mass spectrometry are also disclosed for each C_4F_8 adsorption test.

Mass spectroscopy data was analyzed by taking into account the following considerations. It was assumed that C_4F_8 gas injection (adsorption) periods started once the $C_2F_4^+$ MID peak intensity signal was above its noise level (> 1000 c/s). These gas injection periods were presumed to be finished once the $C_2F_4^+$ MID peak intensity signal value decreased by more than 50% than the average value which was observed during the previous C_4F_8 gas injection (stabilized value as it can be seen in the orange gas injection period represented in **figure IV.19**). Once the previous gas injection period is finished, it is assumed that the subsequent C_4F_8 desorption period starts and lasts until the $C_2F_4^+$ MID peak intensity signal value reaches and stays at the noise level for 3 consecutive measurements (< 1000 c/s).

The chamber pressure in the ICP reactor was continuously monitored during these tests in order to estimate the C_4F_8 partial pressure during the adsorption and desorption phases. As can be seen in **figure IV.19**, which depicts a single C_4F_8 adsorption and subsequent desorption cycle at -145°C, C_4F_8 appears to condense at a steady rate during the gas injection period. During this phase, the $C_2F_4^+$ MID signal intensity is constant. Once the C_4F_8 gas injection is stopped (green zone), the $C_2F_4^+$ MID signal intensity drops to an intermediate level which is also constant and proportional to the C_4F_8 partial pressure in the chamber during its desorption from the SiO_2 sample surface. As the last C_4F_8 multilayers desorb from the surface, the $C_2F_4^+$ MID signal intensity rapidly decreases to reach its noise level during the pumping period where the C_4F_8 partial pressure is equal to 0.0 Pa ($C_2F_4^+$ MID noise level between 200 and 1200 c/s in these experimental conditions).

Table IV.10: Average $C_2F_4^+$ MID ion peak intensity and average intensity percentages of other species measured during C_4F_8 gas injections tests in relation to the c-C_4F_8 flow rate and substrate temperature

Substrate temperature (°C)	c-C_4F_8 flow rate (sccm)	Average $C_2F_4^+$ MID ion peak intensity during C_4F_8 gas injections (c/s)	Average MID ion peak intensity percentages during C_4F_8 gas injections (%)						
			$C_2F_4^+$	CF^+	CF_3^+	$C_3F_5^+$	H_2O^+	Ar^+	Si^+
-130°C	20 sccm	85,000	24.2	7.3	6.6	10.7	9.0	41.4	0.8
	100 sccm	282,859	37.8	11.3	10.4	16.9	6.5	16.4	0.8
-135°C	20 sccm	74,786	21.2	6.4	5.9	9.4	18.4	37.2	1.6
	100 sccm	230,778	35.8	10.6	9.8	15.8	7.8	19.4	0.8
-140°C	20 sccm	65,138	21.6	6.4	5.8	9.4	11.2	44.6	1.1
	100 sccm	184,083	34.4	10.2	9.3	15.2	7.0	23.1	0.7
-145°C	5 sccm	21,367	9.3	2.8	2.6	4.2	12.9	67.1	1.0
	20 sccm	58,161	17.4	5.3	4.9	7.6	16.4	46.8	1.5
-150°C	5 sccm	14,259	6.9	2.0	2.1	3.0	20.9	63.0	2.1
	20 sccm	42,988	15.7	4.8	4.4	6.8	18.1	48.5	1.8

Figure IV.19: Descriptive diagram of a C_4F_8 condensation and subsequent desorption cycle on a SiO_2 substrate at -145°C

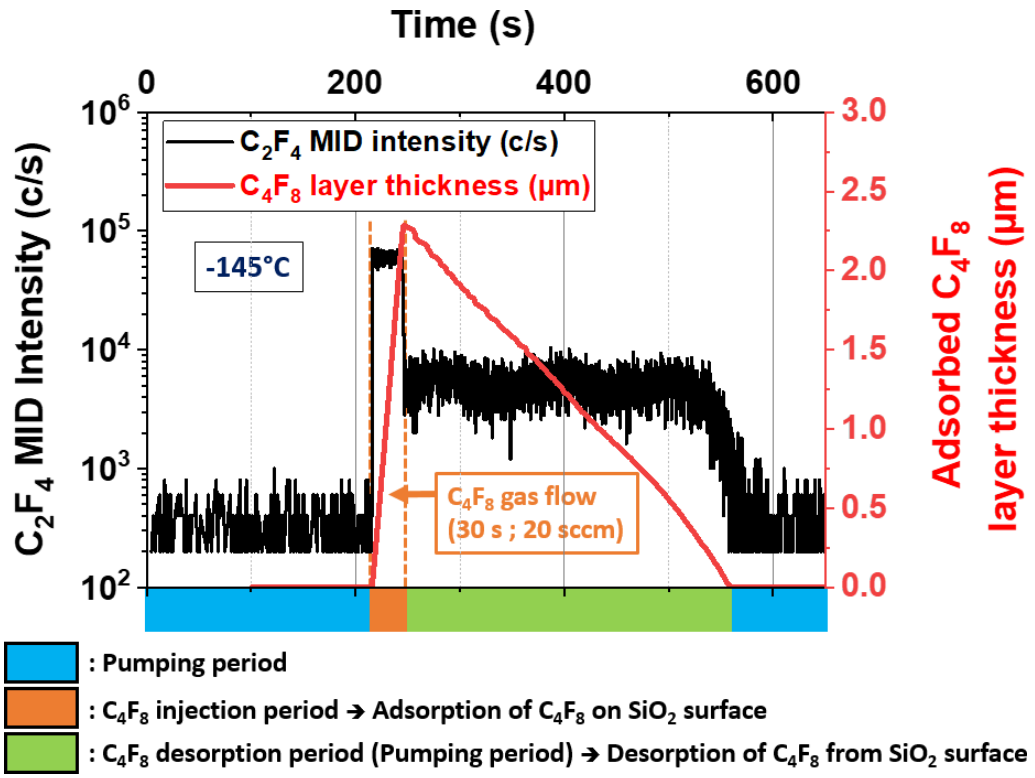

4.3.3.2 Parametric study of c-C_4F_8 adsorption and subsequent desorption cycles in relation to the substrate temperature

In general, C_4F_8 adsorption experiments (**table IV.9**) were successful except for the process point at -140°C using C_4F_8 gas injections at 100 sccm. Indeed, for this particular experiment, the pumping periods were too short to allow the complete desorption of C_4F_8 material from the SiO_2 surface and its condensation rate during the first injection period was too important to model and evaluate using in-situ ellipsometry. The average condensation rates and chamber pressure values during C_4F_8 gas injections are disclosed in **table IV.11** where the respective c-C_4F_8 partial pressures were also evaluated in every case. The average desorption rates and chamber pressure values evaluated during desorption periods are shown in **table IV.12** for condensation process experiments performed at -145°C and -150°C.

In these low pressure conditions, no subsequent C_4F_8 adsorption (in this case physisorption) was detected by in-situ ellipsometry on the SiO_2 surface material when it was thermalized at -130°C and -135°C (C_4F_8 gas injections of 20 or 100 sccm). However, C_4F_8 desorption periods, ranging from 11.5 to 122.1 seconds in average, were clearly monitored through mass spectrometry analysis for these process points. This observation suggests that C_4F_8 may still physisorb but in very low quantities on the SiO_2 surface or that it deposits elsewhere on the substrate holder. With regard to this last statement, it

cannot be ruled out that C_4F_8 may preferentially physisorb or deposit on the wafer carrier rather than on the glued SiO_2 sample as it should be at the same temperature or slightly colder. Very mild C_4F_8 physisorption is observed at -140°C with gas injections of 20 sccm which seems to indicate that the C_4F_8 saturation pressure is achieved at a higher flowrate (between 20 and 100 sccm) at -140°C. Nevertheless, for process points under -140°C, excellent conformity was observed between the mass spectrometry acquisitions and the in-situ ellipsometry acquisitions as it is illustrated in **figure IV.19**. In these cases, their synchronicity during the desorption steps suggests that C_4F_8 adsorbs (in this case condenses) with nearly the same efficiency on the thermalized SiO_2 glued sample and carrier wafer surfaces.

On the whole, C_4F_8 condensation and desorption rates were found to be quite homogeneous for the three cycles applied for each process test as it can be seen in **tables IV.11 and IV.12**. During the C_4F_8 injection and desorption periods, identical and fairly constant chamber pressure values were monitored for each of the three cycles applied during the process tests. For process points tested at temperatures of -140°C and under, the chamber pressure during the C_4F_8 desorption periods was clearly above the base pressure monitored during constant Ar gas injection (>0.072 Pa). This value tended to decrease at the end of the desorption periods to reach 0.072 Pa, each time before the end time determined through mass spectrometry analysis.

Table IV.11: c-C_4F_8 partial pressures and average c-C_4F_8 adsorption rates monitored during the gas injection phases (C_4F_8 adsorption study on SiO_2 substrates)

Substrate temperature (°C)	c-C_4F_8 flow rate (sccm)	Chamber pressure during c-C_4F_8 injection periods (Pa)	c-C_4F_8 partial pressure during gas injection periods (Pa)	Average c-C_4F_8 adsorbed layer thickness after gas injection period (nm)	Average adsorption rate (nm/s)
-130°C	20 sccm	1.56×10^{-1} Pa	8.4×10^{-2} Pa	≈ 0.0	≈ 0.0
	100 sccm	3.93×10^{-1} Pa	3.21×10^{-1} Pa	≈ 0.0	≈ 0.0
-135°C	20 sccm	1.56×10^{-1} Pa	8.4×10^{-2} Pa	≈ 0.0	≈ 0.0
	100 sccm	3.33×10^{-1} Pa	2.61×10^{-1} Pa	≈ 0.0	≈ 0.0
-140°C	20 sccm	1.44×10^{-1} Pa	7.2×10^{-2} Pa	≈ 0.4	$< 9.0 \times 10^{-3}$
	100 sccm	2.83×10^{-1} Pa	2.11×10^{-1} Pa	Not applicable	Not applicable
-145°C	5 sccm	9.2×10^{-2} Pa	2.0×10^{-2} Pa	403.0 ± 29.1	13.4 ± 1.0
	20 sccm	1.23×10^{-1} Pa	5.1×10^{-2} Pa	2275.1 ± 7.8	75.8 ± 0.3
-150°C	5 sccm	8.8×10^{-2} Pa	1.6×10^{-2} Pa	276.1 ± 5.7	18.4 ± 0.4
	20 sccm	1.20×10^{-1} Pa	4.8×10^{-2} Pa	1171.7 ± 5.5	78.1 ± 0.4

Table IV.12: $c\text{-}C_4F_8$ partial pressures and average $c\text{-}C_4F_8$ desorption rates monitored during the desorption periods (C_4F_8 adsorption study on SiO_2 substrates)

Substrate temperature (°C)	$c\text{-}C_4F_8$ flow rate (sccm)	Average $c\text{-}C_4F_8$ desorption period (s)	Chamber pressure during $c\text{-}C_4F_8$ desorption periods (Pa)	$c\text{-}C_4F_8$ partial pressure during $c\text{-}C_4F_8$ desorption periods (Pa)	Average desorption rate (nm/s)
-130°C	20 sccm	11.5 ± 3.9	≈ 7.3 x10^{-2} Pa	≤ 1 x10^{-3} Pa	Not applicable
	100 sccm	30.0 ± 18.3	≈ 7.3 x10^{-2} Pa	≤ 1 x10^{-3} Pa	Not applicable
-135°C	20 sccm	12.1 ± 5.1	≈ 7.3 x10^{-2} Pa	≤ 1 x10^{-3} Pa	Not applicable
	100 sccm	122.1 ± 3.3	≈ 7.3 x10^{-2} Pa	≤ 1 x10^{-3} Pa	Not applicable
-140°C	20 sccm	51.3 ± 14.4	≈ 8.8 x10^{-2} Pa	≈ 1.6 x10^{-2} Pa	Not applicable
	100 sccm	> 195.0	≈ 9.6 x10^{-2} Pa	≈ 2.4 x10^{-2} Pa	Not applicable
-145°C	5 sccm	51.4 ± 15.6	≈ 7.7 x10^{-2} Pa	≈ 5 x10^{-3} Pa	7.8 ± 2.4 nm/s
	20 sccm	299.4 ± 19.2	≈ 7.6 x10^{-2} Pa	≈ 4 x10^{-3} Pa	7.6 ± 0.5 nm/s
-150°C	5 sccm	123.3 ± 7.0	≈ 7.4 x10^{-2} Pa	≈ 2 x10^{-3} Pa	2.2 ± 0.1 nm/s
	20 sccm	463.3 ± 27.6	≈ 7.4 x10^{-2} Pa	≈ 2 x10^{-3} Pa	2.5 ± 0.2 nm/s

The main goal of the collection of this experimental data, was to approximate a $c\text{-}C_4F_8$ sticking coefficient for each substrate temperature that was tested during this parametric study, especially at -145°C and -150°C where a condensation or deposition rate was evaluated through in-situ ellipsometry. However, it was found that the calculation of a sticking coefficient based on **equations IV.2, IV.3 and IV.4**, for the calculation of a molecular impingement rate, as well as **equation IV.13**, for the calculation of a deposition rate due to the adsorption of incident molecules, relies on too many approximations which make the uncertainty surrounding this value far too high to be taken into consideration. Indeed, this calculation relies on the adsorption rate which is obtained through in-situ ellipsometry, the density of the deposited $c\text{-}C_4F_8$ material as well as the chamber pressure measurement given by the Penning gauge. These three parameters are source of variability and error for the following reasons.

The adsorption rate of $c\text{-}C_4F_8$ obtained by in-situ ellipsometry is based on the CF_x ellipsometry model presented in chapter II (**Chapter II.4.1.4.3: Modeling of a fluorocarbonated deposited CF_x layer**). The ellipsometry model fit result was obtained only by fitting the layer thickness and not the CF_x material. It is supposed that the dielectric properties of adsorbed C_4F_8 (presumably in solid state) should be at least slightly different from the fluorocarbonated layer deposited through C_4F_8 plasma. Moreover, it is important to note that the consideration of the adsorption rates obtained by ellipsometry in the approximation of a sticking coefficient calculation necessarily neglects eventual desorption mechanisms which may also occur from the adsorbed layer during the gas injection phases.

Concerning the density of the adsorbed $c\text{-}C_4F_8$ material, no extensive data was found for its liquid and solid phases. It is supposed that its density should range from 1.639 g.cm^{-3} to approximately 2.0 g.cm^{-3} [350,351]. Indeed, it is supposed that its density in the solid phase should be superior to its liquid density at the boiling temperature (1.639 g.cm^{-3}) and substantially lower than the density of polytetrafluoroethylene (PTFE, commonly known as Teflon) which is 2.2 g.cm^{-3}.

The chamber pressure given by the Penning gauge during the C_4F_8 gas injection phases may also be source of error in the approximation of a C_4F_8 sticking coefficient. Indeed, the pressure measurement is obtained indirectly through the measurement of an ion current through an electromagnetic field. Therefore, the pressure measurement is dependent on the gas type whereas it is usually calibrated with nitrogen or air. As a result, the c-C_4F_8 partial pressures determined during the gas injection phases and subsequent desorption periods disclosed in **tables IV.11 and IV.12** may be slightly different in reality. Moreover, two c-C_4F_8 partial pressures values can be distinguished during the gas injection phases in the case of this parametric study. The first value, which can be referred to as the total entry gas phase partial pressure, is obtained by taking into account the c-C_4F_8 partial pressure measured at 20°C where no c-C_4F_8 adsorption occurs (0.028 Pa with 5 sccm ; 0.084 Pa with 20 sccm and 0.321 Pa with 100 sccm). The second value, which can be referred to as the equilibrium gas phase partial pressure, is obtained by retracting the base pressure value due to the continuous Ar flow (20 sccm) during the C_4F_8 gas injection phases. The partial pressure values shown in **tables IV.11 and IV.12** are calculated by following this second method.

By analyzing the results obtained in **tables IV.11 and IV.12**, the experimental data collected through these process tests is in compliance with physisorption theory. Indeed, with the same gas feed, the adsorption rates (and sticking coefficient) of C_4F_8 on SiO_2 increase as the substrate temperature decreases. In the same way, at a fixed substrate temperature, the adsorption rates of C_4F_8 on SiO_2 increase when the gas feed (c-C_4F_8 partial pressure) is increased. In these low pressure conditions, with a maximal c-C_4F_8 partial pressure of 3.21 $x10^{-1}$ Pa (100 sccm at -130°C), mild adsorption (in this case physisorption) is detected starting at -135°C as the chamber pressure decreases during C_4F_8 gas injection. Between -135°C and -140°C, the equilibrium vapor pressure is exceeded which leads to important c-C_4F_8 deposition at -140°C which cannot be adequately monitored using in-situ ellipsometry. Using a maximal C_4F_8 partial pressure of 8.4 $x10^{-2}$ Pa (20 sccm at -130°C), mild physisorption starts to occur at -140°C which is hardly quantified using in-situ ellipsometry (approximately 0.4 nm deposited for each C_4F_8 gas injection step). Important adsorption occurs at -145°C which seems to indicate that the equilibrium vapor pressure is exceeded between -140°C and -145°C. The same observation can also be made using a maximal C_4F_8 partial pressure of 2.8 $x10^{-2}$ Pa (5 sccm at -130°C) although no process tests were realized using this gas feed at -130°C, -135°C and -140°C.

By comparing these results to the extrapolated equilibrium vapor pressure curve of c-C_4F_8 shown in **figure IV.18**, it can be seen that the experimental values closely fit this curve yet a slight shift is observed. Indeed, using the Antoine parameters listed in **table IV.7** the extrapolated equilibrium vapor pressure of c-C_4F_8 indicates an equilibrium vapor pressure of 2.94 $x10^{-1}$ Pa, 9.3 $x10^{-2}$ Pa and 2.6 $x10^{-2}$ Pa at respectively -140°C, -145°C and -150°C. However, it can be seen through experimentation that a c-C_4F_8 partial pressure of 2.8 $x10^{-2}$ Pa at -145°C is sufficient to enable adsorption.

The impact of substrate temperature and partial pressure on c-C_4F_8 adsorption is clearly illustrated in **figures IV.20 and IV.21** where the C_2F4^+ MID signal intensity and C_4F_8 adsorbed layer respectively

monitored through mass spectrometry and in-situ ellipsometry are compared according to different process tests.

In **figure IV.20**, the impact of substrate temperature is depicted during the three gas injection cycles using the same C_4F_8 flow rate (20 sccm).

At -135°C (**figure IV.20.a**), no physisorption is observed on the SiO_2 substrate yet very mild desorption periods can be distinguished subsequently to C_4F_8 gas injection periods.

At -140°C (**figure IV.20.b**), c-C_4F_8 physisorption is very mild on the SiO_2 substrate. It is barely observable using in-situ ellipsometry with a maximal layer of 0.4 nm after a gas injection period of 45 seconds. However, C_4F_8 desorption periods can be clearly identified through mass spectrometry where a $C_2F_4^+$ MID signal subsists above noise level for approximately 50 seconds after a C_4F_8 injection period.

At -145°C (**figure IV.20.c**), an important and steady C_4F_8 adsorption rate is detected by in-situ ellipsometry during C_4F_8 gas injection periods (≈ 76 nm/s). Long-lasting desorption periods are also clearly identified by mass spectrometry where the $C_2F_4^+$ MID signal intensity is mostly stable (approximately 6000 c/s during 5 minutes) after the gas injection periods. During these desorption periods, the C_4F_8 adsorbed layer decreases at a stable rate of approximately 7.6 nm/s.

At -150°C (**figure IV.20.d**), a physisorption rate of roughly 78 nm/s is monitored during the gas injection periods. Desorption periods of approximately 460 seconds can be identified where the $C_2F_4^+$ MID signal intensity is just above the noise level (> 1000 c/s) in these experimental conditions. At this point, the desorption rate is roughly equal to 2.5 nm/s.

More generally, it can be seen through these figures that C_4F_8 adsorption and subsequent desorption properties collected through mass spectrometry and in-situ ellipsometry are mostly repeatable from cycle to cycle for each process test. The decrease of the SiO_2 substrate temperature from -135°C to -150°C in these low-pressure conditions allow C_4F_8 to adsorb more efficiently and to remain on the surface much longer.

Figure IV.20: Evolution of the adsorbed C_4F_8 layer thickness monitored by in-situ ellipsometry on a SiO_2 sample surface and C_2F^+ MID signal intensity acquired through mass spectrometry during C_4F_8 adsorption tests in relation to substrate temperature

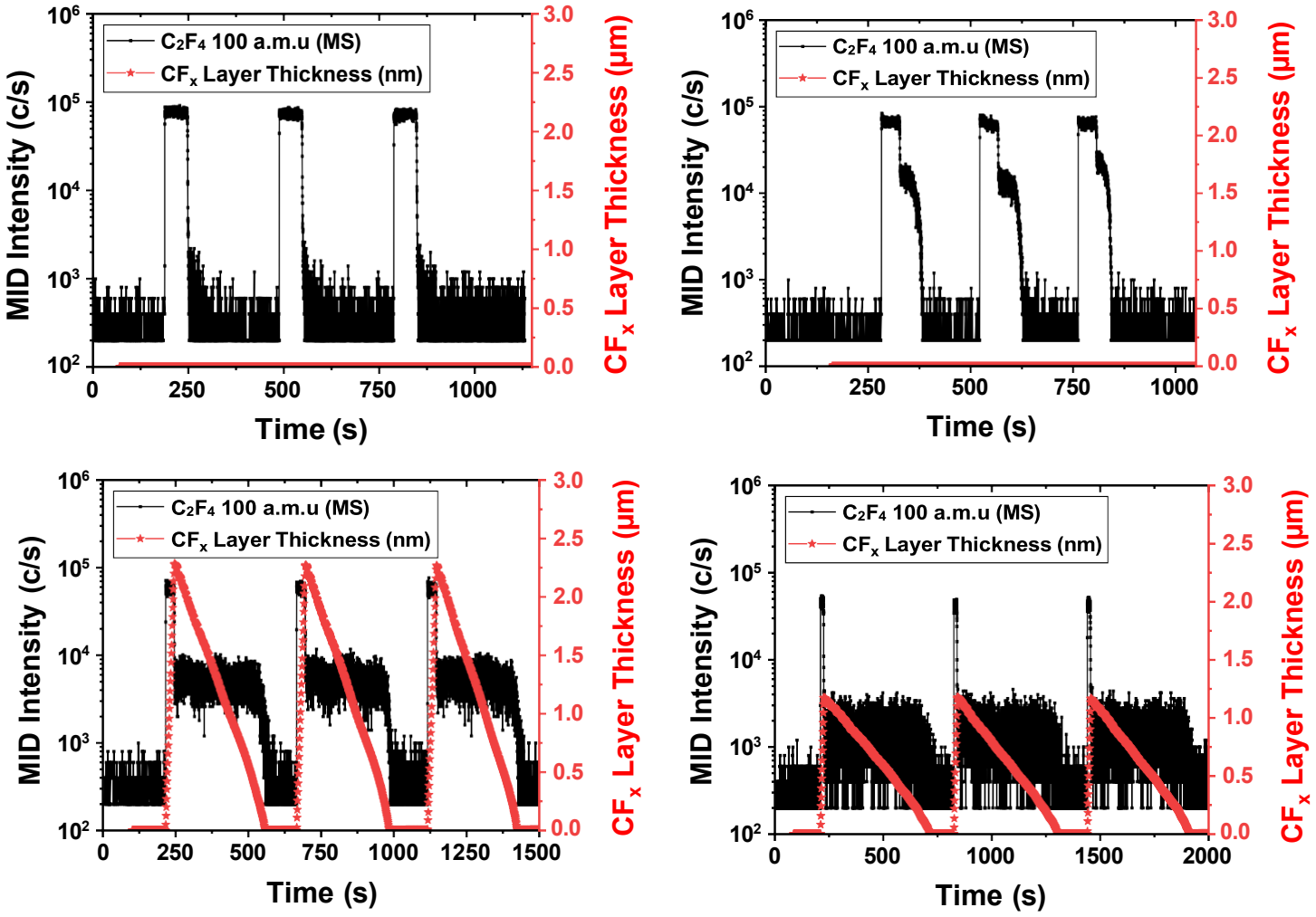

In **figure IV.21**, the impact of C_4F_8 partial pressure on adsorption properties is shown at -145°C and -150°C during a single gas injection cycle.

At -145°C, a physisorption rate of 13.4 nm/s is monitored with a flow rate of 5 sccm which corresponds to a C_4F_8 partial pressure of 2.8 $x10^{-2}$ Pa (**figure IV.21.a**). A desorption period of roughly 50 seconds is then detected through mass spectrometry with an intensity of approximately 6000 c/s where a constant desorption rate of 7.8 nm/s is monitored through in-situ ellipsometry.

Using a C_4F_8 flow rate of 20 sccm which corresponds to a C_4F_8 partial pressure of 8.4 $x10^{-2}$ Pa (**figure IV.21.b**), the adsorption rate is more important during the C_4F_8 gas injection period (approximately 76 nm/s). However, the desorption rate (7.6 nm/s) is nearly identical to one observed in **figure IV.21.a**. Indeed, the chamber pressure (7.7 $x10^{-2}$ Pa after a C_4F_8 gas injection of 5 sccm and 7.7 $x10^{-2}$ Pa after a C_4F_8 gas injection of 20 sccm) and the $C_2F_4^+$ MID signal intensity (also roughly equal to 6000 c/s) are nearly identical. As a result, the desorption period (roughly 5 minutes) is longer and proportional

to the amount of C_4F_8 which has previously adsorbed on the SiO_2 substrate (approximately 2.3 µm after a C_4F_8 gas injection of 20 sccm and 0.4 µm after a C_4F_8 gas injection of 5 sccm).

At -150°C, an adsorption rate of 18.4 nm/s and 78.1 nm/s are monitored with a flow rate of respectively 5 and 20 sccm (**figures IV.21.c and IV.21.d**) which are equivalent to a C_4F_8 partial pressure of 2.8 $x10^{-2}$ Pa and 8.4 $x10^{-2}$ Pa. Following the gas injection periods, a similar desorption rate is monitored in both cases through in-situ ellipsometry, respectively 2.2 and 2.5 nm/s with a $C_2F_4^+$ MID signal intensity just above the noise level (>1000 c/s). The average desorption periods last roughly 2 minutes after a C_4F_8 injection of 5 sccm whereas they last approximately 7 minutes and 40 seconds after a C_4F_8 injection of 20 sccm.

Figure IV.21: Evolution of the adsorbed C_4F_8 layer thickness monitored by in-situ ellipsometry on a SiO_2 sample surface and $C_2F_4^+$ MID signal intensity acquired through mass spectrometry during C_4F_8 adsorption tests at -145°c and -150°C relation to the C_4F_8 flow rate

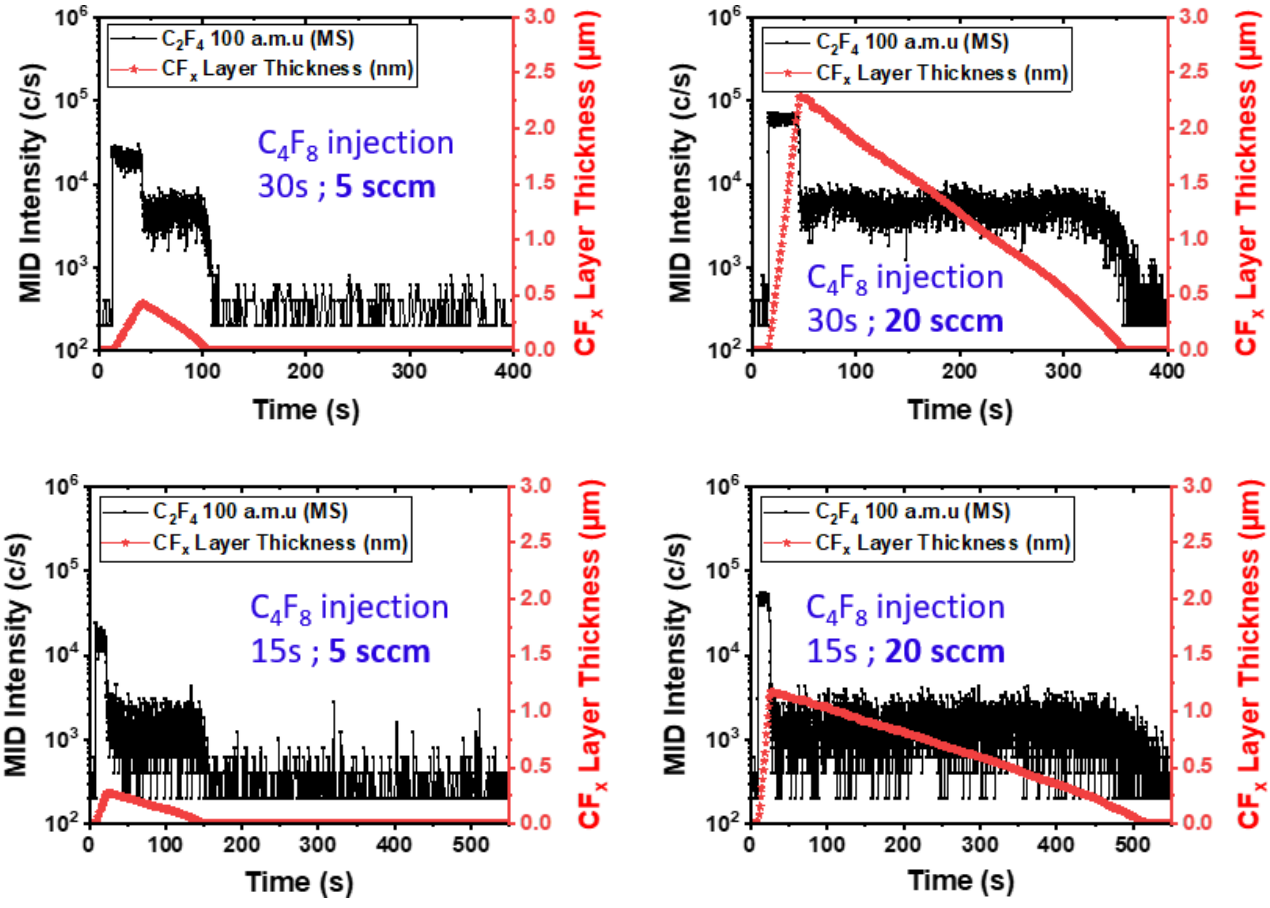

4.3.3.3 Global Analysis

The analysis of experimental data acquired during c-C_4F_8 adsorption tests enables the observation high process repeatability for each adsorption and subsequent desorption cycle. Excellent synchronicity was observed for each characterization technique (in-situ ellipsometry and mass spectrometry) as illustrated in **figures IV.20 and IV.21**. Through this parametric study, it is clearly observed that the substrate temperature and C_4F_8 partial pressure both have an important impact on c-C_4F_8 adsorption and its residence time on SiO_2 substrates once the equilibrium vapor pressure of c-C_4F_8 is approached.

The experimental conditions, setup and methodology did not allow to study extensively c-C_4F_8 physisorption with satisfactory precision. Indeed, this would have required to study the growth of very thin c-C_4F_8 adsorbed films. Moreover, the sensitivity of the mass spectrometer was too high to be able to distinguish very low desorption flows from its proper noise level (several hundred of counts per second). In these very low-pressure conditions, the slight modification of the c-C_4F_8 flow rate resulted in a sharp increase of its partial pressure above the equilibrium vapor pressure. In retrospect, the constant injection of an argon flow (20 sccm) was a good strategy in order to dilute the effect of unique c-C_4F_8 gas injection which limited the impact on its partial pressure in the chamber. Nevertheless, for the study of c-C_4F_8 physisorption, it may have been wiser to carry out this study by fixing a certain APC valve position and to inject a higher constant flow of argon in order to limit more efficiently partial pressure bursts of c-C_4F_8. In instance, at a substrate temperature comprised between -140°C and -130°C, the equilibrium vapor pressure of c-C_4F_8 is theoretically between 0.29 and 2.16 Pa, which may have been a more adequate pressure range to find a suitable process point for this particular study. Indeed, in these experimental conditions, it can be seen that the adsorption regime rapidly shifts from physisorption where only very few c-C_4F_8 molecules adsorb on rare SiO_2 adsorption sites (≥-140°C) to condensation where high c-C_4F_8 deposition rates of up to 78.1 nm/s were observed at lower temperatures with the same C_4F_8 gas injection conditions.

Nevertheless, these experiments enabled to evaluate the c-C_4F_8 equilibrium vapor pressure between -130°C and -150°C and to compare them with theoretical values obtained from the extrapolation of its equilibrium vapor pressure curve. It was found that the differences between the theoretical and experimental values were not significant. For example, at -140°C, a theoretical equilibrium vapor pressure of 2.94 $x10^{-1}$ Pa is estimated for c-C_4F_8 whereas an experimental value in the range of 1.0 $x10^{-1}$ Pa can be roughly evaluated.

By recontextualizing these results in relation to the c-C_4F_8 plasma passivation and Bosch processes studied previously, it can be deduced that c-C_4F_8 physisorption and condensation reactions do not take part in the fluorocarbon deposition mechanisms at -100°C. Indeed, at -100°C, the theoretical c-C_4F_8 equilibrium vapor pressure is in the range of 161 Pa whereas the pressure applied for the fluorocarbon plasma passivation steps did not exceed 2.0 Pa. However, at -150°C, where a c-C_4F_8 plasma passivation process was tested (**Chapter IV.1.2.2; figure IV.5**), the equilibrium vapor pressure was greatly exceeded (2.0 Pa > 0.026 Pa). As a result, c-C_4F_8 physisorption was occurring on the SiO_2 surface alongside fluorocarbon plasma deposition. This phenomenon surely explains why the increase

of the fluorocarbon deposition rate appears to slightly impede at -150°C (**figure IV.5**). Indeed, the portion of physisorbed c-C_4F_8 desorbs from the deposited fluorocarbon layer after the plasma process which also explains why the refractive index of the film appears to decrease at -150°C especially in the case where c-C_4F_8 was injected though the gas-ring channel.

4.3.4 Summary of chapter IV (English)

Further to Bosch process tests at cryogenic temperatures, a parametric study was subsequently carried out on the C_4F_8 plasma passivation step in relation to the substrate temperature. An in-situ ellipsometry study of the deposition rate of fluorocarbon on both polycrystalline silicon (p-Si) and SiO_2 substrates was realized by varying the C_4F_8 gas flow at -100°C and +20°C. This study showed that the thickness of fluorocarbon material deposited is approximately a hundred times thicker at -100°C using the same process conditions. Fluorocarbon deposition was then evaluated in relation to substrate temperature between -150°C and +20°C for both injection channels. A global increase in the refractive index at 2 eV of the fluorocarbon passivated layer was observed at decreasing temperatures. However, no major difference was observed between the refractive index values obtained according to the injection channel between -100°C and +20°C. Mass spectrometry acquisitions of these plasma processes at ambient temperature enabled to show that C_4F_8 source injections leads to further fluorocarbon dissociation in comparison to gas-ring injections near the substrate area. Indeed, the intensity of heavier carbonated species, in this case $C_2F_4^+$ and $C_3F_5^+$, is multiplied by roughly five for gas-ring injections. Therefore, it is strongly believed, judging by these results, that the chemical composition of the fluorocarbon passivation layer should be different according to the C_4F_8 injection channel that is used during the process. This statement can only be confirmed through XPS spectroscopy.

A complementary study was also carried out concerning the physisorption and condensation of c-C_4F_8 on a SiO_2 substrate between -130°C and -150°C. The main objective of this study was to evaluate whether these mechanisms take a substantial role during c-C_4F_8 plasma deposition at cryogenic temperatures. The second aim of this study was to quantify the evolution of the c-C_4F_8 sticking coefficient in relation to the substrate temperature and c-C_4F_8 partial pressure in the chamber. The different types of adsorption mechanisms (physisorption, chemisorption) and phase transition mechanisms (deposition and condensation) were introduced to define the notion of saturation vapor pressure and to evaluate the equilibrium vapor pressure curve of c-C_4F_8 by extrapolation. By carrying out c-C_4F_8 gas injection cycles interspersed with chamber purge periods, the successive adsorption and subsequent desorption phenomena of c-C_4F_8 were characterized in a fairly precise and repeatable manner through in-situ ellipsometry and mass spectroscopy. Different adsorption and desorption rates were recorded in relation to c-C_4F_8 partial pressure between -130°C and -150°C. However, the calculation of a reliable C_4F_8 sticking coefficient for each tested substrate temperature was found to be too hazardous in these experimental conditions. This parametric study did not enable to analyze c-C_4F_8 physisorption precisely but allowed to monitor c-C_4F_8 condensation once the saturation vapor pressure was exceeded within the chamber. The experimental results obtained suggest that physisorption and condensation of c-C_4F_8 are negligible at -100°C during c-C_4F_8 plasma passivation steps at 2.0 Pa studied previously during the Bosch process tests. In these process conditions, c-C_4F_8 condensation only starts to take place at -130°C when its saturation vapor pressure is reached.

4.3.5 Résumé du chapitre IV (français)

A la suite, des essais de gravure Bosch à température cryogénique, une étude paramétrique du procédé de passivation par plasma C_4F_8 a ensuite été réalisée en fonction de la température du porte-substrat. La vitesse de dépôt de la couche de passivation fluorocarbonée a été caractérisée à -100°C et à +20°C en fonction du débit de C_4F_8 sur des échantillons collés de silicium polycristallin (p-Si) et de SiO_2. En caractérisant la couche déposée par éllipsométrie in-situ, celle-ci est environ cent fois plus épaisse pour un procédé réalisé à -100°C par rapport au même procédé réalisé à +20°C. Par la suite, la vitesse de dépôt a été étudiée en fonction de la température entre +20°C et -150°C en injectant le gaz soit par la source ou par le gas-ring. Les résultats indiquent que l'indice de réfraction de la couche fluorocarbonée mesurée à 2 eV augmente sensiblement en abaissant la température du porte-substrat jusqu'à -120°C mais aucune différence significative n'a été relevée entre les dépôts réalisés en injectant le gaz par la source ou par le gas-ring entre -100°C et +20°C. Une étude complémentaire par spectrométrie de masse a démontré que les espèces fluorocarbonées au sein du plasma étaient plus dissociées lorsque le C_4F_8 était injecté par la source par rapport à un procédé identique utilisant le gas-ring. Il est supposé que leurs compositions chimiques de surface soient différentes mais seulement une étude par spectroscopie XPS pourrait le démontrer.

Dans un second temps, une étude auxiliaire a été réalisée concernant la condensation du c-C_4F_8 sur substrat collé de SiO_2 entre -130°C et -150°C. Le but principal de cette étude était d'évaluer si l'adsorption de c-C_4F_8 pouvait avoir une part substantielle dans le dépôt plasma réalisé à température cryogénique mais aussi d'évaluer l'évolution du coefficient de collage du c-C_4F_8 en fonction de la température du porte-substrat et sa pression partielle au sein de la chambre. Les différents types de mécanismes d'adsorption (physisorption, chimisorption) ainsi que les mécanismes de transition de phases (liquéfaction et condensation) ont été introduits pour définir la notion de vapeur saturante et d'évaluer la courbe de pression saturante du c-C_4F_8 par extrapolation. En réalisant des cycles d'injection de gaz c-C_4F_8 entrecoupés de période de purge, les phénomènes d'adsorption et de désorption successives du c-C_4F_8 ont pu être caractérisés de manière assez précise et répétitive par ellipsométrie in- situ et spectroscopie de masse. Différents taux d'adsorption et de désorption ont été relevés en fonction de la pression partielle de c-C_4F_8 entre -130 °C et -150°C. Cependant, les conditions expérimentales n'ont pas permis le calcul de coefficients de collage du c-C_4F_8 suffisamment fiable en fonction de la température. Celles-ci n'ont pas pu permettre d'étudier avec précision le phénomène de physisorption du c-C_4F_8 mais ont plutôt permis d'étudier sa condensation lorsque sa pression de vapeur saturante était dépassée au sein de la chambre. L'approximation expérimentale des pressions saturantes sont dans le même ordre de grandeur que les valeurs théoriques obtenues par extrapolation mais sont sensiblement plus faibles. Ces expériences ont permis de démontrer que la physisorption et la condensation du c-C_4F_8 sont négligeables à -100°C lors des dépôts plasma c-C_4F_8 à 2.0 Pa étudiés précédemment concernant les essais de procédé Bosch. Celles-ci prennent une part plus significative au dépôt fluorocarboné à partir de -130°C où la pression de vapeur saturante est atteinte.

5 Chapter V: Development of a CF_4/SF_6 Bosch-type process at cryogenic temperatures

5.1 Introduction

In this chapter, CF and CF_2 radical densities were first studied in relation to substrate temperature by absorption spectroscopy during fluorocarbon plasma processing. The acquisitions were realized at a vertical distance of 1.25 cm from the sample surface where a 150 mm Si wafer was used (**Chapter II.5.4**: **Absorption spectroscopy**). To begin, the experiments were carried out using C_4F_8 plasma at ambient temperature using roughly the same process conditions applied during the Bosch etching tests and consecutive C_4F_8 passivation tests. However, it was rapidly decided to switch to CF_4 plasma for the study of CF and CF_2 radical densities because it is known to deposit much less on the reactor walls than c-C_4F_8 at ambient temperature [247,169,167,258]. Indeed, it was thought that repeating absorption spectroscopy acquisitions with c-C_4F_8 would rapidly lead to fluorocarbon deposition on the silica portholes and hinder prematurely the optical signal of the experimental set-up. Moreover, it was found interesting to study whether CF_4 could eventually deposit on surfaces thermalized at cryogenic temperatures. Preliminary acquisitions were realized using different source power and pressure conditions but it was decided to study CF and CF_2 radical densities in relation to substrate temperature using a single CF_4 plasma process with fixed parameters. The absolute density of CF and CF_2 radicals was determined and compared in the case of a substrate temperature of +20°C and - 130°C.

Through these acquisitions, it was observed that thick fluorocarbon passivation layers were formed on the Si wafer sample by performing CF_4 plasma at a substrate temperature of -130°C. As a result, a Bosch-type process using CF_4 as a passivation gas was tested at -100°C and +20°C. Based on the process parameters that were fixed during the previous Bosch tests using C_4F_8 , anisotropic etch profiles were obtained using CF_4 at -100°C. The consecutive etching results obtained with the Bosch-type process tests using CF_4 as a passivating gas are then presented and analyzed in relation to substrate temperature and CF_4 passivation step pressure. The main results presented in this chapter were published in the following article [352].

5.2 Density of CF and CF_2 radicals in relation to substrate temperature

Following the parametric study of the C_4F_8 passivation step and to better understand the passivation mechanisms involved at cryogenic temperatures, it was decided to focus on the density of CF and CF_2 radicals in C_4F_8 plasma according to the substrate temperature through absorption spectroscopy. These two radicals are commonly studied during the absorption spectroscopy analysis of fluorocarbon plasmas [231,233,353,235–238,354,355,242].

However, it was rapidly chosen to carry out this study using CF_4 plasma instead of C_4F_8. Indeed, it was found interesting to study whether CF_4 could eventually deposit on surfaces thermalized at cryogenic temperatures. Moreover, it was thought that repeating absorption spectroscopy acquisitions with c-C_4F_8 would rapidly lead to fluorocarbon deposition on the silica portholes and hinder prematurely the optical signal of the experimental set-up. Indeed, the extended acquisition periods which were necessary for absorption spectroscopy in the UV range involved long-lasting fluorocarbon plasma processes. As an example, the acquisitions carried out in the CF spectral range required the application of a continuous fluorocarbon plasma up to a duration of ten minutes. Although the initial objective was to study the same process parameters used during the C_4F_8 passivation parametric study (**Chapter IV.1**), it was rapidly established that it would lead to the deposition of very thick fluorocarbon layers. These thick passivation layers are detrimental to the general study that was aimed to be led. Indeed, it implied the use of extended plasma cleanings between each acquisition to remove the fluorocarbon layer on the silicon substrate used for this study and from the chamber walls. It also implied a rapid deterioration of the silica portholes used to convey the optical beam despite the use of deportation tubes.

The choice to study CF_4 plasmas was made because it is known not to deposit fluorocarbon due its lower carbon content compared to C_4F_8 while still being able to study the density of CF and CF_2 radicals through absorption spectroscopy in relation to the substrate temperature [247,169,167,258]. However, as it was exposed previously by *Coburn et al* [243] and resumed in **figure IV.1**, CF_4 is the fluorocarbon gas which has the highest F/C ratio (equal to 4). It is used essentially for etching applications as it does not generate the formation of CF_x passivation species but rather enhances the presence of fluorine atoms which favor etching reactions at the interface with the Si substrate [167,169,243]. When it comes to Bosch processing, F. Laermer and A. Schilp first developed this process by testing different fluorocarbon gases for their silicon passivation efficiency at ambient temperature as well as their global availability. It resulted that c-C_4F_8 was the best candidate out of a list including CHF_3, $C_2H_2F_2$, C_3F_6, C_4F_6 and C_4F_{10} [253]. Since then, most Bosch processes reported in the literature include c-C_4F_8 as a passivation gas whereas some include C_4F_6. However, they are all performed in the ambient temperature range [128,256–259,266].

Although the impact of process parameters is well-known on the etching or passivation capacity of a fluorocarbon plasma process where the F/C gas ratio and the applied bias voltage have an important

role, the extent at which substrate temperature may also influence the result has not been extensively studied [16–18]. It can be observed in **figure IV.1** that CF_4 plasma processing should most preferably remain in an etching regime due to its high F/C ratio regardless of the bias voltage. However, it was recently found that it can be combined with other compounds such as H_2 or NH_3 for thin-film deposition or surface modification concerning ALE applications [356,357]. Nevertheless, this graph is valid in the ambient temperature range. It is well-known that the decrease of substrate temperature can enhance fluorocarbon condensation and passivation reactions as was shown previously for c-C_4F_8. In the same way, this phenomenon was also shown for fluorocarbon contamination on the chamber walls where their thermalization at +150°C and above prevents any form of deposition during plasma processing [140,247,249]. This is explained by the fact that the sticking coefficient of several reactive species including CF_x radicals are increased at lower temperatures [249,269–272]. Even so, the passivation mechanisms occurring in the cryogenic temperature range are not completely understood.

During the preliminary absorption spectroscopy acquisitions including CF_4 plasma, it was rapidly observed through in-situ ellipsometry that fluorocarbon passivation layers were being formed on the taped silicon substrate when it was thermalized at cryogenic temperatures. Through the refinement of parameters during preliminary testing, where the goal was to maximize the concentration of CF and CF_2 radical species detected through absorption spectroscopy, a CF_4 plasma process was fixed. These process parameters are mentioned in bold in **table V.1** where other pre-tested parameters are also listed. For timing and for practical reasons, the acquisitions were mainly realized and repeated at a substrate temperature of -130°C and at ambient temperature (+20°C).

It was decided to subsequently operate using a 150mm Si wafer which was taped to the substrate holder using kapton because the clamping crown had to be removed to give way to the optical signal at a height of approximately 1.25cm from the wafer surface. The choice of a silicon substrate was made for numerous reasons. Firstly, silicon was the main material of interest in this study where the goal was to evaluate fluorocarbon radical densities near the substrate surface during Bosch processing of Si. Secondly, it enabled to monitor the growth and subsequent removal of the fluorocarbon passivation layer through in-situ ellipsometry during the preliminary tests at cryogenic temperatures. Thirdly, it was seen that supplemental parasite peaks were being generated in the CF and CF_2 spectral domains during absorption spectroscopy acquisitions obtained using a wafer with a 1.2 µm thick SiO_2 surface layer. It is supposed that these peaks result from the presence of additional species in the plasma which are due to chemical reactions between fluorocarbon and oxide species.

Therefore, it was decided to only focus on absorption spectrums obtained with a Si substrate which were far more repeatable. A continuous helium backing flow with a clamping pressure of 500 Pa was introduced to thermalize the wafer. Further details of the absorption spectroscopy equipment, experimental conditions as well as the methods used to treat and analyze the spectrums obtained during this study are mentioned in **Chapter II.5.4** (Absorption spectroscopy section).

Following the results obtained, and given the main observation that thick fluorocarbon passivation could be obtained on a silicon substrate at cryogenic temperatures, it was decided to test a Bosch type process using CF_4 as a passivation gas at -100°C and +20°C. In this sub-chapter, the first section will focus on

the results obtained concerning the comparison of CF and CF_2 radical density at a substrate temperature of -130°C and +20°C. The second section will present several etch profiles obtained through the implementation of a Bosch type process using CF_4 as a passivation gas. The main results will then be resumed and analyzed in the third section.

Table V.1: Experimental conditions used for CF_4 plasma absorption spectroscopy acquisitions

Parameters	CF_4 plasma process
Gas	**CF_4**
Flow rate (sccm)	12 sccm / **50 sccm**
Gas injection mode	**Source inlet**
Pressure (Pa)	1.0 Pa / 2.0 Pa / **4.0 Pa**
Source Power (W)	800 W / **1,500 W**
Bias Power (W)	No bias power
Temperature (°C)	**+20°C** / -100°C / **-130°C**
Substrate	No substrate (bare aluminum chuck) / **Si wafer** / SiO_2 wafer

Following preliminary acquisitions, it was decided to study absorption spectroscopy acquisitions using the same CF_4 plasma process on a taped 6'' Si wafer (CF_4 flow rate: 50 sccm ; Source injection ; Pressure: 4.0 Pa ; Source power: 1,500W ; No bias power). As a result, the following transmission and absorption spectra shown in **figures V.1** and **V.2** were obtained respectively in the CF and CF_2 spectral domains at a substrate temperature of -130°C and +20°C. The spectra plotted in the CF domain were averaged over three acquisitions obtained for each substrate temperature. The spectrums plotted in the CF_2 domain were averaged over two acquisitions obtained for each temperature.

For the analysis of CF absolute density, an $f_{v'v''}$ oscillator strength of 4.76×10^{-3} was taken for the CF A-X[1,0] transition $\text{at } \lambda_0 = 223.9 \text{ nm}$ [237]. An absorption path of $L = 38\ cm$ was fixed as it was observed that the CF absorbance spectra varied significantly according to the substrate temperature and given the fact that CF is known to be reactive on surfaces [236]. The integrated absorbance calculation was made between 222.0 nm and 224.5 nm.

For the analysis of CF_2 absolute density, an absorption cross section of $2.91 \times 10^{-17} cm^2$ was taken at $\lambda_0 = 249.0\ nm$ [231,238]. An absorption path of $L = 63\ cm$ was chosen as it was observed that the CF_2 absorbance spectra in the CF_2 (A(0,v',0)←X(0,1,0)) transition does not change significantly in relation to the substrate temperature and given the fact that it is known not to stick on surfaces [242]. The integrated absorbance calculation was made between 235.0 nm and 270.0 nm.

By comparing the averaged spectra obtained at -130°C and +20°C in CF A-X(1,0) transition domain (**figure V.1.b**), it can be observed that absorption due to the presence of CF radicals in the CF_4 plasma decreases considerably using a substrate temperature of -130°C compared to the situation where it is maintained at +20°C. Indeed, for the CF A-X(1,0) transition around $\lambda_0 = 223.9\ nm$, by taking an oscillator strength $f_{v'v''}$ of 4.76×10^{-3} [237] and an absorption path of $L = 38\ cm$ (**Chapter II.5.4: Absorption spectroscopy**) the integrated absorbance between $222.0\,nm$ and $224.5\,nm$ is equal to 8.0×10^{-3} at 20°C and 4.86×10^{-3} at -130°C. As a result, the absolute CF radical density is approximately equal to $n = 1.0 \times 10^{13} cm^{-3}$ at 20°C and $n = 6 \times 10^{12} cm^{-3}$ at -130°C. Therefore, the

substrate cooling has a significant impact on the CF radical density in the plasma near the wafer surface level as it drops by roughly 40% at -130°C compared to ambient temperature processing (20°C).

Figure V.1: Transmission and absorption spectra in a CF_4 plasma obtained at a chuck temperature of +20°C and -130°C with a taped Si 6'' wafer

a) Left: Transmittance spectra showing $A\,^2\Sigma \leftarrow X\,^2\Pi$ (1,0) and $A\,^2\Sigma \leftarrow X\,^2\Pi$ (2,0) transitions of CF

b) Right: Absorbance spectra showing $A\,^2\Sigma \leftarrow X\,^2\Pi$ (1,0) transition of CF

Process conditions: CF_4 flow rate: 50 sccm ; Pressure 4.0 Pa ; Source power: 1500 W ; No bias power

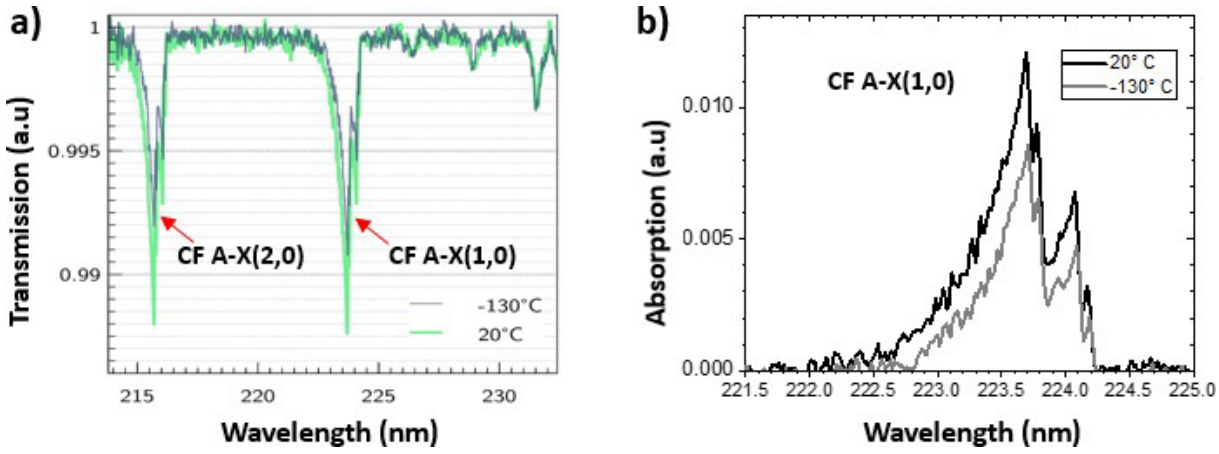

On the other hand, it can be observed that the transmission and absorption spectra in the CF_2 A(0,v',0) ← X(0,0,0) transition is not significantly affected by substrate temperature (**figures V.2.a and V.2.b**). By taking a cross-section value of $\sigma = 2.91 \times 10^{-17} cm^2$ at $249.0\ nm$ [231,238] and an adsorption path of $L = 63\ cm$ (**Chapter II.5.4: Absorption spectroscopy**), an absolute CF_2 radical density of $n = 1.70 \times 10^{13} cm^{-3}$ is determined both at 20°C and -130°C. Only minor differences are observed in the two spectra measured at 20°C and -130 °C that can be attributed to baseline uncertainty of this wide band absorption spectrum caused by eventual lamp source fluctuations. A slightly higher absorption can be observed at 20°C for the peaks around $259.46\ nm$, $262.8\ nm$ and $266.3\ nm$, which are better illustrated in **figure V.3**. These peaks correspond to absorption from the first populated vibrational level of CF_2 (A(0,v',0)←X(0,1,0) which suggests that a cooled surface reduces the production of vibrationally excited CF_2.

The absolute values of the CF and CF_2 radical densities determined in these plasma conditions (CF_4 flow rate: 50 sccm ; Source injection ; Pressure: 4.0 Pa ; Source power: 1,500W ; No bias power) are close to those deduced by *Booth et al* by laser induced fluorescence under similar plasma conditions (ICP reactor; CF_4 flow rate: 25 sccm ; Pressure: 4.4 Pa ; Source power: 250W ; No bias power) applied on a substrate at room temperature (respectively $1.0 \times 10^{13} cm^{-3}$ and $2.0 \times 10^{13} cm^{-3}$ determined at the axial center of the reactor) [354].

These experimental test results correlate with the well-known fact that CF radicals stick on surfaces while CF_2 radicals are typically produced by surfaces due to carbon etching and ion neutralization reactions [236,242]. From in-situ ellipsometry measurements realized on the stuck 6'' Si wafer (using a helium backing pressure of 500 Pa), a CF_x polymer deposition is observed at a rate of about 2.6 $nm.s^{-1}$ at a substrate temperature of -130°C yet no polymer accumulation is detected at 20°C.

Figure V.2: Transmission and absorption spectra in a CF_4 plasma obtained at a chuck temperature of +20°C and -130°C with a taped Si 6'' wafer
a) Left: Transmittance spectra showing A(0, v', 0) ← X(0, 0, 0) transition of CF_2
b) Right: Absorbance spectra showing A(0, v', 0) ← X(0, 0, 0) transition of CF_2

Process conditions: CF_4 flow rate: 50 sccm ; Pressure 4.0 Pa ; Source power: 1500 W ; No bias power

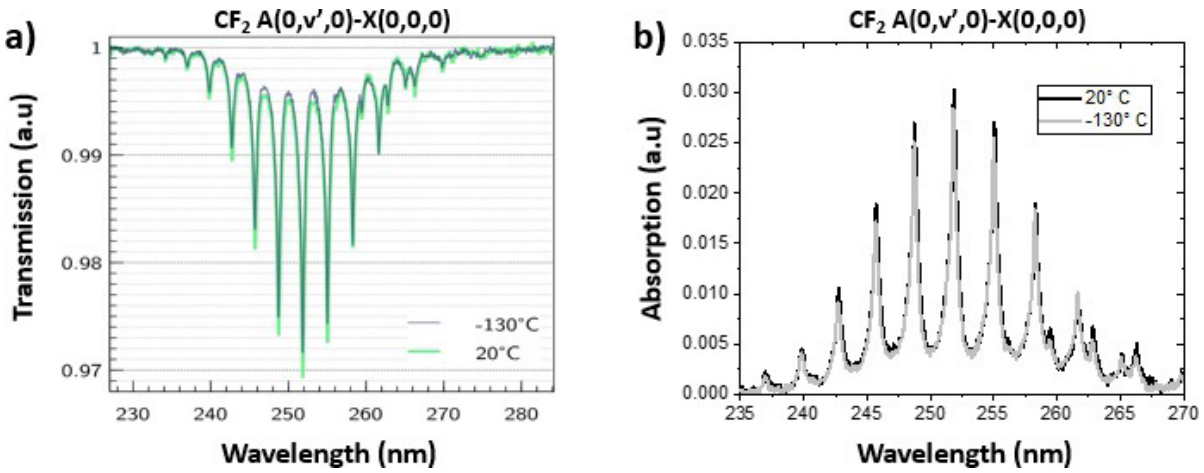

Figure V.3: Close view of the absorption spectra in a CF_4 plasma showing A(0, v', 0) ← X(0, 0, 0) transition of CF_2 obtained at a chuck temperature of +20°C and -130°C with a taped Si 6'' wafer

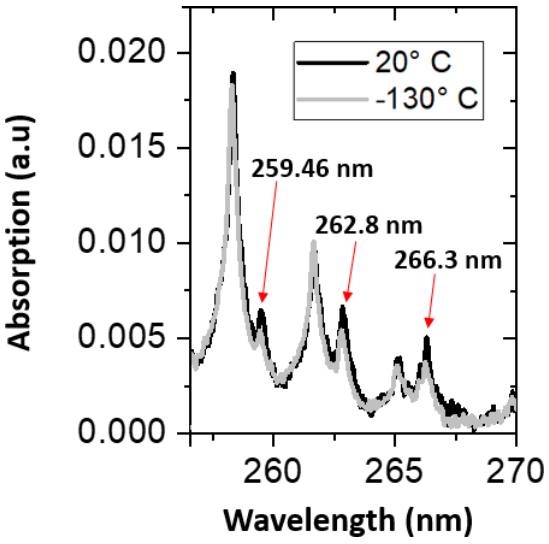

In heavily dissociated ICP fluorocarbon plasmas, the polymer precursors are expected to be C, CF and $C_xF_y^+$ ions. By considering **equation IV.2**, the impingement rate of CF radicals by assuming a gas temperature of 450 K ([354]) near the sample surface thermalized at -130°C is about $1.0 \times 10^{17}\, radicals.cm^{-2}.s^{-1}$. It is one order of magnitude higher than the ion flux determined through Plato probe measurements acquired under similar plasma conditions (**see section V.5**).

Since the carbon atom density is not expected to be high, CF is thus expected to be the main precursor of CF_x film formation at low temperature. As a matter of fact, considering that the cold wafer area is small compared to the total chamber wall surfaces which are maintained at room temperature, the observation of a 40% drop in the CF density when the substrate is cooled from room temperature to -130°C implies that the surface loss rate of CF radicals increases strongly at low temperature and that CF radicals participate significantly to polymer formation on cold surfaces.

It remains difficult to estimate a true CF surface sticking probability from experimental data because the net CF_x polymer deposition rate measured by in-situ ellipsometry results from a deposition/etching competition. Indeed, a significant part of CF radicals that are lost by sticking at the surface do not stay on the surface but are recycled in the plasma in the form of CF_2 and CF_4 volatile products following CF_x polymer ion-enhanced etching by F atoms. Nevertheless, by neglecting this important etching component, a minimal sticking coefficient value (S_C) can be calculated for CF radicals at -130°C using **equation IV.13** where D_R corresponds to the experimental fluorocarbon deposition rate observed and ρ to the polymer density which should be in the range of 2 $g.cm^{-3}$ [351]. As a result, a 10% CF radical sticking probability would explain the measured deposition rate which is observed at -130°C (approximately 2.6 $nm.s^{-1}$).

This sticking probability is already quite high and as discussed above, it is probably underestimated since the film etching by F atoms is not considered in the calculation. Therefore, it is expected that CF radicals play a major role in fluorocarbon polymer film formation on cold surfaces during CF_4 plasma processing at cryogenic temperatures.

5.3 Implementation of a Bosch-type process using CF_4 plasma passivation

Following the absorption spectroscopy acquisitions and the observation of fluorocarbon deposition on a Si substrate using CF_4 plasmas at -130°C, it was decided to evaluate CF_4 passivation efficiency at cryogenic temperatures by implementing a Bosch-like process. Indeed, the objective was to show if anisotropic etch profiles could be obtained through fluorocarbon sidewall passivation using CF_4 plasma steps. A process was implemented based on the fixed set of Bosch parameters tested previously to evaluate the impact of substrate temperature. Only the passivation step parameters were modified according to the CF_4 plasma process which was studied by absorption spectroscopy in the previous section. The exact process parameters which were tested are listed in **Table V.2**.

Table V.2: Set of CF_4/SF_6 Bosch process parameters tested to study the impact of substrate temperature on the etch profiles

Temperature (°C)	+20°C or -100°C	
Thermalization time	30s etching tests at +20°C / 5 min for etching tests at -100°C	
Process duration	200 Bosch cycles (16 min 40 s)	
Process step	**Etching step**	**Passivation step**
Gas	SF_6	CF_4
Flow rate (sccm)	300 sccm	20 sccm
Step time (s)	3 s	2 s
Pressure (Pa)	3.0 Pa (Fixed APC angle position)	1.0 Pa / 4.0 Pa (Fixed APC angle position)
Source Power (W)	1,500 W	1,500 W
Bias Power (W)	15 W	15 W
Equivalent Bias Voltage measured on a Si wafer (V)	≈ 135 V	≈ 65 V / ≈ 160 V
Equivalent Bias Voltage measured on a SiO_2 wafer (V)	≈ 35 V	≈ 15 V / ≈ 45 V

Both SF_6 and CF_4 gases were injected through the source inlet. The chamber pressure for etching and passivation steps was fixed using an automatic pressure controller (APC) rotating valve position which was carefully evaluated for each test. The carrier wafer was mechanically clamped with a pressure of 1,300 Pa using a He backing flow to enhance thermal transfer. A thermalization step of five minutes was set before each Bosch process test. A limit of 200 cycles was again set in order to obtain significantly deep features which could be compared to each other by SEM. A first set of tests at +20°C and -100°C was realized with a CF_4 passivation step pressure of 4.0 Pa. Following the analysis of the etch profiles obtained, a second set of tests using a CF_4 passivation step pressure of 1.0 Pa was realized.

Once again, due to the characteristics of the ICP reactor and the relatively high pulsation frequency that was set for the process tests, the bias voltage measurement was unstable and difficult to evaluate on SiO_2 carrier wafers. Consecutive bias voltage measurements were realized on a Si wafer using the same process parameters where the process steps were extended to retrieve a stable value. Approximately 135 V was obtained for the SF_6 etching step whereas 65 V and 160 V were obtained during the passivation steps with a chamber pressure of respectively 1.0 and 4.0 Pa.

The etch profiles obtained on 6 µm wide trenches with the Bosch process parameters given previously are shown in **Figure V.4**. **Figures V.4.a** and **V.4.b** show the profiles obtained using a pressure of 4.0 Pa during CF_4 passivation steps at a substrate temperature of respectively +20°C and -100°C. **Figures V.4.c** and **V.4.d** show the etch profiles obtained subsequently where a pressure of 1.0 Pa was fixed during CF_4 passivation steps at a substrate temperature of respectively +20°C and -100°C.

Figure V.4: Comparison of the etch profiles obtained with a CF_4/SF_6 Bosch process at +20°C and -100°C using a chamber pressure of 4 Pa and 1 Pa for the CF_4 passivation step (6 µm wide trenches observed by SEM)

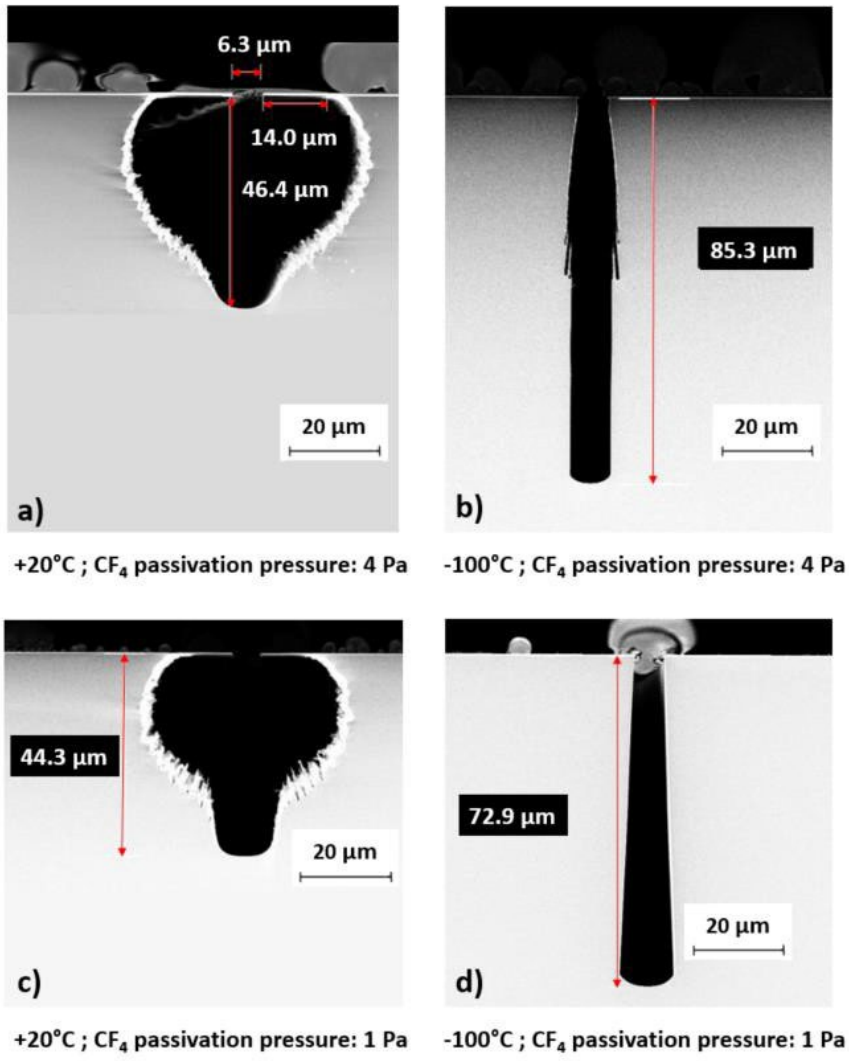

It can be observed that CF_4 sidewall passivation is considerably enhanced at -100°C where quasi-anisotropic profiles are obtained in **figures V.4.b** and **V.4.d** with slightly negative trenches are observed in both cases. An etch depth of 85.3 µm was measured with a CF_4 passivation pressure of 4.0 Pa at -100°C. It corresponds to an etch rate of approximately 5.1 µm/min. In comparison, an etch depth of 72.9 µm was measured for the etch profile obtained at -100°C with a CF_4 passivation step pressure of 1.0 Pa. It corresponds to an etch rate of roughly 4.4 µm/min. It can be seen by comparing these two

profiles that fluorocarbon passivation is more efficient at a pressure of 1.0 Pa in these conditions. Indeed, the sidewalls present no major defects and the resulting etch rate is slightly reduced. The localized defects observed halfway down the trenches in **figure V.4.b** are presumably caused by a tapered mask angle. They are thought to reflect plasma ions which inevitably hit the sidewalls at a specific height and etch the substrate in the incident direction. This defect is not observed in **figure V.4.d** which seems to indicate that the reflected ions do not etch the sidewalls in this area due to an enhanced fluorocarbon passivation efficiency at lower pressures in this case.

At ambient temperature, it is found that fluorocarbon passivation is nearly inexistant in these conditions where isotropic profiles are both obtained in **figures V.4.a** and **V.4.c**. Judging by these two profiles, it can be argued that CF_4 passivation is also less inefficient at 1.0 Pa than at 4.0 Pa where lateral etching and etch depth are slightly reduced. Moreover, the anisotropic etching component that can be observed at the bottom of both profiles is more pronounced in **figure V.4.c**.

Figure V.5 shows the isotropic etch profile obtained at ambient temperature using the process parameters listed in **table V.2** where a maximal CF_4 flow rate of 100 sccm was applied with a passivation pressure of 1.0 Pa during the passivation steps (**figure V.5.b**). The profile is even more isotropic and presents a reduced etch rate in comparison with **figure V.5.a** where a CF_4 flow rate of 20 sccm was used. This result illustrates the scale to which CF_4 plasma sidewall passivation is inefficient at +20°C where the flow rate does not seem to enhance fluorocarbon deposition but rather contributes to further isotropic etching. It highlights the importance of substrate temperature during fluorocarbon passivation.

Figure V.5: Comparison of the etch profiles obtained with a CF_4/SF_6 Bosch process at +20°C by varying the CF_4 flow rate (6 µm wide trenches observed by SEM)

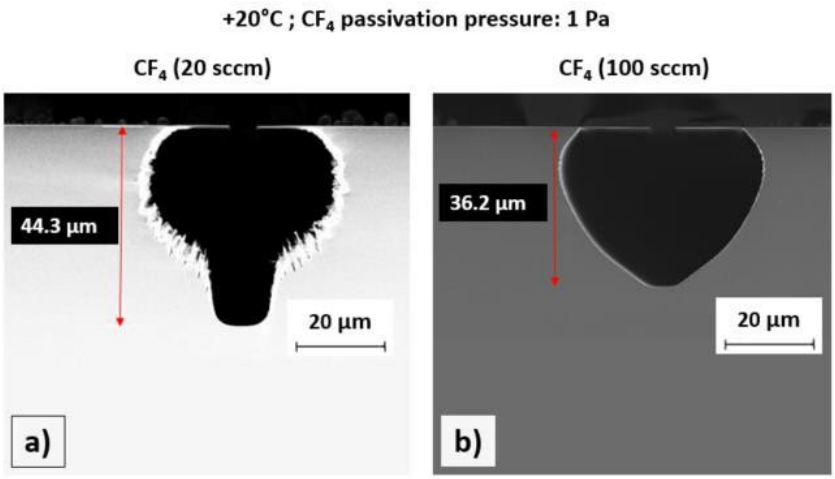

A close view of the etch profiles presented obtained at -100°C in **figure V.4.b** and **V.4.d** near the mask area are shown respectively in **figures V.6.a and V.6.b**. They confirm the fact that CF_4 passivation is more effective at -100°C with a chamber pressure of 1.0 Pa. Indeed, it can be observed that the scalloping marks which are inherent to Bosch processing and testimony of an adequate fluorocarbon passivation are more pronounced at 1.0 Pa in **figure V.6.b** than at 4.0 Pa in **figure V.6.a** where they are difficult to observe.

However, it can also be seen that the performance of CF_4 plasma passivation steps at 1.0 Pa leads to an increased etching of the SiO_2 hard mask than at 4.0 Pa. As a result, the $Si:SiO_2$ etching selectivity is evaluated at approximately 80:1 using a passivation pressure of 1.0 Pa and 205:1 using a passivation pressure of 4.0 Pa at a substrate temperature of -100°C. This tendency is also observed at +20°C where the remaining SiO_2 hard mask layer thickness is evaluated at roughly 220 nm using a passivation pressure of 1.0 Pa and around 600 nm using a passivation pressure of 4.0 Pa. It results in an $Si:SiO_2$ etching selectivity of roughly 45:1 and 80:1 respectively by considering the etch depth of the isotropic profiles obtained at +20°C.

Figure V.6: Close view comparison of the etch sidewalls obtained with a CF_4/SF_6 Bosch process at -100°C : using a chamber pressure of 4 Pa (a) and 1 Pa (b) for the passivation steps (6 µm wide trenches observed by SEM)

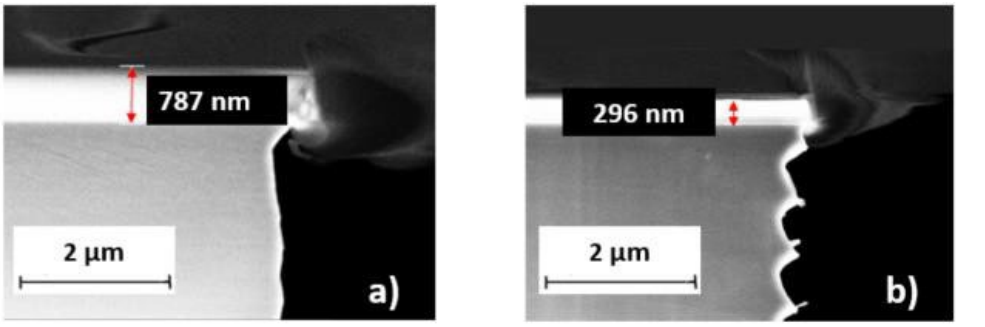

-100°C ; CF_4 passivation pressure: 4 Pa -100°C ; CF_4 passivation pressure: 1 Pa

The comparison of the etch depths obtained for each trench width concerning the anisotropic CF_4/SF_6 Bosch processes realized at -100°C and isotropic processes realized at +20°C is plotted in **figure V.7**. It can be observed that the ARDE is substantially more pronounced in the case where a pressure of 1 Pa was realized during the passivation steps at -100°C. A summary of the main results obtained concerning the profiles shown in **figure V.4** (6 µm wide trenches) is listed in **table V.3**.

Figure V.7: Comparison of the etch profiles obtained with a CF_4/SF_6 Bosch process at +20°C and -100°C using a chamber pressure of 1 Pa for the passivation step (6 µm wide trenches)

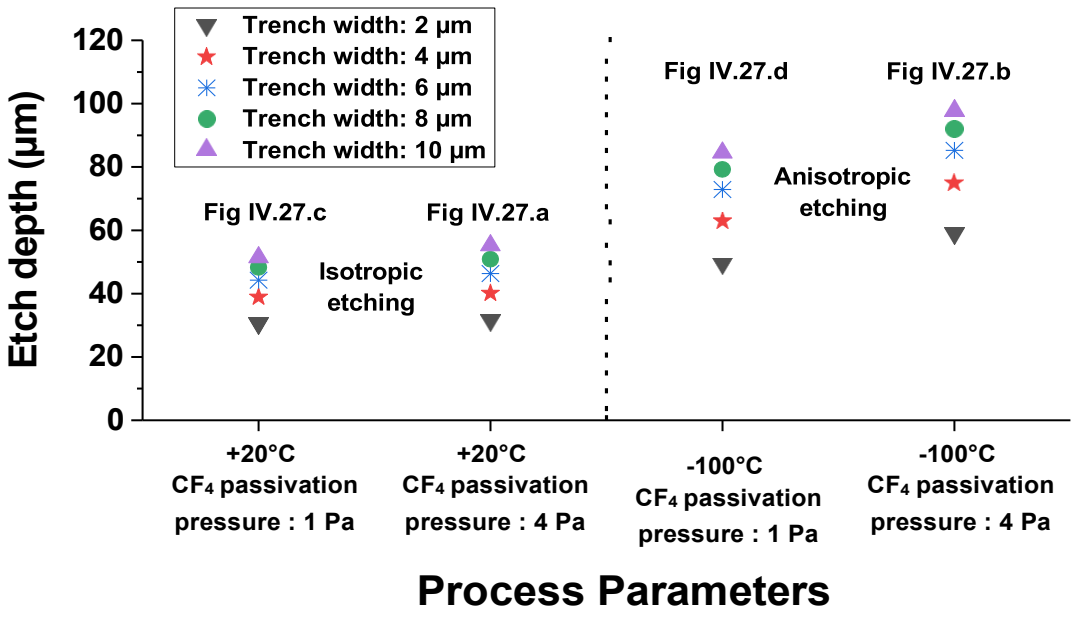

Table V.3: Summary of Bosch etching results obtained at +20°C and -100°C in configurations A, B and C

CF_4 passivation step pressure	1 Pa	4 Pa
Isotropic etch rate at +20°C (6 µm trench width)	2.7 µm/min	2.8 µm/min
Anisotropic etch rate at -100°C (6 µm trench width)	4.4 µm/min	5.1 µm/min
Remaining SiO_2 mask layer at +20°C	≈ 0.22 µm	≈ 0.60 µm
Remaining SiO_2 mask layer at -100°C	≈ 0.30 µm	≈ 0.79 µm
(Si:SiO_2) etching selectivity at +20°C	≈ 45:1	≈ 80:1
(Si:SiO_2) etching selectivity at -100°C	≈ 80:1	≈ 205:1

5.4 Temperature dependence of the CF_4 plasma passivation process step

Complementary CF_4 plasma tests were realized on a SiO_2 blanket samples (**Chapter II** / Samples section) glued on a 4'' Si wafer carrier. With the same plasma process parameters as those applied during the UV absorption spectroscopy experiments (50 sccm CF_4; 4 Pa, 1500 W ICP power, no bias power), using this time a helium backing pressure of 1300 Pa, it was observed by in-situ ellipsometry that a fluorocarbon layer deposits at -130°C whereas it leads to SiO_2 etching et 20°C. The in-situ ellipsometry acquisitions of these CF_4 plasma processes are shown in **figure V.8**. At -130°C, the thickness of the fluorocarbon layer is estimated at 360 nm after a plasma exposure of 1 minute. It can

be seen that deposition actually occurs on the sample surface roughly 15 seconds after the plasma strike whereas immediate and constant SiO_2 etching is observed at ambient temperature.

Figure V.8: Effect of substrate temperature on a CF_4 plasma process applied on a SiO_2 blanket sample

Process parameters: C_4F_8 flow rate: 50 sccm; Pressure: 4.0 Pa; Source power: 1500 W; No bias power; Step time: 1 min

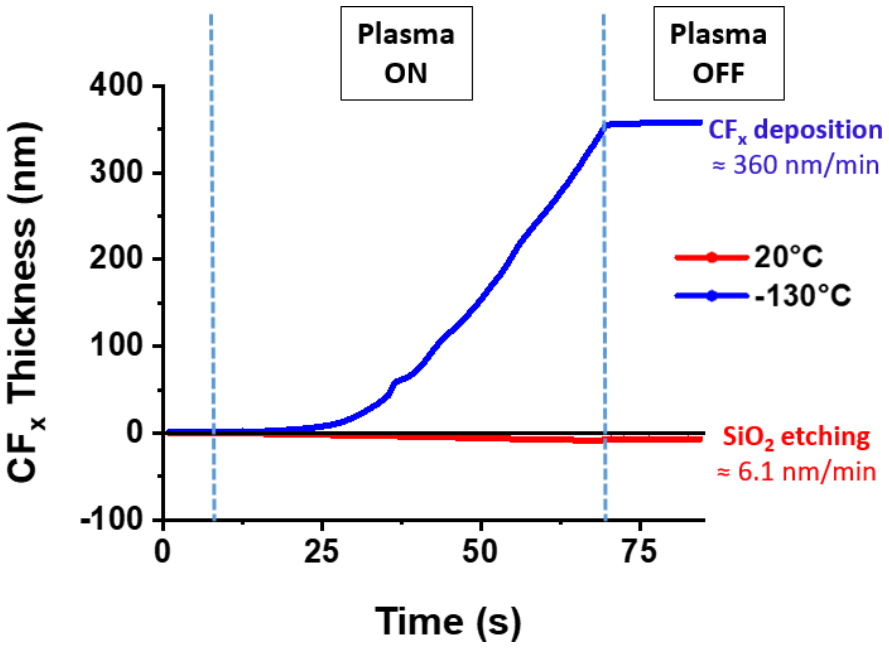

The fluorocarbon layer deposited at -130°C was observed by SEM with roughly the same thickness (339 nm including 4 nm of platinum metallization) that was obtained through in-situ ellipsometry (360 nm). The sample profile is shown in **figure V.9**. It is assumed that the slightly lower fluorocarbon layer observed by SEM (approximately 25 nm) is due to thermal desorption which should have occurred at 60°C when the sample was manually detached from the carrier wafer for SEM observation. Moreover, the CF_x layer thickness determined on the same sample by in-situ ellipsometry after SEM analysis was equal to 335 nm.

Subsequently, by applying the same CF_4 plasma process at ambient temperature (20°C), the CF_x layer deposited previously at -130°C is removed from the sample at a rate of approximately 36.6 nm/min, before etching the SiO_2 layer at a rate of roughly 4.4 nm/min. The evolution of the sample thickness during the CF_4 plasma etching process (15 minutes) is shown in **figure V.10**. These observations demonstrate that no fluorocarbon contamination of the chamber walls should result from the application of this process at low substrate temperatures.

Figure V.9: Fluorocarbon deposited layer profile obtained after a pure CF_4 plasma process (50 sccm; 4 Pa; 1 min) at -130°C observed by SEM on a SiO_2 blanket sample

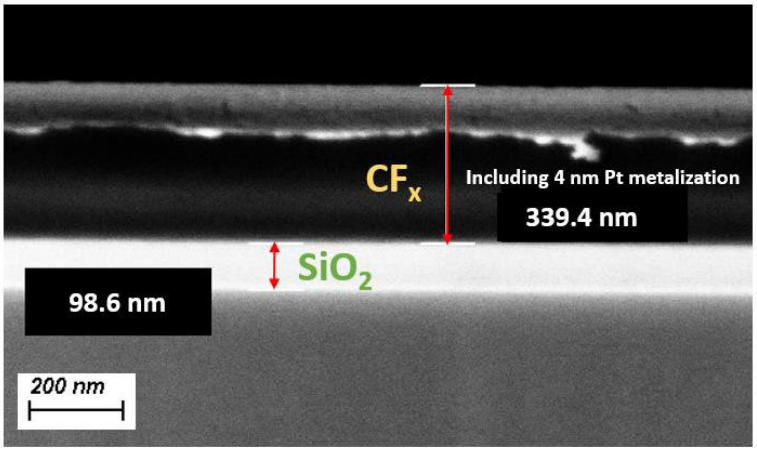

Figure V.10: Etching of a fluorocarbon deposited layer followed by SiO_2 etching using a CF_4 plasma process at ambient temperature

Process parameters: C_4F_8 flow rate: 50 sccm; Pressure: 4.0 Pa; Substrate temperature: +20°C; Source power: 1500 W; No bias power; Step time: 15 min

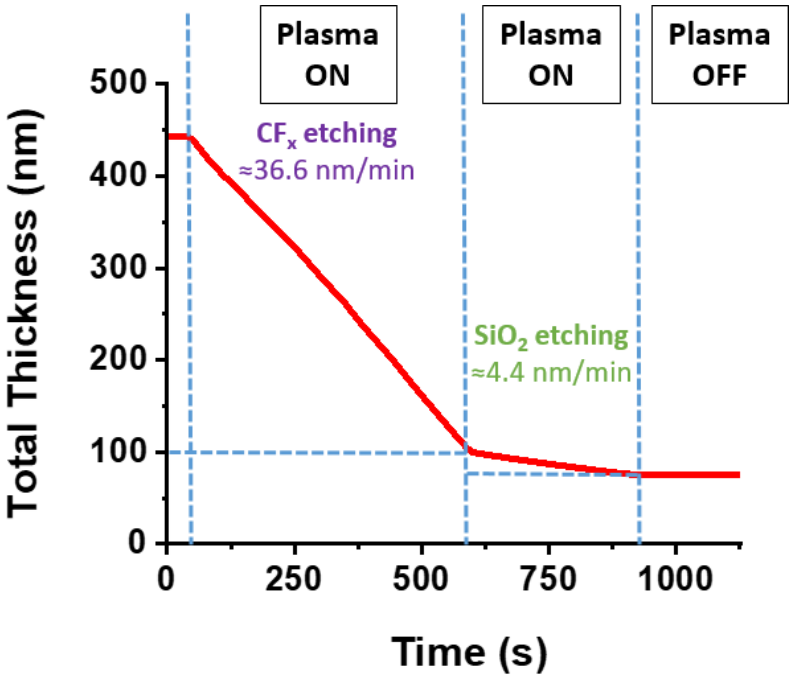

5.5 Capacitive probe analysis of the CF_4 plasma passivation process step

The capacitive probe characterization of the CF_4 passivation step was realized using the Impedans Plato Probe. Using the same process parameters listed in **table V.2** for this step, several I-V characteristics were acquired by varying the pressure (1.0; 2.0 and 4.0 Pa) using at first no bias power and then by using a bias power of 15 W (only source injections). The plasma parameters determined with these acquisitions are listed in **table V.4**. For these specific capacitive probe measurements, the main ion mass which was considered was the one of CF_3^+ (69 a.m.u). Bias voltage values of 6 V and 97.8 V were respectively measured at 1 and 4 Pa by the ICP tool during these acquisitions whereas bias voltage values of approximately 65 and 160 V were respectively found with a clamped 4'' Si wafer in roughly the same plasma conditions (CF_4 flow rate of 20 sccm in this case instead of 50 sccm during the capacitive probe acquisitions).

Table V.4: Plasma parameters obtained from the (I-V) characteristics acquired during capacitive probe characterization of the CF_4 plasma passivation step by varying the pressure and bias power

Process parameters: CF_4 flow rate: 50 sccm (Source injection) ; Pressure: 1 to 4 Pa ; ICP Source power: 1,500 W ; Bias power: 0 to 15 W

Pressure (Pa)	Bias Power (W)	Electronic Temperature (eV)	Ion Flux ($A.m^{-2}$)	Ion Density (m^{-3})	Measured Bias Voltage (V)
1	**0**	3.82	19.01	5.31×10^{16}	1.5
	15	3.84	19.16	5.34×10^{16}	6
2	**0**	3.24	11.89	3.73×10^{16}	0.0
	15	3.34	11.63	3.60×10^{16}	22.1
4	**0**	2.94	4.38	1.61×10^{16}	0.3
	15	3.31	3.73	1.33×10^{16}	97.8

At a pressure of 4 Pa and using no bias power, a value of 2.73×10^{15} ions.cm^{-2}.s^{-1} is obtained for the ion flow which is approximately 40 times less than the estimated flow of CF radicals (1.0×10^{17} radicals cm^{-2}.s^{-1}) which was determined by absorption spectroscopy at -130°C with the same plasma parameters in these experimental conditions.

5.6 General Analysis

Globally, these results show that the substrate temperature, if it can be reduced to cryogenic range, allows inducing a transition from Si etching by F atoms at ambient temperature to CF_x polymer deposition at cryogenic temperatures when applying a CF_4 plasma process. This effect is partly attributed to a significant increase of the surface sticking probability of CF radicals on the cooled wafer surface. Indeed, it was shown through absorption spectroscopy that their absolute density at a height of 1.25 cm from the surface level is reduced by roughly 40% by applying an identical CF_4 plasma process when the substrate temperature is decreased from 20°C to -130°C. Since the sidewalls are not bombarded during feature etching by ions and since it was observed that CF_2 sticking probability does not increase at low temperature, it is expected that CF radicals and possibly C atoms play a major role in the passivation layer formation at cryogenic temperatures. It is also thought that the net deposition rate of CF_x polymer which results from an etching/deposition competition increases as the substrate temperature is decreased.

Concerning the etch profiles which were obtained through these Bosch-type process tests, additional process optimization is needed in order to obtain straight anisotropic profiles at -100°C where the increase of the passivation step duration and CF_4 flow rate should be sufficient to that matter. By consistently increasing these parameters, it is also believed that effective CF_4 fluorocarbon passivation may be possible at a substrate temperature above -40°C where liquid nitrogen cooling infrastructures are not needed. If this was indeed the case, the replacement of c-C_4F_8 gas by CF_4 during Bosch processing would alleviate the major issue of fluorocarbon chamber wall contamination. Indeed, as it was observed through in-situ ellipsometry, CF_4 plasma is not expected to deposit any polymer on the reactor surface areas, which are maintained at room temperature. Furthermore, CF_4 has a 28% lower GWP than c-C_4F_8 [160,161].

By extension to the previous study where c-C_4F_8 plasma passivation was evaluated at cryogenic temperatures, the results obtained concerning CF_4 plasma passivation show that the reduction of substrate temperature offers numerous processing opportunities due to enhanced passivation reactions with the cooled substrate. Cryogenic processing may contribute to reduce the consumption of necessary gases for a variety of processes. In this case, it also shows that process gases which are not suitable at ambient temperature may be used at cooler temperatures to obtain similar etch results. It can open up interesting perspectives towards cost reduction and environmental compliance solutions.

5.7 Summary of chapter V (English)

In this chapter, absorption spectroscopy acquisitions were carried out on a CF_4 plasma process with fixed parameters to evaluate the density of CF and CF_2 radicals at a height of 1.25 cm from a silicon wafer which was thermalized at -130°C and at 20°C. The decision was made to carry out this experiment using CF_4 plasma and not C_4F_8 plasma. Indeed, judging by the process results obtained previously using C_4F_8 (**Chapters III and IV**), it was found interesting to study whether CF_4 plasma, which is known for its silicon etching properties at ambient temperature could eventually result into fluorocarbon deposition at cryogenic temperatures. This was also done to avoid thick fluorocarbon deposition on the substrate and the chamber walls. To perform these acquisitions, the clamping crown had to be removed to avoid the vignetting of the optical path. Therefore, a 6'' Si wafer was taped to the substrate holder.

By comparing the absorbance spectra that were acquired, it was observed that the absolute density of CF radicals decreases by roughly 40% when the substrate temperature is decreased from 20°C to -130°C. In comparison, CF_2 radicals globally conserve their absolute density in the CF_4 plasma even at -130°C. Furthermore, it was observed through in-situ ellipsometry acquisitions that the application of CF_4 plasma at -130°C in these processing conditions led to the formation of thick fluorocarbon layers on the silicon substrate whereas no fluorocarbon deposition was observed at ambient temperature.

Consecutively to these tests, and following the same parameters that were tested previously using C_4F_8 plasma (**Chapter III, table III.1**), a Bosch type process was implemented using CF_4 plasma during the passivation steps. Process tests were realized where the substrate was either thermalized at -100°C or at 20°C. It was effectively shown that quasi-anisotropic etch profiles could be obtained at -100°C whereas isotropic profiles were obtained at ambient temperature using the same process conditions. In addition, capacitive probe acquisitions were also realized on the CF_4 plasma step by varying the chamber pressure to estimate the ion densities and ion fluxes using this technique. Complementary deposition tests realized through in-situ ellipsometry on thin film SiO_2 samples using a CF_4 plasma process enabled to demonstrate a fluorocarbon deposition rate of roughly 360 nm/min at -130°C and a SiO_2 etch rate of 6 nm/min at 20°C. Moreover, it was found that the fluorocarbon layer deposited at -130°C was etched with the same CF_4 plasma process at ambient temperature at a rate of roughly 37 nm/min. These results suggest that no fluorocarbon contamination should result from the performance of cryogenic Bosch processing using CF_4 as the chamber walls are always thermalized higher than 20°C. This is an interesting observation because fluorocarbon contamination on the chamber walls is a major issue in the semiconductor industry when it comes to classical Bosch processing using C_4F_8 at the ambient temperature range.

5.8 Résumé du chapitre V (français)

Ce dernier chapitre présente l'étude de la densité des radicaux CF et CF_2 déterminée par spectroscopie d'absorption au sein d'un plasma CF_4 en fonction de la température du porte-substrat. Ces acquisitions ont été réalisées sans la couronne de clampage en quartz afin de ne pas obstruer le signal optique qui passait à une hauteur de 1.25cm au-dessus du porte-substrat où une plaquette de silicium de 6'' a été scotchée à l'aide de kapton et thermalisée à -130°C et à 20°C. Le choix du CF_4 au lieu du C_4F_8 pour cette étude a été fait pour plusieurs raisons. Premièrement, il a été jugé intéressant au vu des résultats obtenus précédemment sur C_4F_8 (**Chapitres III et IV**) de vérifier si un plasma CF_4, connu pour ses propriétés de gravure du silicium à température ambiante, pouvait donner lieu à un dépôt fluorocarboné à température cryogénique. De plus, cela permettait d'éviter de réaliser des dépôts trop épais aux niveaux des parois du réacteur, du substrat et du dispositif optique.

En analysant les spectres d'absorption obtenus à -130°C et 20°C, il a été observé que la densité de radicaux CF est approximativement 40% moins importante qu'à température ambiante. En revanche, la densité de radicaux CF_2 reste relativement identique en fonction de la température du porte-substrat. De plus, des mesures complémentaires réalisées par ellipsométrie in-situ durant ces essais ont permis de démontrer qu'une couche fluorocarbonée se déposait sur silicium à -130°C.

Suite à l'obtention de ces résultats, une étude d'un procédé de type Bosch a été réalisée en reprenant les mêmes paramètres étudiés précédemment (**Chapitre III, table III.1**) mais cette fois-ci en remplaçant le gaz utilisé pour les étapes de passivation par du CF_4 (au lieu du C_4F_8). Ces essais ont aboutis à l'obtention de profils de gravure quasi-anisotropes à -100°C alors que des profils isotropes ont été observés lorsque les procédés étaient réalisés à température ambiante. Par la suite, des mesures par sonde capacitive (sonde Plato™) ont été réalisées sur plasma CF_4 en faisant varier la pression au sein de la chambre pour estimer la densité et le flux d'ions par cette technique. Enfin, des essais complémentaires de dépôts/gravure par plasma CF_4 sur échantillon SiO_2 (100 nm) ont été étudiés par ellipsométrie in-situ. Ainsi, une vitesse de dépôt d'environ 360 nm/min est observé à -130°C alors que le plasma CF_4 grave le SiO_2 à une vitesse de l'ordre de 6 nm/min lorsque celui-ci est thermalisé à 20°C. De plus, il a été constaté que la couche fluorocarbonée déposée par plasma CF_4 à -130°C était gravée avec le même procédé à température ambiante à une vitesse d'environ 37 nm/min. Ces résultats démontrent que la réalisation de ce procédé n'engendre pas de contaminations des parois du réacteur car celles-ci sont habituellement chauffées à 20°C au minimum. C'est une perspective intéressante car c'est un défaut majeur du procédé Bosch, habituellement réalisé avec du C_4F_8 et à une température supérieure à 20°C, dans l'industrie des semi-conducteurs.

General Conclusion and future perspectives

In a context of continuous innovation in the microelectronics sector, the interest in cryoetching plasma processes has re-emerged in these last years. Introduced by *Tachi et al* in 1988 for deep silicon etching applications, they consist in etching materials at very low temperature, typically around -100°C using liquid nitrogen which enhances passivation mechanisms on the cooled substrate and limits chemical etching reactions on the feature sidewalls. These processes are mainly used to reduce plasma induced damage on the etched surface and to limit reactor wall contaminations in order to avoid process drifts. Lower substrate temperatures can also allow to reach higher etch rates according to the plasma chemistry and to reduce the consumption of gas which is necessary for passivation purposes. Therefore, cryogenic etching processes offer an interesting approach to reduce production costs.

However, extensive understanding of specific passivation and etching mechanisms at cryogenic temperature is not yet fully established. More generally, plasma-surface interactions in relation to substrate temperature are not well documented for many etching processes in the scientific literature. Furthermore, the measurement of cryogenic plasma etching properties is relatively difficult because it implies the use of in-situ characterization techniques which have to be monitored near the thermalized sample surface. It is within this context that this research project was carried out. The aim was to study etching mechanisms involved in multiple cryogenic etching processes on silicon-based materials (p-Si, SiO_2, Si_3N_4) using an ICP reactor (Oxford Instruments Plasma Pro 100 Cobra). Multiple plasma chemistries were studied for this research project yet this manuscript mainly focused on the study of fluorocarbon plasma processes, especially the Bosch process in relation to the substrate temperature.

At first, the traditional Bosch process using c-C_4F_8 as a passivation gas was studied at a substrate temperature of -100°C using a fixed set of process parameters applied where different process configurations were tested. It was found that the c-C_4F_8 gas supply could be effectively reduced to -100°C compared to ambient temperature processing, from 20% to 81% depending on the process configuration. Cryogenic Bosch processing is much more sensitive when it comes to c-C_4F_8 dosing to achieve anisotropic etching. A slight increase in the etch rate (from 2.5% to 46.4%) is observed at -100°C without considering the thermalization time when comparing similar anisotropic profiles. Silicon to silicon oxide (Si:SiO_2) etching selectivity increases significantly at -100°C with a gain of 29% to 94% even though the aspect-ratio dependent etching (ARDE) phenomenon is more important at lower substrate temperatures. Scalloping marks on the etch profile sidewalls were found to be much more pronounced at -100°C in these process conditions. Concerning the study of the gas-injection channel, it was observed that c-C_4F_8 source injections are slightly more efficient to passivate the trench sidewalls using this exact set of process parameters. Nevertheless, it was evaluated that all the process configurations could be further optimized.

Subsequently, a parametric study was carried out on the c-C_4F_8 plasma passivation step using the same process parameters tested previously during the Bosch tests. It was notably observed that the fluorocarbon deposition rate is approximately a hundred times higher at -100°C using the same process

conditions than at ambient temperature. A slight increase of the refractive index (at 2 eV) is observed for the fluorocarbon passivated layer as the substrate temperature is decreased which suggests a slightly higher carbon content. This observation may explain why scalloping marks are more pronounced for the etch profiles obtained at -100°C as the fluorocarbon layer deposited on the sidewalls should be relatively harder to etch as it is less prone to ion bombardment. However, the refractive index value of the deposited fluorocarbon layer does not seem to depend on the gas injection channel, at least between -100°C and +20°C. Mass spectrometry acquisitions of c-C_4F_8 plasma processes at ambient temperature near the substrate level enabled to show that gas injection through the source contributes to a higher fluorocarbon dissociation in the plasma compared to gas-ring injections in these process conditions. As a result, it is suggested that the chemical composition of the fluorocarbon passivation layer, or at least its interfacial layer with the Si substrate, should be different according to the C_4F_8 injection channel that is used during the process. However, this statement can only be verified through complementary XPS spectroscopy characterizations which could not be lead during the research project. Nevertheless, the subsequent etch rate of the fluorocarbon layer using SF_6 plasma with bias voltage is the same regardless of the gas injection channel that was used previously during c-C_4F_8 plasma deposition.

Overall, it is interesting to note that the results obtained during this complementary parametric study do not explain the observations that were made previously during the Bosch process tests. The most striking observation is the fact that the fluorocarbon deposition rate is about a hundred times higher at -100°C than at 20°C. However, the short period (2 seconds) that was originally fixed for the passivation steps during the Bosch process tests was surely not sufficient. Indeed, it was found that the c-C_4F_8 gas supply could only be reduced from 20% to 81% at -100°C depending on the processing configuration but it is assumed that much higher values could have been obtained by increasing the process step durations accordingly (in instance, by doubling or tripling them). Nevertheless, it was shown through these complementary deposition tests that the repetition of c-C_4F_8 plasma steps in these conditions should lead to gradual fluorocarbon accumulation on the chamber walls independently from the substrate temperature that is applied during the process. As a result, process deviations will inevitably occur if the reactor walls are not regularly cleaned and will be much more problematic in the case of cryo-Bosch processing at -100°C where c-C_4F_8 dosing is much more sensitive. Therefore, cryo-Bosch processing using c-C_4F_8 gas loses its interest although it demonstrates interesting etching properties compared to standard ambient temperature processing.

Subsequently, a complementary study was carried out concerning the physisorption and condensation of c-C_4F_8 at cryogenic temperatures. The main goal was to evaluate the impact of these mechanisms during c-C_4F_8 plasma deposition in relation to the substrate temperature and to compare experimental data with the extrapolation of its equilibrium vapor pressure curve. A parametric study was carried out between -130°C and -150°C with a maximal c-C_4F_8 partial pressure of Pa. It was decided to carry out this study at lower c-C_4F_8 partial pressures (between 0.016 Pa and 0.321 Pa) than the cryo-Bosch processes presented previously (2.0 Pa). Indeed, the intention was to monitor very low adsorption and

desorption flows and to remain as much as possible in a physisorption regime (maximum of ten c-C_4F_8 adsorbed monolayers) rather than in a condensation regime. The experiments consisted of gas injection cycles interspersed with chamber purge periods. Repetitive and stable adsorption rates and subsequent desorption rates of c-C_4F_8 were monitored on a SiO_2 surface sample through in-situ ellipsometry and mass spectroscopy. However, the calculation of a reliable C_4F_8 sticking coefficient was not possible in these experimental conditions where c-C_4F_8 physisorption could not be monitored precisely but allowed to monitor c-C_4F_8 condensation once the saturation vapor pressure was exceeded within the chamber. The experimental results obtained suggest that physisorption and condensation of c-C_4F_8 are negligible at -100°C during c-C_4F_8 plasma passivation processes around 2.0 Pa studied previously during the cryo-Bosch process tests. In these process conditions, c-C_4F_8 condensation only starts to take place at -130°C when its saturation vapor pressure is reached in the chamber.

Thereafter, it was decided to study fluorocarbon cryoetching using another gas than c-C_4F_8. Absorption spectroscopy acquisitions were carried out using CF_4 plasma which is known for its etching properties at ambient temperature. The density of CF and CF_2 radicals was evaluated at a height of 1.25 cm from a taped silicon wafer which was thermalized at -130°C and at 20°C. It was observed that the absolute density of CF radicals decreases by roughly 40% when the substrate temperature is decreased from 20°C to -130°C in these process conditions whereas the CF_2 radical density is conserved independently of the substrate temperature. In these conditions, fluorocarbon deposition was observed on the Si substrate at -130°C through in-situ ellipsometry whereas no deposition was observed at ambient temperature. Consecutively, the Bosch process studied previously was tested by replacing c-C_4F_8 by CF_4 plasma during the passivation steps at -100°C or at 20°C. It was effectively shown that quasi-anisotropic etch profiles could be obtained at -100°C whereas isotropic profiles were obtained at ambient temperature using the same process conditions. Complementary deposition tests realized through in-situ ellipsometry demonstrate that no fluorocarbon contamination should result from the performance of cryogenic Bosch processing using CF_4 as the chamber walls are always thermalized higher than 20°C. This process represents an interesting alternative to classical Bosch processing using c-C_4F_8 at the ambient temperature range. Indeed, it should enable a reduction in chamber cleanings and to reduce the consumption of fluorocarbon gas. Both of these advantages may be sufficient enough to minimize the extra time which is needed to thermalize the samples. Further process optimization and exploration should be made to verify whether this could be implemented on an industrial scale. To that matter, the main objective should be to study whether is it possible to induce fluorocarbon deposition using CF_4 plasma on a Si substrate at an intermediate temperature (≥ -40°C) where liquid nitrogen is not needed for wafer thermalization.

Although this manuscript only presented fluorocarbon plasma process results obtained for relatively thick etching processes, cryogenic etching also represents an interesting field for thin-etching research applications such as ALE (atomic layer etching) notably because it reduces plasma-induced surface damage. During this research project, many gas chemistries (SF_6, C_4F_8, CHF_3) were tested for the study of cryogenic ALE processes which consisted in the repetition of a chemical modification step (plasma

or gas-injection step) followed by an Ar plasma etching step. Atomic level precision etching results were observed in many cases where the etching selectivity between Si, SiO_2 and Si_3N_4 substrates could be varied according to the process parameters. However, the reactor configuration did not enable self-limiting etching reactions at cryogenic temperatures which is key for ALE processing. Therefore, these process results were not disclosed. This manuscript mainly focused on the study of thick cryoetching mechanisms.

References

[1] H. Iwai and D. Misra, The Transistor was Invented 75 Years Ago: A Big Milestone in Human History, Electrochem. Soc. Interface **31**, 65 (2022).

[2] W. F. Brinkman, D. E. Haggan, and W. W. Troutman, A history of the invention of the transistor and where it will lead us, **32**, (1997).

[3] J. Bardeen and W. H. Brattain, *Three-Electrode Circuit Element Utilizing Semiconductive Materials*, 2,524,035 (10 March 1950).

[4] W. Fox, *New AI Chips Feature 208 Billion Transistors*, https://www.futuretimeline.net/blog/2024/03/22-nvidia-ai-chip-208-billion-transistors.htm.

[5] AMD, *AMD Instinct™ MI300X Accelerators*, https://www.amd.com/en/products/accelerators/instinct/mi300/mi300x.html.

[6] W. Shockley, A Unipolar "Field-Effect" Transistor, Proc. IRE **40**, 1365 (1952).

[7] D. Kahng, *Electric Field Controlled Semiconductor Device*, 3,102,230 (24 August 1963).

[8] M. M. Atalla, *Semiconductor Triode*, 3,056,888 (10 February 1962).

[9] M. M. Atalla, E. Tannenbaum, and E. J. Scheibner, Stabilization of Silicon Surfaces by Thermally Grown Oxides, Bell Syst. Tech. J. **38**, 749 (1959).

[10] Z. Qingzhu, Z. Yongkui, L. Yanna, and Y. Huaxiang, New structure transistors for advanced technology node CMOS ICs, Natl. Sci. Rev. **11**, (2024).

[11] K. Singh, *Gate-All-Around (GAA) FET – Going Beyond The 3 Nanometer Mark*, https://www.copperpodip.com/post/gate-all-around-gaa-fet-going-beyond-the-3-nanometer-mark.

[12] TechSparks, *Is Smaller Always Better for Transistor Size ?*, https://www.tech-sparks.com/size-of-transistors/.

[13] Techovedas, *5 Laws Shaping Semiconductor Industry For Last 100 Years*, https://techovedas.com/5-laws-shaping-semiconductor-industry-for-last-100-years/.

[14] Samsung, *3nm GAA MBCFET™: A Cutting-Edge Advancement That Brings Unrivaled SRAM Design Flexibility*, https://semiconductor.samsung.com/news-events/tech-blog/3nm-gaa-mbcfet-unrivaled-sram-design-flexibility.

[15] TSMC, *3nm Technology - Taiwan Semiconductor Manufacturing Company Limited*, https://www.tsmc.com/english/dedicatedFoundry/technology/logic/l_3nm.

[16] A. Shilov, *Intel: 4nm, 3nm-Class Nodes on Track, 1.8nm Technology Pulled In*, https://www.tomshardware.com/news/intel-4nm-and-3nm-class-nodes-on-track-18nm-pulled-in.

[17] IBM Research, *Introducing the World's First 2 Nm Node Chip*, https://research.ibm.com/blog/2-nm-chip.

[18] M. Irving, *IBM's New 2-Nm Chips Have Transistors Smaller than a Strand of DNA*, https://newatlas.com/computers/ibm-2-nm-chips-transistors/.

[19] T. Trader, *IBM Research Debuts 2nm Test Chip with 50 Billion Transistors*, https://www.hpcwire.com/2021/05/06/ibm-research-debuts-2nm-test-chip-with-50-billion-transistors/.

[20] J. S. Kilby, *Miniature Semiconductor Integrated Circuit*, 3,115,581 (24 December 1963).

[21] R. N. Noyce, *Semiconductor Device-and-Lead Structure*, 2,981,877 (25 April 1961).

[22] G. E. Moore, Cramming more components onto integrated circuits, Reprinted from Electronics, volume 38, number 8, April 19, 1965, pp.114 ff., IEEE Solid-State Circuits Soc. Newsl. **11**, 33 (2006).

[23] W. M. Haynes, D. R. Lide, and T. J. Bruno, *CRC Handbook of Chemistry and Physics*, 97th Edition (CRC Press, Taylor & Francis Group, 6000 Broken Sound Parkway NW, Suite 300, Boca Raton, FL 33487-2742, 2017).
[24] P. Hess, Thickness of elemental and binary single atomic monolayers, Nanoscale Horiz **5**, 385 (2020).
[25] PubChem, *Atomic Radius | Periodic Table of Elements*, https://pubchem.ncbi.nlm.nih.gov/periodic-table/atomic-radius.
[26] W. Cao, H. Bu, M. Vinet, M. Cao, S. Takagi, S. Hwang, T. Ghani, and K. Banerjee, The future transistors, Nature **620**, 501 (2023).
[27] M. Singh, J. F. Sargent Jr., and K. M. Sutter, Semiconductors and the Semiconductor Industry, Congressional Research Service Report No. R47508, U.S Congress, 2023.
[28] A. Li, *6 Crucial Steps in Semiconductor Manufacturing*, https://www.asml.com/en/news/stories/2021/semiconductor-manufacturing-process-steps.
[29] TSMC, *TSMC Breaks Ground on Fab 18 in Southern Taiwan Science Park*, https://pr.tsmc.com/english/news/1951.
[30] The Economist, Taiwan's dominance of the chip industry makes it more important, The Economist (2023).
[31] K. Ackerman, *The Rise of Natural Disasters and Their Impact on the Industry*, https://www.sourcengine.com/blog/the-rise-of-natural-disasters-and-their-impact-on-the-industry.
[32] Courrier international, *La pénurie de puces électroniques frappe le secteur automobile*, https://www.courrierinternational.com/article/effet-domino-la-penurie-de-puces-electroniques-frappe-le-secteur-automobile.
[33] The White House, *FACT SHEET: CHIPS and Science Act Will Lower Costs, Create Jobs, Strengthen Supply Chains, and Counter China*, https://www.whitehouse.gov/briefing-room/statements-releases/2022/08/09/fact-sheet-chips-and-science-act-will-lower-costs-create-jobs-strengthen-supply-chains-and-counter-china/.
[34] European Commission, *European Chips Act*, https://commission.europa.eu/strategy-and-policy/priorities-2019-2024/europe-fit-digital-age/european-chips-act_en.
[35] N. The Japan Times, *Japan Boosts Aid to Chip Projects amid Global Race*, https://www.japantimes.co.jp/business/2024/02/16/companies/japan-boosts-aid-to-chip-projects/.
[36] J. Choi, *Taiwan Offers Semiconductor Subsidies while South Korea Sticks to Loans*, https://www.businesskorea.co.kr/news/articleView.html?idxno=217725.
[37] L. C. Lee, *China's Big Fund 3.0: Xi's Boldest Gamble Yet for Chip Supremacy*, https://thediplomat.com/2024/06/chinas-big-fund-3-0-xis-boldest-gamble-yet-for-chip-supremacy/.
[38] P. van Gerven, *AI Surge Demands That Moore's Law Transcends Itself - Bits&Chips*, https://bits-chips.nl/article/ai-surge-demands-that-moores-law-transcends-itself/.
[39] A. Fitch, *Nvidia's Ascent to Most Valuable Company Has Echoes of Dot-Com Boom*, https://www.wsj.com/tech/ai/nvidias-ascent-to-most-valuable-company-has-echoes-of-dot-com-boom-dd836c90.
[40] P. Belton, The computer chip industry has a dirty climate secret, The Guardian (2021).
[41] J. C. Hess, *Chip Production's Ecological Footprint: Mapping Climate and Environmental Impact*.
[42] Q. Wang, Environmental data and facts in the semiconductor manufacturing industry: An unexpected high water and energy consumption situation, (2023).
[43] E. Gallagher, P. Bezard, L. Boakes, A. Firrincieli, C. Rolin, and L.-Å. Ragnarsson, Sustainable semiconductor manufacturing: lessons for lithography and etch, Proc. SPIE **12499**, (2023).
[44] Ministère de la transition écologique et de la cohésion des territoires, *L'eau en France : ressource et utilisation – Synthèse des connaissances en 2023*, https://www.statistiques.developpement-durable.gouv.fr/leau-en-france-ressource-et-utilisation-synthese-des-connaissances-en-2023.

[45] S. Beck et al., *Chiffres clés de l'énergie (Edition 2021)*.
[46] G. S. Oehrlein et al., Future of plasma etching for microelectronics: Challenges and Opportunities, J. Vac. Sci. Technol. B Microelectron. Nanometer Struct. **42**, (2024).
[47] European Parliament, Council of the European Union, *Regulation (EU) 2024/573 of the European Parliament and of the Council of 7 February 2024 on Fluorinated Greenhouse Gases, Amending Directive (EU) 2019/1937 and Repealing Regulation (EU) No 517/2014*.
[48] O. US EPA, *Understanding Global Warming Potentials*, https://www.epa.gov/ghgemissions/understanding-global-warming-potentials.
[49] Greenhouse Gas Protocol, *Homepage | GHG Protocol*, https://ghgprotocol.org/.
[50] B. J. Lee, Y. Hwang, D. K. Jo, and J. Jeong, A Study on Greenhouse Gas (PFCs) Reduction in Plasma Scrubbers to Realize Carbon Neutrality of Semiconductors and Displays, (2023).
[51] Statista Research Department, *PFC : émissions totales France 2012-2021*, https://fr.statista.com/statistiques/597290/emissions-pfc-perfluorocarbures-france/.
[52] European Commission, *What Is the EU ETS ?*, https://climate.ec.europa.eu/eu-action/eu-emissions-trading-system-eu-ets/what-eu-ets_en.
[53] *Oerhlein_2024_Future of Plasma Etching for Microelectronics_Challenges and Opportunities.Pdf*.
[54] S. Tachi, K. Tsujimoto, and S. Okudaira, Low-temperature reactive ion etching and microwave plasma etching of silicon, Appl. Phys. Lett. **52**, (1988).
[55] R. Dussart, T. Tillocher, P. Lefaucheux, and M. Boufnichel, Plasma cryogenic etching of silicon: from the early days to today's advanced technologies, J. Phys. Appl. Phys. **47**, (2014).
[56] T. Lill, I. L. Berry, M. Shen, J. Hoang, A. Fischer, T. Panagopoulos, J. P. Chang, and V. Vahedi, Dry etching in the presence of physisorption of neutrals at lower temperatures, J. Vac. Sci. Technol. A **41**, 023005 (2023).
[57] D. B. Graves et al., Science challenges and research opportunities for plasma applications in microelectronics, J. Vac. Sci. Technol. B Microelectron. Nanometer Struct. **42**, (2024).
[58] T. Tillocher, J. Nos, G. Antoun, P. Lefaucheux, M. Boufnichel, and R. Dussart, Comparison between Bosch and STiGer Processes for Deep Silicon Etching, Micromachines **12**, (2021).
[59] S. Hamaguchi, Modeling and simulation methods for plasma processing, IBM J. Res. Dev. **43**, 199 (1999).
[60] A. Bogaerts, E. Bultinck, M. Eckert, V. Georgieva, M. Mao, E. Neyts, and L. Schaederlé, Computer Modeling of Plasmas and Plasma-Surface Interactions, Plasma Process Polym **6**, 295 (2009).
[61] K. J. Kanarik, W. T. Osowlecki, Y. (Joe) Lu, D. Talukder, N. Roschewsky, S. N. Park, M. Kamon, D. M. Fried, and R. A. Gottscho, Human–machine collaboration for improving semiconductor process development, Nature **616**, 707 (2023).
[62] E. Despiau-Pujo, *Dynamique moléculaire: Interaction plasma-surface et gravure plasma*, (unpublished).
[63] D. B. Graves and P. Brault, Molecular Dynamics for Low Temperature Plasma-Surface Interaction Studies, J. Phys. Appl. Phys. **42**, (2009).
[64] E. Neyts and P. Brault, Molecular dynamics simulations for plasma-surface interactions, Plasma Process. Polym. **14**, (2016).
[65] F. H. Stillinger and T. A. Weber, Fluorination of the Dimerized Si(100) Surface Studied by Molecular-Dynamics Simulation, Phys. Rev. Lett. **62**, 2144 (1989).
[66] S. Tinck, E. C. Neyts, and A. Bogaerts, Fluorine−Silicon Surface Reactions during Cryogenic and Near Room Temperature Etching, J Phys Chem C **118**, 30315 (2014).
[67] R. Dussart, T. Tillocher, P. Lefaucheux, and M. Boufnichel, Plasma cryogenic etching of silicon: from the early days to today's advanced technologies, J. Phys. Appl. Phys. **47**, (2014).
[68] SK hynix Inc., *SK Hynix Begins Mass Production of Industry's Highest 238-Layer 4D NAND*, https://news.skhynix.com/sk-hynix-begins-mass-production-of-industrys-highest-238-layer-4d-nand/.

[69] Micron technology Inc., *The Evolution of NAND*, https://sg.micron.com/about/blog/memory/nand/the-evolution-of-nand.
[70] S. Franssila, *Introduction to Microfabrication*, 2nd edition (John Wiley & Sons, Ltd, 2010).
[71] SK hynix Inc., *Semiconductor Front-End Process Episode 2: Oxidation*, https://news.skhynix.com/semiconductor-front-end-process-episode-2/.
[72] R. W. Johnson, A. Hultqvist, and S. F. Bent, A brief review of atomic layer deposition: from fundamentals to applications, Mater. Today **17**, 236 (2014).
[73] G. Belmont, L. Rezeau, C. Riconda, and A. Zaslavsky, *Chapter 1: What Is Plasma ?*, in *Introduction to Plasma Physics*, 1st edition (ISTE Press Ltd - Elsevier Inc, 2019), pp. 1–32.
[74] M. A. Lieberman and A. J. Lichtenberg, *Principles of Plasma Discharges and Materials Processing*, 2nd ed (Wiley-Interscience, Hoboken, N.J, 2005).
[75] F. Chen, *Introduction to Plasma Physics and Controlled Fusion*, 3rd ed. 2016 (Springer International Publishing : Imprint: Springer, Cham, 2016).
[76] P. K. Chu and X. Lu, *Low Temperature Plasma Technology* (CRC Press, 2014).
[77] A. Anders, Tracking Down the Origin of Arc Plasma Science - II. Early Continuous Discharges, IEEE Trans. Plasma Sci. **31**, 1052 (2003).
[78] W. Crookes, On radiant matter, J. Frankl. Inst. **108**, 305 (1879).
[79] W. Crookes, On the illumination of lines of molecular pressure and the trajectory of molecules, Proc. R. Soc. Lond. **28**, (1879).
[80] T. Arabatzis, *Cathode Rays*, in *Compendium of Quantum Physics* (Springer, Berlin, Heidelberg, 2009), pp. 89–92.
[81] H. M. Mott-Smith, History of "'Plasmas,'" Nature **233**, 219 (1971).
[82] L. Tonks and I. Langmuir, A General Theory of the Plasma of an Arc, Phys. Rev. **34**, 876 (1929).
[83] F. F. Chen and J. P. Chang, *Lecture Notes on Principles of Plasma Processing*, 1st edition (Springer New York, NY, 2003).
[84] P. Chabert and N. Braithwaite, *Physics of Radio-Frequency Plasmas* (Cambridge University Press, 2011).
[85] H.-C. Lee, Review of inductively coupled plasmas: Nano-applications and bistable hysteresis physics, Appl Phys Rev **5**, (2018).
[86] D. J. Economou, Modeling and simulation of plasma etching reactors for microelectronics, Thin Solid Films **365**, 348 (2000).
[87] K. Ishikawa, K. Karahashi, T. Ishijima, S. I. Cho, S. Elliott, D. Hausmann, D. Mocuta, A. Wilson, and K. Kinoshita, Progress in nanoscale dry processes for fabrication of high-aspect-ratio features: How can we control critical dimension uniformity at the bottom?, Jpn J Appl Phys **57**, (2018).
[88] S. Hwang and K. Kanarik, *Evolution of Across-Wafer Uniformity Control in Plasma Etch | Semiconductor Digest*, https://sst.semiconductor-digest.com/2016/08/evolution-of-across-wafer-uniformity-control-in-plasma-etch/.
[89] Z. Shi, K. Jefimovs, A. La Magna, M. Stampanoni, and L. Romano, High aspect ratio tilted gratings through local electric field modulation in plasma etching, Appl. Surf. Sci. **588**, (2022).
[90] W. Kafrouni, T. Tillocher, J. Ladroue, P. Lefaucheux, M. Boufnichel, P. Ranson, and R. Dussart, Parametric study of STiGer etching process in order to reduce extended formation of scalloping defects on the sidewalls of silicon submicron trenches, Vacuum **133**, 90 (2016).
[91] J. W. Choi, W. L. Loh, S. K. Praveen, R. Murphy, and E. T. K. Swee, A study of the mechanisms causing surface defects on sidewalls during Si etching for TSV (through Si via), J. Micromechanics Microengineering **23**, 065005 (2013).
[92] K. Hanaoka and K. Takahashi, Vertical silicon etching by using an automatically and fast-controlled frequency tunable rf plasma source, AIP Adv. **11**, (2021).
[93] J. W. Winniczek, F. Y. Lin, A. J. Miller, Q. Xu, S. Heo, J. H. Ham, and S. J. Yoon, *Method for Achieving Smooth Side Walls after Bosch Etch Process*, WO 2012/154764 A2 (15 November 2012).

[94] J. S. Park, D.-H. Kang, S. M. Kwak, T. S. Kim, J. H. Park, T. G. Kim, D.-H. Baek, and B. C. Lee, Low-temperature smoothing method of scalloped DRIE trench by post-dry etching process based on SF6 plasma, Micro Nano Syst. Lett. **8**, (2020).
[95] M. Omura, J. Hashimoto, T. Adachi, Y. Kondo, M. Ishikawa, J. Abe, I. Sakai, H. Hayashi, M. Sekine, and M. Hori, Formation mechanism of sidewall striation in high-aspect-ratio hole etching, Jpn J Appl Phys **58**, (2019).
[96] H. Jansen, M. de Boer, R. Legtenberg, and M. Elwenspoek, The black silicon method: a universal method for determining the parameter setting of a fluorine-based reactive ion etcher in deep silicon etching with profile control, J. Micromechanics Microengineering **5**, 115 (1995).
[97] M. Steglich, T. Käsebier, M. Zilk, T. Pertsch, E.-B. Kley, and A. Tünnerman, The structural and optical properties of black silicon by inductively coupled plasma reactive ion etching, J Appl Phys **116**, (2014).
[98] E. A. Vyacheslavova, I. A. Morozov, D. A. Kudryashov, A. V. Uvarov, A. I. Baranov, A. A. Maksimova, S. N. Abolmasov, and A. S. Gudovskikh, Study of Cryogenic Unmasked Etching of "Black Silicon" with Ar Gas Additives, ACS Omega **7**, (2022).
[99] S. Huang, S. Shim, S. K. Nam, and M. J. Kushner, Pattern dependent profile distortion during plasma etching of high aspect ratio features in SiO2, J Vac Sci Technol A **38**, (2020).
[100] S. L. Lai, D. Johnson, and R. Westerman, Aspect ratio dependent etching lag reduction in deep silicon etch processes, J Vac Sci Technol A **24**, 1283 (2024).
[101] S. Sirard, *Introduction to Plasma Etching*, https://willson.cm.utexas.edu/Teaching/LithoClass2018/Files/Introduction%20to%20Plasma%20Etching_Lecture_110118_Sntzd.pdf.
[102] M. F. Doemling, N. R. Rueger, and G. S. Oehrlein, Observation of inverse reactive ion etching lag for silicon dioxide etching in inductively coupled plasmas, Appl Phys Lett **68**, (1996).
[103] C. K. Chung and H. N. Chiang, Inverse RIE Lag of Silicon Deep Etching, Proc. NSTI Nanotechnol. Conf. **1**, 481 (2004).
[104] J.-K. Lee, I.-Y. Jang, S.-H. Lee, C.-K. Kim, and S. H. Moon, Mechanism of Sidewall Necking and Bowing in the Plasma Etching of High Aspect-Ratio Contact Holes, J. Electrochem. Soc. **157**, D142 (2010).
[105] J. W. Palmour, B. E. Williams, P. Astell-Burt, and R. F. Davis, Crystallographic Etching Phenomenonduring Plasma Etching of SiC (100) Thin Films in SF6, J Electrochem Soc **136**, 491 (1989).
[106] M. A. Blauw, T. Zijlstra, and R. A. Bakker, Kinetics and crystal orientation dependence in high aspect ratio silicon dry etching, J Vac Sci Technol B **18**, 3453 (2000).
[107] L. Xie, T. X. Zhou, R. J. Stöhr, and A. Yacoby, Crystallographic Orientation Dependent Reactive Ion Etching in Single Crystal Diamond, Adv Mater **2018**, 1 (2018).
[108] V. M. Donnelly and A. Kornblit, Plasma etching: Yesterday, today, and tomorrow, J Vac Sci Technol A **31**, 1 (2013).
[109] H. Jansen, H. Gardeniers, M. de Boer, M. Elwenspoek, and J. Fluitman, A survey on the reactive ion etching of silicon in microtechnology, J Micromech Microeng **6**, 14 (1996).
[110] F. Laermer, S. Franssila, L. Sainiemi, and K. Kolari, *Deep Reactive Ion Etching*, in *Handbook of Silicon Based MEMS Materials and Technologies*, 2nd Edition (Elsevier, 2015), pp. 444–469.
[111] S. Franssila and L. Sainiemi, *Reactive Ion Etching (RIE)*, in *Encyclopedia of Microfluidics and Nanofluidics* (Springer, Boston, MA, 2008), pp. 1772–1781.
[112] D. E. Ibbotson, D. L. Flamm, J. A. Mucha, and V. M. Donnelly, Comparison of XeF2 and F atom reactions with Si and SiO2, Appl. Phys. Lett. **44**, 1129 (1984).
[113] D. E. Ibbotson, J. A. Mucha, D. L. Flamm, and J. M. Cook, Plasmaless dry etching of silicon with fluorinecontaining compounds, J. Appl. Phys. **56**, 2939 (1984).
[114] J. W. Coburn and H. F. Winters, Plasma etching—A discussion of mechanisms, J Vac Sci Technol **16**, 391 (1979).
[115] P. J. Holmes and J. E. Snell, A Vapour Etching Technique for the Photolithography of Silicon Dioxide, Microelectron. Reliab. **5**, 337 (1966).

[116] D. L. Flamm, Mechanisms of silicon etching in fluorine- and chlorine-containing plasmas, Pure Appl Chem **62**, 1709 (1990).
[117] P. D. Davidse, RF Sputter Etching - A Universal Etch, J. Electrochem. Soc. **116**, 100 (1969).
[118] S. M. Irving, A Plasma Oxidation for Removing Photoresist Films, Solid State Technol **14**, 47 (1971).
[119] S. M. Irving, K. E. Lemons, and G. E. Bobos, *Gas Plasma Vapor Etching Process*, 3,615,956 (1971).
[120] R. A. H. Heinecke, Control of relative etch rates of SiO2 and Si in plasma etching, Solid-State Electron. **18**, 1146 (1975).
[121] R. G. Poulsen, Plasma etching in integrated circuit manufacture - A review, J. Vac. Sci. Technol. **14**, 266 (1977).
[122] A. R. Reinberg, *Radial Flow Reactor*, 3,757,733 (1973).
[123] N. Hosokawa, R. Matsuzaki, and T. Asamaki, RF Sputter-Etching by Fluoro-Chloro-Hydrocarbon Gases, Jpn. J. Appl. Phys. **13**, 435 (1974).
[124] J. A. Bondur, Dry process technology (reactive ion etching), J Vac Sci Technol **13**, 1023 (1976).
[125] H. B. Pogge, J. A. Bondur, and P. J. Burkhardt, Reactive Ion Etching of Silicon with Cl2/Ar, J Electrochem Soc **130**, 1592 (1983).
[126] C. Cardinaud, M.-C. Peignon, and P.-Y. Tessier, Plasma etching: principles, mechanisms, application to micro- and nano-technologies, Appl. Surf. Sci. **164**, 72 (2000).
[127] F. Laermer and A. Schilp, *Method for Anisotropic Plasma Etching of Substrates*, US5498312A (12 March 1996).
[128] B. Wu, A. Kumar, and S. Pamarthy, High aspect ratio silicon etch: A review, J Appl Phys **108**, 1 (2010).
[129] M. A. Blauw, T. Zijlstra, and E. van der Drift, Balancing the etching and passivation in time-multiplexed deep dry etching of silicon, J. Vac. Sci. Technol. B Microelectron. Nanometer Struct. **19**, (2001).
[130] F. Laermer and A. Urban, *Through-Silicon Vias Using Bosch DRIE Process Technology*, in *Ultra-Thin Chip Technology and Applications*, Joachim Burghartz (Springer New York, NY, 2010), pp. 81–91.
[131] S. L. Burkett, M. B. Jordan, R. P. Schmitt, L. A. Menk, and A. E. Hollowell, Tutorial on forming through-silicon vias, J. Vac. Sci. Technol. A **38**, 031202 (2020).
[132] O. Fursenko, J. Bauer, S. Marschmeyer, and H.-P. Stoll, Through silicon via profile metrology of Bosch etching process based on spectroscopic reflectometry, Microelectron. Eng. **139**, 70 (2015).
[133] H. V. Jansen, M. J. de Boer, S. Unnikrishnan, M. C. Louwerse, and M. C. Elwenspoek, Black silicon method X: a review on high speed and selective plasma etching of silicon with profile control: an in-depth comparison between Bosch and cryostat DRIE processes as a roadmap to next generation equipment, J Micromech Microeng **19**, 1 (2009).
[134] M. J. Walker, Comparison of Bosch and cryogenic processes for patterning high aspect ratio features in silicon, Microelectron. MEMS Technol. (2001).
[135] G. S. Oehrlein and Y. Kurogi, Sidewall surface chemistry in directional etching processes, Mater. Sci. Eng. **24**, 153 (1998).
[136] C. J. D. Craigie, T. Sheehan, V. N. Johnson, S. L. Burkett, A. J. Moll, and W. B. Knowlton, Polymer thickness effects on Bosch etch profiles, J Vac Sci Technol B **20**, 2229 (2002).
[137] C. B. Labelle, V. M. Donnelly, G. R. Bogart, R. L. Opila, and A. Kornblit, Investigation of fluorocarbon plasma deposition from c-C4F8 for use as passivation during deep silicon etching, J. Vac. Sci. Technol. A **22**, (2004).
[138] T. Nonaka, K. Takahashi, A. Uchida, S. Lundgaard, and O. Tsuji, Effects of C4F8 plasma polymerization film on etching profiles in the Bosch process, J Vac Sci Technol A **41**, 1 (2023).
[139] S. McColman, *Advanced Bosch Processing on the Oxford Plasmalab ICPRIE*.
[140] W. S. Kennedy, R. A. Maraschin, and T. E. Wicker, *Semiconductor Processing Equipment Having Radiant Heated Ceramic Liner*, WO 01/22478 A1 (29 March 2001).

[141] M. Puech, *Heating Jacket for Plasma Etching Reactor, and Etching Method Using Same*, US20050224178A1 (13 October 2005).
[142] M. Wasilik and N. Chen, Deep reactive ion etch conditioning recipe, Proc. SPIE **5342**, 103 (2003).
[143] C.-Y. Lee and A. Shen, Residual polymer effect on shallow trench Bosch process stability, AIP Adv. **10**, (2020).
[144] Tachi S., Okudaira S., and Mukai K., *Controlling method of surface reaction*, JPS60158627A (20 August 1985).
[145] S. Tachi, K. Tsujimoto, S. Arai, and T. Kure, Low-temperature dry etching, J. Vac. Sci. Technol. A **9**, 796 (1991).
[146] J. W. Bartha, J. Greschner, M. Puech, and P. Maquin, Low temperature etching of Si in high density plasma using SF6/O2, Microelectron. Eng. **27**, 453 (1995).
[147] T. Wells, M. M. El-Gomati, and J. Wood, Low temperature reactive ion etching of silicon with SF6 /O2 plasmas, J. Vac. Sci. Technol. B Microelectron. Nanometer Struct. **15**, 434 (1996).
[148] R. d'Agostino and D. L. Flamm, Plasma etching of Si and SiO2 in SF6-O2 mixtures, J. Appl. Phys. **52**, 162 (1981).
[149] H. Jansen, M. de Boer, H. Wensink, B. Kloeck, and M. Elwenspoek, The black silicon method. VIII. A study of the performance of etching silicon using SF6/O2-based chemistry with cryogenical wafer cooling and a high density ICP source, Microelectron. J. **32**, 769 (2001).
[150] R. Dussart, M. Boufnichel, G. Marcos, P. Lefaucheux, A. Basillais, R. Benoit, T. Tillocher, X. Mellhaoui, H. Estrade-Szwarckopf, and P. Ranson, Passivation mechanisms in cryogenic SF6/O2 etching process, J. Micromechanics Microengineering **14**, 190 (2004).
[151] X. Mellhaoui, R. Dussart, T. Tillocher, and P. Lefaucheux, SiOxFy passivation layer in silicon cryoetching, J Appl Phys **98**, (2005).
[152] R. Dussart, X. Mellhaoui, T. Tillocher, P. Lefaucheux, M. Boufnichel, and P. Ranson, The passivation layer formation in the cryo-etching plasma process, Microelectron. Eng. **84**, 1128 (2007).
[153] J. Pereira, L. E. Pichon, R. Dussart, C. Cardinaud, C. Y. Duluard, E. H. Oubensaid, P. Lefaucheux, and P. Ranson, In situ x-ray photoelectron spectroscopy analysis of SiOxFy passivation layer obtained in a SF6/O2 cryoetching process, Appl Phys Lett **94**, 1 (2009).
[154] K. Tsujimoto, S. Tachi, K. Ninomiya, K. Suzuki, S. Okudaira, and S. Nishimatsu, A New Side Wall Protection Technique in Microwave Plasma Etching Using a Chopping Method, Ext. Abstr. 18th 1986 Int. Conf. Solid State Devices Mater. 229 (1986).
[155] T. Tillocher, R. Dussart, L. J. Overzet, X. Mellhaoui, P. Lefaucheux, M. Boufnichel, and P. Ranson, Two Cryogenic Processes Involving SF6, O2, and SiF4 for Silicon Deep Etching, J. Electrochem. Soc. **155**, D187 (2008).
[156] R. Dussart, P. Lefaucheux, X. Melhaoui, L. J. Overzet, P. Ranson, T. Tillocher, and M. Boufnichel, *Deep Anisotropic Silicon Etch Method*, US8012365B2 (6 September 2011).
[157] L. Pichon-Balmadier, Etude et optimisation du procédé STiGer de gravure profonde du silicium, Université d'Orléans, 2010.
[158] K. L. Williams, C. I. Butoi, and E. R. Fisher, Mechanisms for deposition and etching in fluorosilane plasma processing of silicon, J. Vac. Sci. Technol. A **21**, 1688 (2003).
[159] T. Tillocher, W. Kafrouni, J. Ladroue, P. Lefaucheux, M. Boufnichel, P. Ranson, and R. Dussart, Optimization of submicron deep trench profiles with the STiGer cryoetching process, J Micromech Microeng **21**, (2011).
[160] *IPCC Global Warming Potential Values (7th August 2024)*, https://ghgprotocol.org/sites/default/files/2024-08/Global-Warming-Potential-Values (August 2024).pdf.
[161] P. Forster et al., *Chapter 7: The Earth's Energy Budget, Climate Feedbacks and Climate Sensitivity*, in *Climate Change 2021: The Physical Science Basis. Contribution of Working Group I to the Sixth Assessment Report of the Intergovernmental Panel on Climate Change* (Cambridge University Press, 2021), pp. 923–1054.

[162] L. M. Ephrath, Selective Etching of Silicon Dioxide Using Reactive Ion Etching with CF4-H2, J. Electrochem. Soc. **126**, 1419 (1979).
[163] G. S. Oehrlein, Y. Zhang, D. Vender, and M. Haverlag, Fluorocarbon high-density plasmas. I. Fluorocarbon film deposition and etching using CF4 and CHF3, J Vac Sci Technol A **12**, 323 (1994).
[164] G. S. Oehrlein, Y. Zhang, D. Vender, and O. Joubert, Fluorocarbon high-density plasmas. II. Silicon dioxide and silicon etching using CF4 and CHF3, J Vac Sci Technol A **12**, 333 (1994).
[165] N. R. Rueger, J. J. Beulens, M. Schaepkens, M. F. Doemling, J. M. Mirza, T. E. F. M. Standaert, and G. S. Oehrlein, Role of steady state fluorocarbon films in the etching of silicon dioxide using CHF3 in an inductively coupled plasma reactor, J Vac Sci Technol A **15**, 1881 (1997).
[166] T. E. F. M. Standaert, M. Schaepkens, N. R. Rueger, P. G. M. Sebel, G. S. Oehrlein, and J. M. Cook, High density FC etching of Si in ICP plasma_Mechanism of etching through a thick steady state FC layer, J. Vac. Sci. Technol. A **16**, 239 (1998).
[167] M. Schaepkens, T. E. F. M. Standaert, N. R. Rueger, P. G. M. Sebel, G. S. Oehrlein, and J. M. Cook, Study of the SiO2-to-Si3N4 etch selectivity mechanism in inductively coupled fluorocarbon plasmas and a comparison with the SiO2-to-Si mechanism, J. Vac. Sci. Technol. A **17**, 26 (1999).
[168] M. Schaepkens and G. S. Oehrlein, A Review of SiO2 Etching Studies in Inductively Coupled Fluorocarbon Plasmas, J. Electrochem. Soc. **148**, C211 (2001).
[169] T. E. F. M. Standaert, C. Hedlund, E. A. Joseph, G. S. Oehrlein, and T. J. Dalton, Role of fluorocarbon film formation in the etching of silicon, silicon dioxide, silicon nitride and amorphous hydrogenated silicon carbide, J. Vac. Sci. Technol. A **22**, 53 (2003).
[170] B. E. E. Kastenmeier, P. J. Matsuo, and G. S. Oehrlein, Highly selective etching of silicon nitride over silicon and silicon dioxide, J Vac Sci Technol A **17**, 3179 (1999).
[171] C. Reyes-Betanzo, S. A. Moshkalyov, M. A. Cotta, M. A. Pavanello, A. C. S. Ramos, and J. W. Swart, Plasma Etching of Silicon Nitride with High Selectivity over Silicon Oxide and Silicon in Fluorine Containing Plasmas, J. Vac. Sci. Technol. A **17**, 3179 (1999).
[172] H. K. Lee, K. S. Chung, and J. S. Yu, Selective Etching of Thick Si3N4, SiO2 and Si by Using CF4/O2 and C2F6 gases with or without O2 or Ar Addition, J. Korean Phys. Soc. **54**, 1816 (2009).
[173] L. Chen, L. Xu, D. Li, and B. Lin, Mechanism of selective Si3N4 etching over SiO2 in hydrogen-containing fluorocarbon plasma, Microelectron. Eng. **86**, 2354 (2009).
[174] J.-E. Jung, Y. Barsukov, V. Volynets, G. Kim, S. K. Nam, K. Han, S. Huang, and M. J. Kushner, Highly selective Si3N4/SiO2 etching using an NF3/N2/O2/H2 remote plasma. II. Surface reaction mechanism, J Vac Sci Technol A **38**, 1 (2020).
[175] M. Lee and W.-J. Lee, The effect of substrate temperature on the etching properties and the etched surfaces of magnetic tunnel junction materials in a CH3OH inductively coupled plasma system, Appl. Surf. Sci. **258**, 8100 (2012).
[176] S.-N. Hsiao, K. Nakane, T. Tsutsumi, K. Ishikawa, M. Sekine, and M. Hori, Influences of substrate temperatures on etch rates of PECVD-SiN thin films with a CF4/H2 plasma, Appl. Surf. Sci. **542**, (2021).
[177] M. Konuma, F. Banhart, and E. Bauser, Damage-free Reactive Ion Etching of Silicon in NF3 at Low Temperature, Mater. Sci. Eng. **B4**, 265 (1989).
[178] T. Mizutani, T. Yunogami, and K. Tsujimoto, Lower plasma induced damage in SiO2/Si at lower temperatures, Appl. Phys. Lett. **57**, (1990).
[179] F. Iacopi, J. H. Choi, K. Terashima, P. M. Rice, and G. Dubois, Cryogenic plasmas for controlled processing of nanoporous materials, Phys Chem Chem Phys **13**, 3634 (2011).
[180] F. Leroy, L. Zhang, T. Tillocher, K. Yatsuda, K. Maekawa, E. Nishimura, P. Lefaucheux, J.-F. de Marneffe, M. R. Baklanov, and R. Dussart, Cryogenic etching processes applied to porous low-k materials using SF6/C4F8 plasmas, Appl Phys (2015).
[181] R. Chanson, L. Zhang, S. Naumov, Y. A. Mankelevich, T. Tillocher, P. Lefaucheux, R. Dussart, S. De Gendt, and J.-F. de Marneffe, Damage-free plasma etching of porous organo-silicate low-k using micro-capillary condensation above -50 °C, Sci. Rep. **8**, (2018).

[182] V. Clericò, J. A. Delgado-Notario, M. Saiz-Bretín, A. V. Malyshev, Y. M. Meziani, P. Hidalgo, B. Méndez, M. Amado, F. Domínguez-Adame, and E. Diez, Quantum nanoconstrictions fabricated by cryo-etching in encapsulated graphene, Sci. Rep. **9**, (2019).
[183] Oxford Instruments, *Plasma Pro®100 Hardware Brochure*.
[184] Oxford Instruments, *Plasma Pro®100 Cobra: Operator Manual (Op 816690)*.
[185] Advanced Energy, *Cesar RF Power Supplies Brochure*.
[186] Advanced Energy, *Cesar® 0230 400V User Manual 57020023-00H*.
[187] Swagelok, *Diaphragm Valves for Atomic Layer Deposition*.
[188] MKS, *MKS G-Series Digital Mass Flow Controllers Instruction Manual*.
[189] Pfeiffer Vacuum, *Adixen ATH 1600 MT Magnetically Levitatted Turbomolecular Vacuum Pump Brochure*.
[190] Horiba Jobin Yvon, *Spectroscopic Ellipsometry User Guide*.
[191] G. E. Jellison, *Ellipsometry*, in *Encyclopedia of Spectroscopy and Spectometry*, Elsevier (1999), pp. 402–411.
[192] Horiba Jobin Yvon, *UVISEL: Spectroscopic Phase Modulated Ellipsometer (Brochure)*.
[193] Horiba Jobin Yvon, *DeltaPsi2 Software Reference Manual*.
[194] G. E. Jellison, Optical functions of silicon determined by two-channel polarization modulation ellipsometry, Opt. Mater. **1**, 41 (1992).
[195] Horiba Jobin Yvon, *Spectroscopic Ellipsometry (TN10): Classical Dispersion Model*.
[196] Horiba Jobin Yvon, *Spectroscopic Ellipsometry (TN12): New Amorphous Dispersion Formula*.
[197] A. R. Forouhi and I. Bloomer, Optical dispersion relations for amorphous semiconductors and amorphous dielectrics, Phys. Rev. B **34**, 7018 (1986).
[198] Hiden Analytical, *Hiden Analytical EQP/EQS Analyser Operator's Manual*.
[199] Hiden Analytical, *Hiden Analytical EQP Series Brochure*.
[200] Hiden Analytical, *Hiden Analytical EQP Mass and Energy Analyser for Plasma Diagnostic* (2020).
[201] Impedans, *IMPEDANS_Langmuir Installation and User Guide.Pdf*.
[202] Impedans, *Langmuir Probe - Theory of Operation*, https://www.impedans.com/langmuir-probe-system-theory-of-operation/.
[203] T. Gilmore, *Langmuir Probe (Technical Documentation)*.
[204] Impedans, *Webinar on Impedans Langmuir Probe* (n.d.).
[205] L. Conde, *An Introduction to Langmuir Probe Diagnostics of Plasmas*.
[206] R. L. Merlino, Understanding Langmuir probe current-voltage characteristics, Am J Phys **75**, 1078 (2007).
[207] Impedans, *Plato Probe Installation & User Guide*.
[208] Impedans, *Plato Probe Technical Presentation*.
[209] N. S. J. Braithwaite, J. P. Booth, and G. Cunge, A novel electrostatic probe method for ion flux measurements, Plasma Sources Sci Technol **5**, 677 (1996).
[210] J.-P. Booth, L. Albarede, J. Kim, and D. Keil, *RF-BIASED CAPACITIVELY-COUPLED ELECTROSTATIC (RFB-CCE) PROBE ARRANGEMENT FOR CHARACTERIZING A FILM IN A PLASMA PROCESSING CHAMBER*, US 8,164,353 B2 (24 April 2012).
[211] V. A. Godyak and B. M. Alexandrovich, Comparative analyses of plasma probe diagnostics techniques, J Appl Phys **118**, (2015).
[212] F. F. Chen, Langmuir probes in RF plasma: surprising validity of OML theory, Plasma Sources Sci Technol **18**, (2009).
[213] F. F. Chen, Langmuir probe analysis for high density plasmas, Phys. Plasmas **8**, 3029 (2001).
[214] H. M. Mott-Smith and I. Langmuir, The Theory of Collectors in Gaseous Discharges, Phys Rev **28**, 727 (1926).
[215] I. B. Bernstein and I. N. Rabinowitz, Theory of Electrostatic Probes in a Low-Density Plasma, Phys. Fluids **2**, 112 (1959).
[216] J. G. Laframboise, Theory of Spherical and Cylindrical Langmuir Probes in Collisionless Maxwellian Plasma at Rest, University of Toronto, Institute for Aerospace Studies, Report No. 100, 1966.

[217] J. E. Allen, R. L. F. Boyd, and P. Reynolds, The Collection of Positive Ions by a Probe Immersed in a Plasma, Proc. Phys. Soc. **Section B**, 297 (1957).
[218] F. F. Chen, Numerical Computations for Ion Probe Characteristics in a Collisionless Plasma, Plasma Phys. J. Nucl. Energy Part C Plasma Phys. Accel. Thermonucl. Res. **7**, 47 (1965).
[219] *RFEA_Impedans_Semion_User Guide.Pdf*.
[220] *Impedans_Semion_BR-0006-02.Pdf*.
[221] Impedans, *Semion RFEA System (Technical)*.
[222] D. Gahan, B. Dolinaj, and M. B. Hopkins, Comparison of plasma parameters determined with a Langmuir probe and with a retarding field energy analyzer, Plasma Sources Sci Technol **17**, (2008).
[223] S. Sharma, D. Gahan, S. Kechkar, S. Daniels, and M. B. Hopkins, A spatially resolved retarding field energy analyzer design suitable for uniformity analysis across the surface of a semiconductor wafer, Rev Sci Instrum **85**, (2014).
[224] T. Baloniak, Calibration of a miniaturized retarding field analyzer for low-temperature plasmas, J Phys Appl Phys **43**, (2010).
[225] W. D. Davis and T. A. Vanderslice, Ion Energies at the Cathode of a Glow Discharge, Phys Rev **131**, (1963).
[226] T. H. M. van de Ven, C. A. de Meijere, R. M. van der Horst, M. van Kampen, V. Y. Banine, and J. Beckers, Analysis of retarding field energy analyzer transmission by simulation of ion trajectories, Rev Sci Instrum **89**, (2018).
[227] J. W. Buiter, Functional Analysis of Retarding FIeld Energy Analyzers for Ion Energy Distribution Measurements in Plasma Enhanced Atomic Layer Deposition, Master Thesis, Eindhoven University of Technology, 2018.
[228] K. Denieffe, C. Mahony, P. Maguire, D. Gahan, and M. Hopkins, Retarding Field Energy Analyzer Ion Current Calibration and Transmission, J. Phys. Appl. Phys. **44**, (2011).
[229] A. W. Molvik, Large acceptance angle retarding potential analyzers, Rev Sci Instrum **52**, 704 (1981).
[230] C. Böhm and J. Perrin, Retarding-fidd analyzer for measurements of ion energy distributions and secondary electron emission coefficients in low-pressure radio frequency discharges, Rev Sci Instrum **64**, (1993).
[231] S. Sharpe, B. Hartnett, H. S. Sethi, and D. Sethi, Absorption cross-sections of CF2 in the $\tilde{A}^1B_1$-$\tilde{X}^1A_1$ transition at 0.5 nm intervals and absolute rate constant for 2 CF2→C2F4 at 298 ± 3K, J. Photochem. **38**, 1 (1987).
[232] M. A. Childs, K. L. Menningen, P. Chevako, N. W. Spellmeyer, L. W. Anderson, and J. E. Lawler, Detection of CH3 during CVD growth of diamond by optical absorption, Phys. Lett. A **171**, 87 (1992).
[233] J.-P. Booth, G. Cunge, F. Neuilly, and N. Sadeghi, Absolute radical densities in etching plasmas determined by broad-band UV absorption spectroscopy, Plasma Sources Sci Technol **7**, 423 (1998).
[234] J. P. Booth, Optical and electrical diagnostics of fluorocarbon plasma etching processes, Plasma Sources Sci Technol **8**, 249 (1999).
[235] J. P. Booth and G. Cunge, CFx Radical Creation and Destruction at Surfaces in Fluorocarbon Plasmas, J. Plasma Fusion Res. **75**, 821 (1999).
[236] G. Cunge and J. P. Booth, CF 2 production and loss mechanisms in fluorocarbon discharges: Fluorine-poor conditions and polymerization, J Appl Phys **85**, 3952 (1999).
[237] J. Luque, E. A. Hudson, and J.-P. Booth, CF $A^2\Sigma+ - X^2\pi$ and $B^2\Delta - X^2\pi$ study by broadband absorption spectroscopy in a plasma etch reactor: Determination of transition probabilities, CF $X^2\pi$ concentrations, and gas temperatures, J Chem Phys **118**, 622 (2003).
[238] N. Bulcourt, J.-P. Booth, E. A. Hudson, J. Luque, D. K. W. Mok, E. P. Lee, F.-T. Chau, and J. M. Dyke, Use of the ultraviolet absorption spectrum of CF2 to determine the spatially resolved absolute CF2 density, rotational temperature, and vibrational distribution in a plasma etching reactor, J Chem Phys **120**, 9499 (2004).

[239] M. Kogelschatz, G. Cunge, and N. Sadeghi, Identification of halogen containing radicals in silicon etching plasmas and density measurement by UV broad band absorption spectroscopy, J. Phys. Appl. Phys. **37**, 1954 (2004).
[240] J. P. Booth, H. Abada, P. Chabert, and D. B. Graves, CF and CF2 radical kinetics and transport in a pulsed CF4 ICP, Plasma Sources Sci Technol **14**, 273 (2005).
[241] G. Cunge, D. Vempaire, M. Touzeau, and N. Sadeghi, Broadband and time-resolved absorption spectroscopy with light emitting diodes: Application to etching plasma monitoring, Appl Phys Lett **91**, 1 (2007).
[242] W. Schwarzenbach, G. Cunge, and J. P. Booth, High mass positive ions and molecules in capacitively-coupled radio-frequency CF 4 plasmas, J Appl Phys **85**, 7562 (2014).
[243] J. W. Coburn and H. F. Winters, Plasma etching—A discussion of mechanisms, J Vac Sci Technol **16**, 391 (1979).
[244] Hamamatsu, *Hamamatsu Energetiq LDLS Datasheet*.
[245] Princeton Instruments, *Operating Instructions Acton Series SP-2750*.
[246] Teledyne Princeton Instruments, *PyLoN 400 Datasheet*.
[247] M. Puech, *Heating Jacket for Plasma Etching Reactor, and Etching Method Using Same*, US20050224178A1 (13 October 2005).
[248] A. Mitrovic, M. Long, P. Moroz, S. Fink, and W. Jones, *Plasma Chamber Wall Segment Temperature Control*, WO 03/012567 A1 (13 February 2003).
[249] M. Schaepkens, R. C. M. Bosch, and J. M. Cook, Influence of reactor wall conditions on etch processes in inductively coupled fluorocarbon plasmas, J Vac Sci Technol A **16**, (1998).
[250] S. McColman, *Advanced Bosch Processing on the Oxford Plasmalab ICPRIE*.
[251] C.-Y. Lee and A. Shen, Residual polymer effect on shallow trench Bosch process stability, AIP Adv. **10**, (2020).
[252] Y. Chinzei, T. Ichiki, R. Kurosaki, J. Kikuchi, N. Ikegami, T. Fukazawa, H. Shindo, and Y. Horiike, SiO2 Etching Employing Inductively Coupled Plasma with Hot Inner Wall, Jpn J Appl Phys **35**, 2472 (1996).
[253] F. Laermer and A. Urban, *Through-Silicon Vias Using Bosch DRIE Process Technology*, in *Ultra-Thin Chip Technology and Applications*, Joachim Burghartz (Springer New York, NY, 2010), pp. 81–91.
[254] J. Nos, R. Dussart, T. Tillocher, P. Lefaucheux, and M. Boufnichel, Evaluation of Bosch processing and C4F8 plasma deposition at cryogenic temperatures, J Micromech Microeng **34**, 1 (2024).
[255] F. Laermer and A. Schilp, *Method for Anisotropic Plasma Etching of Substrates*, US5498312A (12 March 1996).
[256] M. A. Blauw, T. Zijlstra, and E. van der Drift, Balancing the etching and passivation in time-multiplexed deep dry etching of silicon, J. Vac. Sci. Technol. B Microelectron. Nanometer Struct. **19**, (2001).
[257] S. L. Burkett, M. B. Jordan, R. P. Schmitt, L. A. Menk, and A. E. Hollowell, Tutorial on forming through-silicon vias, J. Vac. Sci. Technol. A **38**, 031202 (2020).
[258] O. Fursenko, J. Bauer, S. Marschmeyer, and H.-P. Stoll, Through silicon via profile metrology of Bosch etching process based on spectroscopic reflectometry, Microelectron. Eng. **139**, 70 (2015).
[259] J. W. Choi, W. L. Loh, S. K. Praveen, R. Murphy, and E. T. K. Swee, A study of the mechanisms causing surface defects on sidewalls during Si etching for TSV (through Si via), J. Micromechanics Microengineering **23**, 065005 (2013).
[260] T. Tillocher, J. Nos, G. Antoun, P. Lefaucheux, M. Boufnichel, and R. Dussart, Comparison between Bosch and STiGer Processes for Deep Silicon Etching, Micromachines **12**, (2021).
[261] V. M. Donnelly and A. Kornblit, Plasma Etching: Yesterday, today and tomorrow.pdf, J. Vac. Sci. Technol. Vac. Surf. Films **31**, 1 (2013).
[262] A. Sankaran and M. J. Kushner, Fluorocarbon plasma etching and profile evolution of porous low-dielectric-constant silica, Appl. Phys. Lett. **82**, 1824 (2003).

[263] O. V. Balachova, M. A. R. Alves, J. W. Swart, E. S. Braga, and L. Cescato, CF4 plasma etching of materials used in microelectronics manufacturing, Microelectron. J. **31**, 213 (2000).
[264] J. L. Mauer, J. S. Logan, L. B. Zielinski, and G. C. Schwartz, Mechanism of silicon etching by CF4 plasma, J Vac Sci Technol **15**, 1734 (1978).
[265] K. Suzuki, S. Okudaira, S. Nishimatsu, K. Usami, and I. Kanomata, Microwave Plasma Etching of Si with CF4 and SF6 Gas, J. Electrochem. Soc. **129**, 2764 (1982).
[266] H. Rhee, H. M. Lee, Y. M. Namkoung, C.-K. Kim, H. Chae, and Y. W. Kim, Dependence of etch rates of silicon substrates on the use of C4F8 and C4F6 plasmas in the deposition step of the Bosch process, J Vac Sci Technol B **27**, 33 (2024).
[267] M. Schaepkens and G. S. Oehrlein, A Review of SiO2 Etching Studies in Inductively Coupled Fluorocarbon Plasmas, J. Electrochem. Soc. **148**, C211 (2001).
[268] X. Li, L. Ling, X. Hua, G. S. Oehrlein, Y. Wang, A. V. Vasenkov, and M. J. Kushner, Properties of C4F8 inductively coupled plasmas. I. Studies of Ar/c-C4F8 magnetically confined plasmas for etching of SiO2, J Vac Sci Technol A **A**, 500 (2004).
[269] C. B. Labelle, V. M. Donnelly, G. R. Bogart, R. L. Opila, and A. Kornblit, Investigation of fluorocarbon plasma deposition from c-C4F8 for use as passivation during deep silicon etching, J. Vac. Sci. Technol. A **22**, (2004).
[270] Y. Hikosaka, M. Nakamura, and H. Sugai, Free Radicals in an Inductively Coupled Etching Plasma, Jpn J Appl Phys **33**, 2157 (1994).
[271] D. Zhang and M. J. Kushner, *Sticking Coeffcients of Neutrals in an RF Fluorocarbon Discharge*, https://cpseg.eecs.umich.edu/pub/presentations/dzhang_gec99.pdf.
[272] M. Nagel, Plasma-Wall Interaction in Fluorocarbon Plasmas, Master Thesis, University of Greifswald, 2012.
[273] K. Endo and T. Tatsuni, Controlling Fluorine Concentration of Fluorinated Amorphous Carbon - Thin Films for Low Dielectric Constant Interlayer Dielectrics, Jpn. J. Appl. Phys. **36**, L 1531 (1997).
[274] G. Antoun, P. Lefaucheux, T. Tillocher, R. Dussart, K. Yamazaki, K. Yatsuda, J. Faguet, and K. Maekawa, Cryo atomic layer etching of SiO2 by C4F8 physisorption followed by Ar plasma, Appl. Phys. Lett. **115**, (2019).
[275] G. Antoun, T. Tillocher, P. Lefaucheux, J. Faguet, K. Maekawa, and R. Dussart, Mechanism understanding in cryo atomic layer etching of SiO2 based upon C4F8 physisorption, Sci. Rep. **11**, (2021).
[276] Y. Miyakawa, K. Fujita, N. Hirashita, N. Ikegami, J. Hashimoto, T. Matsui, and J. Kanamori, Thermal Desorption Spectroscopy and x-ray Photoelectron Spectroscopy Study of CFx Layer Deposited on Si and SiO2, Jpn. J. Appl. Phys. **33**, 7047 (1994).
[277] A. V. Vasenkov, X. Li, G. S. Oehrlein, and M. J. Kushner, Properties of c-C4F8 inductively coupled plasmas. II. Plasma chemistry and reaction mechanism for modeling of Ar/c-C4F8/O2 discharges, J Vac Sci Technol A **22**, 511 (2004).
[278] S.-X. Zhao, Y.-R. Zhang, F. Gao, Y.-N. Wang, and A. Bogaerts, Bulk plasma fragmentation in a C4F8 inductively coupled plasma: A hybrid modeling study, J Appl Phys **117**, (2015).
[279] G. Le Dain, A. Rhallabi, A. Girard, C. Cardinaud, F. Roqueta, and M. Boufnichel, Modeling of ICP C4F8 plasma: effects of high RF power on the plasma electrical properties.pdf, Plasma Sources Sci. Technol. **28**, 13 (2019).
[280] D. Zhang and M. J. Kushner, Surface kinetics and plasma equipment model for Si etching by fluorocarbon plasmas, J Appl Phys **87**, 10.1063/1.371980 (2000).
[281] D. Zhang and M. J. Kushner, Investigations of surface reactions during C2F6 plasma etching of SiO2 with equipment and feature scale models, J Vac Sci Technol A **19**, 524 (2001).
[282] O. Kwon and H. H. Sawin, Surface kinetics modeling of silicon and silicon oxide plasma etching. I. Effect of neutral and ion fluxes on etching yield of silicon oxide in fluorocarbon plasmas, J. Vac. Sci. Technol. A **24**, 1906 (2006).

[283] E. Gogolides, P. Vauvert, G. Kokkoris, G. Turban, and A. G. Boudouvis, Etching of SiO2 and Si in fluorocarbon plasmas: A detailed surface model accounting for etching and deposition, J Appl Phys **88**, 5570 (2000).
[284] G. Kokkoris, E. Gogolides, and A. G. Boudouvis, Etching of SiO2 features in fluorocarbon plasmas: Explanation and prediction of gas-phase-composition effects on aspect ratio dependent phenomena in trenches, J Appl Phys **91**, 2697 (2002).
[285] S. Takagi, S. Onoue, K. Nishitani, T. Shinnmura, and Y. Shigesato, Comparison of CF4 and C4F8 gas etching profiles by multiscale simulation, Jpn J Appl Phys **54**, (2015).
[286] O. Ertl and S. Selberherr, Three-dimensional level set based Bosch process simulations using ray tracing for flux calculation, Microelectron. Eng. **87**, 20 (2010).
[287] P. Moroz and D. J. Moroz, Numerical Simulation of Bosch Processing for Deep Silicon Plasma Etching, J. Phys. Conf. Ser. **550**, (2014).
[288] Z. Ouyang, W. Xu, D. N. Ruzic, M. Kiehlbauch, A. Schrinsky, and K. Torek, Finite-element simulation models and experimental verification for through-silicon-via etching: Bosch process and single-step etching, J Vac Sci Technol A **32**, 1 (2014).
[289] G. Le Dain, A. Rhallabi, C. Cardinaud, A. Girard, M. C. Fernandez, M. Boufnichel, and F. Roqueta, Modeling of silicon etching using Bosch process: Effects of oxygen addition on the plasma and surface properties, J Vac Sci Technol A **36**, (2018).
[290] G. Le Dain, A. Rhallabi, M. C. Fernandez, M. Boufnichel, and F. Roqueta, Multiscale approach for simulation of silicon etching using SF6/C4F8 Bosch process, J Vac Sci Technol A **35**, (2017).
[291] A. Dąbrowski, Adsorption — From theory to practice, Adv. Colloid Interface Sci. **93**, 135 (2001).
[292] H. J. Kreuzer and Z. W. Gortel, *Physisorption Kinetics*, 1st edition (Springer, 1986).
[293] R. Schwiedernoch, Partial and Total Oxidation of Methane in Monolithic Catalysts at Short Contact Times, Heidelberg University, 2005.
[294] K. Oura, M. Katayama, A. V. Zotov, V. G. Lifshits, and A. A. Saranin, *Atomic Structure of Surfaces with Adsorbates*, in *Surface Science*, 1st ed. (Springer, Berlin, Heidelberg, 2003), pp. 195–227.
[295] M. R. Murialdo, Anomalous Thermodynamics of Non-Ideal Gas Physisorption on Nanostructured Carbons, California Institute of Technology, 2017.
[296] J. E. Jones, On the determination of molecular fields. —II. From the equation of state of a gas, Proc. R. Soc. Lond. **106**, 463 (1924).
[297] J. Lenhard, S. Stephan, and H. Hasse, On the History of the Lennard-Jones Potential, Ann. Phys. **536**, (2024).
[298] M. Thommes, K. Kaneko, A. V. Neimark, J. P. Olivier, F. Rodriguez-Reinoso, J. Rouquerol, and K. S. W. Sing, Physisorption of gases, with special reference to the evaluation of surface area and pore size distribution (IUPAC Technical Report), Pure Appl Chem **87**, 1051 (2015).
[299] J. Park, S. J. Kwak, S. Kang, S. Oh, B. Shin, G. Noh, T. S. Kim, and C. Kim, Area-selective atomic layer deposition on 2D monolayer lateral superlattices, Nat. Commun. **15**, (2024).
[300] P. A. Redhead, Thermal Desorption of Gases, (1962).
[301] B. Vermang, M. Juel, and S. Raaen, Temperature programed desorption of C2H4 from pure and graphite-covered Pt (111), J Vac Sci Technol A **25**, (2007).
[302] K. Oura, M. Katayama, A. V. Zotov, V. G. Lifshits, and A. A. Saranin, *Elementary Processes at Surfaces I. Adsorption and Desorption*, in *Surface Science*, 1st ed. (Springer, Berlin, Heidelberg, 2003), pp. 295–323.
[303] M. Batzill, Surface Science Studies of Gas Sensing Materials: SnO2, Sensors **6**, 1345 (2006).
[304] D. M. Hoffman, B. Singh, and J. H. Thomas, III, *Handbook of Vacuum Science and Technology*, 1st ed. (Academic Press, 1997).
[305] I. Langmuir, The adsorption of gases on plane surfaces of glass, mica and platinum, J. Am. Chem. Soc. **40**, 1361 (1918).
[306] S. Brunauer, P. H. Emmett, and E. Teller, Adsorption of Gases in Multimolecular Layers, J. Am. Chem. Soc. **60**, 309 (1938).

[307] S. Brunauer and P. H. Emmett, The Use of Low Temperature van der Waals Adsorption Isotherms in Determining the Surface Areas of Various Adsorbents, J. Am. Chem. Soc. **59**, 2682 (1937).
[308] M. Bagley, *Matter: Definition & the Five States of Matter*, https://www.livescience.com/46506-states-of-matter.html.
[309] P. Papon, J. Leblond, and P. H. E. Meijer, *The Physics of Phase Transitions*, 1st ed. (Springer Berlin, Heidelberg, 2002).
[310] A. Safari, R. Saidur, F. A. Sulaiman, Y. Xu, and J. Dong, A review on supercooling of Phase Change Materials in thermal energy storage systems, Renew. Sustain. Energy Rev. **70**, 905 (2017).
[311] J. Wisniak, Historical development of the vapor pressure equation from Dalton to Antoine, J. Phase Equilibria **22**, 622 (2001).
[312] D. Roizard, *Antoine Equation*, in *Encyclopedia of Membranes* (Springer-Verlag Berlin Heidelberg, 2015), pp. 1–3.
[313] D. M. Romps, The Rankine-Kirchhoff approximations for moist thermodynamics, Q J R Meteorol Soc **147**, 3493 (2021).
[314] G. WM. Thomson, The Antoine Equation for Vapor-pressure Data, Chem. Rev. **38**, 1 (1946).
[315] W. Waring, Form of a Wide-Range Vapor Pressure Equation, Ind. Eng. Chem. **46**, 762 (1954).
[316] D. H. Zaitsau, *Experimental Determination of Vapor Pressures*, in *Gibbs Energy and Helmholtz Energy: Liquids, Solutions and Vapours*, Emmerich Wilhelm; Trevor M Letcher (Royal Society of Chemistry, 2021).
[317] W. Wagner, New vapour pressure measurements for argon and nitrogen and a new method for establishing rational vapour pressure equations, Cryogenics **13**, 470 (1973).
[318] W. V. Wilding, R. L. Rowley, and J. L. Oscarson, DIPPR Project 801 evaluated process design data, Fluid Phase Equilibria **150–151**, 413 (1998).
[319] K. Růžička, M. Fulem, and V. Růžička, *Vapor Pressure of Organic Compounds. Measurement and Correlation*.
[320] W. Chen, A. J. Haslam, A. Macey, U. V. Shah, and C. Brechtelsbauer, Measuring Vapor Pressure with an Isoteniscope: A Hands-On Introduction to Thermodynamic Concepts, J. Chem. Educ. **93**, 920 (2016).
[321] M. B. Ewing and J. C. S. Ochoa, Vapour pressures of n-hexane determined by comparative ebulliometry, J Chem Thermodyn. **38**, 283 (2006).
[322] R. Kendler, F. Dreisbach, R. Seif, S. Pollak, and M. Petermann, Measuring low vapor pressures employing the Knudsen effusion technique and a magnetic suspension balance, Rev Sci Instrum **90**, (2019).
[323] B. Koutek, V. Pokorný, T. Mahnel, V. Štejfa, K. Řehák, M. Fulem, and K. Růžička, Estimating Vapor Pressure Data from Gas–Liquid Chromatography Retention Times: Analysis of Multiple Reference Approaches, Review of Prior Applications, and Outlook, J Chem Eng Data **67**, 2017 (2022).
[324] T. B. Douglas and R. F. JR. Krause, Evaluation of a simple static method for measuring vapor pressure, J Chem Thermodyn. **9**, 511 (1977).
[325] E. Brini, C. J. Fennell, M. Fernandez-Serra, B. Hribar-Lee, M. Lukšič, and K. A. Dill, How Water's Properties Are Encoded in Its Molecular Structure and Energies, Chem. Rev. **117**, 12385 (2017).
[326] M. Chaplin, *Water Properties*, https://water.lsbu.ac.uk/water/water_properties.html#d.
[327] National Institute of Standards and Technology, *Water*, https://webbook.nist.gov/cgi/cbook.cgi?ID=C7732185&Mask=4#Thermo-Phase.
[328] A. B. Kletskii and L. E. Petrik, Dependence of Vapor Pressure of Perfluorocyclobutane, Zh Fiz Khim **41**, 1183 (1967).
[329] R. Krauss and K. Stephan, Thermal Conductivity of Refrigerants in a Wide Range of Temperature and Pressure, J. Phys. Chem. Ref. Data **18**, (1989).
[330] Linde, *Sulfur Hexafluoride Datasheet*.
[331] Solvay Special Chemicals, *Sulphur Hexafluoride*.

[332] T. Ohta, O. Yamamuro, and H. Suga, Heat capacity and enthalpy of sublimation of sulfur hexafluoride, J Chem Thermodyn. **26**, 319 (1994).
[333] D. R. Stull, Vapor Pressure of Pure Substances. Organic and Inorganic Compounds, Ind Eng Chem **39**, 517 (1947).
[334] E. L. Pace and J. S. Mosser, Thermodynamic Properties of Silicon Tetrafluoride from 15°K to Its Triple Point. The Entropy from Molecular and Spectroscopic Data, J. Chem. Phys. **39**, 154 (1963).
[335] H. S. Booth and C. F. Swinehart, The Critical Constants and Vapor Pressures at High Pressure of Some Gaseous Fluorides of Group IV, J Am Chem Soc **57**, 1337 (1935).
[336] R. H. Valentine, G. E. Brodale, and W. F. Giauque, Trifluoromethane: Entropy, Low-Temperature Heat Capacity, Heats of Fusion, and Vaporization, and Vapor pressure, J Phys Chem **66**, 392 (1962).
[337] K. Ohgaki, S. Umezono, and T. Katayama, Pressure-Density-Temperature (P-p-T) Relations of CHF3, N2O, and C3H6 in the Critical Region, J. Supercrit. Fluids **3**, 78 (1990).
[338] J. H. Smith and E. L. Pace, Thermodynamic properties of carbon tetrafluoride from 12.deg.K to its boiling point. Significance of the parameter .nu., J. Phys. Chem. **73**, 4232 (1969).
[339] V. W. Menzel and F. Mohry, Die Dampfdrucke des CF4 und NF3 und der Tripelpunkt des CF4, Z. Für Anorg. Allg. Chem. **210**, 257 (1933).
[340] V. V. Altunin, V. Z. Geller, E. A. Kremenvskaya, I. I. Perel'shtein, and E. K. Petrov, *Thermophysical Properties of Freons*, National Standard Reference Data Service of the USSR: A Series of Property Tables, Vol. 9 (1987).
[341] H. Sato, K. Watanabe, J. M. H. Levelt Sengers, J. S. Gallagher, P. G. Hill, J. Straub, and W. Wagner, Sixteen Thousand Evaluated Experimental Thermodynamic Property Data for Water and Steam, J. Phys. Chem. Ref. Data **20**, 1 (1991).
[342] G. T. Brower and G. Thodos, Vapor Pressures of liquid Oxygen between the Triple Point and Critical Point, J. Chem. Eng. Data **13**, 262 (1968).
[343] L. I. Drii and V. A. Rabinovich, Dependence of Vapor Pressure of Argon, Zh Fiz Khim **40**, 709 (1966).
[344] M. P. Edejer and G. Thodos, Vapor Pressures of Liquid Nitrogen Between the Triple and Critical Points, J Chem Eng Data **12**, 206 (1967).
[345] S. Angus, K. M. de Reuck, and R. D. McCarty, *Helium International Thermodynamic Tables of the Fluid State -4*, 1st Edition (Pergamon Press, Pergamon Press Ltd., Headington Hill Hall, Oxford OX3 OBW, England, 1977).
[346] Compressed Gas Association, *Hydrogen Fluoride*, in *Handbook of Compressed Gases* (Springer US, Boston, MA, 1999), pp. 441–447.
[347] W. F. Giauque and C. C. Stephenson, Sulfur Dioxide. The Heat Capacity of Solid and Liquid. Vapor Pressure. Heat of Vaporization. The Entropy Values from Thermal and Molecular Data, J Am Chem Soc **60**, 1389 (1938).
[348] E. L. Pace and B. F. Turnbull, Thermodynamic Properties of Thionyl Fluoride from 13°K to Its Boiling Point. Entropy from Molecular and Spectroscopic Data, J. Chem. Phys. **43**, 1953 (1965).
[349] F. Cemin, A. Girard, and C. Cardinaud, On the low temperature limits for cryogenic etching: A quasi in situ XPS study, Appl. Surf. Sci. **637**, (2023).
[350] Messer Group GmbH, *Octafluorobutane C4F8 Gas Sheet*, https://www.messer.es/documents/921887/0/Oktafluorcyklobutan.pdf/9dd22df5-2063-029f-d5c1-288d7f8ffcc6?t=1681893447274.
[351] PubChem, *Polytetrafluoroethylene*, https://pubchem.ncbi.nlm.nih.gov/compound/Polytetrafluoroethylene.
[352] J. Nos, S. Iséni, M. Kogelschatz, G. Cunge, P. Lefaucheux, R. Dussart, T. Tillocher, and E. Despiau-Pujo, Cryogenic cyclical etching of Si using CF4 plasma passivation steps: the role of CF radicals, Appl. Phys. Lett. (2024).
[353] J.-P. Booth, Optical and electrical diagnostics of fluorocarbon plasma etching processes, Plasma Sources Sci Technol **8**, 249 (1999).

[354] J. P. Booth, H. Abada, P. Chabert, and D. B. Graves, CF and CF2 radical kinetics and transport in a pulsed CF4 ICP, Plasma Sources Sci Technol **14**, 273 (2005).
[355] G. Cunge, D. Vempaire, M. Touzeau, and N. Sadeghi, Broadband and time-resolved absorption spectroscopy with light emitting diodes: Application to etching plasma monitoring, Appl Phys Lett **91**, 1 (2007).
[356] Y. Cho, Y. Kim, S. Kim, and H. Chae, Atomic Layer Etching of SiO2 for surface cleaning using ammonium fluorosilicate with CF4/NH3 plasma, J Vac Sci Technol A **38**, 1 (2020).
[357] V. O. Kuzmenko, A. V. Miakonkikh, and K. V. Rudenko, Investigation of fluorocarbon film deposition from Ar/CF4/H plasma, High Energy Chem. **57**, S100 (2023).

Annex I: List of ion masses of interest during QMS acquisitions

Mass	Main species of interest	Isotopes or other potential species
1	H^+	
4	He^+	
12	C^+	
13		C^+ (iso 1,1%)
14	N+	
15		N^+ (iso 0,4%)
16	O^+	
17	HO^+	
18	H_2O^+	O^+ (iso 0,2%)
19	F^+	H_3O^+
20	HF^+	
28	Si^+	N_2^+ ; CO^+
29		Si^+ (iso 5,1%)
30		Si^+ (iso 3,4%)
31	CF^+	
32	O_2^+ ; CHF^+ ; S^+	CF^+ (iso 1,1%)
33		S^+ (iso 0,8%)
34		S^+ (iso 4,4%)
38	F_2^+	
40	Ar^+	
44	SiO^+	CO_2^+ ; N_2O^+
45		SiO^+ (iso 5,1%)
46		SiO^+ (iso 3,6%) ; NO_2^+
47	SiF^+	
48	SO^+	SiF^+ (iso 5,1%)
49		SiF^+ (iso 3,4%) ; SO+ (iso 0,8%)
50	CF_2^+	SO^+ (iso 4,6%)
51	SF^+ ; CHF_2^+	CF_2^+ (iso 1,1%)
52		SF^+ (iso 0,8%)
53		SF^+ (iso 4,4%)
60	SiO_2^+	
61		SiO_2^+ (iso 5,1%)
62		SiO_2^+ (iso 3,8%)
63	$SiOF^+$	
64	S_2^+ ; SO_2^+	$SiOF^+$ (iso 5,1%)
65		$SiOF^+$ (iso 3,6%) ; S^+ (iso 1,6%) ; SO_2^+ (iso 0,9%)
66	SiF_2^+	S_2^+ (iso 8,9%) ; SO_2^+ (iso 4,8%)
67	SOF^+	SiF_2^+ (iso 5,1%) ; S_2^+ (iso 0,1%)
68		SiF_2^+ (iso 3,4%) ; SOF^+ (iso 0,8%) ; S_2^+ (iso 0,2%)
69	CF_3^+ ; $SOFH_2^+$	SOF^+ (iso 4,6%)
70	SF_2^+ ; CHF_3^+	
71		$SF2^+$ (iso 0,8%) ; CHF_3^+ (iso 1,1%)
72		$SF2^+$ (iso 4,4%)
82	$SiOF_2^+$	
83	S_2F^+ ; SO_2F^+	$SiOF_2^+$ (iso 5,1%)
84		$SiOF_2^+$ (iso 3,6%) ; S_2F^+ (iso 1,6%) ; SO_2F^+ (iso 0,9%)
85	SiF_3^+	S_2F^+ (iso 8,9%) ; SO_2F^+ (iso 4,8%)
86	SOF_2^+ ; $C_4F_2^+$	SiF_3^+ (iso 5,1%) ; S_2F^+ (iso 0,1%)
87		SiF_3^+ (iso 3,4%) ; SOF_2^+ (0,8%) ; S_2F^+ (iso 0,2%)
88	CF_4^+	SOF_2^+ (iso 4,6%)
89	SF_3^+	CF_4^+ (iso 1,1%)
90		SF_3^+ (iso 0,8%)

91	Si_2OF^+	SF_3^+ (iso 4,4%)
92		Si_2OF^+ (iso 10,2%)
93	$C_3F_3^+$	Si_2OF^+ (iso 7,2%)
94	$Si_2F_2^+$	$C_3F_3^+$ (iso 3,2%) ; Si_2OF^+ (iso 0,4%)
95		$Si_2F_2^+$ (iso 10,1%) ; Si_2OF^+ (iso 0,1%)
96		$Si_2F_2^+$ (iso 7%)
97		$Si_2F_2^+$ (iso 0,3%)
98		$Si_2F_2^+$ (iso 0,1%)
100	$C_2F_4^+$	
101		$C_2F_4^+$ (iso 2,2%)
102	$S_2F_2^+$; $SO_2F_2^+$	
103		$S_2F_2^+$ (iso 1,6%) ; $SO_2F_2^+$ (iso 0,9%)
104	SiF_4^+	$S_2F_2^+$ (iso 8,9%) ; $SO_2F_2^+$ (iso 4,8%)
105	SOF_3^+	SiF_4^+ (iso 5,1%) ; $S_2F_2^+$ (iso 0,1%)
106		SiF_4^+ (iso 3,4%) ; SOF_3^+ (iso 0,8%) ;$S_2F_2^+$ (iso 0,2%)
107		SOF_3^+ (iso 4,6%)
108	SF_4^+	
109		SF_4^+ (iso 0,8%)
110		SF_4^+ (iso 4,4%)
119	$C_2F_5^+$	
120		$C_2F_5^+$ (iso 2,2%)
127	SF_5^+	
128		SF_5^+ (iso 0,8%)
129		SF_5^+ (iso 4,4%)
131	$C_3F_5^+$	
132		$C_3F_5^+$ (iso 3,2%)
146	SF_6^+	
147		SF_6^+ (iso 0,8%)
148		SF_6^+ (iso 4,4%)
150	$C_3F_6^+$	
151		$C_3F_6^+$ (iso 3,2%)
200	$C_4F_8^+$	
201		$C_4F_8^+$ (iso 4,3%)
202		$C_4F_8^+$ (iso 0,1%)
250	$C_5F_{10}^+$	
251		$C_5F_{10}^+$ (iso 5,4%)
252		$C_5F_{10}^+$ (iso 0,1%)

Jack NOS

Etude de procédés de cryogravure à base de gaz fluorocarbonés

Résumé :

Cette thèse a été réalisée au GREMI dans le cadre du projet ANR PSICRYO, en collaboration avec le laboratoire des technologies de la microélectronique (LTM) et l'institut des matériaux de Nantes Jean Rouxel (IMN). Le but de ce projet de recherche était d'étudier les interactions plasma-surface dans les procédés de cryogravure avancés. Les procédés de cryogravure par plasma se caractérisent par une thermalisation du substrat en dessous de -40°C ce qui permet de renforcer certains mécanismes de passivation. Ces procédés sont à l'étude dans le secteur de la microélectronique car ils permettent des gravures d'une grande précision avec une altération moindre des couches minces de surface. Ce manuscrit résume les résultats de cryogravure obtenus sur des matériaux à base de silicium (principalement Si et SiO_2) en utilisant des procédés cycliques de type Bosch avec la répétition de plasmas fluorocarbonés (c-C_4F_8 et CF_4) suivi de plasma SF_6. Ce travail a été réalisé avec un réacteur ICP qui dispose d'un porte-substrat cryogénique utilisant de l'azote liquide pouvant atteindre -150°C. L'étude s'est principalement portée sur la relation entre les propriétés de gravure obtenues et les paramètres du plasma qui ont pu être caractérisés en fonction de la température du porte-substrat entre 20°C et -150°C. La caractérisation des profils, vitesses et sélectivités de gravure a été réalisée par microscopie électronique par balayage (MEB) et ellipsométrie in-situ. La caractérisation des propriétés des plasmas étudiés a été réalisée par spectrométrie de masse, spectroscopie d'absorption UV ainsi que par sonde capacitive. L'étude s'est principalement portée sur les procédés de type Bosch où il a été démontré que la diminution de la température permettait de renforcer les mécanismes de passivation apportés par plasmas c-C_4F_8. Par la suite, un procédé cyclique utilisant du CF_4 comme gaz de passivation a pu être développé permettant d'obtenir des profils de gravure anisotropiques à -100°C.

Mots clés : Gravure plasma, Cryogravure, Procédé Bosch, Interactions plasma-surface

Study of cryoetching plasma processes using fluorocarbon gases

Summary :

This PhD thesis was carried out at the GREMI laboratory as part of the ANR PSICRYO project in collaboration with the Laboratoire des Technologies de la Microélectronique (LTM) and the Institut des Matériaux de Nantes Jean Rouxel (IMN). The aim of this research project was to study plasma-surface interactions in advanced cryo-etching processes. Plasma cryoetching processes are characterized by a substrate thermalization below -40°C, which enhances certain passivation mechanisms. These processes are currently studied in the microelectronics industry, as they enable high-precision etching with reduced surface damage. This manuscript summarizes cryo-etching test results obtained on silicon-based materials (mainly Si and SiO_2) using cyclical Bosch type processes consisting in the repetition of fluorocarbon plasmas (c-C_4F_8, CF_4) followed by SF_6 plasma steps. This work was carried out using an ICP reactor equipped with a cryogenic substrate holder using liquid nitrogen which can reach -150°C. The study focused on the relationship between the etching properties obtained and the plasma parameters which were characterized in relation to the substrate temperature between 20°C and -150°C. Characterization of etching profiles, etch rates and selectivities were carried out using scanning electron microscopy (SEM) and in-situ ellipsometry. Plasma characteristics were analyzed by mass spectrometry, UV absorption spectroscopy and capacitive probe measurements. The study focused mainly on Bosch-type processes, where it was demonstrated that the decrease of substrate temperature enhanced fluorocarbon passivation mechanisms provided by c-C_4F_8 plasma. Subsequently, a similar cyclical process using CF_4 plasma for sidewall passivation was developed which allowed to obtain anisotropic etch profiles at -100°C.

Keywords : Plasma etching, Cryoetching, Bosch process, Plasma-surface interactions

Groupe de Recherches sur l'Energétique des Milieux Ionisés (GREMI)
14 rue d'Issoudun BP 6744 45067 Orléans Cedex 2